Institut für Physik und Astronomie
H.E.S.S. Gruppe

Crab Flare Observations with H.E.S.S. Phase II

Dissertation

zur Erlangung des akademischen Grades
"doctor rerum naturalium"
(Dr. rer. nat.)
in der Wissenschaftsdisziplin "Physik"

eingereicht an der
Mathematisch-Naturwissenschaftlichen Fakultät
der Universität Potsdam

von

Arnim Balzer

1. Gutachter: Prof. Christian Stegmann
2. Gutachter: Prof. Thomas Lohse
3. Gutachter: Prof. Hans-Christian Schulz-Coulon

Potsdam, den 15. Dezember 2014

Abstract

The H.E.S.S. array is a third generation Imaging Atmospheric Cherenkov Telescope (IACT) array. It is located in the Khomas Highland in Namibia, and measures very high energy (VHE) gamma-rays. In Phase I, the array started data taking in 2004 with its four identical $13\,\mathrm{m}$ telescopes. Since then, H.E.S.S. has emerged as the most successful IACT experiment to date. Among the almost 150 sources of VHE gamma-ray radiation found so far, even the oldest detection, the Crab Nebula, keeps surprising the scientific community with unexplained phenomena such as the recently discovered very energetic flares of high energy gamma-ray radiation. During its most recent flare, which was detected by the Fermi satellite in March 2013, the Crab Nebula was simultaneously observed with the H.E.S.S. array for six nights. The results of the observations will be discussed in detail during the course of this work.

During the nights of the flare, the new $24\,\mathrm{m} \times 32\,\mathrm{m}$ H.E.S.S. II telescope was still being commissioned, but participated in the data taking for one night. To be able to reconstruct and analyze the data of the H.E.S.S. Phase II array, the algorithms and software used by the H.E.S.S. Phase I array had to be adapted. The most prominent advanced shower reconstruction technique developed by de Naurois and Rolland, the template-based model analysis, compares real shower images taken by the Cherenkov telescope cameras with shower templates obtained using a semi-analytical model. To find the best fitting image, and, therefore, the relevant parameters that describe the air shower best, a pixel-wise log-likelihood fit is done. The adaptation of this advanced shower reconstruction technique to the heterogeneous H.E.S.S. Phase II array for stereo events (i.e. air showers seen by at least two telescopes of any kind), its performance using MonteCarlo simulations as well as its application to real data will be described.

Kurzfassung

Das H.E.S.S. Experiment misst sehr hochenergetische Gammastrahlung im Khomas Hochland von Namibia. Es ist ein sogenanntes abbildendes atmosphärisches Cherenkov-Teleskopsystem welches in der 1. Phase, die im Jahr 2004 mit der Datennahme begann, aus vier identischen $13\,\mathrm{m}$ Spiegelteleskopen bestand. Seitdem hat sich H.E.S.S. als das erfolgreichstes Experiment in der bodengebundenen Gammastrahlungsastronomie etabliert. Selbst die älteste der mittlerweile fast 150 entdeckten Quellen von sehr hochenergetischer Gammastrahlung, der Krebsnebel, fasziniert immernoch Wissenschaftler mit neuen bisher unbekannten und unerwarteten Phänomenen. Ein Beispiel dafür sind die vor kurzem entdeckten sehr energiereichen Ausbrüche von hochenergetischer Gammastrahlung. Bei dem letzten deratigen Ausbruch des Krebsnebels im März 2013 hat das H.E.S.S. Experiment für sechs Nächte simultan mit dem Fermi-Satelliten, welcher den Ausbruch entdeckte, Daten genommen. Die Analyse der Daten, deren Ergebnis und deren Interpretation werden im Detail in dieser Arbeit vorgestellt.

Während dieser Beobachtungen befand sich ein neues $24\,\mathrm{m} \times 32\,\mathrm{m}$ großes Spiegelteleskop, das H.E.S.S. II-Teleskop, noch in seiner Inbetriebnahme, trotzdem hat es für eine dieser sechs Nächte an der Datennahme des gesamten Teleskopsystems teilgenommen. Um die Daten rekonstruieren und analysieren zu können, mussten die für die 1. Phase des Experiments entwickelten Algorithmen und die Software des H.E.S.S.-Experiments angepasst werden. Die fortschrittlichste Schauerrekonstruktionsmethode, welche von de Naurois und Rolland entwickelt wurde, basiert auf dem Vergleich von echten Schauerbildern, die mit Hilfe der Cherenkov-Kameras der einzelnen Teleskope aufgenommen wurden, mit Schauerschablonen die mit Hilfe eines semianalytischen Modells erzeugt wurden. Das am besten passende Bild und damit auch alle relevanten Schauerparameter, wird mit Hilfe einer pixelweisen Loglikelihood-Anpassung ermittelt. Die nötigen Änderungen um Multiteleskopereignisse, welche vom heterogenen H.E.S.S. Phase II Detektor gemessen wurden, mit Hilfe dieser fortschrittlichen Schauerrekonstruktionsmethode analysieren zu können, sowie die resultierenden Ergebnisse von MonteCarlo-Simulationen, als auch die Anwendung auf echte Daten, werden im Rahmen dieser Arbeit präsentiert.

Contents

Change is inevitable.
Progress is optional.

> Tony Robbins

1

Introduction

With the discovery of the cosmic radiation by Victor Francis Hess [1] in 1912 for which he was granted the Nobel Price in Physics in 1936, the era of astroparticle physics started. A photo of Victor Hess at the beginning of one of his famous balloon trips is shown in Figure 1.1a. During his trips he showed that the level of ionizing radiation increased with altitude, indicating a penetrating radiation from outer space, named "cosmic rays" by Andrew Millikan in 1925. During the first half of the 20$^\text{th}$ century, cosmic rays where used as a laboratory for high energy particles:

- Discovery of the positron by Anderson [2] in 1932.

- Discovery of the muon by Anderson and Neddermeyer [3] in 1936.

- Discovery of the pion by Lattes, Occhialini, and Powell [4] in 1947.

- Discovery of the kaon by Rochester and Butler [5] in 1947.

During the second half of the 20$^\text{th}$ century, the radiation produced in accelerator facilities took over the part of the cosmic radiation due to their much higher luminosities and ease of accessibility. However, the highest energies reached by now in accelerators, like the LHC at CERN, do not exceed 14 TeV. Cosmic rays however show an almost perfect power-law behaviour over more than 12 orders of magnitude as seen in Figure 1.1b with particle energies exceeding 50 EeV. The majority of cosmic rays consists of charged particles, which loose their information of direction during their travel to Earth due to the galactic and inter-galactic magnetic fields. Only the highest energy particles can be used to identify the cosmic accelerators and first indications of their location have been found by the Pierre Auger Collaboration et al. [8]. Another approach to learn about the sources of cosmic rays is to use the gamma-ray component of the cosmic rays, which retains the information about its origin.

Due to the low flux of gamma rays at highest energies large detection areas are needed and space-based detectors become unfeasible. Ground-based experiments cannot detect the cosmic gamma-ray radiation directly because of the absorption of gamma rays in the Earth's atmosphere, therefore an indirect approach using the Cherenkov light generated by the air showers, is used. This light was first observed in 1953 by Galbraith and Jelley [9], shown in Figure 1.2a, and the success story of very high energy (VHE; $E > 10$ GeV) gamma-ray astronomy started. While the first detector was still using ad-hoc

(a) *Photograph of Victor Francis Hess before take-off to one of his famous balloon flights between 1911 and 1913 during which he discovered a penetrating radiation from outer space. It was named "cosmic radiation" by Robert Andrews Millikan in 1925 and several new particles where discovered using this unique laboratory provided by nature. Victor Hess was awarded the Nobel Prize in 1936 "for his discovery of cosmic radiation" together with Carl David Anderson "for his discovery of the positron". Figure taken from [6].*
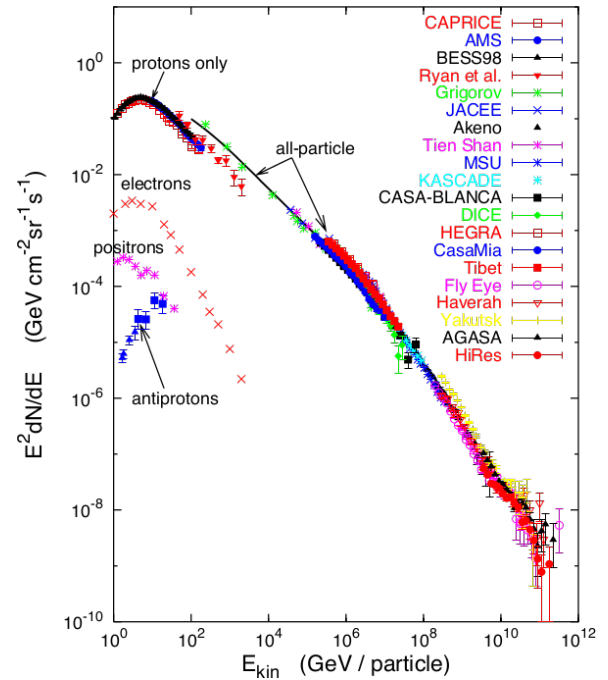
(b) *All-particle spectrum of cosmic rays together with the single spectra of the most abundant particles. The all-particle spectrum follows a power law over a range of more than 12 magnitudes. The "knee" in the spectrum at roughly 10^{15} eV at which point it is believed that extra-galactic particles start to dominate the spectrum, is visible as an increase in the spectral index. At particle energies around 10^{17} eV a decrease in the spectral index, the "ankle" is seen. The origin of this spectral feature is still unclear. Figure taken from [7].*

Figure 1.1.

assembled parts, including a trash bin, as seen in Figure 1.2b, by now the third generation of imaging atmospheric Cherenkov telescopes (IACT) are in operation since a decade. They consist of large optical telescopes with tessellated mirrors with diameters between 10 m and 28 m to detect the faint Cherenkov light flashes. The H.E.S.S. array in Namibia (see Aharonian et al. [11]), is described in detail in Chapter 3, MAGIC on the island of La Palma (see Ferenc and MAGIC Collaboration [12] and Aleksić et al. [13]) and VERITAS in Arizona (see Weekes et al. [14]). Moreover, the first prototypes of the next generation IACT array are already being built and the CTA experiment, see Actis et al. [15], will be an improvement in all aspects over the current third generation experiments.

By now almost 150 sources of VHE gamma-ray radiation are known [16, 17] with most of them being discovered by the H.E.S.S. experiment. The location of these sources are not limited to our own galaxy, but also extra-galactic VHE gamma-ray accelerators have been found. By now a zoo of different source classes exists:

Pulsar wind nebulae (PWNe) Powered by a central fast rotating neutron star (pulsar) these objects
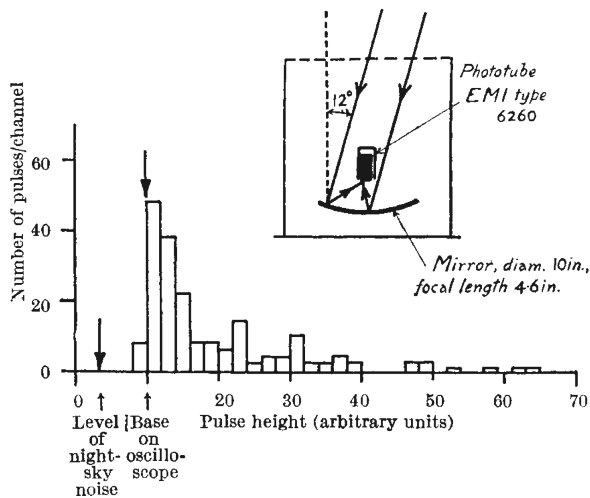
(a) *Number of light pulses per channel versus pulse height of a photo multiplier pointed at the night sky. A clear high intensity signal above the night sky background is visible. The source of the signal is the Cherenkov radiation of air showers induced by cosmic rays hitting the Earth's atmosphere. Figure taken from [9].*
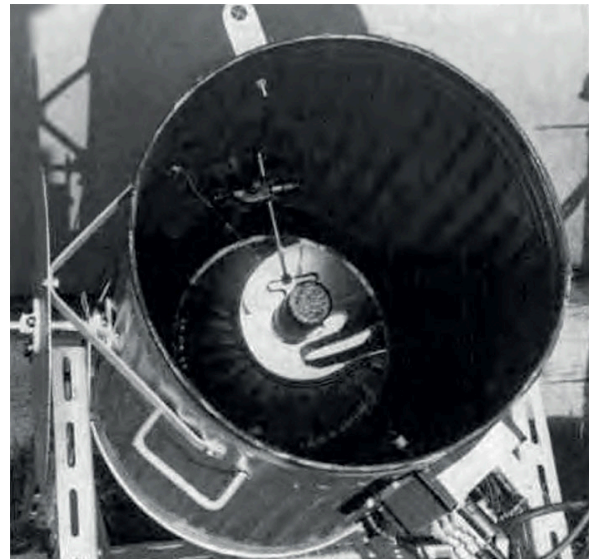
(b) *Photograph of the ad-hoc assembly used for the first detection of Cherenkov light flashes in the night sky. A photo multiplier tube was shielded from surrounding light sources with the help of a trash bin. It was encircled by an array of 18 Geiger-Müller counters, which are not seen on the picture, to test for coincidences with cosmic-ray induced air showers. Figure taken from [10].*

Figure 1.2.

feature a flow of relativistic particles, which were accelerated to highest energies by the large magnetic and electric fields in the vicinity of the pulsar. The emitted electromagnetic radiation spans all wave bands from radio to VHE gamma-rays.

Supernova remnants (SNRs) Shock waves formed by supernova explosions sweeping through their circumstellar media. Around 10% of the kinetic energy of these explosions are used to accelerate particles; thus SNRs are believed to be responsible for the majority of the cosmic rays detected on Earth.

Molecular clouds Giant clouds of gas acting as passive sources for VHE gamma-rays. High energy particles of nearby accelerators interact with the dense medium of the molecular cloud and emit VHE gamma-rays.

Binary systems System of two stellar objects, where one is accreting mass from the other, forming an accretion disk. Particles can be accelerated to very high energies and modulations corresponding to the orbital positions are observed.

Active galactic nuclei Super-massive black holes at the center of galaxies surrounded by huge accretion disks and two jets perpendicular to the plane of the disks. Highly variable sources of electromagnetic radiation in all wave bands.

Starburst galaxies Galaxies with a high star formation rate and, therefore, featuring a high rate of supernova explosions and a plasma wind. The termination shock of the wind is thought to be able to accelerate particles to highest energies.
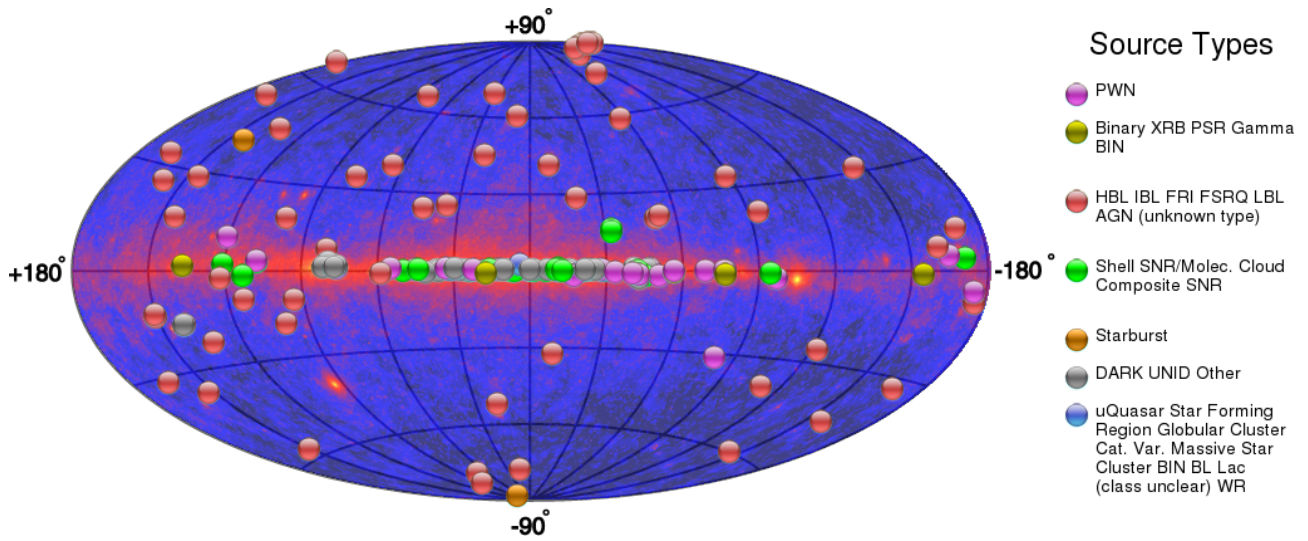
Figure 1.3.: *Shown are the known sources of VHE gamma-ray radiation on top of the Fermi-LAT all sky map in high energy gamma-rays. The center of the Milky Way is seen in the middle of the plot and the galactic disk is aligned with the horizontal axis. Figure taken from [16, 17].*

Globular clusters Large number of massive stars with strong colliding stellar winds, forming several powerful termination shocks act, as acceleration sites for particles.

. . .

One of the most prominent sources of VHE gamma-radiation is the Crab Nebula. It has been used as the standard candle in VHE gamma-ray astronomy over the last decades. A summary of the current knowledge of the Crab Nebula and its observational history will be given in the following chapter.

The H.E.S.S. telescope system has entered its second phase in 2012 with the addition of a fifth bigger telescope to the existing four-telescope array. The new system is well-suited to study gamma rays down to energies of $50\,\text{GeV}$ [18] as will be shown in Chapter 3.

The challenges of the new system include but are not limited to the high efficient operation of the full array as well as the reconstruction of gamma-ray events of the first detector consisting of different telescope types (hybrid system). This thesis describes a reconstruction scheme developed for the reconstruction of gamma-ray events measured with the H.E.S.S. Phase II hybrid system. The reconstruction algorithm will be described in detail in Chapter 4 together with its performance obtained from MonteCarlo simulations.

The thesis concludes with the analysis of data taken during the most recent Crab Nebula flare in March 2013 applying the new reconstruction algorithm to real data.

The pessimist complains about the wind;
the optimist expects it to change;
the realist adjusts the sails.

William Arthur Ward

2

The Crab Nebula

This chapter gives a short overview about our current knowledge about the Crab Nebula. For a more detailed review, the reader is asked to take a look at the following papers which this chapter is based on: Buehler and Blandford [19], Hester [20], Gaensler and Slane [21] and Meyer, Horns, and Zechlin [22].

In July 1054 AD the Chinese astronomer Yang Wêlt observed "the appearance of a guest star" in the night sky. He witnessed a supernova (SN) explosion of Type II (core collapse) [23] (SN 1054) which was visible during the daytime for three weeks and at night for the next 22 months [24]. The remnants of this explosion, the Crab Nebula and the Crab Pulsar have been observed for centuries and are among the best studied sources outside of our own solar system. The third component of the explosion, the freely expanding shell of the supernova itself has only been observed indirectly [23]. The high luminosity of the Crab Pulsar around $1.3 \cdot 10^{38}$ erg cm^{-2} [20] and its proximity of ~ 2 kpc [25] renders the Crab Nebula and the Crab Pulsar one of our prime laboratories for studying non-thermal processes in the Universe. Although the Crab Nebula was only rediscovered in 1731 by the English astronomer John Belvis, it is the first historical supernova that could be associated to a known object in the sky [26, 27]. Charles Messier took the nebulous appearance of the Crab as a reason to assemble the famous Messier catalogue of nebulous non-cometary objects naming the Crab Nebula as its first source M1. The Crab Nebula in optical can be seen in Figure 2.1a. The fine grained features seen via the emission lines of thermal gas are called "filaments" whereas the thin arcs of higher emission in the synchrotron Nebula are labeled "wisps".

2.1. Observations & Characteristics

At first, it was believed that the visible Crab Nebula was the result of the freely expanding SNR of 1054. However, from spectroscopic observations of the filaments in the Crab Nebula, an ejecta mass of the order of 2–5 $M_\odot$ can be obtained [28] which is less than the minimum mass ejected during a core collapse supernova. Moreover, the expansion velocity of the filaments of less than ~ 1500 km/s [29] is significantly below the expected velocities of 5000–10000 km/s known from other young SNRs like Cas A [20]. The resulting kinetic energy output obtained for SN 1054 of $3 \cdot 10^{49}$ ergs is a factor of 30 below the canonical value of 10^{51} ergs. Frail, Kassim, Cornwell, and Goss [30] proposed an atypical low-energy explosion to explain these measurements, however, Chevalier [23] showed that SN 1054 was
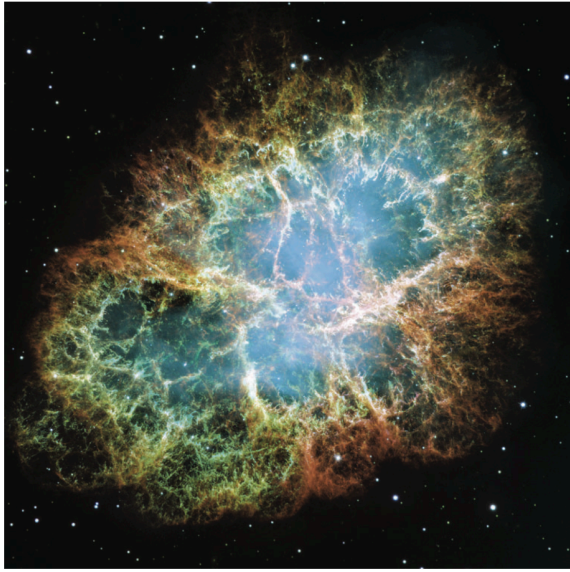
(a) *Composite* Hubble Space Telescope *image of the Crab Nebula. An O III line is shown in red, two S II lines in green and an O I line in blue. The fine structures called "filaments" are due to Rayleigh-Taylor instabilities and are pointing inwards to the pulsar. The thermal ejecta confine the synchrotron nebula which is shown in blue as well. Figure taken from [20].*

(b) *Composite image of the Crab Nebula in different energy bands. Radio in red, optical in green and X-ray in blue. The size of the Nebula is clearly inverse proportional to the energy of the radiation. Figure taken from [19].*

Figure 2.1.: *Crab Nebula seen in different energy bands.*

most likely a Type II supernova explosion using light curves extracted from detailed historical records. The explanation for this predicament is that the observed Crab Nebula is not the freely expanding shell of SN 1054, but instead a PWN driven by a central engine within (the Crab Pulsar). The 16th magnitude star embedded in the Crab Nebula was confirmed to be emitting pulsed radiation with a spin period P of 33.6 ms in the optical and radio wavebands by Staelin and Reifenstein [31] and Cocke, Disney, and Taylor [32]. SN 1054 formed a rapidly rotating young neutron star with a spin down luminosity $\dot{E}$ of $\approx 5 \cdot 10^{38}$ erg/s corresponding to a slowing down in rotation $\dot{P} = 4.2 \cdot 10^{-13}$ [33, 34] using the formula:

$$\dot{E} = -\frac{\mathrm{d}E_{\mathrm{rot}}}{\mathrm{d}t} = 4\pi^2 I \frac{\dot{P}}{P^3} \tag{2.1}$$

Here I is the moment of inertia of the neutron star which, for a mass of $1.4 \, \mathrm{M}_\odot$ and a radius of 10 km, has the value of $1.1 \cdot 10^{45}$ gm/cm². The energy loss of the Crab Pulsar compared to other known pulsars is the second highest observed to date. Assuming an initial spin down period of the pulsar of P_0 such that $\dot{\Omega} = -k\Omega^n$ (where $\Omega = 2\pi/P$, k is a constant and n is the braking index), the initial age of the system τ can be calculated [35]:

$$\tau = \frac{P}{(n-1)\dot{P}} \left[1 - \left(\frac{P_0}{P} \right)^{n-1} \right] \tag{2.2}$$

Using a breaking index $n = 2.51$ [36], Bejger and Haensel [37] estimated P_0 to be ≈ 19 ms for the Crab Pulsar. As a result, it has lost about $\sim 3.6 \cdot 10^{49}$ ergs until now which corresponds to an average

luminosity of $\sim 1.2 \cdot 10^{39}\,\mathrm{erg/s}$. Only $1\,\%$ of this energy is emitted as electromagnetic radiation.

The pulsations are due to the fact that the radiation is emitted in highly collimated beams which sweep the field of view of the Earth in regular intervals. The phase-averaged spectral energy distribution (SED) of the Crab Pulsar is shown in Figure 2.2. It consists of three distinct components. One responsible for the radio emission, a dominant component in the X-ray band and one responsible for the emission above $\sim 100\,\mathrm{MeV}$.
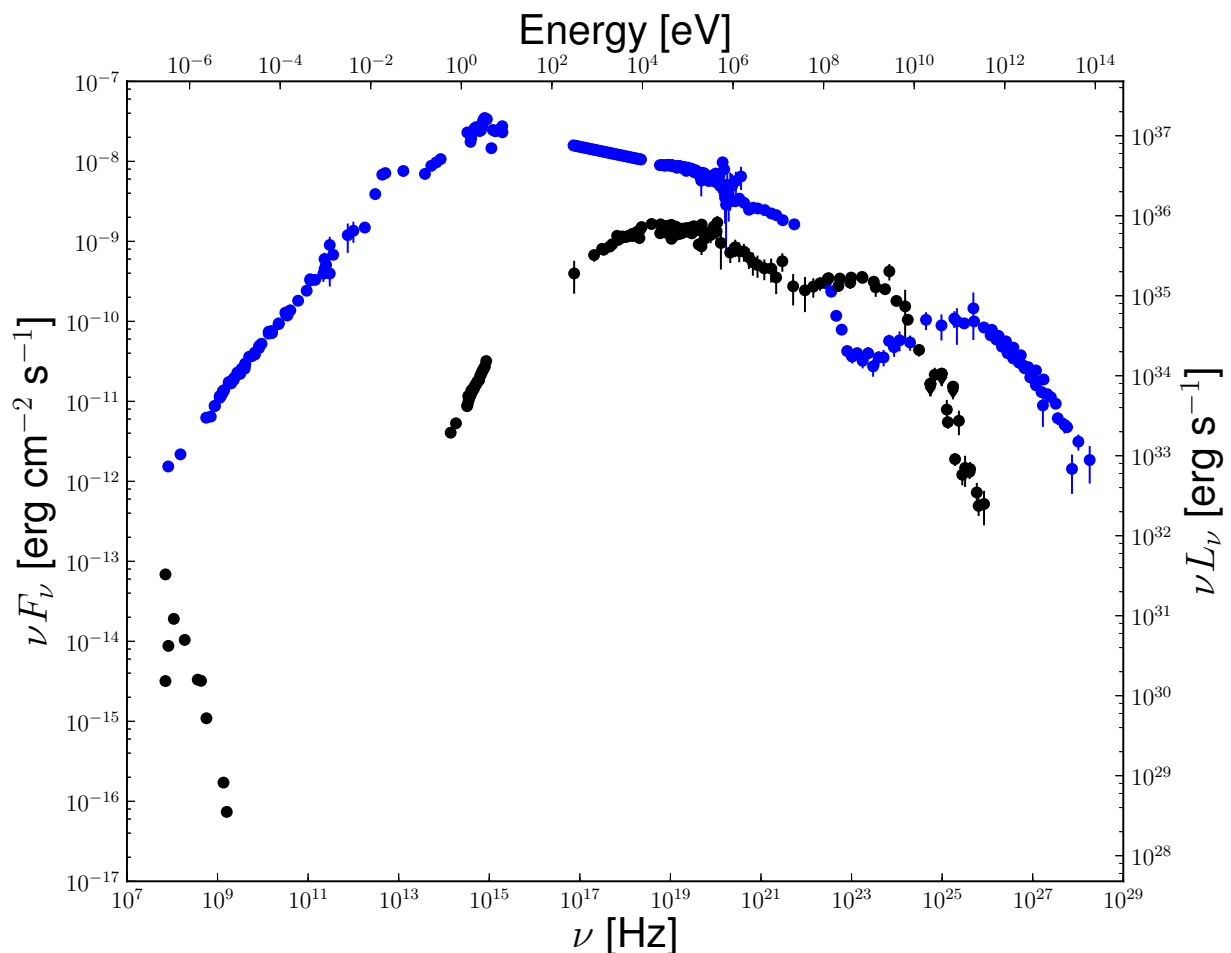
Figure 2.2.: *Spectral energy distribution (SED) of the average emission of the Crab Nebula in blue and phase averaged emission of the Crab Pulsar in black. The pulsar SED consists of three distinct components whereas the nebula SED is described by two. Figure taken from [19].*

Recently, pulsed emission from the Crab Pulsar has been detected up to energies of $400\,\mathrm{GeV}$ by the VERITAS Collaboration et al. [38] and Aleksić et al. [39, 40] for the first time for a pulsar in the VHE gamma-ray regime. This is a surprising result because typically the emission of a pulsar follows an exponential cutoff power-law as shown by Abdo et al. [34]:

$$\nu F_\nu \propto \exp\left(\frac{E}{E_{\mathrm{Cut}}}\right) \tag{2.3}$$

The high-energy (HE) part of the phase-averaged SED of the Crab Pulsar can be seen in Figure 2.3. The Fermi-LAT HE measurement shows a harder than exponential fall of the spectrum which is, however,

not unusual [34]. Nonetheless, the VHE emission measured by VERITAS Collaboration et al. [38] and Aleksić et al. [39, 40] is not in agreement with an extrapolation of the Fermi-LAT spectrum. Instead the spectrum can be described by one power law function with an index around -3.8 above $4\,\mathrm{GeV}$ [38] and no cutoff has been observed up to energies of $\sim 400\,\mathrm{GeV}$ until now.
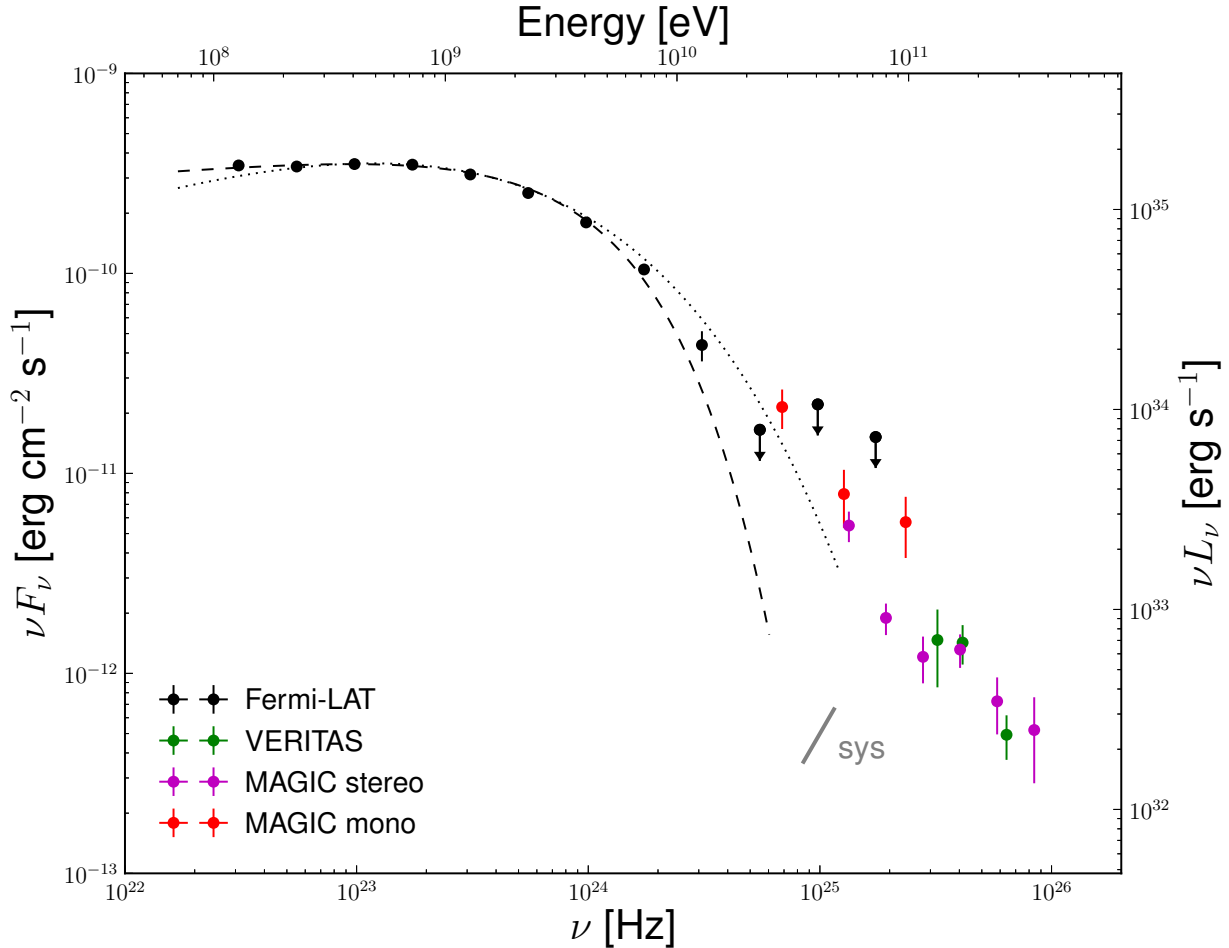
Figure 2.3.: *Phase averaged spectral energy distribution of the Crab Pulsar in gamma-rays. The gray line indicates the systematic error of $\pm15\,\%$ inherent to VHE gamma-ray instruments. The dashed/dotted line indicates the best-fit of the Fermi-LAT data to a power law function with an exponential/sub-exponential cutoff. Figure taken from [19].*

Looking at the distribution of the radiation as a function of the phase ϕ in the different wave bands shown in Figure 2.4, one can see that only small shifts $\Delta\phi \leq 0.01$ between energy bands exist. The main pulse P1 is located at $\phi \approx 0.0$ and the inter-pulse P2 at $\phi \approx 0.4$. The relative flux of P2 with respect to P1 increases from radio to hard X-rays ($100\,\mathrm{keV} < E < 200\,\mathrm{keV}$) and from HE ($100\,\mathrm{MeV} < E < 300\,\mathrm{MeV}$) gamma-rays to VHE ($50\,\mathrm{GeV} < E < 400\,\mathrm{GeV}$) gamma-rays. The Crab Pulsar shows high irregularities on short time scales ($\sim P_{\mathrm{Crab}}^{-1}$) for the radio pulses in P1 and P2 with a flux 1000 times the average [41–43] called "giant pulses". A corresponding increase in optical emission has been observed [44, 45] but not at higher energy bands [46–48].

Pulsar glitches, a rapid increase in spin-down frequency up to $\sim 10^{-5}\,\mathrm{Hz}$ for a limited time, are observed ~ 1 per year [48–50]. The radio emission of the pulsar is also highly polarized and the Crab Pulsar is

Figure 2.4.: *Phase distribution of the flux of the Crab Pulsar in different energy bands. Radio at* 1.4 GHz, *optical between* 1.5 eV *and* 3.5 eV, *X-ray from* 100 keV *to* 200 keV, *HE gamma-rays between* 100 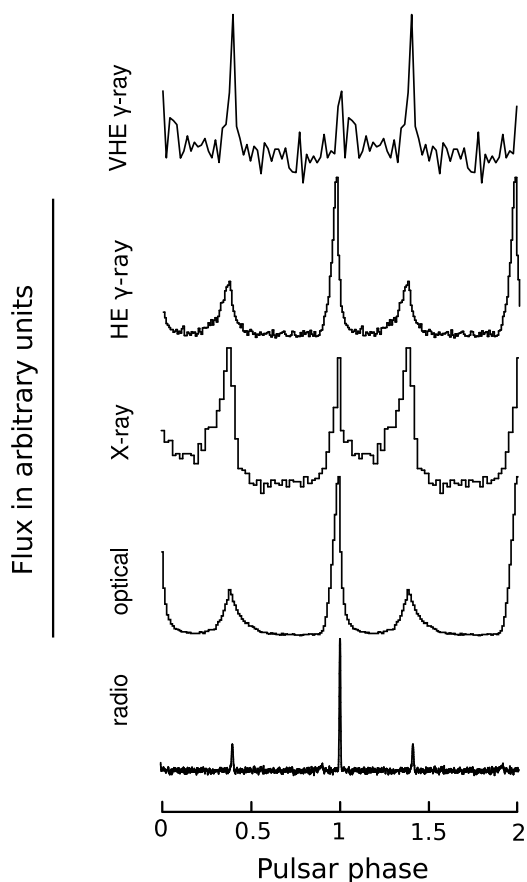MeV *and* 300 MeV *and VHE gamma-rays ranging from* 50 GeV *to* 400 GeV. *The main pulse P1 at* $\phi \approx 0.0$ *and the inter-pulse P2 at* $\phi \approx 0.4$ *are clearly visible in all wavelengths without a major shift. The peaks are getting narrower from optical energies to higher energies. The flux ratio between P1 and P2 for X-rays and VHE gamma-rays is significantly different than in the other energy bands. Figure taken from [19].*

one of the few pulsars for which polarisation has also been detected in the optical wave band [51, 52]. For further details about the characteristics of the polarization the reader is asked to have a look at Buehler and Blandford [19] and references therein.

The Crab Nebula emission in different energy bands can be seen in Figure 2.1b. Its shape is roughly ellipsoidal with a length of the major axis of roughly 4.4 pc and ~ 2.9 pc for the minor one. It is inclined with respect to the plane of the sky by 30 ° [53, 54] and fills a volume of approx. 30 pc^3. The size of the Nebula is decreasing with higher energies due to the particles suffering from synchrotron cooling and energy loss because of adiabatic expansion. The main fraction of the energy released by the pulsar is believed to be a flow of a relativistic magnetized plasma mainly composed of electron positron pairs (in the following only referred to as electrons).

Particles of the nebula loose their energy mainly due to synchrotron and inverse Compton radiation. This process is remarkably efficient and about 26 % of the energy output of the pulsar are converted into synchrotron radiation which is of the same order of magnitude as the expansion work done on the filaments of the nebula. The filaments are the result of Rayleigh-Taylor instabilities acting at the interface between the confined synchrotron nebula and the thermal ejecta. Their structure is often head-to-tail or finger-like and they are pointing inward to the center of the nebula. They are typically less than an arcsecond across and their gas density is roughly 10 times higher than the density in other regions. Their observed expansion velocities between $\sim 700\,\mathrm{km/s}$ and $\sim 1800\,\mathrm{km/s}$ [29] can be compared to known proper motions to obtain a distance estimate to the Crab Nebula of 2 kpc. Two other bright and interesting structures seen in the optical images are the so-called "sprite" and the "inner knot". The former being a fuzzy region at the base of the jet emerging from the pulsar, the latter is detected

$\sim 0.6\ ''$ south east of the pulsar. Their scale is of the order of several arc seconds and they are variable down to time scales of a few hours [55, 56]. However, they do not show any spectral variation from infrared to X-ray energies [57–60].
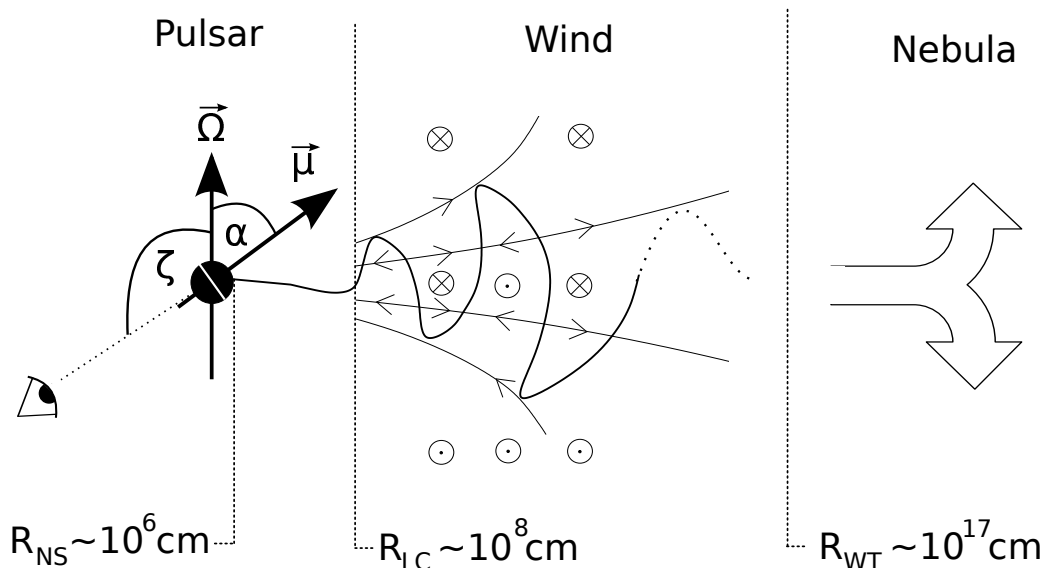
2.2. Particle Acceleration

Figure 2.5.: *Schematic break down of the Crab Nebula in its three components. The pulsar is viewed by the observer via an angle ζ and the magnetic momentum $\vec{\mu}$ is inclined by an angle α to the momentum of the rotation $\vec{\Omega}$. The current sheet is represented by the thicker black line and its undulation is clearly visible. The thinner black lines and the circles represent the open magnetic field lines and the toroidal magnetic field around the pulsar. From observations we know that $\zeta \approx 60\,°$ [61]. The inclination angle α is not known and typically a value of $\approx 45\,°$ is used in modelling [62, 63]. The nebula is formed at the so called termination shock where the particle and fields are randomized. Figure taken from [19].*

The PWN can be divided in three distinct regions. The pulsar with its magnetosphere, the cold pulsar wind and the synchrotron nebula. The magnetosphere extends out to the light cylinder radius:

$$R_{\mathrm{LC}} = \frac{cP}{2\pi} \approx 1.4 \cdot 10^8\ \mathrm{cm} \tag{2.4}$$

In first order, the pulsar can be described as a rotating, perfectly conducting sphere creating a dipole magnetic field. It is an "oblique rotator" because the rotational axis $\vec{\Omega}$ is not parallel to the magnetic moment $\vec{\mu}$, thus tilted by an angle α as seen in Figure 2.5. The compression of the magnetic field of the progenitor star onto the neutron star with a radius of $R_{\mathrm{NS}} \sim 10\,\mathrm{km}$ results in a magnetic field of $B \approx 3.8 \cdot 10^{12} \left(\frac{P}{P_{\mathrm{Crab}}}\right)^{1/2} \left(\frac{\dot{P}}{\dot{P}_{\mathrm{Crab}}}\right)^{1/2}$ G at the equatorial surface. As a result, the electric potential created between the poles and the equator is strong enough to fill the magnetosphere with a plasma of particles which where removed from the surface of the neutron star [64]. The description of the charge separated magnetosphere (to cancel the electric potential [65]) is often done using force free electrodynamics (FFE) approximations, extensions of magneto hydrodynamics (MHD) in which plasma is abundant and inertia free. Magnetic fields $\vec{B}$ and electric fields $\vec{E}$ are shortened out ($\vec{E} \cdot \vec{B} = 0$) and no particle acceleration occurs as well as no resistivity [66]. Li, Spitkovsky, and Tchekhovskoy [67] showed that there is a smooth transition between the vacuum solution and the FFE approximation for

the potential drop over the open field lines and the total spin-down luminosity indicating that the real magnetosphere is in between these two cases.

Because neither FFE nor MHD simulations can explain particle acceleration in the magnetosphere, several different solutions using so-called "gaps" where proposed. They are produced when current is flowing out of the light cylinder following the open field lines and charge starved regions are created behind them. A drop in electronic potential can build up and the resulting discharge via electronic pair cascades leads to particle acceleration. The pulsed emission of radiation is due to the fact, that the particles follow the direction of the magnetic field lines closely and, therefore, co-rotating cones of light are emitted. Several different locations for the gaps have been proposed, for instance the polar gap [68–71] but most notably the outer gap [72–75]. The reader is asked to consult Buehler and Blandford [19] and references therein for further information.

From the FFE approximations it is believed that the magnetic field lines of neutron stars are asymptotically radial outside of the light cylinder [76, 77] and they can be approximated by a monopole in each half of the sphere with the border being at the equator of the neutron star. The field lines reverse their polarity at this border and the approximation is therefore called the "split-monopole" approximation. Due to the trailing of the magnetic field lines of the pulsar rotation, a helical pattern is created. An undulating current sheet aligned to the axis of the magnetic momentum is formed at which the field lines reverse their polarity and create a toroidal magnetic field. The resulting "stripped wind" is magnetically dominated, i.e. the ratio of magnetic to kinetic energy σ is much bigger than one ($\sigma \gg 1$). As a result the "stripped wind" is called "cold" because it does not emit any detectable radiation until it starts to interact with the ejected material from the supernova. At the point where the pressure of the pulsar wind is equal to the pressure of the plasma and magnetic fields caught in the nebula, the pulsar wind is terminated. This "inner ring" is seen in X-rays at a distance of the wind termination (WT) $R_{\mathrm{WT}} \sim 3 \cdot 10^{17}$ cm. There, the wind is abruptly slowed down and the particles and fields are randomized, therefore, emitting synchrotron and inverse Compton radiation as seen in Figure 2.2 (implying small σ values). The current understanding of the acceleration mechanism is, that magnetic reconnection is responsible for the non-thermal particle acceleration [78] and not diffuse shock acceleration [79]. Recent 3D simulations done by Mizuno, Lyubarsky, Nishikawa, and Hardee [80] and Porth, Komissarov, and Keppens [81] can reproduce the Crab morphology using a highly magnetized "stripped wind". A torus with a corresponding jet emerges and also "wisps" with an increased brightness (due to Doppler beaming towards our line of sight [82]) are produced. Due to the increased turbulences the so-called "σ-problem" (high σ values at the origin of the wind and very low ones at its termination) is alleviated [83] in the 3D models and it is likely that the origin of the latter where due to simplifications made in the 1D and 2D models.

The integrated SED of the Crab Nebula is normally modelled using two distinct populations of electrons. In addition to the ones injected by the pulsar wind, a second population of relic electrons is needed to explain the radio emission [84, 85]. Due to the fact, that the radio and infrared spectra connect smoothly, it is unlikely that the relic electrons were produced during the supernova explosion. More likely is a recent idea proposed by Sironi and Spitkovsky [86] that the electrons of the pulsar wind can also explain the radio emission if a high enough magnetization is assumed ($\sigma > 30$) and if the electron injection rate is $\dot{N}_{\pm} \approx 10^8 \cdot N_{GJ}$ where N_{GJ} is the "Godlreich-Julien" current [87]. However, it yet remains to be seen, if 3D simulations can reproduce these results.
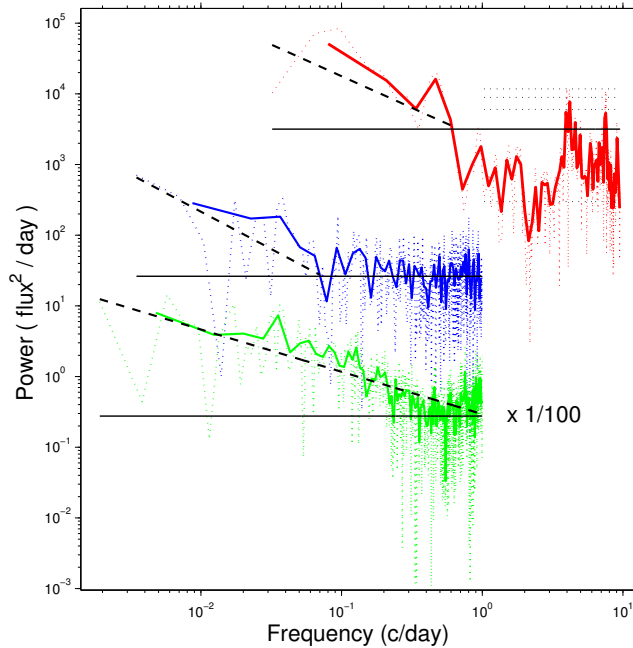
Figure 2.6.: *Fourier power density spectrum (PDS) of the Crab Nebula from the first 35 month of* Fermi *observations. The solid green line is the PDS for the full time interval (scaled down by a factor of 100), the blue one corresponds to a low activity period and the red one represents the exceptional flare from April 2011. All spectra were smoothed with a running average and the unsmoothed ones are shown by the corresponding dotted lines. The different PDS were fit with a power law function (dashed back line) and a constant white noise component (solid black line). Dotted black lines indicate the $\pm 1\sigma$, the $+2\sigma$ and $+3\sigma$ confidence intervals derived from white noise simulations. Figure taken from [88].*

2.3. Flux Variations

A huge surprise for the scientific community was the detection of several strong gamma-ray flares by the Fermi and the AGILE satellites [89, 90]. Unpulsed emission from the Crab Nebula above 100 MeV with a a flux increase by a factor of ~ 30 on timescales down to ~ 6 hours was observed [89–92]. The expectation was that the flux of the nebula itself should be constant up to $\sim 0.1\%$ limited by the decrease in spin-down luminosity. The average flux of the Crab Nebula above 100 MeV is $F_{100} = (7.2 \pm 0.3) \cdot 10^{-7} \, \mathrm{cm}^{-2} \, \mathrm{s}^{-1}$ and found to be variable on various time scales in HE gamma-rays. The power density spectrum (PDS) shown in Figure 2.6 is compatible with a power-law $PDS \propto \nu^{-0.9}$ [88]. Variations with time scales down to ≈ 10 hours can be resolved with no apparent break in the spectrum. It is yet unclear whether the flares are the high-energy end of this power density spectrum or if they have a different origin. By now six flares have been detected [88, 93–95] and the two brightest of these flares clearly show a new spectral component in the SED as seen in Figure 2.7 while others show no apparent change. All flares have a photon flux of $F_{100} > 35 \cdot 10^{-7} \, \mathrm{cm}^{-2} \, \mathrm{s}^{-1}$ and the flux level is increased for a period of ~ 1 week with respect to the average flux over a duration of one month. Moreover, all of them show significant emission up to $\sim 1 \, \mathrm{GeV}$.

The light curve of the flare from April 2011 is shown in Figure 2.8 and flux variations down to time scales of $\sim 20 \, \mathrm{min}$ are observed while the flux itself doubled in less than 8 h. The corresponding spectral evolution is shown in Figure 2.9 and can be described by a power law with exponential cut-off. The cut-off energy E_C as well as the total energy flux F_{100} vary, whereas the spectral index of the new component remains constant within measurement uncertainties at a value of $\gamma = 1.27 \pm 0.12$. At the maximum of the flare, the total luminosity of the flaring component reaches roughly 1 % of the spin-down power of the pulsar and the maximum cut-off energy is $375 \pm 26 \, \mathrm{MeV}$ [88]. During the flare the variation of the total flux and the cut-off energy were related via $F_{100} \propto E_C^{3.4 \pm 0.86}$ [88].

Up until now, no corresponding flux variations during any of the six flares of the Crab Nebula in the HE gamma-ray energy range have been found in any other wavelength [96–101]. Despite simultaneous observations during the September 2010, April 2011 and March 2013 flares, no increased emission has
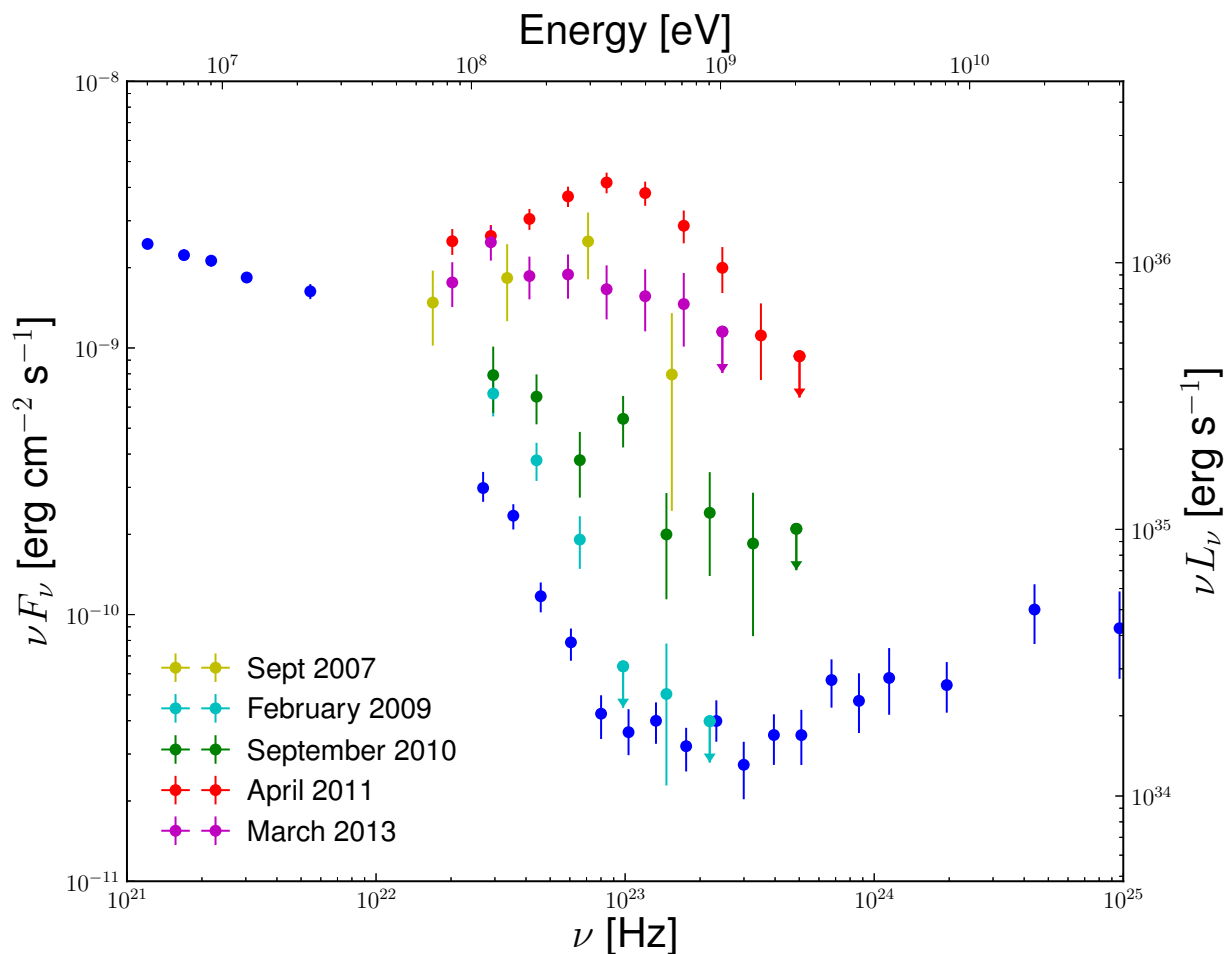
Figure 2.7.: *Spectral energy distribution for the average Crab Nebula flux in blue together with five of the six gamma-ray flares of the Crab Nebula. The emergence of a new component for the high intensity flares is clearly visible. Figure taken from [19].*

been detected from radio to X-rays and in VHE gamma rays. There is a claim for an increased flux by the ARGO-YBJ experiment [102], but it could not be verified by any other experiment. Neither the spin-down period nor any other pulsar properties changed during the flaring periods [88, 89, 97]. Moreover, no pulsed component was found in the gamma-ray emission of the flares. Although the time scales of the recurrence of gamma-ray flares and pulsar glitches appear to be similar, no correlation between these events has been found. Furthermore, the angular resolution of current HE gamma-ray experiments of $> 0.3°$ does not allow to pinpoint the exact location of the emission region of the gamma-ray flares.

Models trying to describe the still unknown emission process behind the HE gamma-ray flares need to be able to explain all their observed properties. For instance, the size of the emission region of $c \cdot t_d \sim 10^{-4}$ pc is much smaller than any of the observed structures within the nebula by at least a factor of ≈ 100. Moreover, synchrotron radiation is the only radiation process which could sustain the flare emission up to ≈ 1 GeV, but maximum energies from MHD flows do not exceed 160 MeV [103, 104]. Alternative solutions like diffuse shock acceleration cannot reproduce a hard enough spectrum
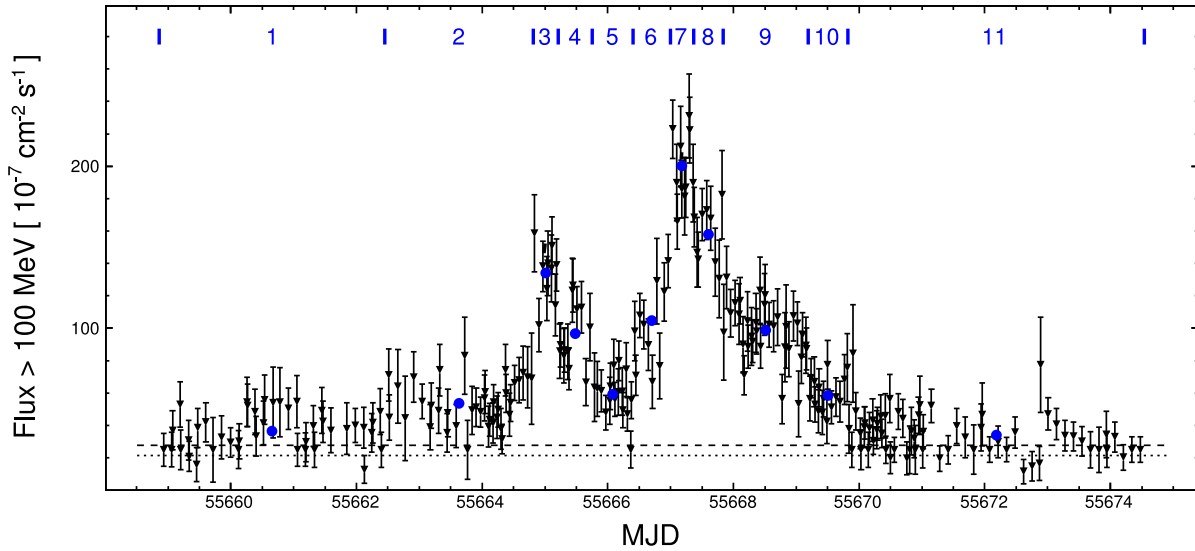
Figure 2.8.: *Light curve above* $100\,\mathrm{MeV}$ *of the Crab Nebula during its flare in April 2011. The dotted line indicates the sum of the* 33 *month average flux from the stable inverse-Compton component of the nebula and the stable contribution of the pulsar. The dashed line shows the average over the same time interval for the varying synchrotron flux of the nebula. The points represent the sum of the nebula and the pulsar flux during the flare. The blue vertical lines indicate periods of constant flux within statistical uncertainties and the blue points show the corresponding flux in each interval. Figure taken from [88].*

and are, moreover, expected to be inefficient at the termination shock [79, 105, 106]. The absorption of ion cyclotron waves does not fit the time scales of the observed gamma-ray flares and can be excluded as well [107]. A promising idea is particle acceleration due to magnetic reconnection [108, 109] as MHD conditions are not valid during such events and Doppler boosting of the beam is expected in the reconnection layer [104, 110–112]. The flare of April 2011 can be reproduced in such way, including the relation between cutoff energy and total luminosity as well as the temporal behaviour of the flare. Different locations for the magnetic reconnection process have been proposed [113–117] but no conclusive evidence has yet been brought to light to exclude any of them.

In March 2013, a new flare emerged from the Crab. It was the second brightest flare detected so far, and for the first time, simultaneous data could be taken with the H.E.S.S. array in the VHE domain. The analysis and interpretation of the data taken during the Crab flare is one of the main subjects of this thesis and will be described in Chapter 5. In the next chapter the H.E.S.S. experiment will be explained in detail together with an overview of the basic data calibration, reconstruction and analysis techniques.

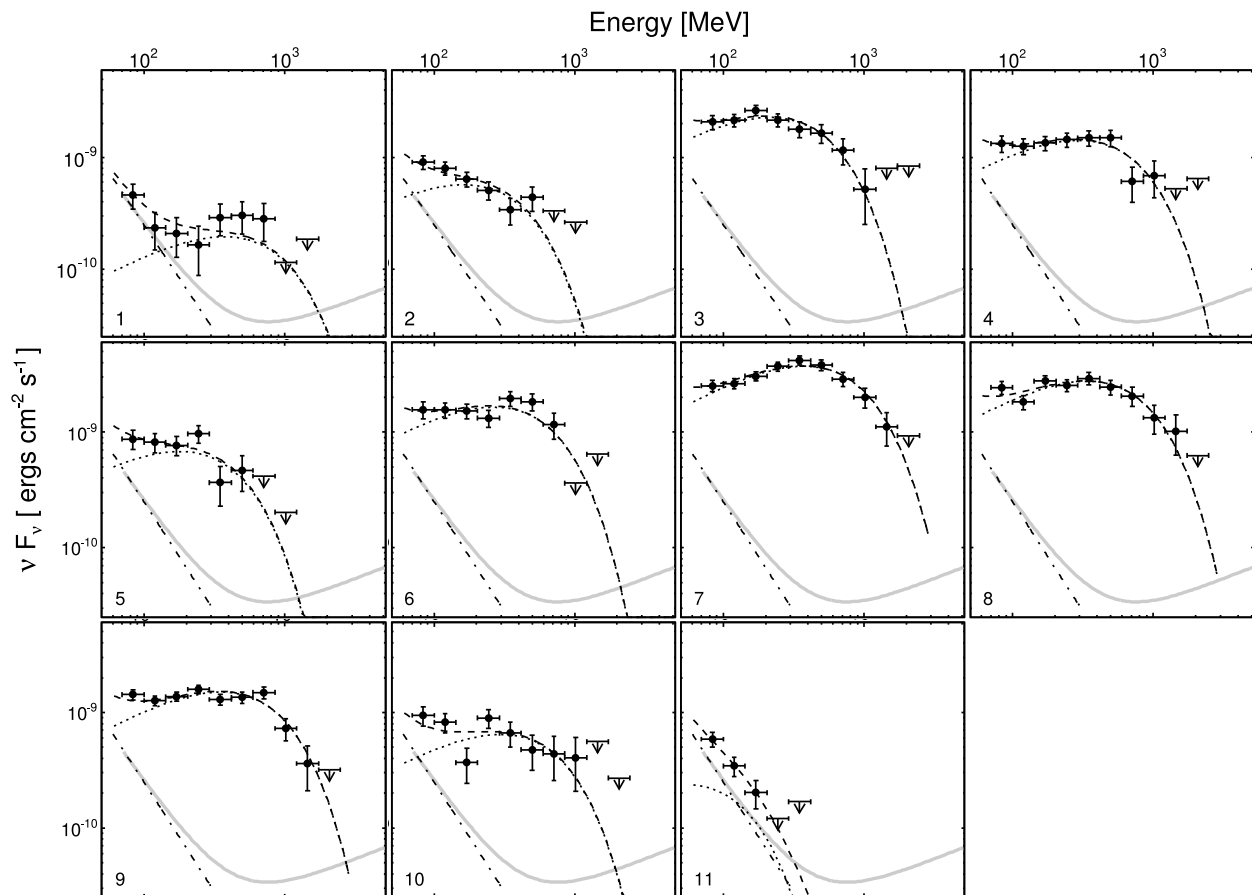Figure 2.9.: *Spectral energy distributions corresponding to the different intervals of constant flux shown in Figure 2.8. The dotted-dashed line is the constant background of the synchrotron nebula, the dotted line represents the flaring component and the dashed line is the sum of both components. For comparison the average Crab Nebula spectrum of the first 33 month of* Fermi *data is shown in gray. Figure taken from [88].*

3

The H.E.S.S. Experiment

The H.E.S.S. experiment is located in the Khomas Highland approximately $100\,\mathrm{km}$ south-west of the capital of Namibia, Windhoek. It is a so-called Imaging Atmospheric Cherenkov Telescope (IACT) system. The Phase I of the array, consisting of four identical $13\,\mathrm{m}$ diameter telescopes (the H.E.S.S. I telescopes), was inaugurated in 2003. Since then H.E.S.S. has played an important role in VHE gamma-ray astronomy [11, 118–125], demonstrating the capability of this young branch of astroparticle physics. By now almost 150 sources [17] have been found in the VHE gamma-ray domain. With the most recent addition of a fifth telescope, called H.E.S.S. II or CT5 (short for Cherenkov Telescope 5), the H.E.S.S. experiment entered Phase II. The interaction of VHE gamma-rays with the atmosphere, the detection of the subsequent air showers as well as the H.E.S.S. experiment itself will be explained in detail.

3.1. Air Showers

In the last decades different ground-based cosmic air shower experiments like the Auger Observatory [126] helped in understanding the nature of the cosmic radiation hitting the Earth's atmosphere. Like the H.E.S.S. experiment, Auger relies on the fact that high energy particles form extensive air showers can be observed and used to obtain information about the primary particle that induced the shower. Contrary to Auger which was built to measure mainly protons and heavier nuclei, the H.E.S.S. experiment was designed to detect VHE gamma-rays. If such a VHE gamma-ray enters the Earth's atmosphere, it starts to interact (mainly with nitrogen, oxygen and argon nuclei) at a typical height of 15 to $35\,\mathrm{km}$ and looses most of its energy on its way to the ground forming a cascade of billions of secondary particles. The atmosphere is acting as a calorimeter with a thickness of $\sim 27\,\mathrm{X_0}$, here $X_0 \approx 37\,\mathrm{g/cm^2}$ is the radiation length in the air. The gamma-ray undergoes pair-production in the Coulomb field of the nuclei of the Earth's atmosphere creating an electron-positron pair. The electron and positron in turn will also interact with the Coulomb field of the nuclei and emit gamma rays due to Bremsstrahlung (the term electron will be used for positrons and electrons hereafter). These two processes will repeat for all the secondary particles until ionization losses of the electrons start to become dominant as depicted in Figure 3.1a. The electromagnetic (EM) cascade formed by the secondary particles will have a lateral spread with regards to the main shower direction of a few meters

due to multiple Coulomb scattering of the electrons. Electron induced air showers behave very similar to the gamma-ray induced ones. However, the shower maximum, defined as the point where most of the secondary particles are created, is shifted to higher altitudes for electron induced air showers by a constant factor of $\approx 0.5\,X_0$ [127, 128]. The majority of air showers, created by cosmic radiation hitting the Earth's atmosphere, are of hadronic origin, i.e. mostly protons. The most frequent secondary particles are neutral and charged pions in hadronic induced air showers with a ratio of $\approx 1 : 2$ as shown in Figure 3.1b. Neutral pions immediately decay into two photons, creating EM sub-showers within the hadronic one. The sum of neutral pions are the dominant source for the EM shower component. Charged pions will interact before decaying into muons and neutrinos. Together with other heavier components like baryons and kaons, the charged pions form the long-lived hadronic shower core [129]. The muons, $90\,\%$ of which were created through the decay of the charged pions and kaons, do not suffer high energy losses and are the only particles of highly inclined air showers reaching the ground (zenith angle $\theta > 65\,°$) besides the EM particles created by the decay of these muons.

(a) *Gamma-ray induced cascade.*   (b) *Proton induced cascade.*
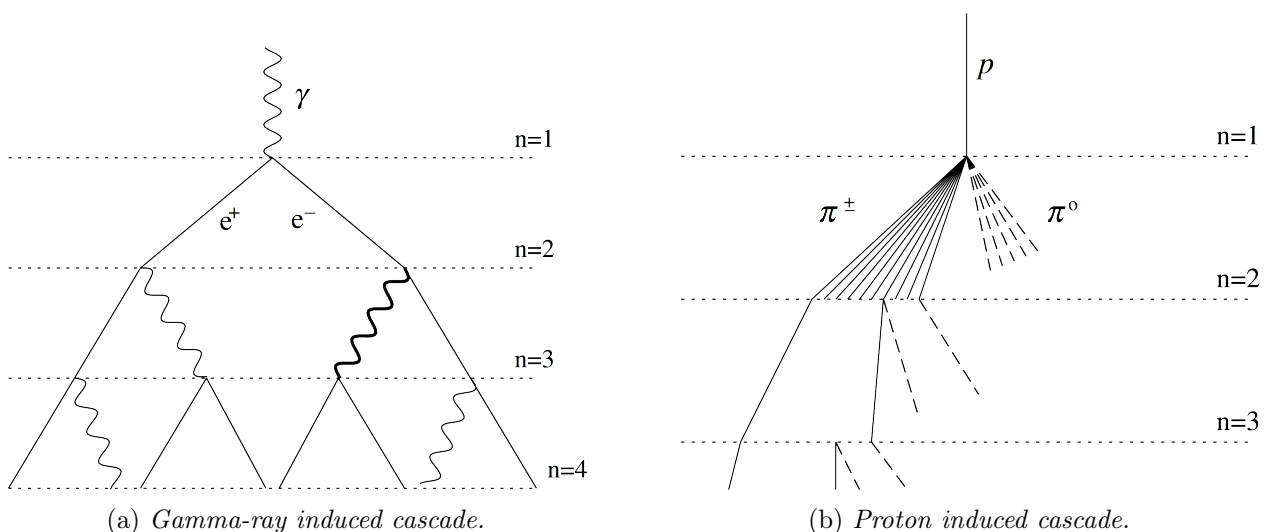
Figure 3.1.: *Schematic view of a gamma-ray induced air shower on the left and a proton induced air shower on the right. n denotes the generation of the secondary particles. Not all pion lines are shown for the second and higher generation particles in b and none of the two diagrams is to scale. Figures taken from [130].*

The dominant processes in the development of an electromagnetic air shower are [131]:

- Bremsstrahlung of $e^{\pm}$ in the Coulomb field of the nuclei of the atmosphere.

- Pair-Production of high energy gamma rays also in the Coulomb field of the nuclei of the atmosphere.

- Multiple Coulomb scattering of electron-positron pairs.

- Energy losses of $e^{\pm}$ through ionization and atomic excitation.

To describe the basic longitudinal features of an EM shower the so-called Heitler model [132] can be used; it was originally proposed by Carlson and Oppenheimer [133]. The idea is that each interaction takes place after a fixed track length, the *splitting length* $\lambda = X_0 \ln 2$. An electron will radiate a new gamma ray via Bremsstrahlung, loosing half of its energy to the newly generated particle, whereas a gamma ray will undergo pair-production creating an electron-positron pair, each with half of its energy. In essence, every interaction of a single particle with energy E, electron or gamma-ray, will result in

two outgoing particles, each with an energy $\frac{E}{2}$. Therefore, the total shower size N, i.e. the amount of particles in the shower, at a certain depth $X = n \cdot \lambda$ can be written as $N(X) = 2^n = 2^{(\frac{X}{\lambda})}$, where n is the number of generations (the number of consecutive interactions). The energy of a particle is defined via $E(X) = E_0/2^{(\frac{X}{\lambda})}$, here E_0 denotes the initial energy of the primary particle, i.e. the particle that started the cascade ($n = 0$). The particle multiplication is stopped once the energy of the particles drops below the critical energy $E_c \approx 83\,\text{MeV}$ in dry air. The maximum size of the cascade $N_{\max}$ is reached, if all particles have an energy $E = E_c$ so that $E_0 = E_c \cdot N_{\max}$ and the following relations can be obtained:

$$N_{\max} = \frac{E_0}{E_c} \qquad\qquad X_{\max}(E_0) \sim \lambda \ln\left(\frac{E_0}{E_c}\right) \tag{3.1}$$

The Heitler model therefore reproduces two basic features of an EM shower:

- The maximum number of particles in the shower $N_{\max}$ is proportional to the energy of the primary particle E_0.

- The depth of the shower maximum increases logarithmically with respect to the primary energy E_0.

Rossi and Greisen [134] showed that the average depth of the shower maximum of EM air showers is given by

$$\langle X_{\max}\rangle \approx X_0 \ln\left(\frac{E_0}{E_c}\right) + \frac{1}{2} \tag{3.2}$$

confirming the predictions of the Heitler model. However, the model overestimates the ratio of electrons to photons as already mentioned by Heitler [132]. By now several extensions of the Heitler model have been proposed [130, 134] and more sophisticated shower models are available. For instance, the semi-analytical model developed by Le Bohec et al. [135] and refined by de Naurois and Rolland [136]. For the simulation of air showers during the MonteCarlo simulation used by the H.E.S.S. experiment the *Corsika* [137] and *Kaskade* [138] tool-kits are used.

The lateral spread of an EM cascade is due to multiple Coulomb scattering of electrons on air atoms [139]. For low energy particles, the length scale of the lateral distribution is characterized by the Molière unit $r_1 = (21\,\text{MeV}/E_c)X_0 \approx 9.3\,\text{g/cm}^2$ which corresponds to roughly $80\,\text{m}$ at sea level and is increasing with altitude.

3.2. Cherenkov Radiation

The particles in an air shower travel at a speed faster than the speed of light in the surrounding medium $c > v \geq c' = \frac{c}{n}$. The charged particles emit Cherenkov radiation as discovered by Čerenkov [140] and explained using classical electrodynamics by Tamm and Frank [141] and their famous formula for the amount of Cherenkov radiation emitted on a given frequency:

$$\mathrm{d}E = \frac{q^2}{4\pi}\mu(\omega)\omega\left(1 - \frac{c^2}{v^2 n^2(\omega)}\right)\mathrm{d}x\,\mathrm{d}\omega \tag{3.3}$$

Here $\mathrm{d}E$ denotes the emitted energy per track length $\mathrm{d}x$ of the particle for the angular frequency $\mathrm{d}\omega$. $n(\omega)$ is the frequency dependent refractive index whereas q is the electric charge of the particle and

$\mu(\omega)$ is the frequency dependent permeability of the medium. It is interesting to note that the emitted energy does not depend on the sign of the charge of the particle, therefore, electrons, positrons, muons, protons, ... will emit Cherenkov radiation with the same characteristics.
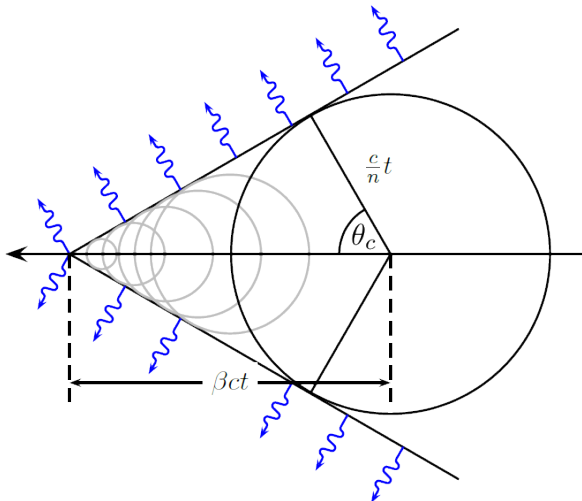
(a) *Shock front of Cherenkov light (blue lines) created by a particle traveling with a speed $\beta = \frac{v_p}{c}$ greater than the speed of light in the medium $\frac{c}{n}$ with a refractive index n. The particle induces dipoles which upon relaxation emit spherical waves that interfere constructively forming the Cherenkov cone of light. The characteristic opening angle θ_c and its dependence of n and β are shown. Figure taken from [142].*
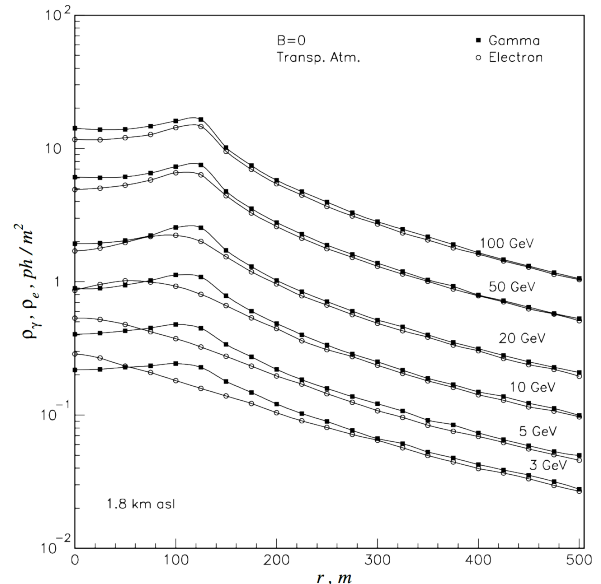
(b) *Lateral distributions of Cherenkov light for different primary energies at a height of 1.8 km above sea level obtained from simulations of gamma-ray and electron induced air showers without the influence of the geomagnetic field and no attenuation of light. The "Cherenkov ring" is visible as the bump approximately at a radius of 120 m in the lateral distributions. Figure taken from [128].*

Figure 3.2.

Moreover, the relative intensity of a given frequency is proportional to the frequency itself, resulting in the blueish light of visible Cherenkov radiation because shorter wavelength (higher frequencies) are more intense. The spectrum of Cherenkov radiation in air is highly absorbed in the UV waveband and as a result Cherenkov radiation detectors normally have a peak efficiency around ≈ 350 nm. The total amount of energy radiated per track length for Cherenkov radiation is given by:

$$\frac{\mathrm{d}E}{\mathrm{d}x} = \frac{q^2}{4\pi} \int_{v > \frac{c}{n(\omega)}} \mu(\omega)\omega \left(1 - \frac{c^2}{v^2 n^2(\omega)}\right) \mathrm{d}\omega \tag{3.4}$$

The emitted Cherenkov radiation of a particle traveling with a speed greater than the speed of light in the medium forms a shock front, see Figure 3.2a, similar to those observed in bow shocks or during a sonic boom. The light emitted by a particle at a certain point at a time $t = 0$ travels a distance of $x_{\mathrm{em}} = v_{\mathrm{em}}t = \frac{c}{n}t$ in the time interval t while the particle itself travels a distance $x_{\mathrm{p}} = v_{\mathrm{p}}t = \beta ct$. For geometric reasons, the angle θ_c of the shock front with respect to the direction of motion of the particle is given by:

$$\cos\theta_c = \frac{1}{n\beta} \tag{3.5}$$

For typical energies of a gamma-ray induced air shower, the opening angle of the cone of light formed by the emitted Cherenkov radiation of the secondary particles in the shower is $\approx 1°$. The area illuminated on the ground by the Cherenkov light is approximately a circle with a diameter around $\approx 250\,\mathrm{m}$ as seen in Figure 3.2b. The average duration of the emission of Cherenkov light generated by an air shower is $\approx 20\,\mathrm{ns}$ at ground level. Light emitted at the start of a vertical air shower reaches the ground before the light from its tail as seen in Figure 3.3.
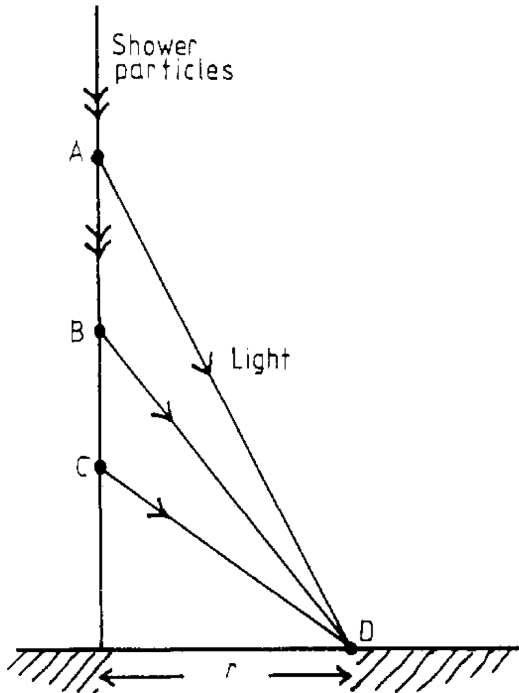
(a) *Schematic of an air shower seen by a detector at position D with a zenith angle of 0 °.*
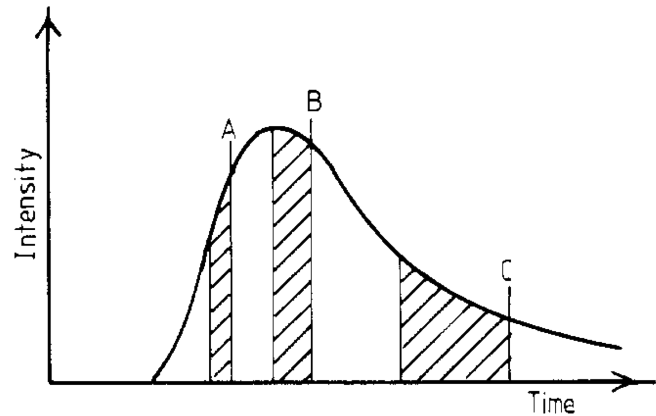
(b) *Cherenkov light intensity versus time seen by the detector in a.*

Figure 3.3.: *The arrival time of Cherenkov light emitted by an air shower is proportional to the time when it was emitted. Figures taken from [143].*

Figure 3.5 shows example MonteCarlo air shower events obtained using the Corsika shower simulation for the H.E.S.S. experiment [137, 144, 145] for a gamma-ray and a proton induced air shower. The proton air shower is much more heterogeneous due to the bigger lateral spread and the several EM sub-showers induced by neutral pion decay. For the gamma-ray shower, the circular Cherenkov light pool on the ground is clearly visible (see Figure 3.5c).

3.3. Imaging Atmospheric Cherenkov Technique

By now the third generation of Imaging Atmospheric Cherenkov Telescopes (IACTs) is in use; namely the H.E.S.S., MAGIC and VERITAS array. The first Cherenkov telescope was the Whipple telescope [146] which was able to detect the Crab Nebula in 1989. It did not yet use stereoscopic information of multiple telescopes observing the same air shower. Hillas [147] proposed to use his famous and still used Hillas parameterization of the Cherenkov light images of extensive air showers to extract the *Shower Parameters* from the image. During the work presented here the following definition of the *Shower Parameters* are used:

- The zenith angle of the air shower with respect to the center of the telescope array.

- The azimuth angle of the air shower with respect to the center of the telescope array.

- The distance of the shower impact on the ground to the center of the telescope array.

- The source position in the sky from which the primary particle originated.

- The primary energy of the particle which induced the air shower.

- The primary depth, i.e. the first interaction depth, of the particle.

- The type of the primary particle, i.e. gamma-ray or background (electrons, positrons, protons, . . .).

The translation of the Cherenkov light emitted by an air shower to the camera in the focal plane of an IACT is depicted in Figure 3.4a. The resulting elliptical shaped image for a gamma-ray induced air shower is clearly visible. Due to the short duration of the Cherenkov light emission during an air shower, the cameras of the telescopes need to be very fast, i.e. on a nanosecond level. For a better direction reconstruction of an air shower and background suppression, multiple telescopes are placed next to each other within the circle of light on the ground that is illuminated by Cherenkov radiation as seen in Figure 3.4b. The HEGRA telescope array [148, 149] was the first IACT array to use stereoscopic observation of air showers [150].
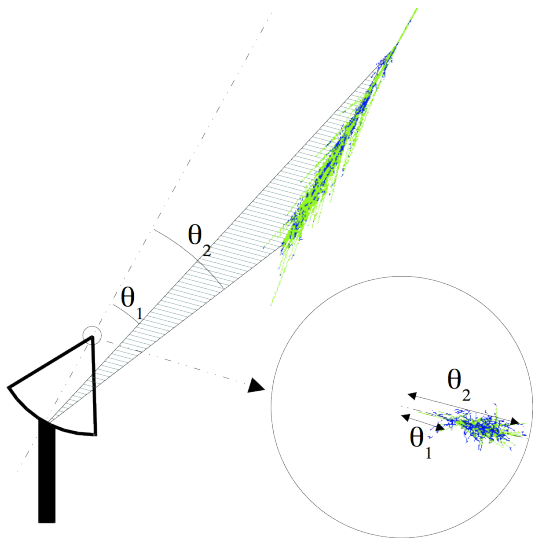
(a) *Schematic of an air shower seen by an optical telescope with an angular extension from θ_1 (shower start) to θ_2 (shower end) with respect to the telescope pointing. The air shower develops from the center of the camera towards its outer edge.*
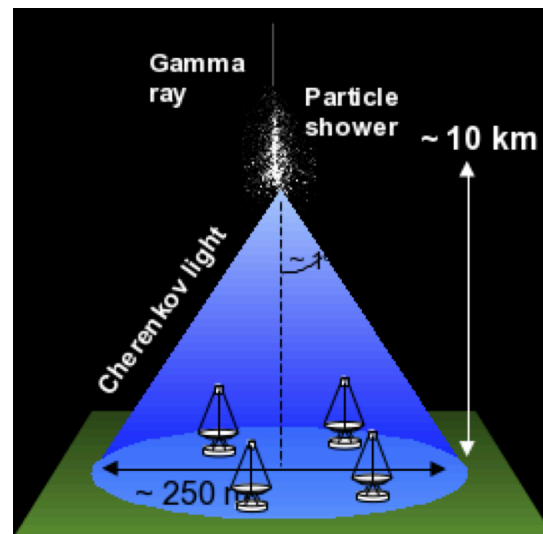
(b) *A gamma-ray induced air shower at a height of maximum emission of $\approx 10\,\mathrm{km}$ with its resulting cone of Cherenkov light with an opening angle of $\approx 1\,°$ (not to scale). Multiple telescopes are placed within the pool of Cherenkov light on the ground for stereoscopic observation.*

Figure 3.4.: *Figures taken from [131].*
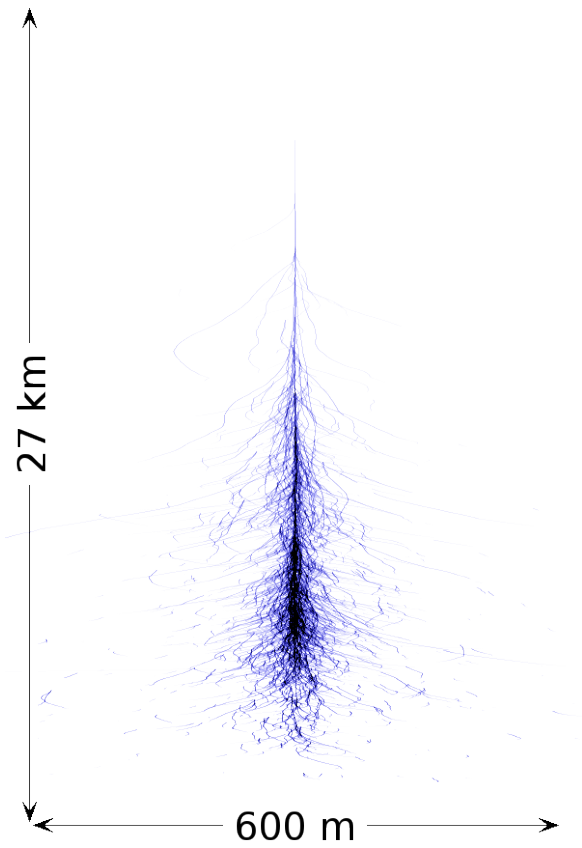
(a) *Longitudinal Cherenkov light distribution of a MonteCarlo gamma-ray induced air shower.*
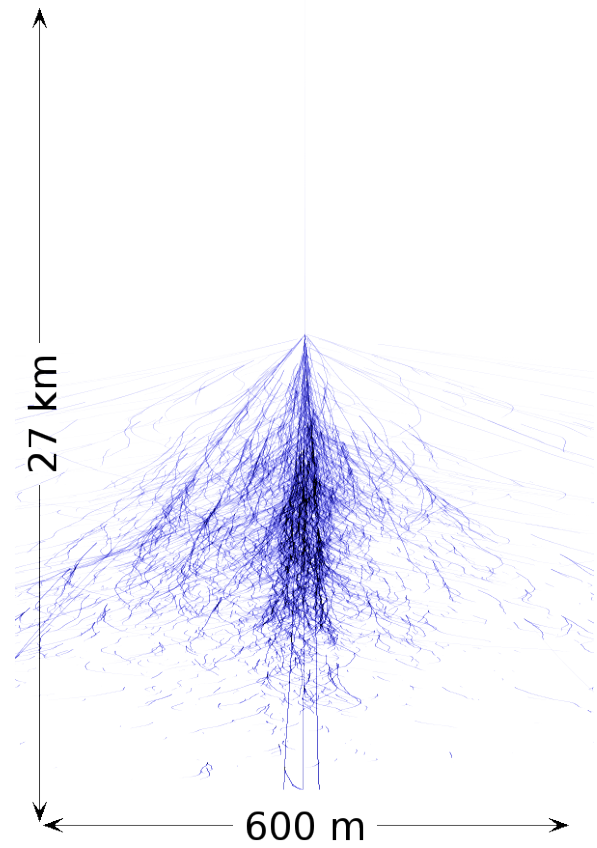
(b) *Longitudinal Cherenkov light distribution of a MonteCarlo proton induced air shower.*
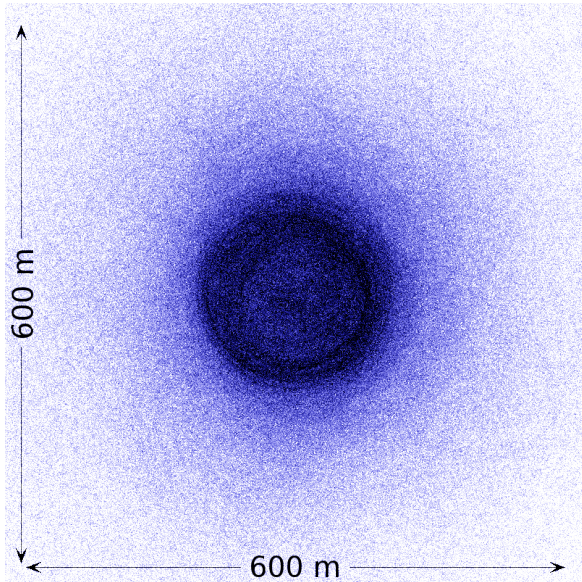
(c) *Lateral Cherenkov light distribution of a Monte-Carlo gamma-ray induced air shower on the ground.*
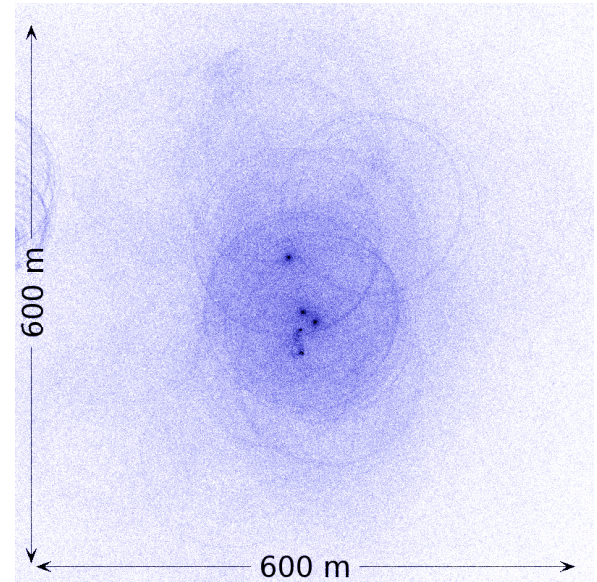
(d) *Lateral Cherenkov light distribution of a Mon-teCarlo proton induced air shower on the ground.*

Figure 3.5.: *Figures taken from [151].*

3.4. The H.E.S.S. Array

The High Energy Stereoscopic System or H.E.S.S. is located in the Khomas Highland of Namibia, southern Africa. The area around the Gamsberg is well known by astronomers for its excellent observation conditions [152, 153]. The first phase of the H.E.S.S. array started construction in August 2000 with the work on the foundations of the four 13 m diameter telescopes on site in Namibia. The first telescope was inaugurated on September 2$^{\text{nd}}$ 2002 and the full four telescope array of H.E.S.S. Phase I started operation in 2004. The four telescopes are placed at the edges of a square with a side length of 120 m to allow for stereoscopic observation of air showers but not too close to trigger multiple telescope on the Cherenkov light cone produced by atmospheric muons. The total weight of the four telescopes (CT1 to CT4) is 60 t each. The tessellated mirrors with a radius of 6.83 m consist of 380 circular segments with a radius of 30 cm each, forming a total mirror area of $\approx 107 \, \text{m}^2$ per telescope using the Davies-Cotton design [154] for better off-axis imaging. The focal length of the telescopes is 15 m and the shadowing due to the steel structure and the camera is on average 11 %.
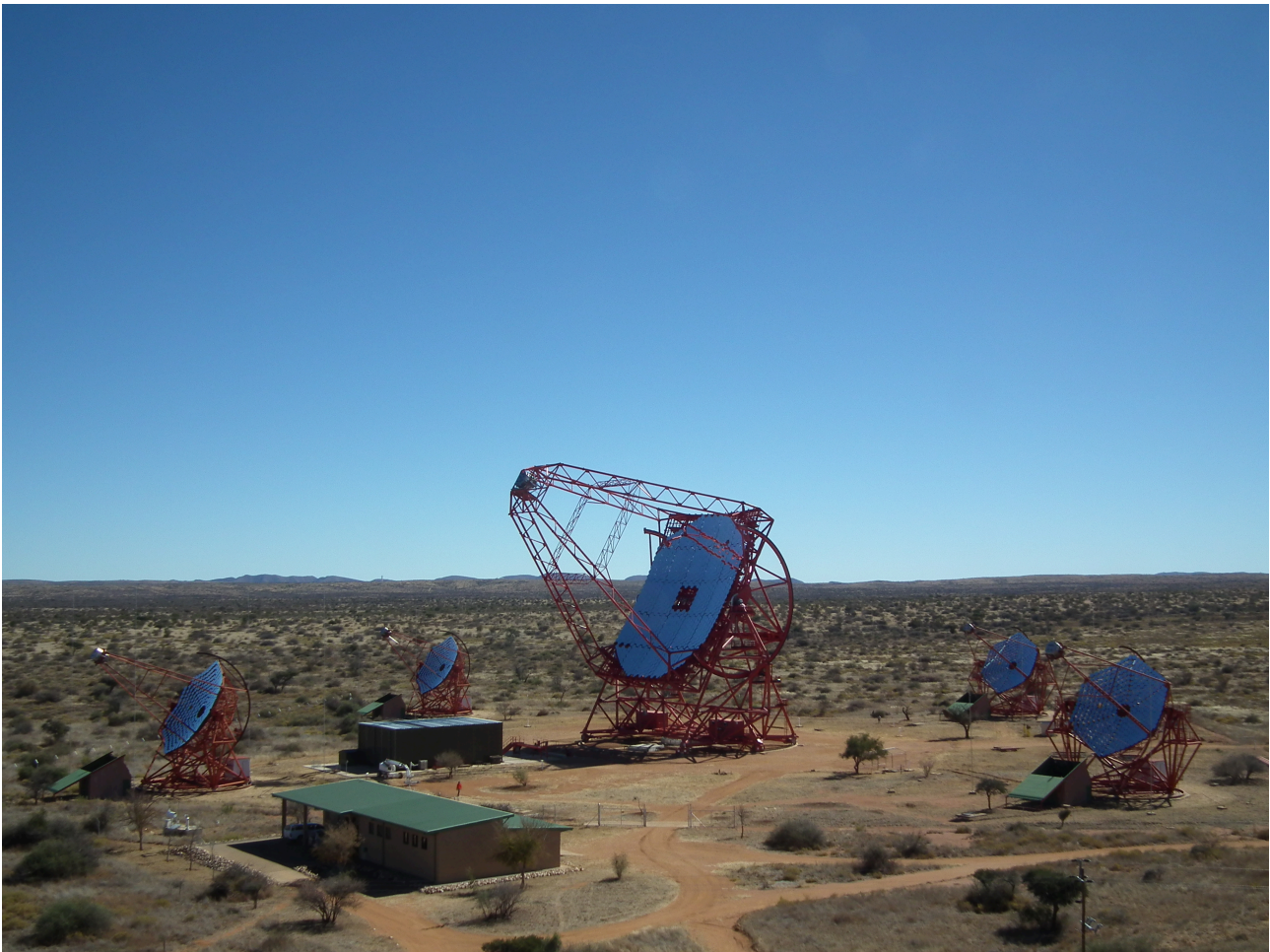
Figure 3.6.: *Picture of the H.E.S.S. site in Namibia. The telescopes from right to left are CT1, CT2, CT5, CT3, and CT4. The building in the front houses the central computing farm as well as the central control room of the array.*

The optical reflectivity of the mirrors were degraded from their original value between 80 % and 90 % to below 60 % and where therefore exchanged in the last years restoring the reflectivity to values between

70 % and 80 %. With a slewing rate of $\approx 100\,°/\text{min}$ using its altitude-azimuth mount, the telescopes can reach any target in the sky within $\approx 2\,\text{min}$. The minimal pointing uncertainty of the system is around 6 ″ per axis as shown in Acero et al. [155] for dedicated observations, during normal observation the uncertainties are around 20 ″ [156]. The Cherenkov camera located at the focal point of the telescope consists of 960 photo multiplier tubes (PMT) each with a field of view of $0.16\,°$ resulting in a total field of view of the camera of $\approx 5\,°$ [157].

On July 26$^{\text{th}}$ 2012 the H.E.S.S. II telescope saw its first light and the H.E.S.S. Phase II array was inaugurated in September 2012. The fifth telescope placed at the center of the array features a $24.3\,\text{m} \times 32.6\,\text{m}$ parabolic mirror with a surface of $\approx 614\,\text{m}^2$, roughly the size of two tennis courts. The mirror consists out of 875 hexagonal shaped segments each with a 90 cm flat-to-flat diameter and a focal length of 36 m for the parabolic mirror. The reflectivity of the mirrors is similar to the ones for the H.E.S.S. I telescopes and the shadowing due to the steel structure and the camera is on average 7.5 %. The total weight of the telescope is $\approx 580\,\text{t}$ and it also uses an altitude-azimuth mount. To be able to react to target of opportunity alerts (ToO) quickly, the slewing speed for the azimuth drive is $\approx 200\,°/\text{min}$ and for the elevation drive it is $\approx 100\,°/\text{min}$ [158]. The Cherenkov camera of the H.E.S.S. II telescope consists of 2048 PMT, each with a field of view of $0.067\,°$ resulting in a total field of view of the camera of $\approx 3.2\,°$ [159].

An overview picture of the H.E.S.S. site can be seen in Figure 3.6. Although the telescopes are parked out during day time in the picture, the H.E.S.S. array only observes during astronomical darkness, i.e. the sun is $18\,°$ below the horizon and the moon has not yet risen either. In total, this results in roughly 1000 h of dark time per year that can be used for observation. This demands a very high efficiency of the different subsystems of the array, especially for a single point of failure component like the data acquisition system.

3.5. Data Acquisition

The network layout of the H.E.S.S. experiment can be seen in Figure 3.7. It nicely illustrates the main data flow in the array. The data recorded by the Cherenkov camera is split in two parts. A direct optical connection to the *Central Trigger* of each telescope is used as an input for a stereoscopic coincidence trigger using the first part. An air shower has to trigger the cameras of at least two telescopes within a time window of $\approx 80\,\text{ns}$ for the event to be read out of the buffers in the cameras and to be digitized using the other part of the data stream. Afterwards, the data is sent using a $1\,^{\text{Gb}}/_{\text{s}}$ Ethernet optical fiber connection to the central computer farm where the final event building is done and the data is stored on disk. For the H.E.S.S. II telescope monoscopic events are stored as well, i.e. the newest telescope can trigger on its own to make use of its ability to detect much fainter air showers due to its huge mirror area.

A photo of a so-called drawer of the H.E.S.S. II camera is seen in Figure 3.8 together with a schematic view of the corresponding electronic read out chain in Figure 3.9. A drawer is a unit of 4×4 pixel which are grouped together in a single component for easier camera maintenance. The H.E.S.S. II camera consists of 128 drawers whereas the H.E.S.S. I cameras consists of 60 each. The electronics used in the CT5 camera is a complete redesign of the ones used in CT1-4 including several improvements but the general read out principle remains the same. Moreover, a slightly updated version of the Photonis XP-2960 PMT, the Photonis XP-29600, is used in the CT5 camera which features a higher quantum efficiency of 30 % compared to 25 %. For a detailed review of the H.E.S.S. camera electronics, the reader is referred to Aharonian et al. [157] and Bolmont et al. [159].
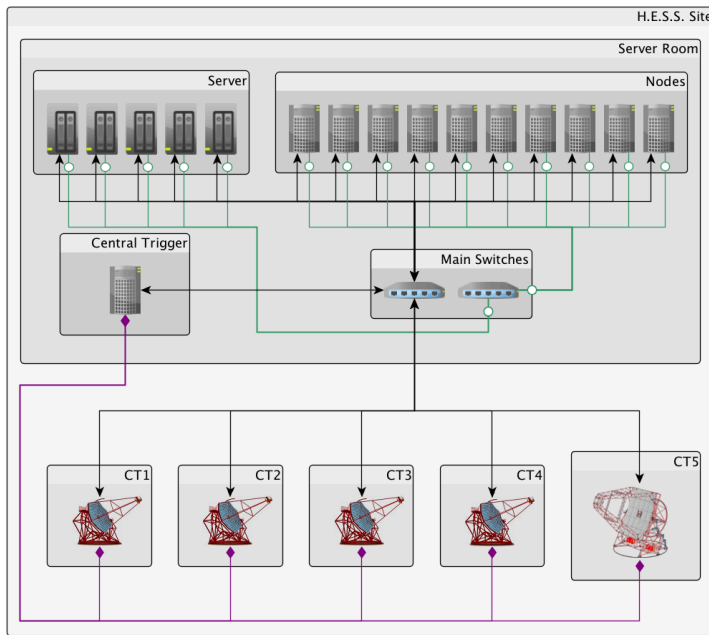
Figure 3.7.: *Schematic of the network layout of the H.E.S.S. site shown in Figure 3.6. Black lines indicate $1^{\,\text{Gb/s}}$ ethernet connections, note that the connections to CT1-4 are $100^{\,\text{Mb/s}}$ only. The separate network for the network file systems are shown by the solid green lines. The direct optical fiber connections between the* Central Trigger *and the camera triggers are plotted in purple. Figure taken from [160].*

Each PMT (or pixel) of every telescope is equipped with a Winston cone light guide [161] to minimize the dead space between adjacent pixels. Due to the same physical size of the different PMT types, a diameter of $29\,\text{mm}$ and a Winston cone flat-to-flat distance of $42\,\text{mm}$ together with a similar $\frac{f}{D}$ ratio of the different telescope mirror types, results in approximately the same night sky background (NSB) rate of every pixel of $\approx 100\,\text{MHz}$. The Winston cones of CT5 have a better optical efficiency below $400\,\text{nm}$ compared to the ones used in H.E.S.S. Phase I. The high voltage (HV) for each of the pixel is generated by a Cockcroft-Walton-generator located on a circular base soldered to the back of the PMT. The signal at the PMT base is read out and amplified with three different gains. The highest amplification is used for the analog trigger signal generation. The other two channels, called *Low Gain* and *High Gain* are sent to an analogue memory (analog ring sampler (ARS) for H.E.S.S. I or the SAM chip for H.E.S.S. II) and sampled at a rate of $1\,\text{GHz}$ corresponding to a cell size of $1\,\text{ns}$. The camera trigger generation is done in two steps. Each pixel has to be above a fixed *Pixel Threshold* to count as triggered (first level or L0 trigger) and for a given trigger sector (an area equivalent to 4 drawers), the number of pixel triggered must be above the *Sector Threshold* for the camera trigger deciding in favor of a Cherenkov event (second level trigger or L1 trigger). The different trigger sectors are overlapping to achieve a homogeneous trigger behaviour throughout the camera. In essence, the camera trigger is a simple cluster trigger algorithm which is enough to reduce the average trigger rate of $100\,\text{MHz}$ of a single pixel to an average camera trigger rate of around $3.5\,\text{kHz}$. Once the camera trigger decides in favor of a Cherenkov event, the signal stored in the analogue memory is digitized and integrated over a read out window of $16\,\text{ns}$ for each of the two data channels. The camera back-end electronic then generates a single camera event packet that is sent to the central processing farm using one $100^{\,\text{Mb/s}}$ optical fiber for H.E.S.S. I type telescopes or two $1^{\,\text{Gb/s}}$ optical fibers for H.E.S.S. II.

The data of the different telescopes is sent to one *Node Receiver* process which receives all data from all telescopes for $4\,\text{s}$, the *Central Trigger* pace, and buffers it in memory. After that, another *Node Receiver* process is chosen to accept the data of all telescopes and the former can start the array event building and save the data to disk. This round-robin load-balancing scheme [162], can be easily adjusted to handle different data rates, for example the much higher data rates of the H.E.S.S. Phase II array could be handled without problem. The software framework used for controlling the H.E.S.S. array is
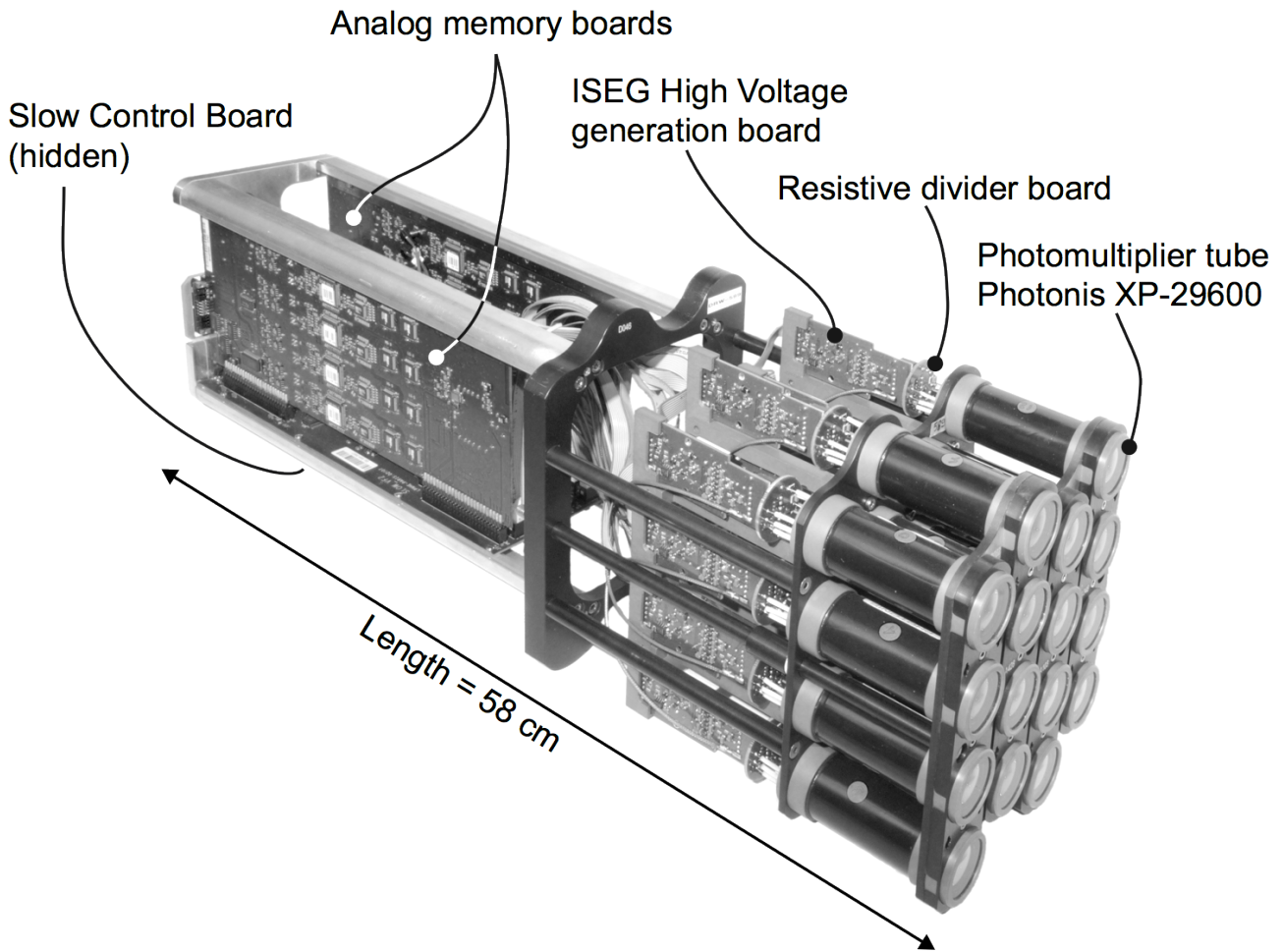
Figure 3.8.: *Black and white picture of a drawer of the H.E.S.S. II camera. In the front the 16 PMTs are visible. The read out electronics together with the two analog boards and one slow control board are also seen. Figure taken from [159].*

called the H.E.S.S. Data Acquisition (DAQ) and is described in detailed in Balzer et al. [160]. The H.E.S.S. DAQ is used to control, monitor and read out every piece of equipment of every subsystem on site in Namibia. This also includes the high-level error handling; note that each piece of equipment is responsible for its own safety and the DAQ just ensures that the rest of the array is brought to a safe state after an error occurred in the system. To achieve this functionality, every piece of equipment on site is mapped by at least one *Controller*. Complicated hardware like the Cherenkov cameras are represented by several different *Controllers*, each responsible for a different part of the camera, i.e. the *Camera HV Controller*, the *Camera Trigger Controller*, the *Camera Lid Controller*, etc. Each *Controller* has to implement a common state machine which is shown in Figure 3.10. The state machine used by the H.E.S.S. DAQ is flat, i.e. there is only one state transition for one of the directions, ascending or descending. The *Safe* state is used to represent deactivated and powered-off hardware, in *Ready* the hardware is turned on and slow control data is read out and saved at arbitrary rates. In the *Configured* state the hardware has received all information to start a so-called *Run*, i.e. it is ready to do physics data taking whereas in *Running* the hardware is taking data.

There are several different run types implemented in the H.E.S.S. DAQ, divided in three distinct groups of runs. *Observation runs* are used to observe sources of VHE gamma-rays during the night, *calibration*
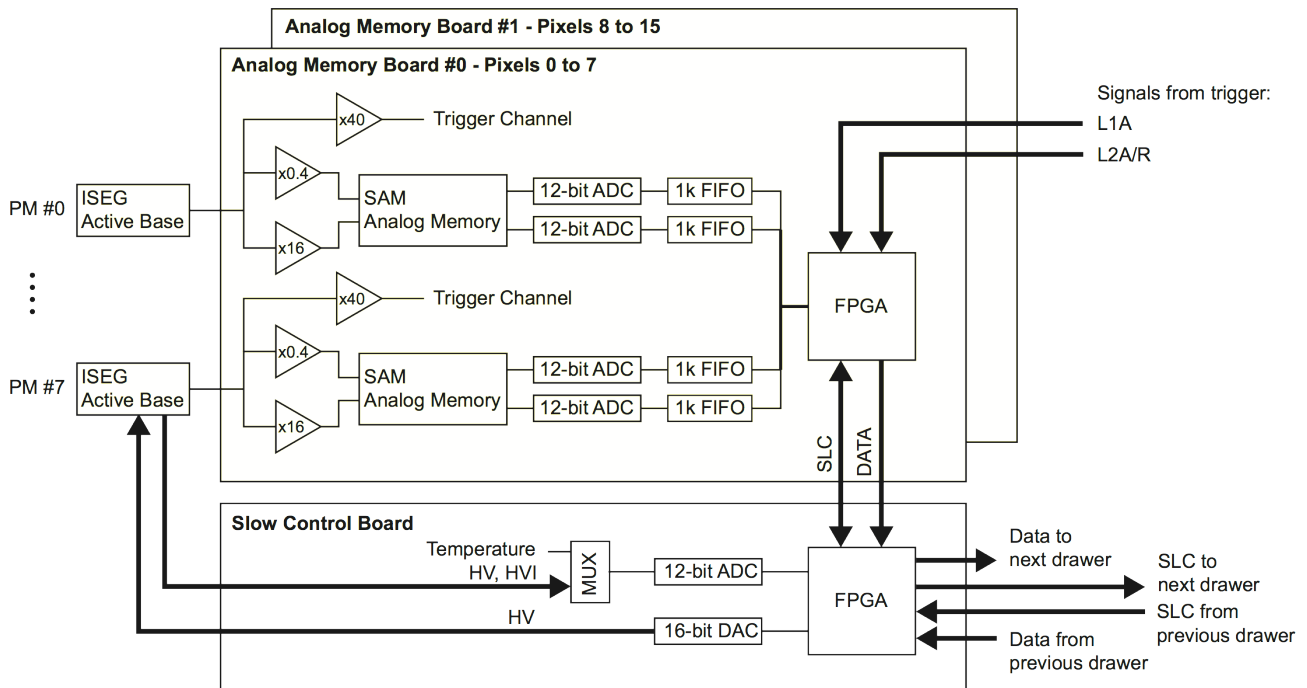
Figure 3.9.: *Schematic of the electronic read out chain of the drawer seen in Figure 3.8. The signal is split in three and attenuated using different gains. The two channels used for data acquisition include analogue memory and digitization electronics together with a FIFO for short time data storage. Each of the two analog boards and one slow control board contain a FPGA for command and control purposes. Figure taken from [159].*

runs are used to calibrate the different parts of the detector and lastly *maintenance runs* to test the various subsystems of the array and their performance. To switch between the different runs, state transitions are used to get the array from a *Running* state to *Ready* and then back to *Running*. This effectively changes the configuration of the different detector components, the amount of telescopes used, etc. During these state transitions the hardware is, for example, turned on or configuration parameters are sent to the equipment. So-called *Dependencies* are used to manage the order of the state transitions of the different processes in the DAQ. For example, the HV of the PMTs must not be turned on while the telescope is still moving. An arbitrary example for the starting of a run is shown in Figure 3.11. Note that only a small subset of the processes within the H.E.S.S. DAQ are used in the example and the time intervals are not representative.

The H.E.S.S. DAQ is a multi-process, multi-threaded multi-machine system that uses the omniORB [163] implementation of the CORBA [164] inter-process communication standard. Currently, it consists of roughly 230 processes distributed over 10 worker nodes in the central computer farm. For data storage 6 RAID server are used offering a *NFS* [165] and a *GlusterFS* [166] network file system. During the course of this work the network and computing hardware as well as the software of the H.E.S.S. DAQ was upgraded and adapted to encompass the needs of H.E.S.S. Phase II. One of the achievements of the H.E.S.S. DAQ is its high data taking efficiency. It only contributed with $0.8\,\%$ to the total amount of dark time lost by the H.E.S.S. array in the time frame from 2009 to 2012. For a more detailed description of the DAQ, the reader is referred to Balzer et al. [160]. The Python based [167] software frame work used to obtain these numbers, the *Transition-Time-Tools* or *TT-Tools* were also developed during the course of this work. Each DAQ process writes several time stamps to a MySQL database [168] during each of its transitions. One at the start, one once all dependencies are

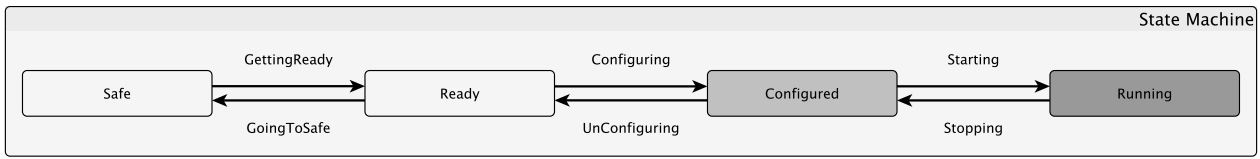Figure 3.10.: *Visualization of the state machine used in the H.E.S.S. DAQ. The boxes represent the states a Controller (and its respective device) can be in, while the arrows show the available transitions. This state machine is linear by design, which simplifies the synchronization of multiple Controllers. As all the hardware Controllers are mapped to the same state machine, it becomes quite easy to determine the state of the whole array or any subset, e.g. when all processes of telescope CT1 are* Ready, *the whole telescope is* Ready *for observation. Figure and caption taken from [160].*
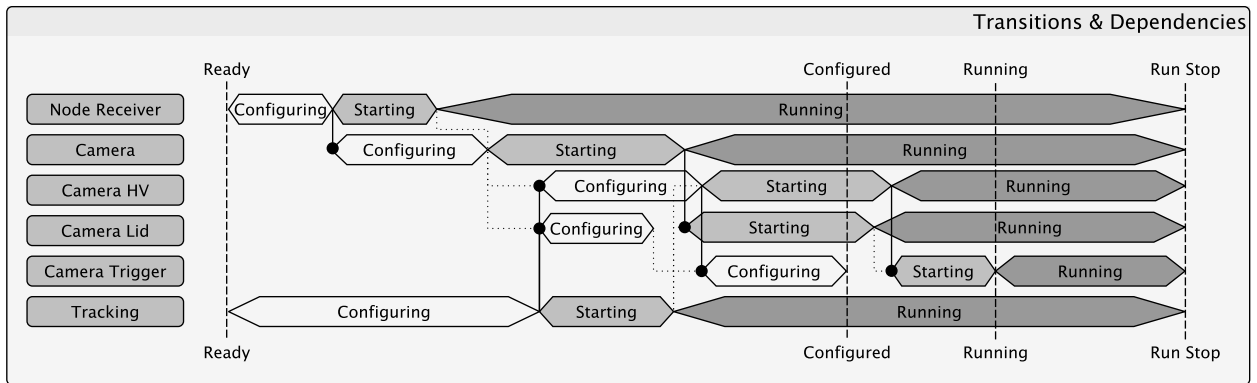
Figure 3.11.: *An example interaction of various important H.E.S.S. DAQ processes during the start of an observation run. The change of the state of the corresponding SubArray (i.e. the sum of all processes) is indicated by the dashed lines and ranges from* Ready, *over* Configured *to* Running. *The hexagonal boxes represent state transitions of the corresponding DAQ Controllers. The solid and dotted black lines with a filled circle at the end indicate dependencies between processes within the H.E.S.S. DAQ, i.e. the HV of the PMTs in the camera must not be turned on while the telescope is still moving and the camera trigger should not be activated before the camera HV is turned on. As a result a process only starts with its transition if all of its dependencies have successfully finished their own corresponding transition. The solid lines indicated the slowest dependency of a given process while the dotted lines represent dependencies that already reached the required state. The global state of the SubArray is determined by the slowest process, i.e. once the last process finished its transitions from* Ready *to* Configured *the whole SubArray is considered to be* Configured. *Figure and caption taken from [160].*

satisfied and finally one at the end of the transition. Using this information of every process in the DAQ, the dark time efficiency, telescope participation, etc. can be calculated with an accuracy of $\approx 1\,\mu$s. During the first years of H.E.S.S. Phase I a pearl script was used to calculate the dark time efficiency of the array. It relied on the parsing of log files of the different DAQ processes that are stored for each night. However, it was not able to properly deal with observations using several *SubArrays*. A *SubArray* is an arbitrary subset of processes of the H.E.S.S. DAQ which can be used to do observations with different telescopes at different targets at the same time. Currently, the H.E.S.S. array is the only IACT system with this ability. The *TT-Tools* properly take into account observations with several *SubArrays* or missing telescopes due to hardware failure by properly weighting calculated values using the amount of telescopes that participated in a given run and the current overall amount of telescopes that were available (4 for H.E.S.S. Phase I and 5 for H.E.S.S. Phase II).

The *Real Time Pipeline* (RTP) of the H.E.S.S. DAQ is a *Hillas Parameters* based analysis using the ROOT [169] TMVA framework for gamma-hadron separation as described in Ohm, van Eldik, and Egberts [170]. It is running in parallel to the data taking of the array and does a real time event reconstruction and analysis of every event recorded by the H.E.S.S. DAQ (not yet including the H.E.S.S. II telescope). It is based on the work done by Sebastian, Funk [171] which uses the *WobbleChain* analysis software [11] of the H.E.S.S. collaboration. As support for this software was dropped several years ago, the RTP was developed as its replacement during the course of this work. Several new features were added to the RTP, for example the ability to store analysis results over arbitrary time intervals thus being able to display summed analysis results to the on-site personal. Moreover, the data calibration procedure was extended to correct for common mode oscillations (see Brun [172] or Balzer, A. [151]) and to be able to deal with data from the H.E.S.S. II telescope (calibration of the data only, not event reconstruction).

Due to the huge collection area and the faster slewing speeds of the H.E.S.S. II telescope, it is ideal to observe short scale transient events like gamma-ray bursts (GRBs) [173, 174]. They are the most violent processes in the known universe (after the Big Bang) and are randomly distributed throughout the sky. Like all IACT experiments, the H.E.S.S. array has a very narrow field of view ($5\,°$) compared to all-sky experiments like the Fermi satellite with its two experiments the LAT [175, 176] and the GBM [177, 178]. The latter was built to detect GRBs in the HE gamma-ray range and sends out target of opportunity (ToO) alerts (among other experiments) called "GCN alerts" using the Gamma-Ray Burst Coordinates Network[1] to which the H.E.S.S. array is connected. For H.E.S.S. Phase II the ToO alert system of the H.E.S.S. experiment [179] has been upgraded to allow for quick responses to transient events like GRBs which are still undetected in the VHE gamma-ray regime. As shown in Balzer et al. [180], the H.E.S.S. DAQ is able to react to a ToO alert and starts data taking on the new target within less than $1\,\text{min}$ for an angular distance of $\approx 70\,°$.

3.6. Data Calibration

The final event data that is saved to disk by the H.E.S.S. DAQ contains the analog-to-digital-converted (ADC) count rate for each of the two gain channels of each PMT in each camera that is read out. Moreover, a global GPS time stamp is attached to the data from the telescopes and the telescopes that triggered but were already reading out another event are tagged as being busy. The latter information is relevant to properly calculate the dead time of the array which is needed during the computation of the measured flux of a gamma-ray source. The ADC counts of the different PMTs for the *Low Gain* and *High Gain* channel have to be converted to a common physical unit, the density of Cherenkov photons, to be able to get a direct measure of the emitted light. This is done using the following formula:

$$I_{HG} = \frac{\text{ADC}_{HG} - P_{HG}}{\gamma_{HG}} \cdot FF_{HG} \qquad\qquad I_{LG} = \frac{\text{ADC}_{LG} - P_{LG}}{\gamma_{HG}} \cdot \frac{HG}{LG} \cdot FF_{LG} \qquad (3.6)$$

Here I is the intensity in photo electrons (p.e.) seen in the respective gain channel; HG for the *High Gain* and LG for the *Low Gain* channel. P is the value of the pedestal, i.e. the baseline of the PMT, consisting of electronic noise and NSB contributions. FF denotes the *flatfield coefficient* used to correct for differences in the response of the single PMTs. γ_{HG} is the conversion factor of ADC counts to one photo electron in the *High Gain* channel. For the *Low Gain* channel, this factor cannot be measured and the one for the *High Gain* channel is used properly weighted by the gain ratio $\frac{HG}{LG}$.

---

[1]The Gamma-Ray Burst Coordinates Network (GCN) distributes information about the location of a Gamma-Ray Burst detected by various spacecraft http://gcn.gsfc.nasa.gov/

A brief summary of the calibration procedure used by the H.E.S.S. experiment will be given now, for more details the reader is referred to Aharonian et al. [157], de Naurois [131] or Balzer, A. [151]. Note that the H.E.S.S. collaboration uses two independent calibration chains called the *French* and the *Heidelberg* calibration for cross check purposes.

The pedestal P for each gain channel of every pixel has to be measured during observation due to significant changes in the baseline over the timescales of one run of 28 min. The pedestal can be estimated from camera images of air showers using the parts of the camera that were not illuminated by the Cherenkov light. Roughly 5000 events are used to obtain an average pedestal value for a given channel in a given pixel. The *French* calibration uses a linear interpolation in time between average pedestal values whereas the other uses the average value only. Both calibration chains correct for common mode oscillations in the baselines of the H.E.S.S. I cameras due to power fluctuations generated by the two power supplies (one for each camera half), after consecutive event readouts. The main contribution to the baseline of a pixel is due to electronic noise. Changes in the electronic noise will result in a different mean and rms of the pedestal distribution whereas changes in the NSB will only result in a different rms.

The conversion factor from ADC counts to photo electrons is determined using dedicated *calibration runs*, so-called *SinglePeRuns*. The cameras are illuminated by an LED flasher capable of generating single photon events in each of the camera PMTs in the absence of night sky background. For H.E.S.S. I the telescopes are parked in and the cameras are located within a shelter where they are shielded from star light and other artificial light sources. For the H.E.S.S. II telescope, the camera is either unloaded and brought into the shelter or a dedicated calibration laser is used to illuminate the camera which is covered by a special filter plate that absorbs the NSB photons. The distribution of ADC counts obtained during these runs is described by the so-called photo multiplier response function. It can be described analytically using the following assumptions [157]:

- The photo electron number n follows a Poisson distribution.

- The electronic noise, i.e. the pedestal distribution, can be described by a Gaussian distribution with a mean P in ADC counts and width of σ_p.

- The distribution for a given signal of n p.e. is also described by a Gaussian distribution with a mean of $P + n\gamma$ in ADC counts and width of $\sqrt{n}\sigma_\gamma$.

- The width of the pedestal peak σ_p is much smaller than the width of the single p.e. peak σ_γ.

For a mean light intensity μ the photo multiplier response function than reads as:

$$
\begin{aligned}
S(x) = N \cdot \Bigg(& \frac{e^{-\mu}}{\sqrt{2\pi\sigma_p^2}} \exp\left[-\frac{1}{2}\Big(\frac{x-P}{\sigma_p}\Big)^2 \right] \\
& + \kappa \sum_{n=1}^{m\gg 1} \frac{e^{-\mu}}{\sqrt{2\pi\sigma_\gamma^2}} \frac{\mu^n}{n!} \exp\left[-\frac{1}{2}\Big(\frac{x-(P+n\gamma)}{\sqrt{n}\sigma_\gamma}\Big)^2 \right] \Bigg)
\end{aligned}
\tag{3.7}
$$

Here N denotes the overall normalization and κ the one for the photo electron peaks. An example distribution can be seen in Figure 3.12 together with the fitted PMT response function.

The fitted value of γ is used as the ADC to p.e. coefficient in Equation (3.6). It can not be measured in the *Low Gain* channel because the gain is not high enough to separate the pedestal from the single
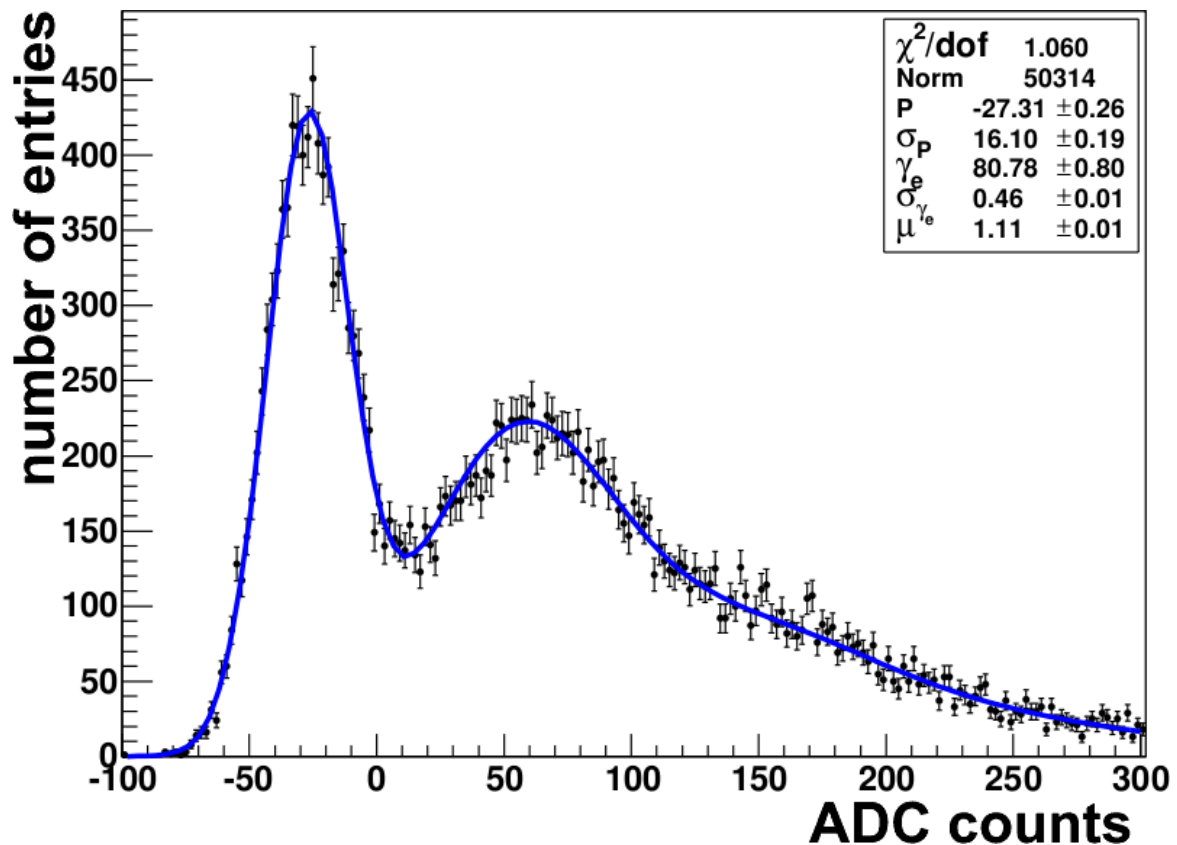
Figure 3.12.: *Distribution of an example* SinglePeRun. *The cameras are illuminated with a light source capable of generating single photo electron illumination per pixel. The black points indicate the measured data whereas the blue curve is the fit of Equation* (3.7) *to the data. Figure taken from [151].*

p.e. peak. The averaged value for one calibration period (the time from one full moon to another) over all *SinglePeRuns* is used for a given gain channel of a pixel in a camera to reduce the effect of statistical fluctuations.

The *High Gain* to *Low Gain* ratio can be obtained using the data from normal observation runs. It is defined as the slope of the distribution of the *High Gain* to *Low Gain* ADC counts for pixel intensities that are within the linear range of operation of the PMT (also averaged over one calibration period).

To correct for different quantum and light collection efficiencies as well as different signal gains in the PMTs of a camera, the *flatfield coefficient* is used. It is also obtained from dedicated *calibration runs*, the *FlatFieldRuns*. During these runs all cameras are illuminated with a homogeneous light source which illuminates all PMTs with the same amount of light. The resulting p.e. distributions in every channel of every camera (assuming a *flatfield coefficient* of 1 in Equation (3.6)) are of a Gaussian shape. The means of these distributions can be calculated and the *flatfield coefficient* is defined as the ratio of the mean pixel intensity to the mean of the whole camera for the given gain channel (also averaged over one calibration period).

For the inter-camera calibration the Cherenkov light of atmospheric muons are used. Their radiation spectrum is very similar to the one of gamma-ray induced air showers with the only difference being that the muons are more penetrating and therefore suffer from less ultra-violet absorption. Moreover, the image recorded by a Cherenkov camera that was triggered by an atmospheric muon will resemble

a ring or a ring segment. Due to the highly-relativistic nature of the movement of the muons, the emitted amount of Cherenkov light does not depend on the energy of the particle. Instead only the track length is relevant and the expected amount of radiation for a muon passing by at a given distance can be analytically calculated and used to calibrate each camera to a common reference light source. Unfortunately, the use of a coincidence trigger suppresses almost all muon events. However, due to random coincidences with air showers seen by other telescopes, the amount of muon rings detected by each telescope in one calibration period is enough to calculate stable muon correction factors.

The information of the two gain channels, *High Gain* and *Low Gain* has to be merged to obtain one image from a camera that has been read out during an air shower event. For this two slightly different approaches are used within the calibration chains. Due to the high amplification in the *High Gain* channel, it is used for low intensity pixel events, i.e. between 0 and ≈ 1000 p.e. for H.E.S.S. I type telescopes and ≈ 375 p.e. for the H.E.S.S. II telescope. For high intensity events, the *Low Gain* channel is used, because the *High Gain* channel is not in its linear range of operation anymore. The *French* calibration switches at the upper threshold from the *High Gain* to the *Low Gain* channel. The *Heidelberg* calibration uses a linear interpolation in the transition region of the two gain channels.

Lastly, the calibration has also to take care of hardware defects within the cameras. They range from one broken channel in a pixel for a certain amount of time during a run (for example by a bright star in the field of view of the pixel) up to the loss of several drawers due to electronic problems. The pixels are flagged as broken during analysis and are not used. Note, that in case of one of the two gain channels being broken, the other one is used regardless of the intensity in the pixel.

3.7. Hillas Reconstruction

The next step in the processing of the data is the event reconstruction. From all the available camera images for a given event, the *Shower Parameters* have to be reconstructed. As a first step, the *Hillas Parameters* [147] of each shower image are calculated. The shower shape in the camera can be approximated by an ellipse and the moments of this ellipse as depicted in Figure 3.13b are called the *Hillas Parameters*. The relevant parameters during this work are:

- The length l of the Hillas ellipse in the direction of the major axis.

- The width w of the Hillas ellipse in the direction of the minor axis.

- The center of gravity of the Hillas ellipse.

- The azimuth angle ϕ of the main axis of Hillas ellipse.

- The orientation angle α of the Hillas ellipse in the camera with respect to the camera center.

- The nominal distance, i.e. the distance of the center of gravity of the Hillas ellipse to the camera center.

- The size or total image amplitude contained within the Hillas ellipse.

To be able to reconstruct the origin of a primary particle that induced an air shower (the source position), the impact point of the shower on the ground (the shower core) and the height of maximum emission, several coordinate transformations have to be done. A detailed description of the coordinate systems used within the H.E.S.S. software can be found in [156]. A brief description of the systems used within this work will be given in the following. The *Camera System* is a 2D Cartesian coordinate
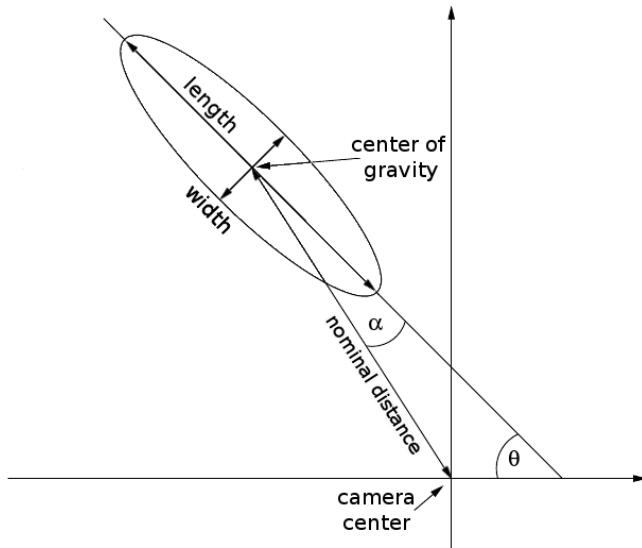
(a) *Schematic of a Hillas ellipse together with the geometric* Hillas Parameters. *Only the size of the total image amplitude contained within the ellipse is not shown.*
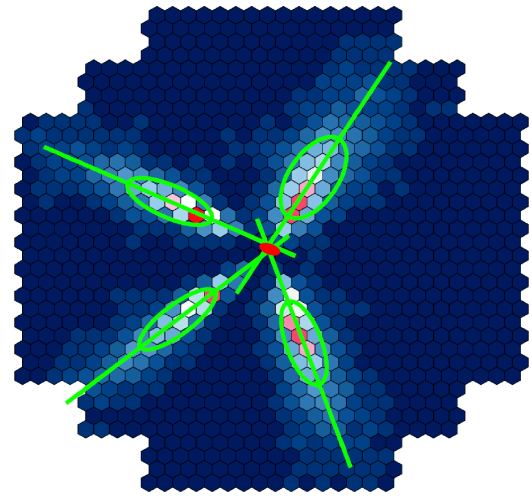
(b) *Superimposed camera image of an event seen by the four H.E.S.S. I type telescopes. The Hillas ellipses and the shower direction in each camera are shown in light green. The intersection of the different major axes of all ellipses is the source position in the* Nominal System.

Figure 3.13.: *Figures taken from [151], based on Figures taken from [181] and [182].*

system that describes positions in the focal plane of the detector in units of meters. The origin of the system is the center of the camera and the x axis is facing downwards for a telescope elevation of $0°$. The y axis is orthogonal to the x axis and faces to the left if the camera is viewed from the dish. In total there are five different camera systems for H.E.S.S. Phase II, one for each camera. The *Ground System* is a 3D Cartesian coordinate system with its origin being at the center of the telescope array, i.e. at the position of CT5. Its unit is meters as well. The x axis is facing north and the y axis is facing west and the z axis is facing zenith. The shower core position is normally given in the *Ground System*. The *Tilted System* is also a 3D Cartesian coordinate system with meters as its unit. The z axis is facing towards the pointing direction of the telescope array. For an array orientation using an azimuth angle of $0°$ and an altitude of $90°$, the x axis is facing north and the y axis is facing west and the coordinate axes of the *Tilted System* and the *Ground System* are aligned. However, the coordinates of the *Tilted System* are the projected coordinates of the *Camera System* in a focal plane using a focal length of $1\,\mathrm{m}$. The actual shower core reconstruction is done in the *Tilted System*. The *Nominal System* is used for the reconstruction of the shower source position. It is a 2D Cartesian system using the same orientation for the x axis and y axis as the *Tilted System*. Due to the fact that the telescopes are mirror telescopes, the sign of the coordinates are switched in the *Nominal System* with respect to the *Tilted System*. Together with the knowledge of the exact date and time, the weather and the location, the *Nominal System* can be used to convert coordinates to astronomical systems. For example into the *AltAz System*, a spherical coordinate system which uses altitude and azimuth angles. Using the *Horizon System*, coordinates can be transformed to other astronomical coordinate systems like the *Galactic System* or the *RaDec J2000 System*.

To reconstruct the shower source position in the *Nominal System*, the weighted mean of the intersection points of the major axis of the Hillas ellipses of all telescope pairs is used. The center of gravity of the Hillas ellipse and the azimuth angle of the shower for the respective telescope define a straight line. The intersection point of the two lines of a telescope pair is weighted by the size of the Hillas ellipses and the sine of the angle of the intersection. As a result, the brighter images and images seen from different azimuth angles have a higher weight. For the shower core, the *Tilted System* is used and the same weighting and intersect procedure is used except that the weighting only uses the sine of the intersection angle. For the height of maximum emission, the mean of the height of the shower maximum of each telescope pair is used. The projected difference of the center of gravity of the Hillas ellipses of the two telescopes in the direction of the air shower δ is calculated. This represents an angular distance in the *Nominal System* which is similar to the difference angle between θ_1 and θ_2 seen in Figure 3.4a. Using the small angle approximation $\delta \approx \sin\delta$, the distance to the shower maximum from the telescope pair l can be calculated as $l = d\delta$ with d being the distance between the two telescopes in the *Ground System*. The height of the shower maximum h is than obtained using $h = l\sin\beta$ with β being the latitude angle of the shower direction vector, i.e. the inclination of the air shower with respect to the z axis in the *Ground System*.

The energy reconstruction using *Hillas Parameters* is done using dedicated lookup tables obtained from MonteCarlo simulations. For each telescope type, a lookup table is filled using the zenith angle of the observation, the impact distance of the shower core to the telescope (not to the center of the array) and the logarithm of the size of the Hillas ellipse as lookup parameters. For each telescope that participated in the event, the mean energy and the spread of the energy is obtained from the respective lookup table. The weighted average energy using the inverse of the energy spread as a weight is calculated and used as the primary energy of the particle.

Hillas Parameters based reconstructions have been the backbone of every IACT array for the last decades. However, by now more advanced reconstruction techniques have been developed. Most prominently, multi-variate analyses (MVA) [170, 183, 184] and the use of a semi-analytical model together with a pixel-wise log-likelihood fit as presented by de Naurois and Rolland [136]. This reconstruction technique will be adapted to the needs of H.E.S.S. Phase II in this work.

3.8. Gamma Hadron Separation

The cosmic radiation consists mostly of protons and heavier nuclei (see Chapter 1). These particles create a background of hadronic air showers that has to be suppressed by several orders of magnitude in rate to be able to do VHE gamma-ray astronomy. Due to the possible transfer of large lateral momenta during hadronic interactions (mostly pions), the resulting air showers look much more asymmetric; especially at higher energies. Using stereoscopic observation of air showers helps not only during the direction reconstruction, but also during gamma-hadron-separation. While a hadronic air shower can look like a gamma-ray induced one from one side, a different viewing angle may reveal the sub showers and therefore its hadronic origin. To quantify the asymmetry of an air shower the Hillas length L and width W have been used successfully over the last decade as shown for example in Aharonian et al. [11]. Because these two parameters heavily depend on the energy of the primary particle, the impact distance of the shower to the respective telescopes and the zenith and azimuth angle of the observation, the *Reduced Scaled Length RSL* and *Reduced Scaled Width RSW* are used:

$$RSW = \frac{W - \langle W \rangle_{\mathrm{MC}}}{\sigma_{W_{\mathrm{MC}}}} \qquad\qquad RSW = \frac{L - \langle L \rangle_{\mathrm{MC}}}{\sigma_{L_{\mathrm{MC}}}} \qquad (3.8)$$

The mean $\langle W \rangle_{\mathrm{MC}}$ and width $\sigma_{W_{\mathrm{MC}}}$ of the reference distributions are obtained from MonteCarlo simulations using the same observation conditions as during the actual data taking and are stored in lookup tables (for are more detailed explanation of lookup tables see Section 4.4 and Appendix A). Normally, a minimum image amplitude contained within a Hillas ellipse is required for the telescope to be used during event reconstruction. The reason is that low energy hadronic showers look very similar to gamma-ray showers. Moreover, Hillas ellipses of only a few pixels in a camera are very susceptible to fluctuations due to NSB and the orientation of the ellipse starts to be degenerate. Image truncation at the edges of the camera is also a problem, especially for large air showers at high energies. Therefore, a cut on the nominal distance of the center of gravity of the Hillas ellipse to the camera center is performed. Only showers in the inner parts of the cameras are used. To combine the information of N_{Tel} different telescopes t the *Mean Reduced Scaled Length MRSL* and *Mean Reduced Scaled Width MRSW* are calculated:

$$MRSW = \frac{\sum_t RSW_t}{N_{\mathrm{Tel}}} \qquad\qquad MRSL = \frac{\sum_t RSL_t}{N_{\mathrm{Tel}}} \qquad (3.9)$$

MonteCarlo simulations are used to create reference distributions for gamma-ray and proton induced air showers of the *Mean Reduced Scaled* parameters. These distributions are then used to obtain cut parameters that optimize the signal to noise ratio. For more information see Section 4.4 and Aharonian et al. [11]. By now more sophisticated gamma-hadron separation methods have been developed. Some of them rely on neural networks or boosted decision trees for cut optimization as shown in Ohm, van Eldik, and Egberts [170] and Becherini, Punch, and H.E.S.S. Collaboration [183]. Another possibility for gamma-hadron separation using the goodness of fit of a log-likelihood comparison was introduced by de Naurois and Rolland [136] and will be used in this work.

3.9. Source Detection and Spectral Analysis

To be able to detect sources of VHE gamma-radiation in the sky, the signal of gamma rays from a source has to be extracted from the background of diffuse gamma ray emission and events of hadronic nature that where classified as gamma-like (electron induced air shower also contribute to this group of events). A simple way to quantify the significance S of a source is to compare the number of events in a source region N_{ON} with the number of events in a control region N_{OFF}. Using a correction factor α which takes into account different exposure times in the control and source region as well as instrumental effects, etc., the number of predicted background events in the source region N_{B} can be obtained via:

$$N_{\mathrm{B}} = \alpha N_{\mathrm{OFF}} \qquad (3.10)$$

The number of events from the source N_{S} is then given by:

$$N_{\mathrm{S}} = N_{\mathrm{ON}} - N_{\mathrm{B}} = N_{\mathrm{ON}} - \alpha N_{\mathrm{OFF}} \qquad (3.11)$$

As shown by Li and Ma [185], the following ways to quantify the significance S of a source detection are error prone:

$$S = \frac{N_{\mathrm{ON}} - \alpha N_{\mathrm{OFF}}}{\sqrt{N_{\mathrm{ON}} - \alpha^2 N_{\mathrm{OFF}}}} \qquad S = \frac{N_{\mathrm{ON}} - \alpha N_{\mathrm{OFF}}}{\sqrt{\alpha(N_{\mathrm{ON}} - N_{\mathrm{OFF}})}} \qquad S = \frac{N_{\mathrm{S}}}{\sqrt{\alpha N_{\mathrm{OFF}}}} \qquad S = \frac{N_{\mathrm{S}}}{\alpha\sqrt{N_{\mathrm{OFF}}}} \qquad (3.12)$$

Instead they proposed to define the significance of a source detection by using a log-likelihood ratio γ of the probabilities P_0 (the *null hypothesis*, i.e. no signal) and P, the probability of a signal:

$$S = \sqrt{-2 \ln \gamma} \qquad \gamma = \frac{P_0(N_{\mathrm{ON}}, N_{\mathrm{OFF}} | \langle N_{\mathrm{B}} \rangle)}{P(N_{\mathrm{ON}}, N_{\mathrm{OFF}} | \langle N_{\mathrm{S}} \rangle, \langle N_{\mathrm{B}} \rangle)} \qquad (3.13)$$

The final formula for γ is given by:

$$\gamma = \left[\frac{\alpha}{1 + \alpha} \left(\frac{N_{\mathrm{ON}} + N_{\mathrm{OFF}}}{N_{\mathrm{OFF}}} \right) \right]^{N_{\mathrm{ON}}} \cdot \left[\frac{1}{1 + \alpha} \left(\frac{N_{\mathrm{ON}} + N_{\mathrm{OFF}}}{N_{\mathrm{OFF}}} \right) \right]^{N_{\mathrm{OFF}}} \qquad (3.14)$$

The observation time of the H.E.S.S. array is split in runs with a duration of 28 min, i.e. sources of VHE gamma-radiation are observed multiple times and the amount of runs for targets with deep observation can exceed 200 runs. The different number of events used in Equation (3.14) can be obtained by simple summation and for the α factor the weighted mean using the number off events is calculated:

$$N_{\mathrm{ON}} = \sum_i N_{\mathrm{ON}}^i \qquad N_{\mathrm{OFF}} = \sum_i N_{\mathrm{OFF}}^i \qquad \alpha = \frac{\sum_i \alpha^i N_{\mathrm{OFF}}^i}{\alpha^i} \qquad (3.15)$$
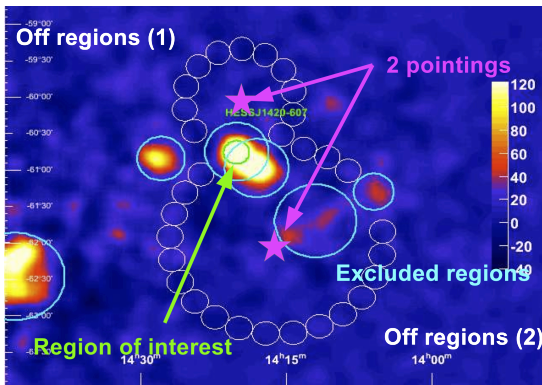
(a) *The* Reflected Background *technique is shown for two different observation positions. The region of interest is surrounded by multiple background regions using the same radial distance to the observation position. Known sources of VHE gamma-radiation are excluded and not used during background estimation.*
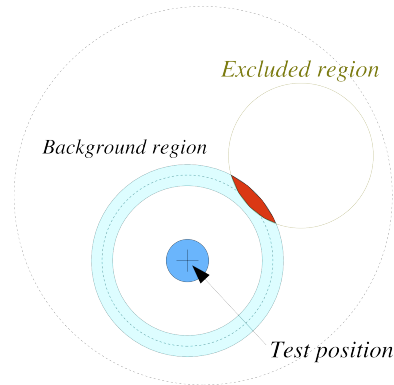
(b) *Schematic of the* Ring Background *subtraction technique. The source region is surrounded by an annular background region. Regions containing sources of known VHE gamma-ray radiation are excluded.*

Figure 3.14.: *Figures taken from [131].*

To obtain all the necessary event counts and the α factor for a given run, so-called count maps are filled. They are a binned 2D representation of a part of the sky. Known sources of VHE gamma-radiation in the field of view are excluded during the analysis and the parts of the map are not filled. To extract the number of background events from these maps, several different techniques were used during this work, the *Reflected Background*, the *Ring Background* and the *Template Background* technique. For a detailed description of the following techniques, the reader is asked to have a look at Berge, Funk, and Hinton [186], de Naurois [131] and Aharonian et al. [11]. All techniques do not require dedicated *ON-OFF* observations, but the background is extracted from the same field of view. Because the acceptance of the detector depends heavily on the radial distance to the center of the camera, the H.E.S.S. array performs observation in *Wobble Mode*. The observation position for a given run is offset to the actual

source position by 0.5° normally. As a result, different control (or background) regions can be found around the observation position that have the same radial offset as the source region as shown in Figure 3.14a. Therefore, the α factor is easily obtained through the ratio of the different size of the source and background regions. For the *Ring Background* technique, an annular region around the source position is used as shown in Figure 3.14b. The background estimation is not done on a run-by-run basis and therefore a precise knowledge of the acceptance of the detector is required to obtain a correct α factor. A completely different approach is used by the *Template Background* technique. Instead of using gamma-like events from other regions in the field of view, background-like events from the same region are used, for details see Rowell [187] and Lemoine-Goumard and H.E.S.S. Collaboration [188].

The acceptance of the detector for gamma-rays of different energies is obtained from MonteCarlo simulation. For the acceptance of gamma-ray like background events the actual data that is analysed is used. A binned 2D map of event counts and a binned 2D map of exposure times for portions of the sky of different energy bands are filled and summed for all runs. The final acceptance map is the ratio of the count map and the exposure map in the respective energy band, as shown in Figure 3.15. The acceptance maps predict the amount of predicted gamma-ray like background photons in the field of view of the observations and can be used to obtain a correct α factor for the *Ring Background* technique.
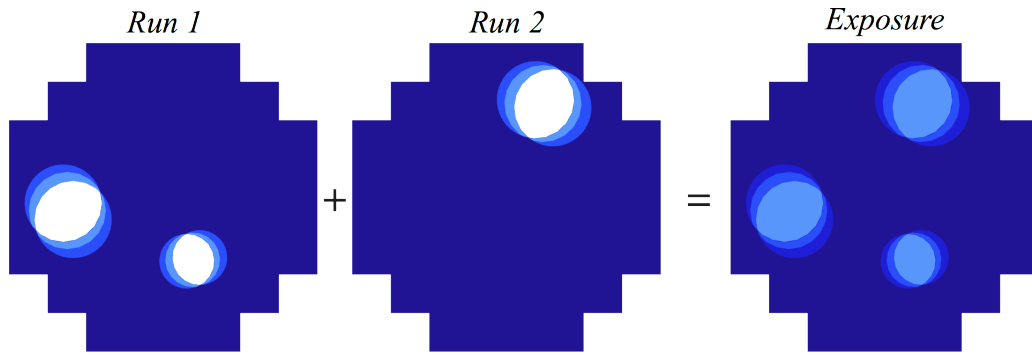
(a) *Two different exposure maps for two separate runs are filled and summed up. Holes in the exposure maps are the result of exclusion regions. The edges of the holes are blurred due to the trajectory of the excluded regions in the camera during an observation run.*
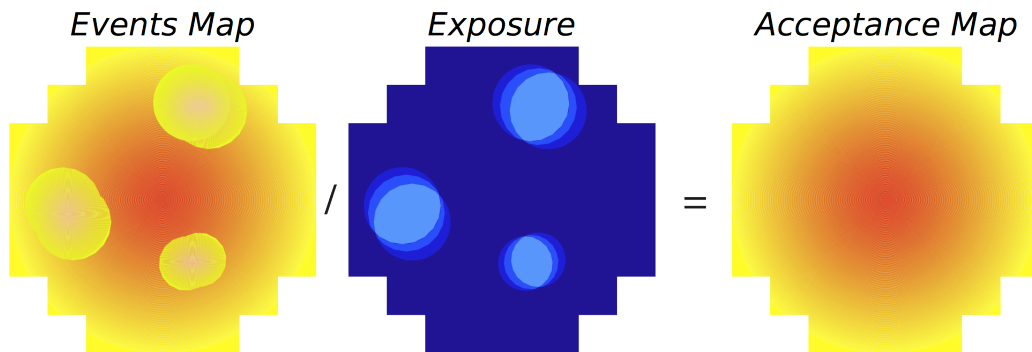
(b) *The acceptance map is calculated by simple division of the summed up events and exposure maps.*

Figure 3.15.: *Figures taken from [131].*

Another important property of a source of VHE gamma-ray radiation is its energy spectrum ϕ. If the

effective area and the energy resolution of the detector for different energies is known the amount of emitted photons N per energy E, area A and time interval t can be calculated:

$$\phi(E) = \frac{\mathrm{d}^3 N(E)}{\mathrm{d}E\,\mathrm{d}A\,\mathrm{d}t} \tag{3.16}$$

Because E is the true energy of the particles which is different from the reconstructed energy, the instrument response has to be taken into account. It is corrected for by using the effective area and the energy resolution obtained from MonteCarlo simulations. For a detailed description of the procedure, the reader is referred to de Naurois [131] and Aharonian et al. [11].

To follow the evolution of the activity of a source so-called light curves are used. A fixed spectral shape is assumed and the resulting flux for the source in a given energy range for several consecutive time intervals is calculated. Changes in the flux of a source can easily be identified using this technique and the temporal behaviour of transient events can be characterized.

The H.E.S.S. collaboration uses two main analysis chains for cross-check purposes. The *HAP* event reconstruction using the *Heidelberg* calibration chain together with boosted decision trees for cut optimization as stated in Ohm, van Eldik, and Egberts [170]. Recently a shower template based reconstruction has been added to *HAP* which was developed by Parsons and Hinton [184] but it was not used during the course of this work. The *Model Analysis* is using the *Paris* calibration during event reconstruction and relies on a more advanced shower reconstruction technique as shown in de Naurois and Rolland [136]. During the course of this work, both analysis chains have been used. Moreover, the event reconstruction of the *Model Analysis* was adjusted to the needs of H.E.S.S. Phase II and is explained in detail in Chapter 4. It was applied to data taken on the Crab Nebula as well an the results are shown in Chapter 5.

Make it work.
Make it right.
Make it fast.

Kent Beck

4

Model Analysis

4.1. Semi-Analytical Model

Since its introduction to VHE gamma-ray astronomy in 1985 the *Hillas Parameters* haven been used by all IACT experiments as a robust gamma-ray shower reconstruction technique [147]. Several enhancements to the method have been developed, for example the usage of the *Mean Reduced Scaled Length (MRSL)* and *Mean Reduced Scaled Width (MRSW)* [11]. A more sophisticated approach to the reconstruction of gamma-rays has been developed by Le Bohec et al. [135] for the CAT experiment and refined by de Naurois and Rolland [136] for the H.E.S.S. Phase I experiment. The idea is to compare the observed distribution of Cherenkov light with the predicted distribution using a semi-analytical model of air showers. The predicted shower images are obtained using the longitudinal, lateral and angular distributions of charged particles in an electromagnetic air shower. Using these distributions the Cherenkov light contributing to the final camera image can be calculated taking into account, for example, the collection efficiency of the detector as well as the atmospheric absorption of the Cherenkov Light. For H.E.S.S. Phase II the so-called *Model Analysis* had to be adjusted and enhanced to include, for example, different telescope types. This work is based on the developments done by de Naurois and Rolland [136]. Unaltered sections of the paper that are used in this work will be pointed out accordingly.

4.1.1. Model Generation

As stated in de Naurois and Rolland [136] and used unaltered within this work the light density due to Cherenkov light within the camera can be calculated using an eight-fold integral:

- The integral over the altitude or depth, i.e. the longitudinal shower development.

- The integral over the energy of the secondary particles within the air shower.

- The integral over the direction of the secondary particles with respect to the telescope.

- The integral over the position of the secondary particles with respect to their direction.

- The integral over the wavelength of the Cherenkov photons.

- The integral over the azimuth angle of the Cherenkov photons around the secondary particles.

The formula for the Cherenkov light density I in units of $\left[\frac{\text{p.e.}}{\text{rad}^2}\right]$ at a given point $P(X_t, Y_t)$ in radian in a two dimensional camera system is then given by:

$$
\begin{aligned}
I(X_t, Y_t) = \int \mathrm{d}z \int \mathrm{d}E \cdot \frac{\mathrm{d}N_e}{\mathrm{d}E}(D, E) \cdot \frac{\mathrm{d}D}{\mathrm{d}z}(E) \\
\int \mathrm{d}u \cdot F_u(u(E, s)) \int \frac{\mathrm{d}\phi}{2\pi} \\
\int \mathrm{d}X_r \int \mathrm{d}Y_r \cdot F_{XY}(X_r, Y_r, E, s, u) \\
\int \mathrm{d}\phi_{ph} \int \frac{\mathrm{d}\lambda}{\lambda^2} \cdot \frac{\mathrm{d}^2 n_\gamma}{\cos\theta \, \mathrm{d}z \, \mathrm{d}\lambda} \cdot \exp(-\tau(z, \lambda)) \cdot Q_{eff}(\lambda) \cdot \\
Col(z, X_r, Y_r, u, \phi, \phi_{ph}, X_t, Y_t)
\end{aligned}
\tag{4.1}
$$

The different integrals are defined as following:

- $\mathrm{d}N/\mathrm{d}E(D, E)$ is the energy dependent longitudinal distribution of charged particles within the air shower where E is the energy in TeV and D the shower depth within the atmosphere in radiation length (from eq. (1) and eq. (5) in [136]).

- $F_u(u(E, s))$ is the normalized angular distribution of particles (from eq. (4) and eq. (11) in [136]). s is the shower age with respect to the point of first interaction. u is the rescaled reduced angle between the secondary particle and the shower direction defined as $u = \frac{w}{\langle w \rangle}$ where w is the reduced angle as described in Moliere theory, i.e. $w = 2(1 - \cos\theta) \cdot \left(\frac{E}{21\,\text{MeV}}\right)^2$.

- $F_{XY}(X_r, Y_r, E, s, u)$ is the normalized lateral distribution of particles (from eq. (13) to eq. (16) from [136]). $X_r = \frac{x_e - \langle x_e \rangle}{\sigma_{x_e}}$ and $Y_r = \frac{y_e}{\sigma_{y_e}}$ are the reduced lateral distributions.

- $\frac{1}{\lambda^2} \cdot \frac{\mathrm{d}^2 n_\gamma}{\cos\theta \, \mathrm{d}z \, \mathrm{d}\lambda}$ is the Cherenkov photon production rate for a wavelength λ of the secondary particle at height z for an angle θ with respect to the shower axis.

- $\exp(-\tau(z, \lambda))$ is the absorption of Cherenkov light in the atmosphere above the detector.

- $Q_{eff}(\lambda)$ is the quantum efficiency of the detector including mirror reflectivity, etc.

- $Col(z, X_r, Y_r, u, \phi, \phi_{ph}, X_t, Y_t)$ is the average geometrical collection efficiency for photons emitted by a secondary particle at position X_r, Y_r, z with a flight direction defined by (u, ϕ) and an azimuthal photon angle ϕ_{ph} around the particle seen by a pixel with coordinates (X_t/Y_t) in the camera plane.

The implementation of Equation (4.1) in the model generation code is done using a binned approach for each of the different steps of the integration. Each integral is sliced into an adjustable amount of bins and solved individually. At each bin the possibility of the particles to contribute to the final image is checked and if found to be negligible the processing of the bin is aborted. To reduce the computation time the computing intensive tasks are speed up using lookup tables during the model generation process. For further information see de Naurois and Rolland [136].

For a given telescope type, shower templates are generated for:

- 21 different zenith angles θ equally spaced in $\cos\theta$ using the formula $i_\theta = 20 \cdot (1/\cos\theta - 1)$. Therefore, model templates in a zenith angle range from $0\,°$ to $60\,°$ are available.

- 50 different impact distances ranging from $0\,\mathrm{m}$ to $(500\,\mathrm{m}/\cos\theta)$ of the shower core to the telescope.

- 75 different energies in a range from $(5\,\mathrm{GeV}/\cos\theta)$ up to $(100\,\mathrm{TeV}/\cos\theta)$ equally spaced in $\ln(E/E_c)$ with E_c being the critical energy in air, see Equation (4.9).

- 10 different first interaction depths from $0.03\,\mathrm{X_0}$ to $12.2\,\mathrm{X_0}$ equally spaced in $\ln(D)$. Note that this is different to the approach used by de Naurois and Rolland [136] who used an equally spaced binning in D instead.

To reduce the amount of templates needed, the telescope is assumed to be perfect, i.e. no broadening of the point spread function with increasing offset. Therefore, the shower templates are all generated on-axis and a change in direction can be done using a simple rotation and translation in the camera frame, see de Naurois and Rolland [136].

After generating a camera image using Equation (4.1) several instrumental effects have to be taken into account. For example, the point spread function of the telescope, the electronic response of the camera, especially the trigger generation and the length of the read out window.

4.1.2. Trigger and Read Out

The output of the model generation routine is the three dimensional distribution of the Cherenkov photon density in the camera plane over time, the *Time Evolution Template* (*TET*). The coordinate system of the camera plane is the *Nominal System*, see Section 3.7 or Gillessen [156]. The position of the source in the *X-Y* camera plane is at the coordinate $\vec{S} = (0,0)$, i.e. on-axis. The X axis is chosen to be aligned with the direction of the major axis of the Hillas ellipse, i.e. the projected shower direction in the camera frame. To save memory, the shower template is assumed to be axially symmetric with respect to the Y axis and therefore only the positive half of the *TET* needs to be stored. The binning of a *TET* is chosen to be sufficiently small with respect to the size of a single PMT of the camera of the given telescope type in the *Nominal System*. For ease of use, the bin size in the X and Y dimension are the same. In detail, the bin size L is chosen such that the area of the bin A is a constant fraction α of the area F of a single PMT in steradian. Using the flat-to-flat distance d of a hexagonal PMT, the telescope focal length f_{Tel} and the formula for the area of a hexagon one obtains:

$$L = \sqrt{A} = \sqrt{\alpha \cdot F} = \sqrt{\frac{\alpha \cdot d^2 \cdot \sqrt{3}}{2 \cdot f_{Tel}^2}} \tag{4.2}$$

During the generation of the *TET*, the extension in X is eight times the field of view of the telescope and four times in Y (Y being symmetric). This is done to make sure that the *TET* is not truncated. The Z dimension stores the information about the time evolution of the *TET* using a 1 ns binning (the size of a cell in the read out electronics, see Section 3.5) ranging from $-10\,\mathrm{ns}$ to $100\,\mathrm{ns}$. The *TET* is then multiplied with the area of the PMT to convert the photon density in actual pixel intensities, folded with the photo multiplier response (see Section 3.6) and shrunk to the relevant part of the image using a fixed threshold divided by the amount of bins in the Z dimension. Currently a threshold of $0.05\,\mathrm{p.e.}$ is used (not yet divided by the 110 bins in time). An example *TET* which is already shrunk can be seen in Figure 4.1a for a zenith angle of $18\,°$, a primary energy of $36\,\mathrm{TeV}$, an impact distance of $75\,\mathrm{m}$ and a first interaction depth of $0.4\,\mathrm{X_0}$ using the H.E.S.S. II detector configuration. Different projections
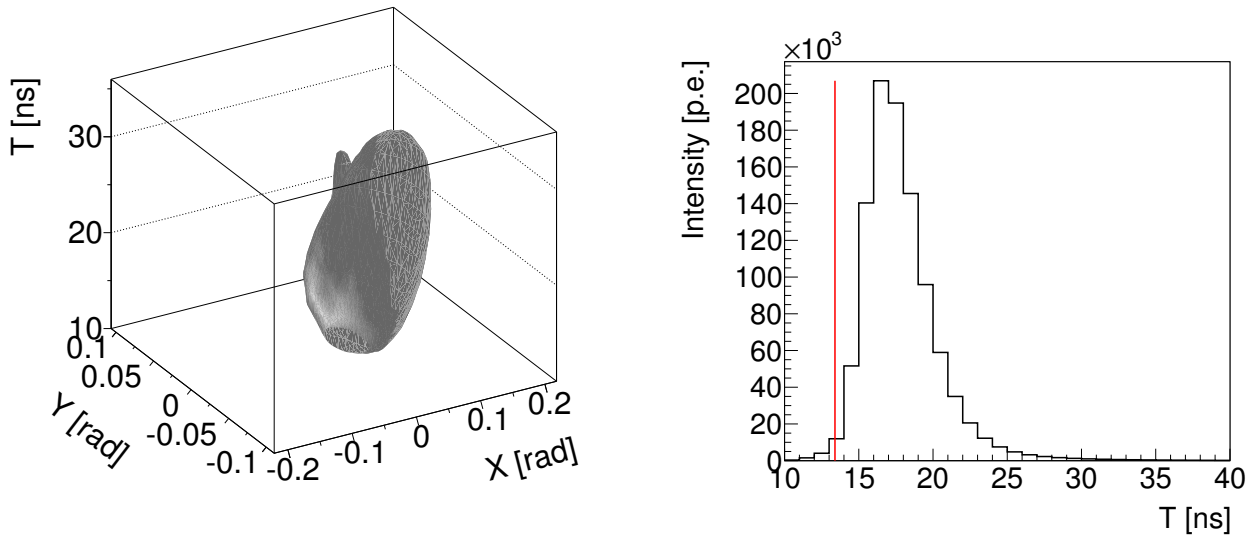
(a) *Time evolution of a shower template for a zenith angle of* 18 °*, a primary energy of* 36 TeV*, an impact distance of* 75 m *and a primary depth of* 0.4 X_0*. The* TET *is already folded with the response of the PMT and shrunk to the relevant part of the three dimensional shower template using a fixed threshold. The actual image is zoomed in to the relevant part of the shower. The three dimensional histogram was rebinned in the X and Y dimension by a factor of 10 for a better visualization.*

(b) *Time profile of the* TET *from a. The red line indicates the trigger time of the shower template. To extract the two dimensional shower template, a slice with a width equivalent to* 16 ns *is extracted, the read out window of the ARS. The time profile is zoomed in to the relevant part of the shower.*

Figure 4.1.

of the *TET* are shown in Figure 4.2 to visualize the three dimensional evolution of a simulated air shower. These templates are saved to disk as an intermediate step of the model generation process. To simulate the trigger response, the time profile of the *TET* is fitted with a rising-edge function:

$$f(t) = A \cdot \frac{1}{1 + \exp\left(-\frac{t-\mu}{\sigma}\right)} \tag{4.3}$$

where t is the time in nanoseconds, μ the half-maximum and σ the width of the curve. The trigger time is then set to the point where the signal has reached $P = 5\%$ of its maximum value, i.e.:

$$t_{trig} = -\sigma \ln(\frac{1}{P} - 1) + \mu \tag{4.4}$$

The time profile for the shower shown in Figure 4.1a can be seen in Figure 4.2f and in Figure 4.1b together with the calculated trigger time.

The raw 2D *Shower Template* (*ST*) is then obtained by summation of all time bins from t_{trig} until $t_{trig} + N_D$ where N_D is the length of the read out window, see Section 3.5. An example raw *ST* can be seen in Figure 4.3a. After these steps, all the effects of the camera electronics have been applied.
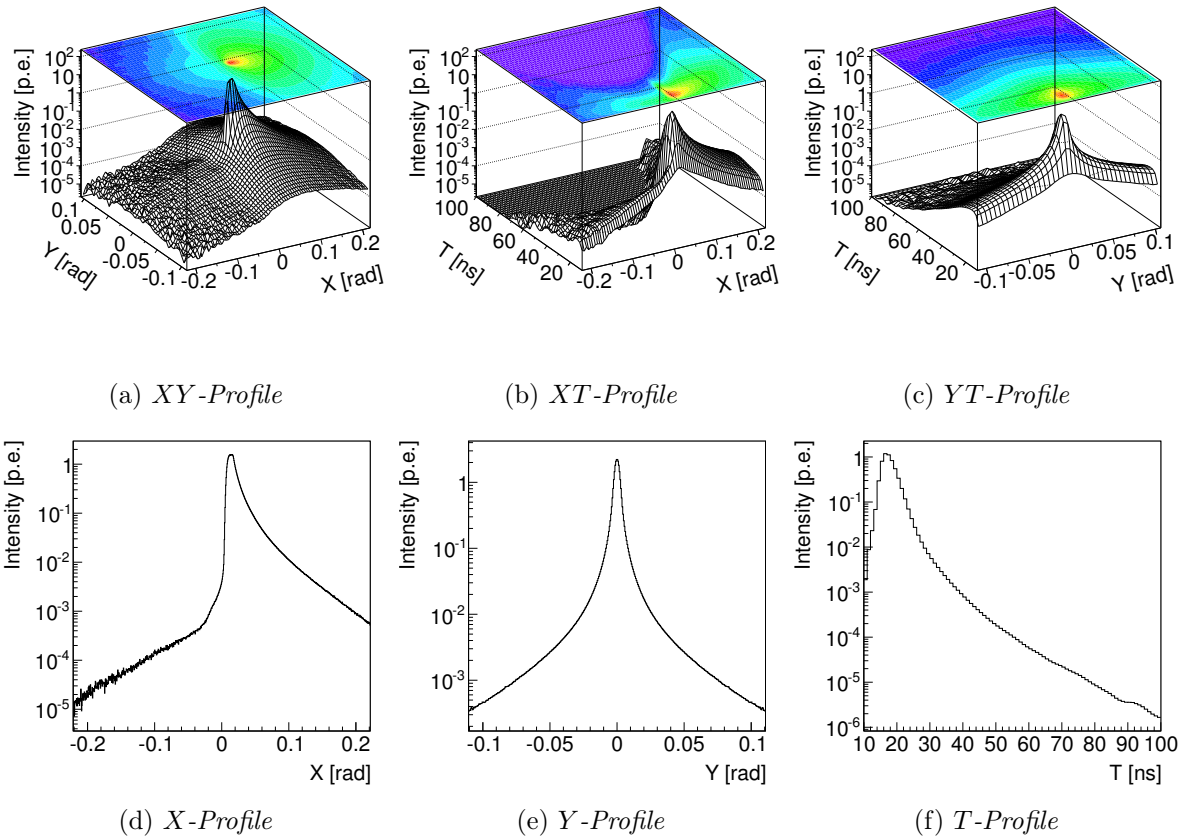
(a) *XY-Profile*

(b) *XT-Profile*

(c) *YT-Profile*

(d) *X-Profile*

(e) *Y-Profile*

(f) *T-Profile*

Figure 4.2.: *Different projections of the* TET *shown in Figure 4.1a. The Z axis for the two dimensional histograms are in log scale and show the mean value in the respective dimension. The same applies for the Y axis of the one dimensional histograms. The X and Y dimension were rebinned by a factor of 10 for a better visualization.*

4.1.3. PSF and PMT Influence

The next step in the process of the generation of the final two dimensional ST is a smoothing of the raw image, as e.g. shown in Figure 4.3a. A Gaussian kernel is used during this process. The width of the Gaussian kernel is chosen so that 99.9% of the integral of the Gaussian is within a given range R. The range is defined as the square root of the squared values of the radius of the PMT in radian and the optical point spread function of the telescope in radian:

$$R = \sqrt{r_{\mathrm{Pix}}^2 + r_{99.9\%}^2} \tag{4.5}$$

Here r_{Pix} is the radius of the PMT (approximated by a circle) and $r_{99.9\%}$ is the 99.9 percentile of the the point spread function. It is estimated from the (measured) 80 percentile of the PSF using the ratio of the same percentiles of the standard normal distribution P_{Norm}. Note that P_{Norm} is defined from $-\infty$ and the 80 percentile of the PSF from 0. To correct for that P_{Norm} has to be evaluated at position $50 + 50 \cdot 0.8$ to calculate the correct ratio:

$$r_{99.9\%} = r_{80\%} \cdot \frac{P_{\mathrm{Norm}}(99.9)}{P_{\mathrm{Norm}}(50 + 50 \cdot 0.8)} \tag{4.6}$$

Due to the sharp rise of the shower at the lower edge of the X dimension, the template size is increased before the smoothing to prevent a sharp cut off near the edge. A smoothed template can be seen in
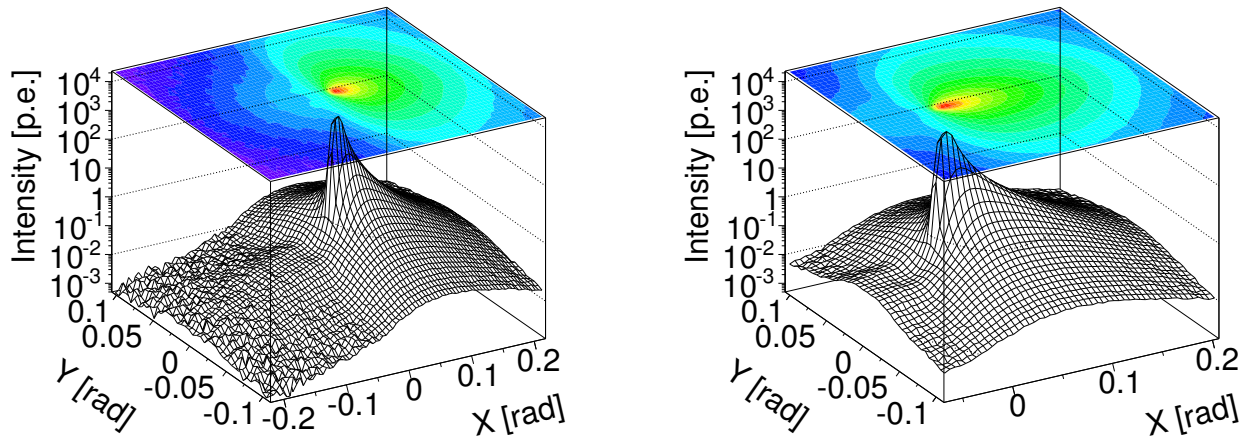
(a) *Raw* ST *extracted from the* TET *in Figure 4.1a using the trigger time shown in Figure 4.1b. All effects due to the camera electronics have now been applied. The X and Y dimension were rebinned by a factor of 10 for a better visualization.*

(b) *Smoothed and shrunk* ST *using the raw template from a. The reduced template extension due to the fixed threshold at* 0.05 p.e. *is clearly visible. The X and Y dimension were rebinned by a factor of 10 for a better visualization.*

Figure 4.3.

Figure 4.3b.

After the smoothing of the template, it is shrunk again to save memory. The same fixed threshold of 0.05 p.e. is used. Once shrunk, the template is normalized to an integral content of unity and the total integral is saved separately. Moreover, the center of gravity of the image is calculated and stored as well. Note that the Y dimension is symmetric, therefore, only the center of mass in the X dimension has to be calculated. The equation used for the coordinate X and the intensity I is

$$\text{CoM}_I = \frac{\sum_i (X_i \cdot I_i)^3}{I_{\text{Tot}}} \tag{4.7}$$

to move the center of mass close to the point of maximum emission. These final templates are saved to disk and used for the later lookup.

4.2. Full 5D Model

The final normalized 2D shower templates are filled into three dimensional lookup tables for each zenith angle bin depending on the primary energy of the particle E, the impact distance of the shower core to the telescope R as well as the primary interaction depth D (summarized as *outer dimensions*). These objects are the so-called *Full Model*. Together with the X and Y dimension of the camera plane (dubbed *inner dimensions*), this gives a five dimensional lookup table for pixel intensities. In addition to the shower templates, the total image intensity and the center of mass and the trigger time (for sanity checks) are stored in three dimensional lookup tables, using the same dimension definition. A *Full Model* consists of $75 \cdot 50 \cdot 10 = 37500$ shower images and uses on average 410 MB disk space for a H.E.S.S. I type telescope and 1528 MB for a H.E.S.S. II type (lookup tables are compressed using

the bzip2 [189] filters of the BOOST *iostream* library [190]). Note that the difference in size is due to the smaller pixel size of a H.E.S.S. II PMT although the field of view of the telescope is smaller. Figure 4.4 shows example distributions for a H.E.S.S. II type telescope for the total intensity of the shower template as well as their center of masses versus the three *outer dimensions*. The semi-analytical model produces smooth templates over a wide range in primary energy, impact distance and primary depth.

(a) *Integral H.E.S.S. I* (b) *Center of mass H.E.S.S. I* (c) *Bins H.E.S.S. I*

(d) *Integral H.E.S.S. II* (e) *Center of mass H.E.S.S. II* (f) *Bins H.E.S.S. II*
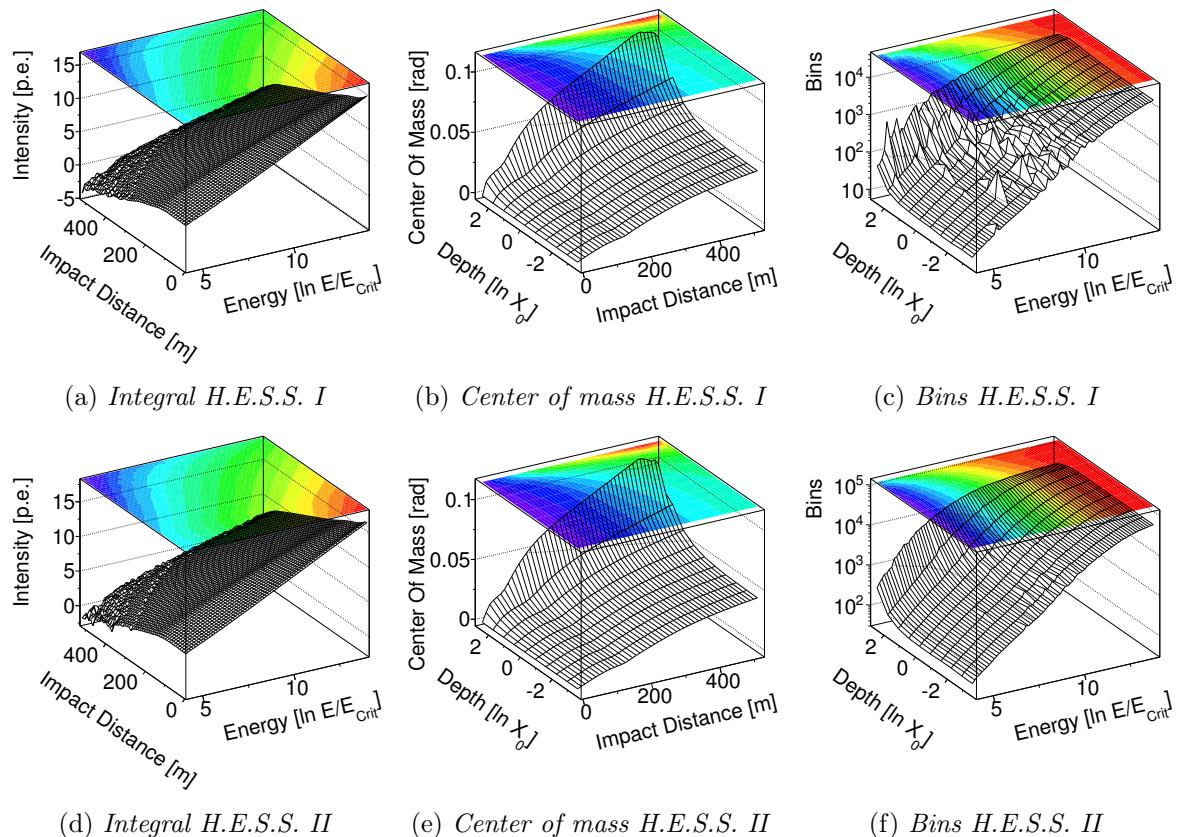
Figure 4.4.: *Example projections of the three dimensional distributions of the total image intensity, the center of mass and the number of bins for a given template. The distributions for H.E.S.S. I and H.E.S.S. II type telescopes look similar.*

4.2.1. Template Interpolation

To reduce the amount of model templates needed as well as to improve the overall shower reconstruction, a linear interpolation between the model templates is used. This interpolation is done in all dimensions of the *Full Model*. A detailed description of the *Linear Tables* can be found in Appendix A. Next to the interpolated intensity also gradient information is available, again see Appendix A. As already mentioned, the shower templates stored in the *Full Model* are generated for a source position in the *Nominal System* at $\vec{S} = (0,0)$ which corresponds to a source position of $\vec{S} = (0,0,1)$ in the *Tilted System*, see Section 3.7 or Gillessen [156]. Since the H.E.S.S. array normally observes in *Wooble mode*, see Section 3.9, the source is not located in the center of the camera and the model templates need to be translated. Moreover, the shower orientation in the camera is not parallel to the X axis and the templates need to be rotated accordingly. Note that in the following the zenith and azimuth angle is assumed to be at a fixed value

because during one event the zenith angle (and azimuth angle) change is negligible.

Shower Parameters

An air shower detected by the H.E.S.S. array is described by the following *Shower Parameters* (see Section 3.3):

- Zenith and azimuth angle of the shower.

- Particle source position $\vec{S} = (S_x, S_y, 1)$ in radian in the *Tilted System*.

- Shower core position $\vec{C} = (C_x, C_y, 0) = (R, \pi/2, \phi)$ in meter in the *Tilted System*.

- Particle energy E in TeV.

- Particle first interaction depth D in units of the radiation length in air X_0.

Note that the source z position is set to be at infinity which translates to a value of 1 in the *Tilted System*, a telescope system with a focal length of $1\,\mathrm{m}$. The z component of the core position is by definition 0 in the *Tilted System* and, therefore, the θ angle needs to be $\pi/2$.

The *Shower Parameters* used to obtain the expected signal μ for a given pixel at position (X_c, Y_c) in a camera must, therefore, be translated into the variables used by the *Full Model*:

$$\begin{aligned}
\mu\big(S_x, S_y, E, R, \phi, D, X_c, Y_c\big) &= \mu\big(S_x, S_y, \epsilon, \rho, \varphi, \tau\big) \\
&= I\big(\epsilon, \rho, \tau\big) \cdot A\big(S_x, S_y, \epsilon, \rho, \varphi, \tau, X_t, Y_t\big)
\end{aligned} \tag{4.8}$$

Here I is the total intensity contained in the shower template. It depends on the three parameters of the *outer dimensions*:

- The logarithm of the primary energy in units of the critical energy in air.

$$\epsilon(E) = \ln \frac{E\,[\mathrm{TeV}]}{E_{Crit}} = \ln \frac{E\,[\mathrm{TeV}]}{83\,\mathrm{MeV}} \tag{4.9}$$

- The impact distance in units of meter of the shower to the telescope $\rho(S_x, S_y, R, \phi)$ in the *Tilted System*. For a detailed explanation see Section 4.2.1.

- The logarithm of the primary interaction depth in units of radiation length.

$$\tau(D) = \ln(D\,[\mathrm{X}_0]) = \ln(D\,[366.6 * \mathrm{kg/m}^{-2}]) \tag{4.10}$$

The normalized amplitude A at a given position (X_t, Y_t) within a shower template depends on ϵ, ρ and τ as well. To correct for the assumed source position S at $(0, 0)$ and the on-axis shower incidence during the model generation, the shower templates have to be rotated and translated and the pixel coordinates adjusted accordingly, i.e. transformed from (X_c, Y_c) to (X_t, Y_t).

Coordinate Transformations

The coordinate transformation from $\vec{C} = (C_x, C_y, 0) = (R, \pi/2, \phi)$ in the *Tilted System* to the relevant coordinates for the *Full Model* $\vec{C} = (\rho, \pi/2, \varphi)$ is shown in Figure 4.5. A single telescope in the *Ground System*, see Section 3.7 or Gillessen [156], and *Tilted System* is shown. The viewing direction is chosen such that it is parallel to the Y axis of the *Tilted System*. The impact distance is given by the length of the rejection vector of the vector from the shower core $\vec{C}$ to the telescope position $\vec{T}$ with the source direction vector $\vec{S}$:

$$
\begin{aligned}
\rho &= \sqrt{|\vec{C} - \vec{T}|^2 - (\cos\beta \cdot |\vec{C} - \vec{T}|)^2} \\
&= \sqrt{|\vec{C} - \vec{T}|^2 - \left(\frac{(\vec{C} - \vec{T}) \cdot \vec{S}}{|\vec{S}|}\right)^2}
\end{aligned}
\tag{4.11}
$$

using

$$
\cos\beta = \frac{(\vec{C} - \vec{T}) \cdot \vec{S}}{|\vec{C} - \vec{T}| \cdot |\vec{S}|}
\tag{4.12}
$$

This distance is the distance between the shower axis and the telescope. The equation for φ is simply given by:

$$
\varphi = \arctan\left(\frac{T_y - C_y}{T_x - C_x}\right)
\tag{4.13}
$$

which is the angle at which the shower is seen by the telescope and just depends on the core position. The signs are switched due to the fact that the shower direction is given in *Nominal System* and the telescopes are mirror telescopes, see Section 3.7.

To correct for the offset of the source position $\vec{S}$ from the actual pointing position (see Section 3.9) the following translation matrix is used:

$$
T_S = \begin{pmatrix} 1 & 0 & -S_x \\ 0 & 1 & -S_y \\ 0 & 0 & 1 \end{pmatrix}
\tag{4.14}
$$

The rotation of the shower template around the telescope due to different viewing angles φ is done using the rotation matrix:

$$
R_\varphi = \begin{pmatrix} \cos\varphi & \sin\varphi & 1 \\ -\sin\varphi & \cos\varphi & 1 \\ 0 & 0 & 1 \end{pmatrix}
\tag{4.15}
$$

Finally a center of mass correction term Δ_{CoM} is applied as an offset in the X dimension to access each template in its center of mass system during interpolation of several shower templates:

$$
T_{\Delta_{\mathrm{CoM}}} = \begin{pmatrix} 1 & 0 & \Delta_{\mathrm{CoM}} \\ 0 & 1 & 0 \\ 0 & 0 & 1 \end{pmatrix}
\tag{4.16}
$$

The center of mass correction Δ_{CoM} for a given template while interpolating a set of shower templates is defined as:
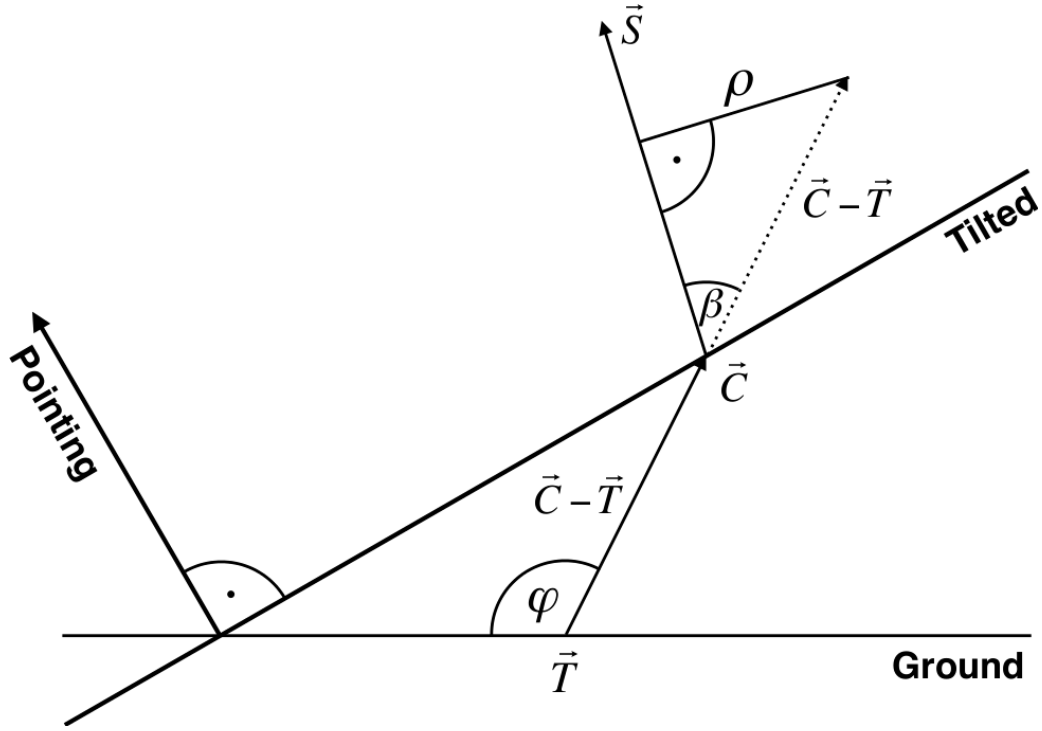
Figure 4.5.: *Example visualization of the coordinate transformation from the* Tilted System *to the coordinates of the* Full Model.

$$\Delta_{\mathrm{CoM}} = \langle \mathrm{CoM} \rangle - \mathrm{CoM} \tag{4.17}$$

Note that the center of masses of each template are also stored in a lookup table and depend on ϵ, ρ and τ as well (like the total image intensity I).

The final equation to transform a pixel coordinate from the *Nominal System* to the *Full Model* coordinate system then reads:

$$X_t(S_x, S_y, \varphi, \Delta_{\mathrm{CoM}}) = (X_c - S_x) \cos \varphi + (Y_c - S_y) \sin \varphi - \Delta_{\mathrm{CoM}} \tag{4.18}$$

$$Y_t(S_x, S_y, \varphi) = -(X_c - S_x) \sin \varphi + (Y_c - S_y) \cos \varphi \tag{4.19}$$

4.2.2. Template Validation

To verify the shower templates generated using the semi-analytical model, a comparison with MonteCarlo generated gamma-ray shower images can be used. For each MonteCarlo shower the corresponding shower template using the MonteCarlo true parameters is obtained. *Hillas Parameters* are calculated for both shower images and compared. To simulate night sky background which is not present in the model templates, a simple Gaussian distribution with a mean of 0 p.e. and a sigma of 1.6 p.e. is assumed for its contribution to the intensity in every pixel. Figure 4.6 shows the mean and the rms of the distributions of the *Size* versus the true primary energy and the *Length* of the Hillas ellipse. Moreover, the *Width* versus the true primary depth is shown. The distributions for the different telescope types look similar as expected (the dish structure is not too different and the increase in collected Cherenkov

light should only scale the resulting distributions). Except for the Hillas *Width* the model and the MonteCarlo showers match nicely. The offset of the Hillas *Length* distributions for the H.E.S.S. II telescope type as well as the discrepancy at higher energies for the Hillas *Width* distributions is worth to be investigated but is beyond the scope of this work. In Figure 4.7 the true *Impact Distance* of the shower to the telescope versus the reconstructed Hillas *Length*, *Width* and *Nominal Distance* is shown. The results are similar to the ones seen in Figure 4.6. The Hillas *Length* distributions differ but are within acceptable limits.

(a) *H.E.S.S. I*

(b) *H.E.S.S. II*

(c) *H.E.S.S. I*

(d) *H.E.S.S. II*

(e) *H.E.S.S. I*

(f) *H.E.S.S. II*

Figure 4.6.: *Comparison between the MonteCarlo* Hillas Parameters *in black and the* Full Model Hillas Parameters *in red obtained using the MonteCarlo true shower information. For the definition of the unit of the energy see Equation* (4.9). *The mean of the distributions for each bin matches nicely. The difference seen for the Hillas* Length *and* Width *distributions remain acceptable.*

(a) *H.E.S.S. I*

(b) *H.E.S.S. II*

(c) *H.E.S.S. I*

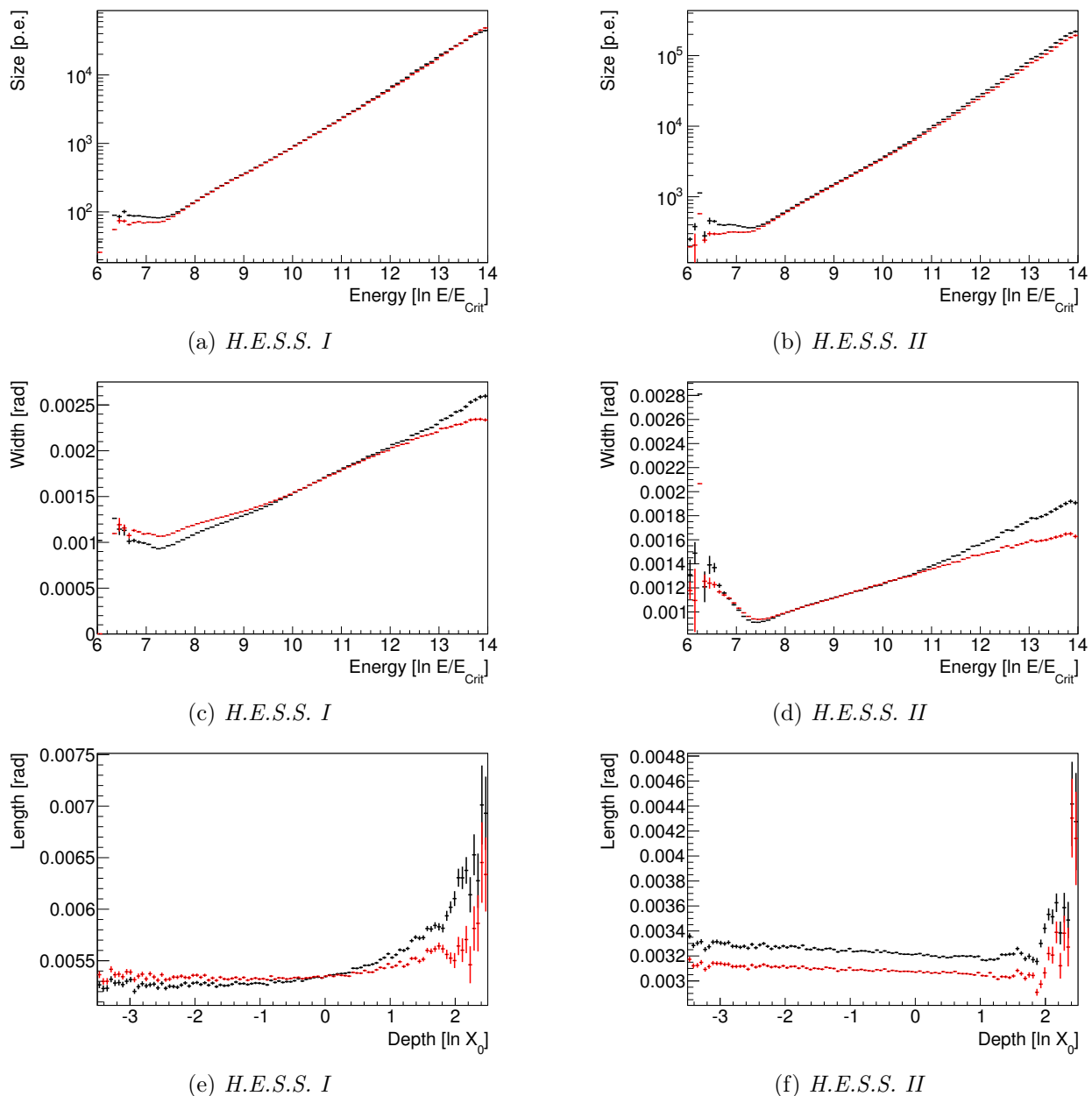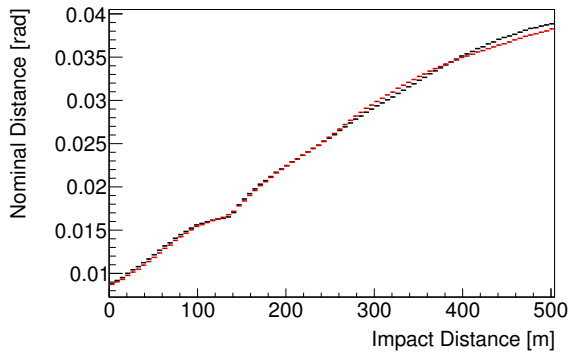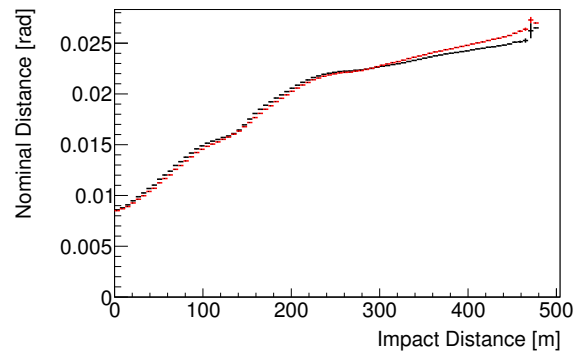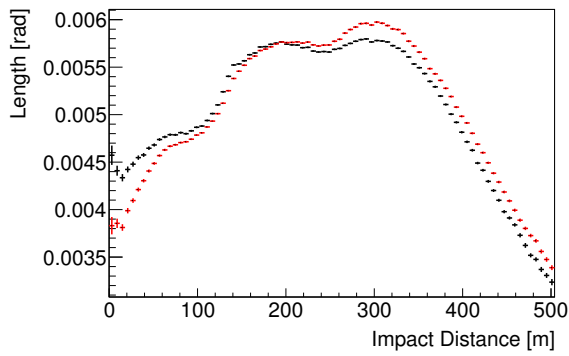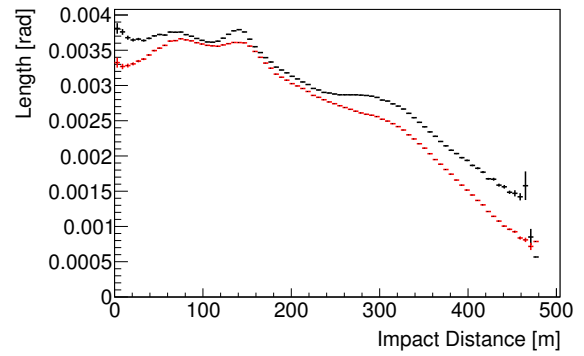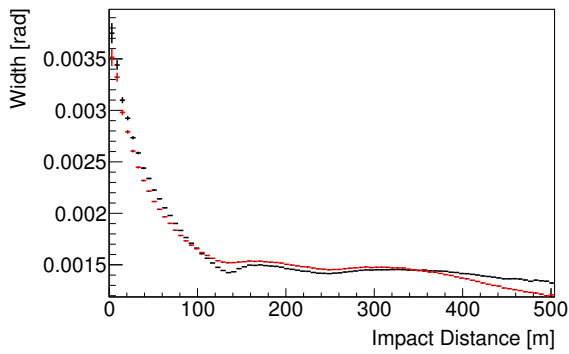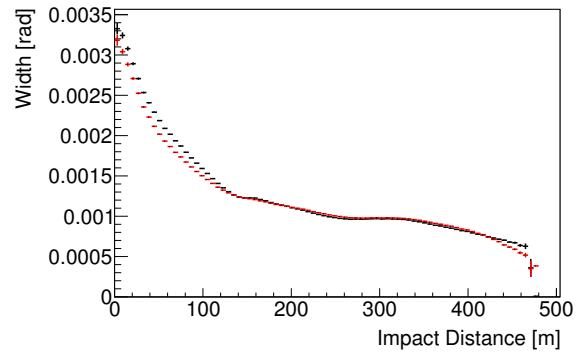(d) *H.E.S.S. II*

(e) *H.E.S.S. I*

(f) *H.E.S.S. II*

Figure 4.7.: *Comparison between the MonteCarlo* Hillas Parameters *in black and the* Full Model Hillas Parameters *in red obtained using the MonteCarlo true shower information. The distributions match nicely. The difference seen for the Hillas* Length *distributions remain acceptable.*

4.3. Shower Reconstruction

A predicted camera image for any given gamma-ray shower that can be observed by the detector can be obtained using the semi-analytical model described in Section 4.1. Using the Maximum Likelihood Method first proposed by Fisher [191, 192] the best fitting shower template can be calculated as well as an estimator for the goodness of the fit. The different steps necessary for the fitting procedure will now be explained in detail using the example MonteCarlo event shown in Figure 4.8 with the *Shower Parameters*:

- Zenith angle of $18°$

- Source position at $(0.000220\,\mathrm{rad}, -0.00872\,\mathrm{rad})$ in the *Nominal System*

- Impact distance of $215.1\,\mathrm{m}$

- Azimuth angle of $-22.3°$

- Primary energy of $1.35701\,\mathrm{TeV}$

- Primary depth of $0.6\,\mathrm{X_0}$
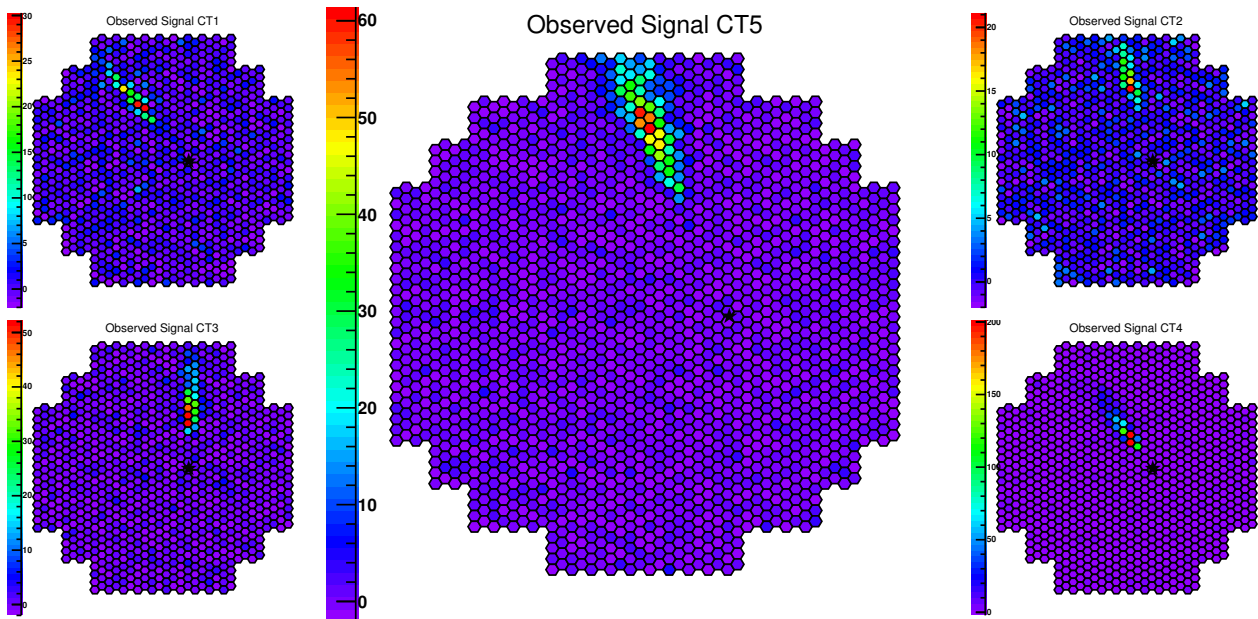
Figure 4.8.: *Exemplary five telescope MonteCarlo event for an gamma-ray induced air shower. The source position in the* Nominal System *is indicated by the black star. Note that the actual size of the CT5 camera is smaller than the other four, see Section 3.4.*

4.3.1. Probability Density Function

The response of a PMT can be described using a Gaussian with a width of

$$\sigma = \sqrt{\sigma_p + n\sigma_\gamma} \qquad (4.20)$$

σ_p is the width of the pedestal peak, σ_γ the width of a single photo electron peak and n the number of photo electrons. To take the intrinsic fluctuation of air showers into account, an additional parameter is added to the photo multiplier response. σ_f is depending on the expected signal μ and reflects the increasing inter-shower fluctuations at higher energies

$$\sigma = \sqrt{\sigma_p + n\sigma_\gamma + \sigma_f} \tag{4.21}$$

with

$$\sigma_f(\mu) = \mu \cdot \delta \tag{4.22}$$

where δ is adjusted using MonteCarlo data. Currently a value of 0.05 is used, i.e. 5 %, which has been proven to work well with H.E.S.S. Phase I.

The probability density function (PDF) to observe a signal s when expecting a signal μ is then given by the convolution of the Poisson distributed photo electron number n and the Gaussian photo multiplier response function (3.7):

$$P(s|\mu,\sigma) = \sum_n \overbrace{\frac{\mu^n e^{-\mu}}{n!}}^{\text{Poisson}} \cdot \overbrace{\frac{1}{\sqrt{2\pi\sigma^2}} \cdot \exp\left(-\frac{(s-n)^2}{2\sigma^2}\right)}^{\text{Gaussian}} \tag{4.23}$$

A fitted expected signal μ for the example event seen in Figure 4.8 is shown in Figure 4.9.
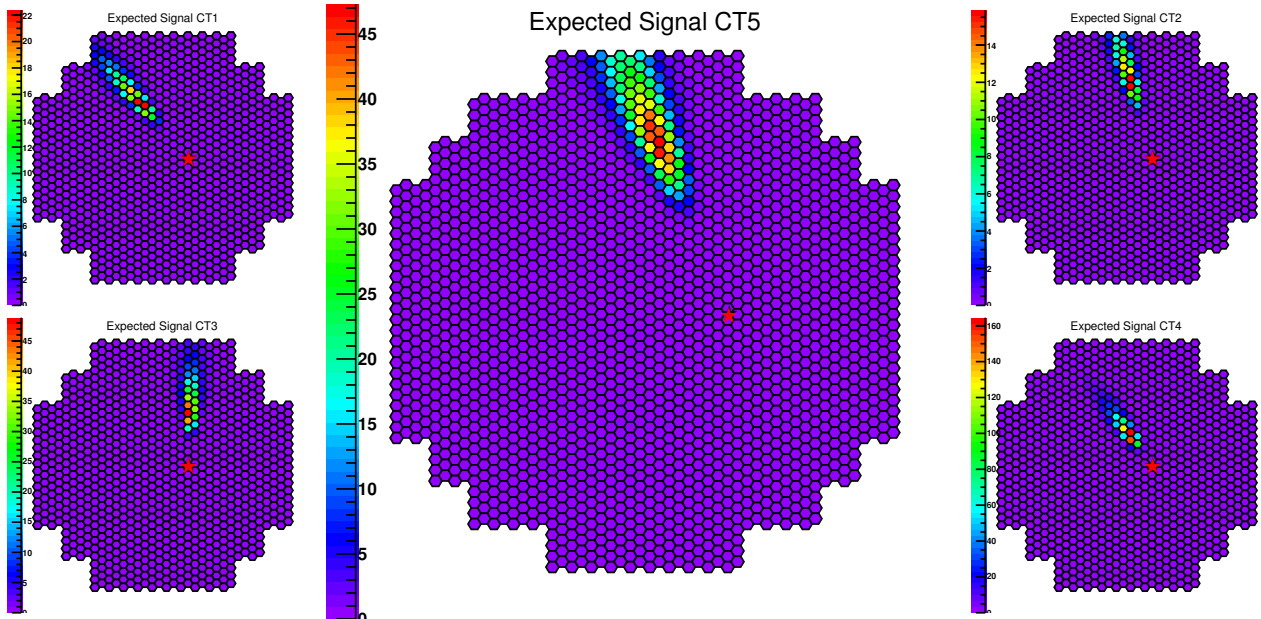
Figure 4.9.: *Fitted expected signal for the example MonteCarlo event shown in Figure 4.8. The source position in the* Nominal System *is indicated by the black star. The red star indicates the fitted source position. The fitted image resembles the observed quite well. The bigger offset of the black and red star in the CT5 camera image is due to the smaller camera size of H.E.S.S. II.*

To better cope with floating point precision the following representation of the formula Equation (4.23) is used:

$$
\begin{aligned}
\ln P &= \ln \left[e^{-\mu} \cdot (2\pi)^{-\frac{1}{2}} \sum_n \frac{\mu^n}{n!} \sigma^{-1} \exp \left(- \frac{(s-n)^2}{2\sigma^2} \right) \frac{e^\kappa}{e^\kappa} \right] \\
&= \ln \left[e^{-\mu} \cdot (2\pi)^{-\frac{1}{2}} \cdot e^\kappa \sum_n \frac{\mu^n}{n!} \sigma^{-1} \exp \left(- \frac{(s-n)^2}{2\sigma^2} - \kappa \right) \right] \\
&= -\mu - \frac{1}{2} \ln (2\pi) + \kappa + \ln \left[\sum_n \frac{\mu^n}{n!} \sigma^{-1} \exp \left(- \frac{(s-n)^2}{2\sigma^2} - \kappa \right) \right] \\
&= -\mu - \frac{1}{2} \ln (2\pi) + \kappa + \ln \left[\sum_n \sigma^{-1} \exp \left(n \ln (\mu) - \ln (n!) + \frac{(s-n)^2}{4\sigma^2} + \frac{\kappa}{2} \right) \right]
\end{aligned}
\tag{4.24}
$$

Here κ is the biggest value of the exponent $(-\frac{(s-n)^2}{2\sigma^2})$ and used to adjust each addend to the same order of magnitude. Therefore, floating point inaccuracies due to huge differences in the magnitude of the different addends of the summation can be avoided.

In the case of no expected signal ($\mu = 0$), i.e. only night sky background, the average value of the pixel log-likelihood can be calculated analytically. The PDF simplifies to a Gaussian of width σ_p:

$$
P(s|\mu = 0, \sigma_p) = \frac{1}{\sqrt{2\pi\sigma_p^2}} \exp \left(- \frac{s^2}{2\sigma_p^2} \right)
\tag{4.25}
$$

The Poisson distribution can be replaced by a Gaussian of width $\sqrt{\mu}$ for sufficiently high expected signals μ. The resulting PDF is the convolution of two Gaussians:

$$
P(s|\mu \gg 0, \sigma_p, \sigma_\gamma, \sigma_f) \approx \frac{1}{\sqrt{2\pi\left(\sigma_p^2 + \mu(1 + \sigma_\gamma^2) + \sigma_f\right)}} \exp \left(- \frac{(s-n)^2}{2\left(\sigma_p^2 + \mu(1 + \sigma_\gamma^2 + \delta)\right)} \right)
\tag{4.26}
$$

An example PDF is shown in Figure 4.10 which is a recreation of Fig. 14 in [136].

4.3.2. Maximum Likelihood Method

The maximum likelihood method was introduced by Fisher [191, 192]. It is used for the fitting of the real shower camera images with the shower templates obtained from the *Full Model* on a pixel-by-pixel basis. For ease of use, the logarithm of the negative likelihood is minimized to obtain the best fitting shower template. The pixel-wise log-likelihood using Equation (4.23) is given by

$$
\ln L(s|\mu, \sigma) = -2 \cdot \ln P(s|\mu, \sigma)
\tag{4.27}
$$

and behaves asymptotically like a χ^2 distribution. The pixel-wise log-likelihood for the example event seen in Figure 4.8 using the expected signal from Figure 4.9 is shown in Figure 4.11

In the absence of an expected signal, the pixel log-likelihood is easily obtained using Equation (4.25):

$$
\ln L(s|\mu = 0, \sigma_p) = -2 \ln P = \ln(2\pi) + \ln \sigma_p^2 + \frac{s^2}{\sigma_p^2}
\tag{4.28}
$$

To calculate the variance of the log-likelihood, the expected pixel log-likelihood and expected squared pixel log-likelihood need to be calculated.

$$
\sigma^2(\ln L) = \langle \ln^2 L \rangle - \langle \ln L \rangle^2
\tag{4.29}
$$
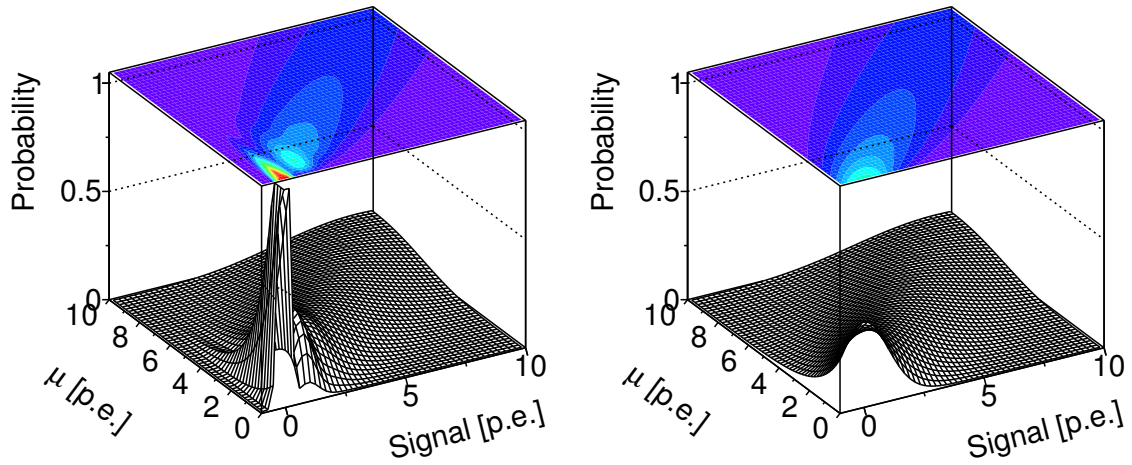
(a) *Left:* High Gain *H.E.S.S. I, Right:* Low Gain *H.E.S.S. I*
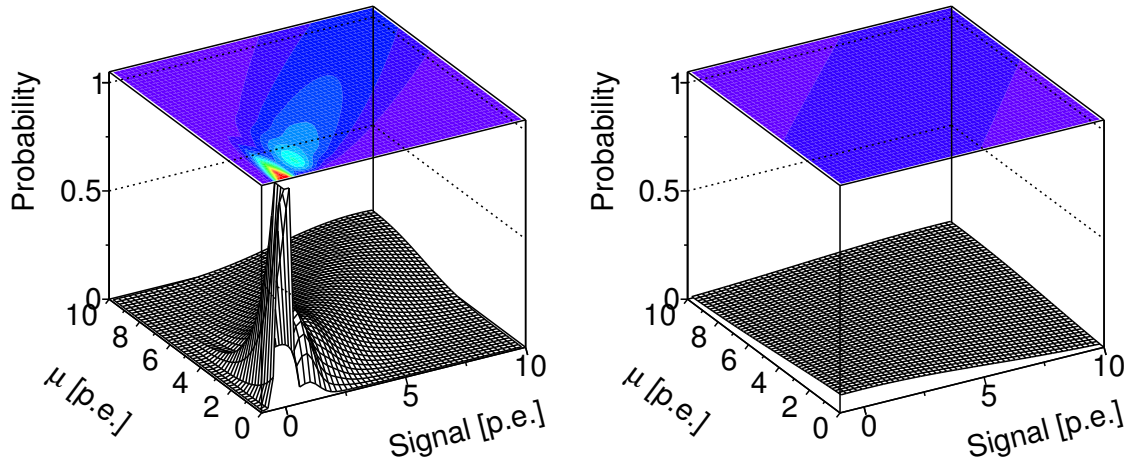
(b) *Left:* High Gain *H.E.S.S. II, Right:* Low Gain *H.E.S.S. II*

Figure 4.10.: *Probability density functions (PDFs) from Equation (4.23) for the detector configurations of the H.E.S.S. I and the H.E.S.S. II telescopes for both gain channels. The pedestal peak of the PDFs are clearly visible for the* High Gain *channels, the part of the PDF with higher observed and expected signal values is the pure Gaussian regime of the PDF. Due to the smaller amplification in the* Low Gain *channels, the pedestals peaks are not that dominant. Note that the gain ratios for H.E.S.S. I and H.E.S.S. II type cameras are different.*

For a given random variable x and a function $g(x)$ the expected value of $\langle g(x) \rangle$ can be calculated using the PDF $f(x)$:

$$\langle g(x) \rangle = \int_{-\infty}^{\infty} g(x) \cdot f(x) \mathrm{d}x \tag{4.30}$$

Applying these for the log-likelihood Equation (4.28) yields:

Figure 4.11.: *Pixel-wise log-likelihood for the example event shown in Figure 4.8 using the expected signal from Figure 4.9. The source position in the* Nominal System *is indicated by the black star. The red star indicates the fitted source position. Ideally the distribution of the pixel-wise log-likelihoods in a camera after a successful fit should look like a random distribution with a small rms. Single pixel with a high log-likelihood are mostly due to fluctuations in the night sky background.*

$$
\begin{aligned}
\langle \ln L(s) \rangle|_{\mu=0} &= \int_{-\infty}^{\infty} \mathrm{d}s \, \ln L(s|\mu=0,\sigma_p) \cdot P(s|\mu=0,\sigma_p) \\
&= \int_{-\infty}^{\infty} \mathrm{d}s \left(\ln(2\pi) + \ln \sigma_p^2 + \frac{s^2}{\sigma_p^2} \right) \frac{1}{\sqrt{2\pi\sigma_p^2}} \exp(-\frac{s^2}{2\sigma_p^2})
\end{aligned}
\tag{4.31}
$$

and

$$
\begin{aligned}
\langle \ln^2 L(s) \rangle|_{\mu=0} &= \int_{-\infty}^{\infty} \mathrm{d}s \, \ln^2 L(s|\mu=0,\sigma_p) \cdot P(s|\mu=0,\sigma_p) \\
&= \int_{-\infty}^{\infty} \mathrm{d}s \left(\ln(2\pi) + \ln \sigma_p^2 + \frac{s^2}{\sigma_p^2} \right)^2 \frac{1}{\sqrt{2\pi\sigma_p^2}} \exp(-\frac{s^2}{2\sigma_p^2})
\end{aligned}
\tag{4.32}
$$

The two equations Equation (4.31) and Equation (4.32) are Gaussian integrals of the type:

$$
I_i(x) = \int_{-\infty}^{\infty} \mathrm{d}x \, x^{2i} \exp^{ax^2} = \sqrt{\frac{\pi}{a}} \frac{(2i-1)!!}{(2a)^i}
\tag{4.33}
$$

Solving Equation (4.31) and Equation (4.32) using Equation (4.33) yields:

$$
\langle \ln L \rangle|_{\mu=0} = 1 + \ln(2\pi) + \ln \sigma_p^2 \qquad\qquad \langle \ln^2 L \rangle|_{\mu=0} = 1 + \ln(2\pi) + \ln \sigma_p^2 + 2 \tag{4.34}
$$

The mean of the log-likelihood distribution is then simply given by:

$$\sigma^2(\ln L)|_{\mu=0} = \langle \ln^2 L \rangle|_{\mu=0} - \langle \ln L \rangle^2|_{\mu=0} = 2 \tag{4.35}$$

For sufficiently high expected signal values, see Equation (4.26), this results in:

$$\langle \ln L \rangle|_{\mu \gg 0} = 1 + \ln(2\pi) + \ln(\sigma_p^2 + \mu(1 + \sigma_\gamma^2) + \sigma_f^2)) \tag{4.36}$$

$$\langle \ln^2 L \rangle|_{\mu=0} = (1 + \ln(2\pi) + \ln(\sigma_p^2 + \mu(1 + \sigma_\gamma^2) + \sigma_f^2)) + 2 \tag{4.37}$$

$$\sigma^2(\ln L)|_{\mu \gg 0} = \langle \ln^2 L \rangle|_{\mu \gg 0} - (\langle \ln L \rangle|_{\mu \gg 0})^2 = 2 \tag{4.38}$$

Note that Equation (4.34) and Equation (4.35) are obtained from Equation (4.36) if $\mu = 0$. However, in the transition regime from $\mu = 0$ to $\mu \gg 0$ the analytical expression of Equation (4.36) is no longer valid. For details see fig. 15 in [136]. The expected log-likelihood for the example event is shown in Figure 4.12.
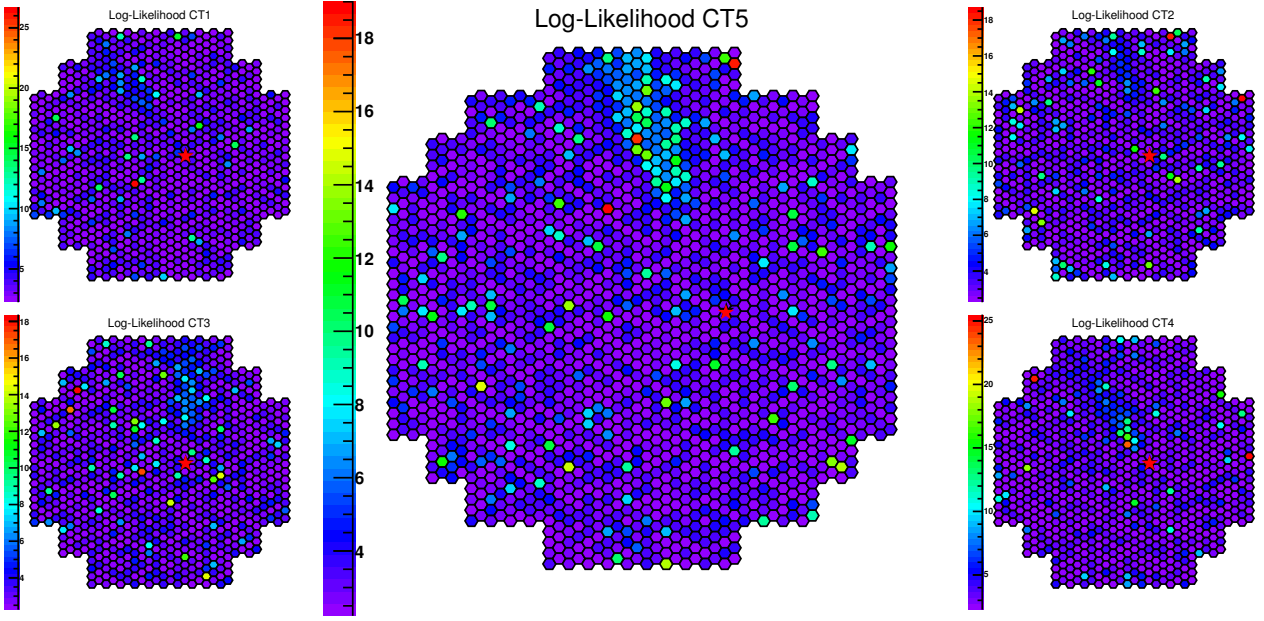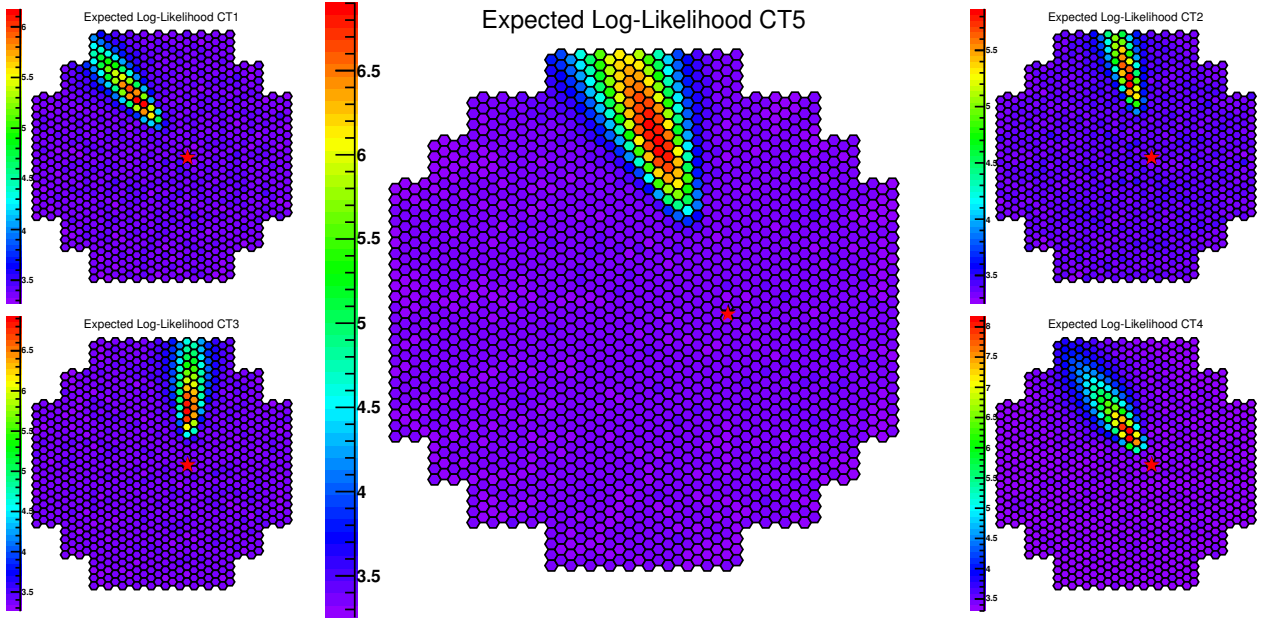

Figure 4.12.: *Pixel wise expected log-likelihood for the example event using the expected signal from Figure 4.9. The source position in the* Nominal System *is indicated by the black star. The red star indicates the fitted source position.*

4.3.3. Expected Log-Likelihood Correction

A dedicated lookup table is used to store the difference between the numerical and the analytical solution of Equation (4.36) and the result is adjusted accordingly. The lookup parameters are the expected signal μ as well as the measured pedestal width in the given gain channel of a PMT that was used to measure the observed signal s. The expected signal s only depends on the *Shower Parameters* and does not need to be calibrated. However, the width of the pedestal peak depends of the electronic noise in the gain channel of the PMT as well as the night sky background rate. A change in the electronic noise does not broaden the pedestal peak, instead its position is shifted. Only a change in the night sky background rate will change the width of the pedestal peak. It is therefore possible to correct

for the influence of different night sky background rates on the expected log-likelihood. As shown by de Naurois and Rolland [136], this eliminates the influence of the night sky background on the model reconstruction.

The lookup table needs to be generated for each of the two gain channels separately. Note that this lookup table does use non-linear bin distances, see Appendix A. For the expected signal dimension 60 log-bins of the expected signal in the range from $10^{-3} < \log \mu < 10^3$ plus one bin for an expected signal of $\mu = 0$ are used. For the pedestal width dimension a slightly different approach is chosen. For a given night sky background frequency a pedestal distribution (in p.e.) is simulated and the obtained width is used for the lookup table. For this 30 log-bins of the nigh sky background frequency ranging from $1\,\mathrm{MHz}$ to $1\,\mathrm{GHz}$ are used. In detail, the PMT is assumed to be a perfect oscillating circuit and therefore the following initial integrated charge value I_{Initial} in p.e. is assumed:

$$I_{\mathrm{Initial}} = N_{\mathrm{Ph}} \cdot Gauss(0, \sigma_p) \tag{4.39}$$

N_{Ph} is the expected amount of night sky background photons obtained from $N_{\mathrm{Ph}} = N_d \cdot f_{\mathrm{NSB}}$ where f_{NSB} is the night sky background frequency and N_d the length of the readout window. Moreover, $Gauss(0, \sigma_p)$ is a value obtained using a random Gaussian distribution with a mean value of 0 and a sigma of σ_p. Here σ_p is the width of the pedestal peak in a PMT in the absence of night sky background light, i.e. just the electronic noise.
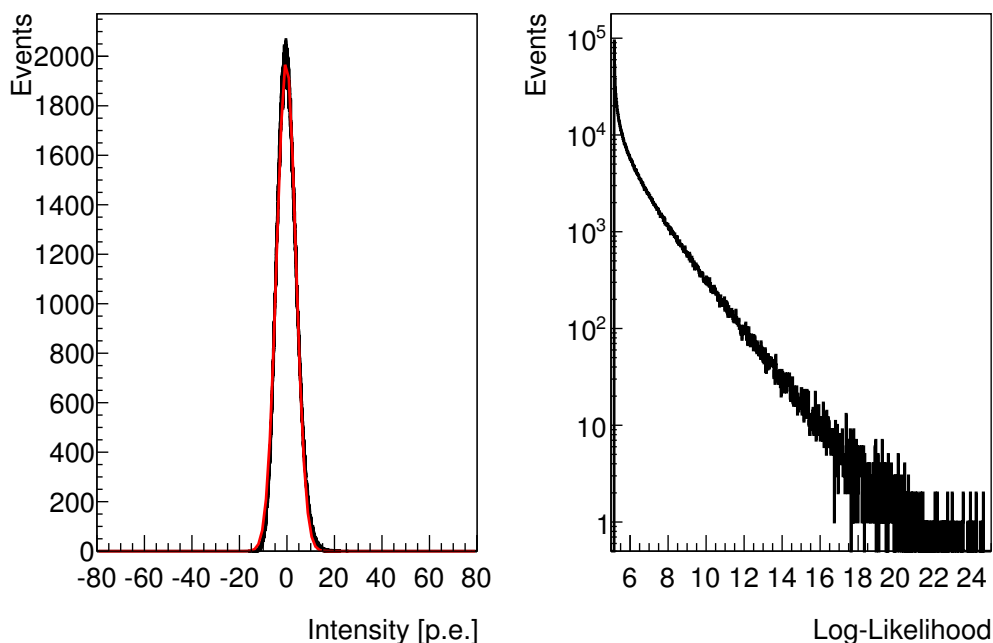
Figure 4.13.: *Simulated pedestal distribution using the H.E.S.S. II detector configuration and a night sky background level of $1\,\mathrm{GHz}$ for 10^6 events on the left. In red the fitted Gaussian with a mean of $-0.286\,\mathrm{p.e.}$ and a width of $4.022\,\mathrm{p.e.}$ On the right the distribution of the difference between the analytical and numerical solution of the expected log-likelihood function for again 10^6 events using the simulated pedestal width and an expected signal of $10\,\mathrm{p.e.}$ The mean of -0.013 of this distribution is used as the expected log-likelihood correction.*

The initial charge is then modified by simulated night sky background photons that can contribute to the measured charge during the integration window. The arrival rate of these photons follow an

exponential decay distribution with a mean live time $\tau = 1/f_{\mathrm{NSB}}$. The contribution of a NSB photon is properly simulated using the photo multiplier response function Equation (3.7) and multiplied with the PMT detection probability, i.e. the PMT efficiency. This procedure is done 10^6 times and the results are filled into a histogram. The resulting pedestal distribution is fitted using a Gaussian function and the width of the Gaussian is used for the lookup table, see Figure 4.13 for a simulated pedestal peak.

The expected log-likelihood correction is then calculated by filling a histogram 10^6 times with the difference of the combination of Equation (4.27) and Equation (4.23) and Equation (4.36), i.e. the difference between the numerical and the analytical solution of the expected log-likelihood function (seen as well in Figure 4.13). The mean of the resulting distribution is then used as the expected log-likelihood correction value for the given expected signal and pedestal width. Figure 4.14 shows the lookup tables for the H.E.S.S. I and H.E.S.S. II telescope types.
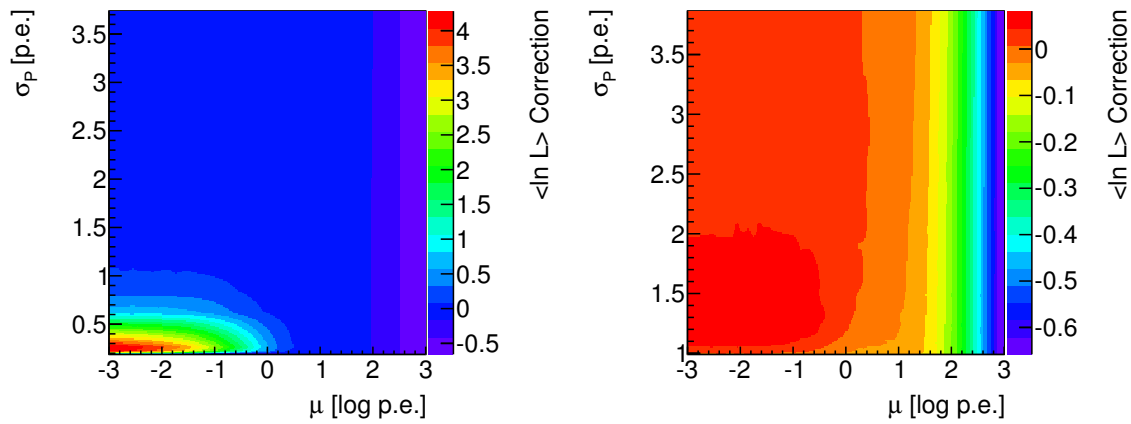
(a) *Left:* High Gain *H.E.S.S. I, Right:* Low Gain *H.E.S.S. I*
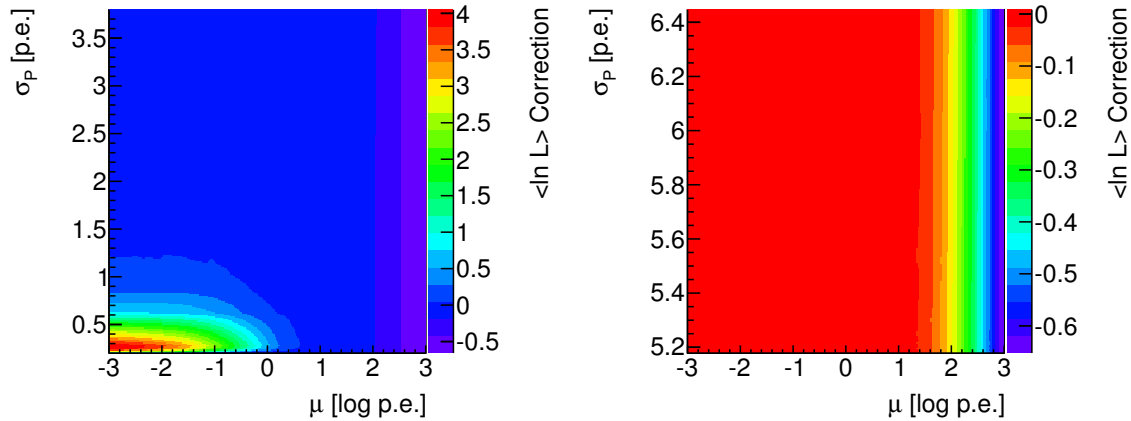
(b) *Left:* High Gain *H.E.S.S. II, Right:* Low Gain *H.E.S.S. II*

Figure 4.14.: *Expected log-likelihood correction for the H.E.S.S. I (upper row) and H.E.S.S. II (lower row) telescope types for both gain channels;* High Gain *on the left and* Low Gain *channel on the right. The lookup is done using the expected signal as well as the width of the pedestal distribution as a measure for the night sky background level. This effectively removes the influence of the night sky background on the log-likelihood. Big corrections are only necessary for low intensity signals with a low night sky background rate (and therefore a small pedestal width).*

4.3.4. The Levenberg-Marquardt Algorithm

For the minimization of the log-likelihood defined by Equation (4.27) the Levenberg-Marquardt algorithm (LMA) is used [193]. It is used for solving non-linear least-squares problems and can be applied for the minimization of the negative likelihood (i.e. finding the maximum likelihood) as shown by Charnes, Frome, and Yu [194]. A nice overview of the LMA can be found in Ranganathan [195] on which this section is based. The LMA is a combination of the Gauss-Newton algorithm (GNA) [196] and the method of gradient descent (GDM) [197] using a dampening factor λ. For a given function $f(x)$ where $x = (x_1, x_2, \ldots, x_n)$ the next step using the GDM is defined as:

$$x_{i+1} = x_i - \lambda \cdot \nabla f(x_i) \tag{4.40}$$

A problem of the GDM is that once near the minimum the convergence slows down significantly. Moreover, the GDM behaves poorly for certain functions, for example functions with flat gradients in one dimension (the classic "error valley" problem).

For the GNA the next step is defined as

$$x_{i+1} = x_i - \left(\nabla^2 f(x_i)\right)^{-1} \nabla f(x_i) = x_i - H^{-1} \nabla f(x_i) \tag{4.41}$$

The GNA is a rapidly converging algorithm which makes use of the information of the second derivative, the Hessian H. It can be approximated by the product of the transposed Jacobi matrix and the Jacobi matrix itself if the second derivative is assumed to behave linearly around the current position x_i.

$$\nabla^2 f(x) = H(x) = \nabla f(x)^T \nabla f(x) = J(x)^T J(x) \tag{4.42}$$

The disadvantage of the GNA is that it is sensitive to the starting position or to be precise to the linearity of the starting position. Two combine the advantages of both methods Levenberg and Marquardt proposed the following combination:

$$x_{i+1} = x_i - (H + \lambda \cdot diag[H])^{-1} \nabla f(x_i) \tag{4.43}$$

The λ factor acts as a dampening parameter that is adjusted after each fit step. It is used to change the weight between the GNA and GDM during the fit ensuring a rapid convergence. For high values of λ the Hessian matrix is not used and the LMA behave like the GDM, for small values of λ the GDM behaves like the GNA. The LMA uses the second derivative information to scale each component according to the curvature of the function. This results in larger steps along the directions where the gradient is smaller and small steps in regions of steep incline in the gradient.

For this work the GSL implementation of the LMA is used [198]. It implements the LMA using a trust-region approach [199] to find the minimum. Trust-region methods differ from the just presented "line-search" methods. A finite region Δ (the trust-region) around the current position is modeled using a quadratic approximation m of the function f. The next fit step is taken into the direction of the minimum of the quadratic model m and the resulting next step is compared to the expectation value of the model m and λ is adjusted accordingly.

The evolution of the log-likelihood during the LMA for the example event is shown in Figure 4.15.

4.3.5. Log-Likelihood Gradient Estimation

To be able to use the LMA the first derivative information of Equation (4.27) needs to be available. From Section 4.1.1 we know that the expected signal μ is a function of six parameters, the *Fit Parameters* (the zenith angle θ is known for a given event and is not a free parameter):

(a) *Log-Likelihood*   (b) *Parameter*   (c) *Gradient*
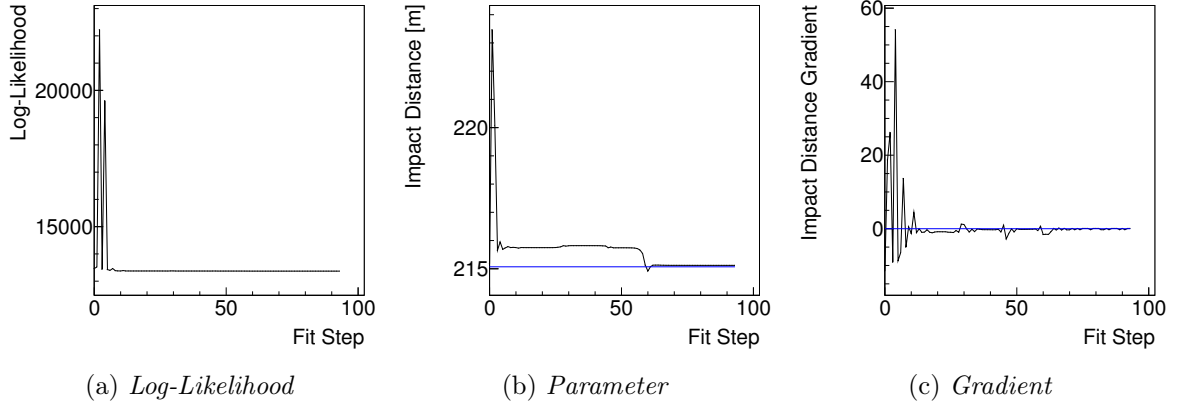
Figure 4.15.: *Evolution of the log-likelihood on the left, the Impact distance in the middle and its gradient on the right during the LMA fit of the example event shown in Figure 4.8. The horizontal blue line indicates the MonteCarlo true value in the middle and a gradient value of zero on the right. The LMA fit nicely minimizes the log-likelihood, the gradient shown approaches zero and the parameter converges to its MonteCarlo true value.*

- The source x position S_x.

- The source y position S_y.

- The primary energy of the gamma-ray ϵ.

- The impact distance of the shower to the telescope R.

- The azimuth angle of the shower ϕ.

- The primary interaction depth of the gamma-ray τ.

Therefore, the log-likelihood function can be written in the following way:

$$\ln L(P) = \ln L(P(s, \mu, \sigma)) = \ln L\Big(P\big(s, \mu(S_x, S_y, \epsilon, R, \phi, \tau), \sigma(\mu)\big)\Big) \tag{4.44}$$

Differentiating the log likelihood with respect to one of the *Fit Parameters K* yields:

$$\frac{\mathrm{d}\ln L}{\mathrm{d}K} = \frac{\partial \ln L}{\partial P}\left(\frac{\partial P}{\partial \mu}\frac{\mathrm{d}\mu}{\mathrm{d}K} + \frac{\partial P}{\partial \sigma}\frac{\partial \sigma}{\partial \sigma_f}\frac{\partial \sigma_f}{\partial \mu}\frac{\mathrm{d}\mu}{\mathrm{d}K} \right) \tag{4.45}$$

Using Equation (4.27), Equation (4.21), Equation (4.22) and Equation (4.23) one obtains:

$$\frac{\partial \ln L}{\partial P} = -\frac{2}{P} \qquad\qquad\qquad \frac{\partial P}{\partial \mu} = \sum_n P_n\left[-1 + \frac{n}{\mu} \right] \tag{4.46}$$

$$\frac{\partial P}{\partial \sigma} = \sum_n P_n\left[-\frac{1}{\sigma} + \frac{(s-n)^2}{2\sigma^3} \right] \qquad \frac{\partial \sigma}{\partial \sigma_f} = \frac{\sigma_f}{\sigma} \qquad \frac{\partial \sigma_f}{\partial \mu} = \delta \tag{4.47}$$

Here P_n is one addend of the sum in Equation (4.23) defined as:

$$P_n = \frac{\mu^n e^{-\mu}}{n!} \cdot \frac{1}{\sqrt{2\pi\sigma^2}} \cdot \exp\left(-\frac{(s-n)^2}{2\sigma^2} \right) \tag{4.48}$$

Inserting Equation (4.46) and Equation (4.47) into Equation (4.45) yields:

$$\frac{\mathrm{d}\ln L}{\mathrm{d}K} = -\frac{2}{P}\sum_{n} P_n\left[-1 + \frac{n}{\mu} - \frac{\delta\sigma_f}{\sigma^2} + \frac{\delta\sigma_f(s-n)^2}{2\sigma^4}\right]\cdot\frac{\mathrm{d}\mu}{\mathrm{d}K} \qquad (4.49)$$

As stated before the expected signal μ can be written as:

$$\mu(S_x, S_y, \epsilon, R, \phi, \tau, X_t, Y_t) = I(\epsilon, \rho, \tau)\cdot A(\epsilon, \rho, \tau, X_t, Y_t) \qquad (4.8)$$

Here the expected signal parameters that are dependent of the *Fit Parameters* are:

- $\rho = \rho(S_x, S_y, R, \phi)$

- $\varphi = \varphi(R, \phi)$

- $X_t = X_t(S_x, S_y, \varphi, \Delta_{\mathrm{CoM}})$

- $\Delta_{\mathrm{CoM}} = \Delta_{\mathrm{CoM}}(\epsilon, \rho, \tau)$

- $Y_t = Y_t(S_x, S_y, \varphi)$

The total derivative of the expected signal μ from one of the *Fit Parameters* K is given by:

$$\frac{\mathrm{d}\mu}{\mathrm{d}K} = \frac{\partial\mu}{\partial I}\frac{\mathrm{d}I}{\mathrm{d}K} + \frac{\partial\mu}{\partial A}\frac{\mathrm{d}A}{\mathrm{d}K} = A\frac{\mathrm{d}I}{\mathrm{d}K} + I\frac{\mathrm{d}A}{\mathrm{d}K} \qquad (4.50)$$

Using Equation (4.50) and solving it for each of the *Fit Parameters* results in:

$$\frac{\mathrm{d}\mu}{\mathrm{d}S_x} = A\frac{\partial I}{\partial\rho}\frac{\mathrm{d}\rho}{\mathrm{d}S_x} + I\left[\frac{\partial A}{\partial\rho}\frac{\mathrm{d}\rho}{\mathrm{d}S_x} + \frac{\partial A}{\partial X_t}\left(\frac{\mathrm{d}X_t}{\mathrm{d}S_x} + \frac{\partial X_t}{\partial\Delta_{\mathrm{CoM}}}\frac{\partial\Delta_{\mathrm{CoM}}}{\partial\rho}\frac{\mathrm{d}\rho}{\mathrm{d}S_x}\right) + \frac{\partial A}{\partial Y_t}\frac{\mathrm{d}Y_t}{\mathrm{d}S_x}\right] \qquad (4.51)$$

$$\frac{\mathrm{d}\mu}{\mathrm{d}S_y} = A\frac{\partial I}{\partial\rho}\frac{\mathrm{d}\rho}{\mathrm{d}S_y} + I\left[\frac{\partial A}{\partial\rho}\frac{\mathrm{d}\rho}{\mathrm{d}S_y} + \frac{\partial A}{\partial X_t}\left(\frac{\mathrm{d}X_t}{\mathrm{d}S_y} + \frac{\partial X_t}{\partial\Delta_{\mathrm{CoM}}}\frac{\partial\Delta_{\mathrm{CoM}}}{\partial\rho}\frac{\mathrm{d}\rho}{\mathrm{d}S_y}\right) + \frac{\partial A}{\partial Y_t}\frac{\mathrm{d}Y_t}{\mathrm{d}S_y}\right] \qquad (4.52)$$

$$\frac{\mathrm{d}\mu}{\mathrm{d}\epsilon} = A\frac{\partial I}{\partial\epsilon} + I\left[\frac{\partial A}{\partial\epsilon} + \frac{\partial A}{\partial X_t}\frac{\partial X_t}{\partial\Delta_{\mathrm{CoM}}}\frac{\partial\Delta_{\mathrm{CoM}}}{\partial\epsilon}\right] \qquad (4.53)$$

$$\frac{\mathrm{d}\mu}{\mathrm{d}R} = A\frac{\partial I}{\partial\rho}\frac{\mathrm{d}\rho}{\mathrm{d}R} + I\left[\frac{\partial A}{\partial\rho}\frac{\mathrm{d}\rho}{\mathrm{d}R} + \frac{\partial A}{\partial X_t}\left(\frac{\partial X_t}{\partial\varphi}\frac{\mathrm{d}\varphi}{\mathrm{d}R} + \frac{\partial X_t}{\partial\Delta_{\mathrm{CoM}}}\frac{\partial\Delta_{\mathrm{CoM}}}{\partial\rho}\frac{\mathrm{d}\rho}{\mathrm{d}R}\right) + \frac{\partial A}{\partial Y_t}\frac{\partial Y_t}{\partial\varphi}\frac{\mathrm{d}\varphi}{\mathrm{d}R}\right] \qquad (4.54)$$

$$\frac{\mathrm{d}\mu}{\mathrm{d}\phi} = A\frac{\partial I}{\partial\rho}\frac{\mathrm{d}\rho}{\mathrm{d}\phi} + I\left[\frac{\partial A}{\partial\rho}\frac{\mathrm{d}\rho}{\mathrm{d}\phi} + \frac{\partial A}{\partial X_t}\left(\frac{\partial X_t}{\partial\varphi}\frac{\mathrm{d}\varphi}{\mathrm{d}\phi} + \frac{\partial X_t}{\partial\Delta_{\mathrm{CoM}}}\frac{\partial\Delta_{\mathrm{CoM}}}{\partial\rho}\frac{\mathrm{d}\rho}{\mathrm{d}\phi}\right) + \frac{\partial A}{\partial Y_t}\frac{\partial Y_t}{\partial\varphi}\frac{\mathrm{d}\varphi}{\mathrm{d}\phi}\right] \qquad (4.55)$$

$$\frac{\mathrm{d}\mu}{\mathrm{d}\tau} = A\frac{\partial I}{\partial\tau} + I\left[\frac{\partial A}{\partial\tau} + \frac{\partial A}{\partial X_t}\frac{\partial X_t}{\partial\Delta_{\mathrm{CoM}}}\frac{\partial\Delta_{\mathrm{CoM}}}{\partial\tau}\right] \qquad (4.56)$$

An exemplary pixel gradient camera image obtained using the *Full Model* for the MonteCarlo example event seen in Figure 4.8 is shown in Figure 4.16.

The partial derivatives for a given parameter χ for $\frac{\partial I}{\partial\chi}$, $\frac{\partial A}{\partial\chi}$ and $\frac{\partial\Delta_{\mathrm{CoM}}}{\partial\chi}$ are obtained using the two 3 dimensional and one 5 dimensional lookup tables of the *Full Model*.

For the parameter ρ the total derivatives using Equation (4.11) and the following abbreviation $\vec{V} = \vec{C} - \vec{T}$ are given by:
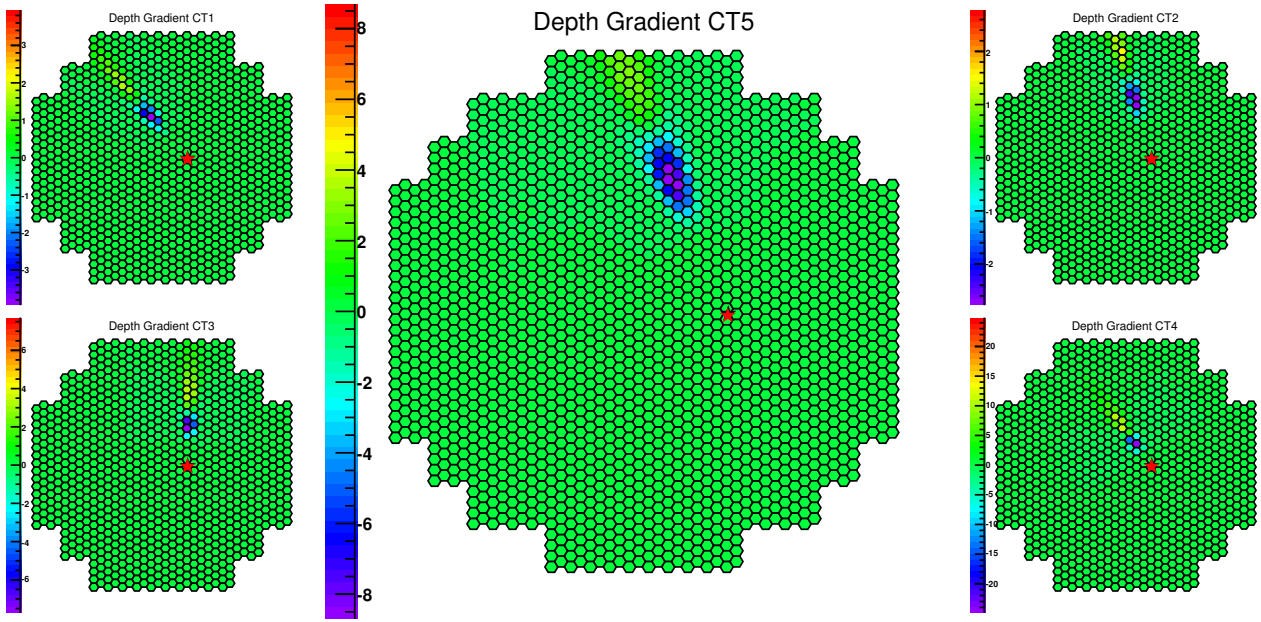
Figure 4.16.: *Primary depth gradient of the example event in Figure 4.8. The source position in the* Nominal System *is indicated by the black star. The red star indicates the fitted source position. The sum off all pixel gradients of all camera pictures is almost zero.*

$$\frac{\mathrm{d}\rho}{\mathrm{d}S_x} = \frac{\partial\rho}{\partial(\vec{V}\cdot\vec{S})}\frac{\mathrm{d}(\vec{V}\cdot\vec{S})}{\mathrm{d}S_x} + \frac{\partial\rho}{\partial|\vec{S}|^2}\frac{\mathrm{d}|\vec{S}|^2}{\mathrm{d}S_x} \qquad \frac{\mathrm{d}\rho}{\mathrm{d}S_y} = \frac{\partial\rho}{\partial(\vec{V}\cdot\vec{S})}\frac{\mathrm{d}(\vec{V}\cdot\vec{S})}{\mathrm{d}S_y} + \frac{\partial\rho}{\partial|\vec{S}|^2}\frac{\mathrm{d}|\vec{S}|^2}{\mathrm{d}S_y} \tag{4.57}$$

$$\frac{\mathrm{d}\rho}{\mathrm{d}R} = \frac{\partial\rho}{\partial|\vec{V}|^2}\frac{\mathrm{d}|\vec{V}|^2}{\mathrm{d}R} + \frac{\partial\rho}{\partial(\vec{V}\cdot\vec{S})}\frac{\mathrm{d}(\vec{V}\cdot\vec{S})}{\mathrm{d}R} \qquad \frac{\mathrm{d}\rho}{\mathrm{d}\theta} = \frac{\partial\rho}{\partial|\vec{V}|^2}\frac{\mathrm{d}|\vec{V}|^2}{\mathrm{d}\theta} + \frac{\partial\rho}{\partial(\vec{V}\cdot\vec{S})}\frac{\mathrm{d}(\vec{V}\cdot\vec{S})}{\mathrm{d}\theta} \tag{4.58}$$

Inserting the missing total derivatives:

$$\frac{\mathrm{d}|\vec{S}|^2}{\mathrm{d}S_x} = 2S_x \qquad\qquad \frac{\mathrm{d}|\vec{S}|^2}{\mathrm{d}S_y} = 2S_y \tag{4.59}$$

$$\frac{\mathrm{d}|\vec{V}|^2}{\mathrm{d}R} = 2(V_x\cos\theta + V_y\sin\theta) \qquad\qquad \frac{\mathrm{d}|\vec{V}|^2}{\mathrm{d}\theta} = 2(C_x V_y - C_y V_x) \tag{4.60}$$

$$\frac{\mathrm{d}(\vec{V}\cdot\vec{S})}{\mathrm{d}S_x} = V_x \qquad\qquad \frac{\mathrm{d}(\vec{V}\cdot\vec{S})}{\mathrm{d}S_y} = V_y \tag{4.61}$$

$$\frac{\mathrm{d}(\vec{V}\cdot\vec{S})}{\mathrm{d}R} = S_x\cos\theta + S_y\sin\theta \qquad\qquad \frac{\mathrm{d}(\vec{V}\cdot\vec{S})}{\mathrm{d}\theta} = C_x S_y - C_y S_x \tag{4.62}$$

into Equation (4.57) results in:

$$\frac{\mathrm{d}\rho}{\mathrm{d}S_x} = -\frac{V_x}{\rho}\frac{\vec{V}\cdot\vec{S}}{|\vec{S}|^2} + \frac{S_x}{\rho}\Big(\frac{\vec{V}\cdot\vec{S}}{|\vec{S}|^2}\Big)^2 \tag{4.63}$$

$$\frac{\mathrm{d}\rho}{\mathrm{d}S_y} = -\frac{V_y}{\rho}\frac{\vec{V}\cdot\vec{S}}{|\vec{S}|^2} + \frac{S_y}{\rho}\Big(\frac{\vec{V}\cdot\vec{S}}{|\vec{S}|^2}\Big)^2 \tag{4.64}$$

$$\frac{\mathrm{d}\rho}{\mathrm{d}R} = \frac{1}{\rho}\Big[V_x\cos\theta + V_y\sin\theta - \frac{\vec{V}\cdot\vec{S}}{|\vec{S}|^2}(S_x\cos\theta + S_y\sin\theta)\Big] \tag{4.65}$$

$$\frac{\mathrm{d}\rho}{\mathrm{d}\theta} = \frac{1}{\rho}\Big[C_x V_y + C_y V_x - \frac{\vec{V}\cdot\vec{S}}{|\vec{S}|^2}(C_x S_y + C_y S_x)\Big] \tag{4.66}$$

Similar calculations for ϕ using Equation (4.13) yield the following equations:

$$\frac{\mathrm{d}\phi}{\mathrm{d}S_x} = 0 \qquad\qquad \frac{\mathrm{d}\phi}{\mathrm{d}R} = \frac{V_x\sin\theta - V_y\cos\theta}{V_x^2 + V_y^2} \tag{4.67}$$

$$\frac{\mathrm{d}\phi}{\mathrm{d}S_y} = 0 \qquad\qquad \frac{\mathrm{d}\phi}{\mathrm{d}\theta} = \frac{C_x V_x - C_y V_y}{V_x^2 + V_y^2} \tag{4.68}$$

Lastly the coordinate transformation of the camera system coordinates X_c and Y_c to X_t and Y_t using Equation (4.18) and Equation (4.19) are given by:

$$\frac{\mathrm{d}X_t}{\mathrm{d}S_x} = -\cos\phi \qquad \frac{\mathrm{d}X_t}{\mathrm{d}S_y} = -\sin\phi \qquad \frac{\mathrm{d}X_t}{\mathrm{d}\phi} = Y_t \qquad \frac{\mathrm{d}X_t}{\mathrm{d}\Delta_{\mathrm{CoM}}} = -1 \tag{4.69}$$

$$\frac{\mathrm{d}Y_t}{\mathrm{d}S_x} = \sin\phi \qquad \frac{\mathrm{d}Y_t}{\mathrm{d}S_y} = -\cos\phi \qquad \frac{\mathrm{d}Y_t}{\mathrm{d}\phi} = -X_t - \Delta_{\mathrm{CoM}} \tag{4.70}$$

4.3.6. Fitting Procedure

Like every fitting procedure the model reconstruction needs sensible starting parameters. To obtain these several dedicated Hillas reconstructions are done using different tail cuts, size cuts and nominal distance cuts, see Table 4.1. For each Hillas reconstruction not only the tail-cutted image is used but also the image containing only the biggest cluster. This is needed for low tail-cut pairs to prevent multiple clusters due to night sky background fluctuations within the camera image.

A Hillas shower reconstruction is done to get an estimate for the shower core position and the height of the shower maximum. For this work only a stereoscopic Hillas shower reconstruction was available. Therefore, only stereoscopic events were used during the model reconstruction. Note that the entire model reconstruction is set up to work with monoscopic events as well, i.e. the model reconstruction does not care about the number of telescopes. The initial guess for the primary energy is obtained using dedicated lookup tables for each telescope type and set of starting parameters generated from gamma-ray shower MonteCarlo productions. The lookup parameters are:

- The type of starting parameters used, see Table 4.1.

- The cosine of the zenith angle θ.

- The impact distance of the shower core to the respective telescope in the *Tilted System*.

Table 4.1.: *Different Hillas reconstructions are used as starting parameters. The biggest cluster as well as the full tail-cutted image are used.*

Name	Tail Cut [p.e.]		Minimum Size Cut [p.e.]		Nominal Distance Cut [rad]	
	Lower	Upper	H.E.S.S. I	H.E.S.S. II	H.E.S.S. I	H.E.S.S. II
Clean-0510	5	10	60	40	2.0	1.15
Clean-0507	5	7	60	40	2.0	1.15
Clean-0205	2	5	60	40	2.0	1.15
Clean-0103	1	3	30	20	2.0	1.15
Biggest-0510	5	10	60	40	2.0	1.15
Biggest-0507	5	7	60	40	2.0	1.15
Biggest-0205	2	5	60	40	2.0	1.15
Biggest-0103	1	3	30	20	2.0	1.15

- The log of the total image intensity in the camera of the telescope.

For H.E.S.S. Phase I also the azimuth angle is used as a lookup parameter, due to lack of time this was not done during the course of this work. The lookup tables store the mean of the primary energy $< E >$ as well as the spread σ_E for a given set of lookup parameters. The primary energy E of the full shower is estimated using the mean energy $< E_t >$ of each of the t telescopes of the event obtained using the lookup tables for the given telescope type. They are weighted using the respective energy spread σ_{E_t}:

$$E = \frac{\sum_t w_i^2 \cdot E_t}{\sum_t w_t^2} = \frac{\sum_t (1/\sigma_{E_t})^2 \cdot E_t}{\sum_t (1/\sigma_{E_t})^2} \tag{4.71}$$

The squared energy spread is used to increase the weight of the telescopes with a better primary energy estimate. The energy lookup tables for a zenith angle of $18°$ of the *Clean-0510* starting parameters are shown in Figure 4.17.

The primary depth is not estimated using a lookup table. Instead an initial guess is calculated from the natural logarithm of the primary energy in units of the critical energy ϵ and the maximum shower depth T_{Max} in units of radiation length obtained from the Hillas analysis, see Equation (3.1):

$$X_0 = \epsilon - T_{Max} \tag{4.72}$$

Note that a pref-fit with a fixed primary depth to one radiation length (and therefore one less free parameter) did not improve the reconstruction and therefore is not used in this work.

Since the fitting process is very computing intensive, only the best starting parameters are used. They are obtained by using the initial minimum log-likelihood value of all starting parameters, i.e. the initially best fitting image. Because the log-likelihoods are not normalized by the amount of telescopes that are part of a given set of starting parameters, the telescope intersection of all starting parameters is calculated. Only the camera images of those telescopes that are part of the intersection are used during the fit. The LMA is then started using these best fitting images including all available camera pixels. Only pixels which are flagged as broken are not used during the fit. This is different to the fitting procedure used in [136] where at first only pixels contained within the Hills ellipsis plus adjacent ones are fitted. Including also non-shower pixel, i.e pixel without Cherenkov light contribution are fitted, results in a better gamma-hadron separation due to the more inhomogeneous nature of hadronic air
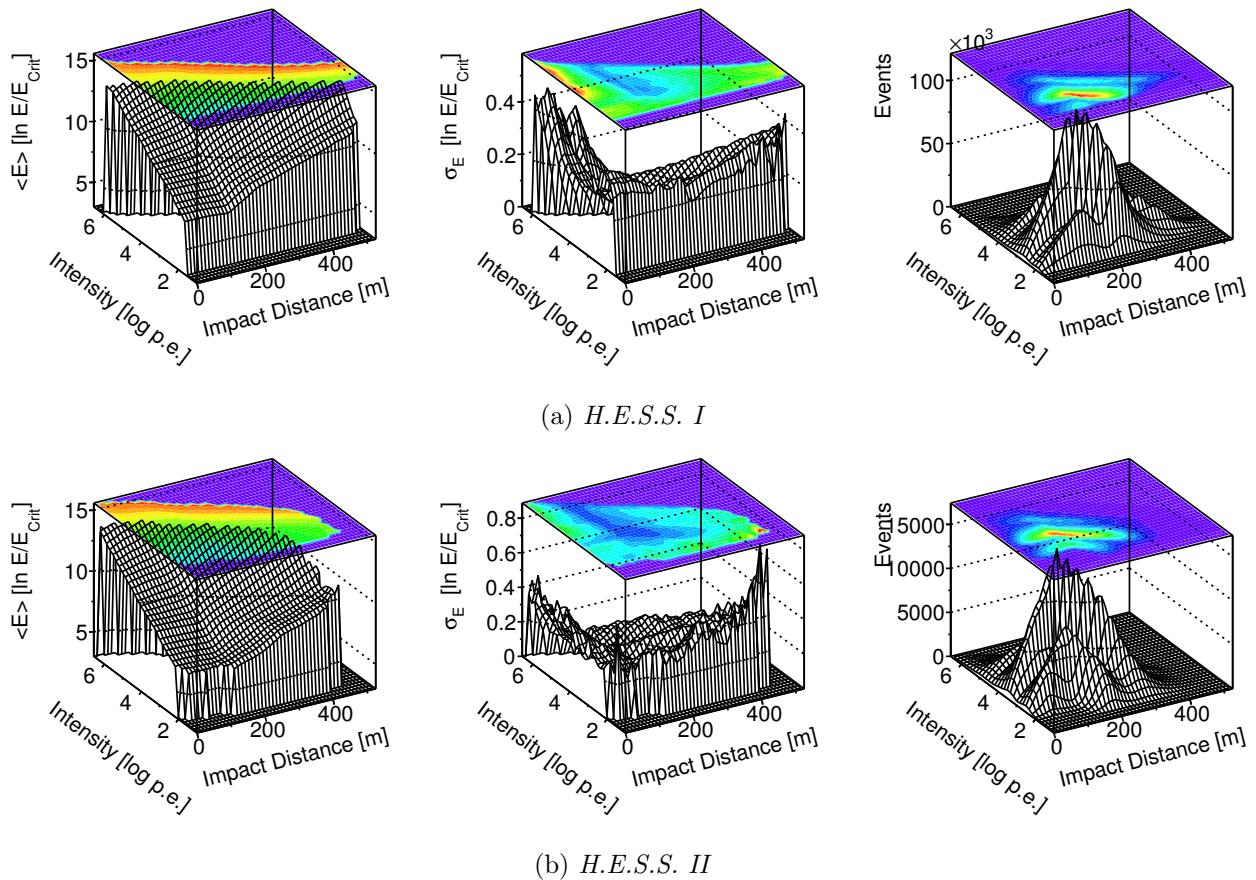
(a) *H.E.S.S. I*

(b) *H.E.S.S. II*

Figure 4.17.: *Energy lookup tables generated using gamma-ray MonteCarlo simulations for a zenith angle of 18 °. The lookup is done using the current zenith angle, the impact distance of the shower core to the respective telescope in the* Tilted System *as well as the log of the total image intensity in the camera. Lookups are created for all available starting parameters, the one shown here is for Clean-0510. The sharp cut off at high intensities is due to the maximum primary energy of 105 TeV used during the MonteCarlo simulations. At low primary energies as well as at small impact distance the spread of the energy lookup tables increases due to degeneration of the shower images.*

showers which might be cut away during a tail-cut. Should the fit not converge for any reason, the event is still used for analysis, as long as a log-likelihood could be calculated. Note that contrary to the implementation of the model reconstruction for H.E.S.S. Phase I, the fit is immediately started using all available camera pixels. Doing a two step fit by fitting pixels belonging to the shower (i.e. pixels with high intensities and their neighbors) first and a full camera fit with the result of the first fit as a starting parameter next, did not improve the final result.

The resulting best fitted image using the LMA for the example event shown in Figure 4.8 can be seen in Figure 4.9 as well as the corresponding gradient in the primary depth dimension in Figure 4.16. The pixel-wise log-likelihood and expected log-likelihood for the best fitting image are shown in Figure 4.11 and Figure 4.12. The resulting fitted *Shower Parameters* including the fit errors are:

- Zenith angle of $18°$ (not part of the fitting process)

- Source position at $(-0.00045 \pm 0.000034\,\mathrm{rad}/-0.00867 \pm 0.00027\,\mathrm{rad})$ in the *Nominal System*

- Impact distance of $215.1 \pm 3.5\,\mathrm{m}$

- Azimuth angle of $-21.77 \pm 0.84\,°$

- Primary energy of $1.55547 \pm 0.00018\,\mathrm{TeV}$

- Primary depth of $0.67 \pm 0.81\,\mathrm{X_0}$

To validate that the fit converged at a minimum, the one dimensional log-likelihood distribution for a given *Fit Parameter* around the best fit position is calculated, i.e. the other *Fit Parameters* are fixed at the best fit position while varying the remaining parameters. The resulting distributions are shown in Figure 4.18. This can also be done for the gradient of each of the *Fit Parameters* which is shown in Figure 4.19.

Figure 4.18.: *One dimensional log-likelihood distributions around the best fit position for all* Fit Parameters. *One parameter is varied while the others remain fixed. The vertical red line indicates the best fit position, the vertical green line the MonteCarlo true parameter. The horizontal blue line is the minimum log-likelihood obtained using the* FullModel. *The fit converged to the local minimum for all six* Fit Parameters. *The MonteCarlo true position does not coincide perfectly with the local minimums due to inadequacies in the* Full Model.
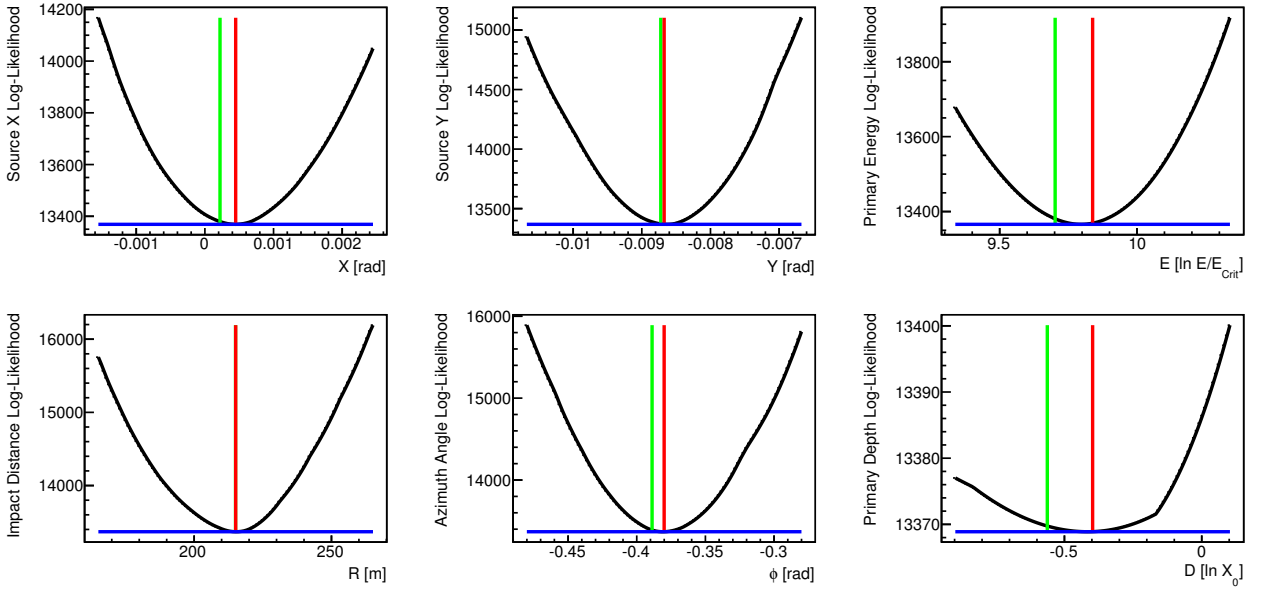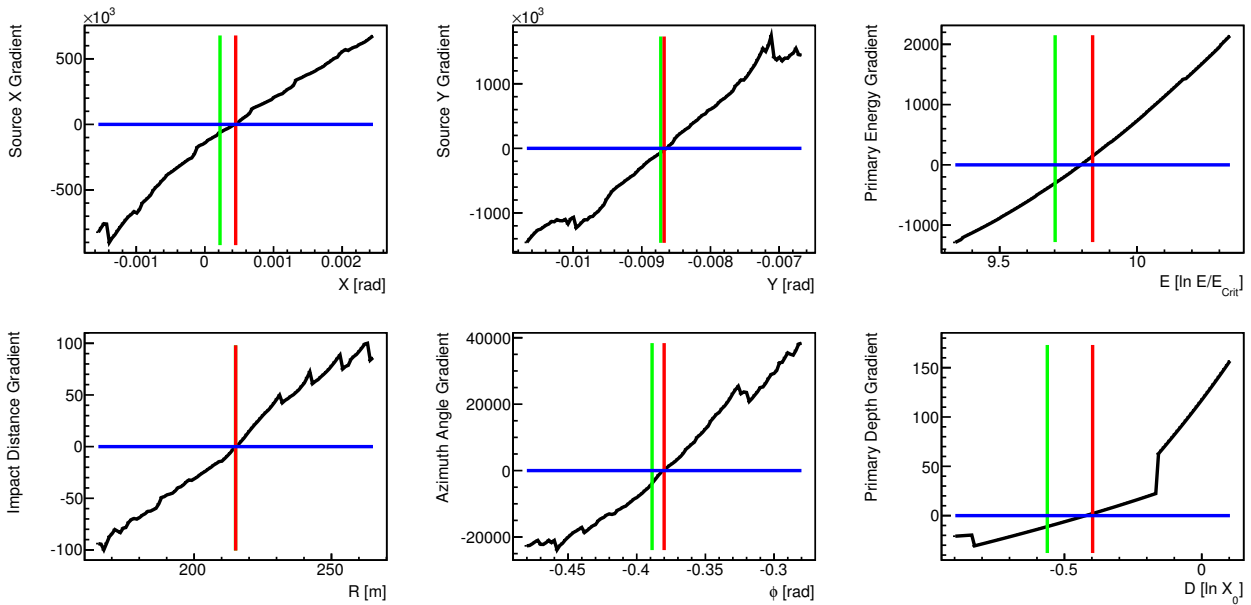
Figure 4.19.: *One dimensional gradient distributions around the best fit position for all* Fit Parameters. *One parameter is varied while the others remain fixed. The vertical red line indicates the best fit position, the vertical green line the MonteCarlo true parameter. The horizontal blue line indicates a gradient value of zero. As expected, the minimal log-likelihood is found at the position where all gradients of the* Fit Parameters *are zero. The jumps at the left and right end of the x axis are due to the gradient getting degenerate if only one* Fit Parameter *is changed and also due to changes of the lookup bins that are used for the interpolation (see Appendix A). The MonteCarlo true position does not coincide perfectly with the best fit position due to inadequacies in the* Full Model.

4.4. Gamma-Hadron Separation

A shower reconstruction algorithm must also be able to discriminate between gamma-ray and hadron induced air showers. For a Hillas reconstruction the *Mean Reduced Scaled Width* and *Mean Reduced Scaled Length* are used as separation parameters as shown in Aharonian et al. [11]. For the model reconstruction a different approach using the goodness of the fitted image is pursued.

4.4.1. Goodness of Fit

In order to separate the gamma-like events from the hadron-like events a parameter for the goodness of the fit has to be defined, i.e. how well does the image match the expectation of a gamma-ray induced air shower. In particle physics so-called *pulls* [200] are often used. Given a set of random variables x which follow a Gaussian distribution of mean μ and width σ the *pull* of a variable x is defined as:

$$g(x) = \frac{x - \mu}{\sigma} \tag{4.73}$$

The distribution of *pulls* is again a Gaussian distribution centered at zero with a width of unity. To obtain μ and σ the value x and x^2 are summed up and the mean value $\langle x \rangle$ and mean squared value $\langle x^2 \rangle$ are calculated by dividing by the amount of filled events n. μ and σ are then given by:

$$\mu = \frac{\sum_i x_i}{n} \qquad\qquad \sigma = \sqrt{\langle x^2 \rangle - \langle x \rangle^2} \tag{4.74}$$
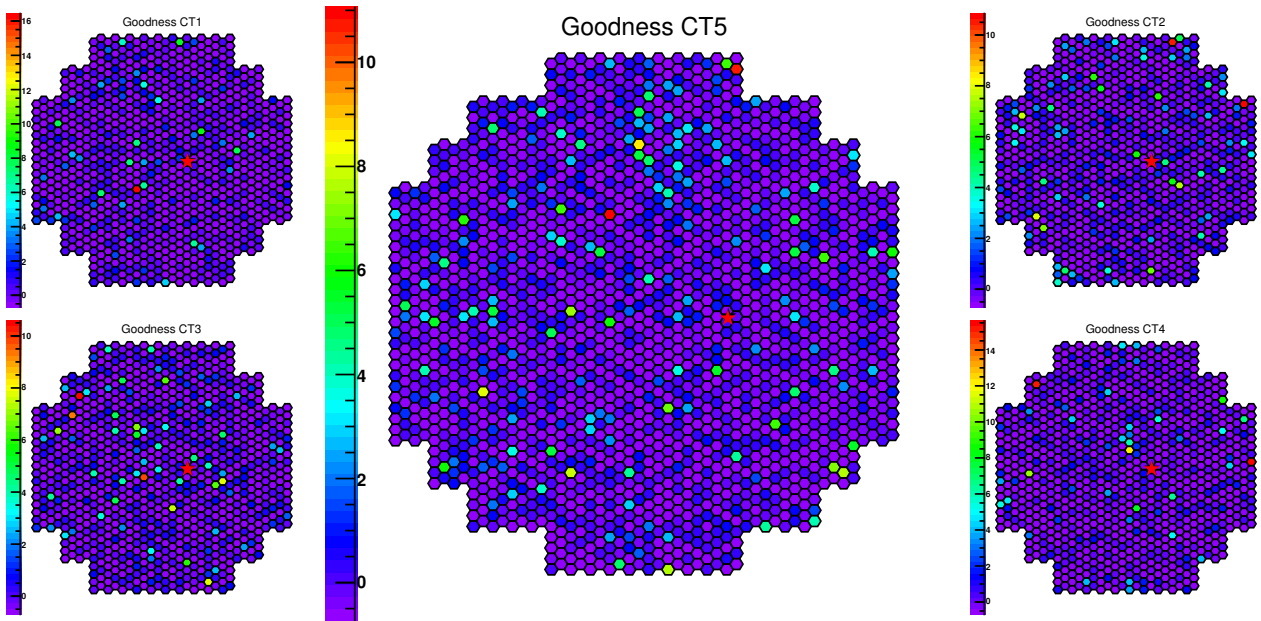
Figure 4.20.: Pixel Goodness *for the example event shown in Figure 4.8 calculated using the log-likelihood from Figure 4.11 and the expected log-likelihood from Figure 4.12 for the expected signal from Figure 4.9.*

Since the measured signal of a pixel is a random variable, the log-likelihood of the measured signal with respect to the expected signal is also a random variable. Therefore, a *Pixel Goodness* G_{Pixel} for a single pixel can be defined as following:

$$G_{Pixel} = \frac{\ln L - \langle \ln L \rangle}{\sigma_{\ln L}} = \frac{\ln L - \langle \ln L \rangle}{\sqrt{2}} \tag{4.75}$$

For the example event shown in Figure 4.8 the final *Pixel Goodness* for each pixel in every camera is shown in Figure 4.20.

This can be extended to the sum of the log-likelihoods of all pixels i used during the fit:

$$G = \sum_i \frac{\ln L(s_i, \mu_i) - \langle \ln L \rangle|_{\mu_i}}{\sqrt{2 \cdot N_{Pixel}}} \tag{4.76}$$

The *Goodness* is a measure to quantify how well the image is described by a gamma-ray shower template, i.e. how gamma-like is the event. Hadron-like air shower are expected to have *Goodness* distributions that are not centered at zero and also have a broader width, see Figure 4.21.
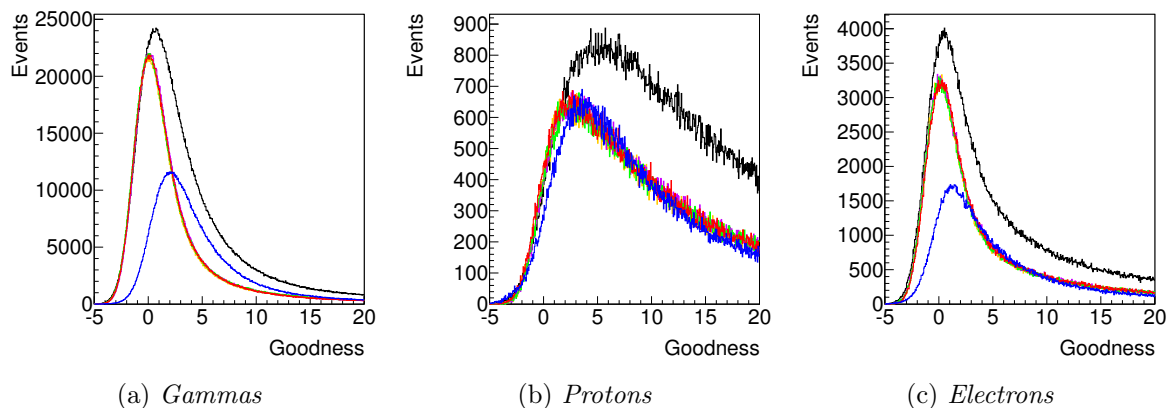

(a) *Gammas* (b) *Protons* (c) *Electrons*

Figure 4.21.: *MonteCarlo* Goodness *distributions for gamma-ray showers on the left, proton induced air showers in the middle and electron ones on the right for each of the five H.E.S.S. telescopes individually (CT1 in orange, CT2 in violet, CT3 in green, CT4 in red and CT5 in blue). The solid black line indicates the mean value weighted by the square root of the number of telescopes used during the fit in the event. The proton distributions are considerably wider than the gamma ones and the electron distribution resembles the latter. The distributions for CT5 are shifted to higher values due to the CT5 camera having more pixel than the others.*

Using MonteCarlo simulations to obtain example distributions for gammas, protons and electrons show that the resulting gamma-ray *Goodness* distributions depend on the zenith angle, on the impact distance and on the total image intensity in the respective camera, as seen in Figure 4.22. For H.E.S.S. Phase I also the azimuth angle is used as a lookup parameter, due to lack of time this was not done during the course of this work.

Therefore, using the unscaled *Goodness* to define cut parameters is not the optimal solution. To obtain stable *Goodness* distributions dedicated lookup tables for each telescope type are created [201] (Note that for H.E.S.S. Phase I lookup tables for each telescope were used). As stated the lookup dimensions are:

- The cosine of the zenith angle θ

- The impact distance of the shower core to the respective telescope in the *Tilted System*

- The log of the total image intensity in the camera of the telescope
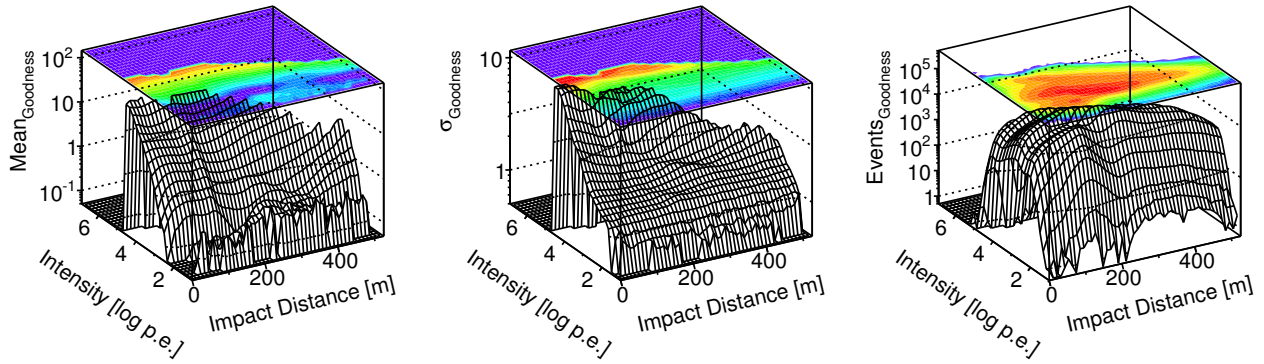
(a) *Left: Mean H.E.S.S. I, Middle: Sigma H.E.S.S. I, Right: Events H.E.S.S. I*
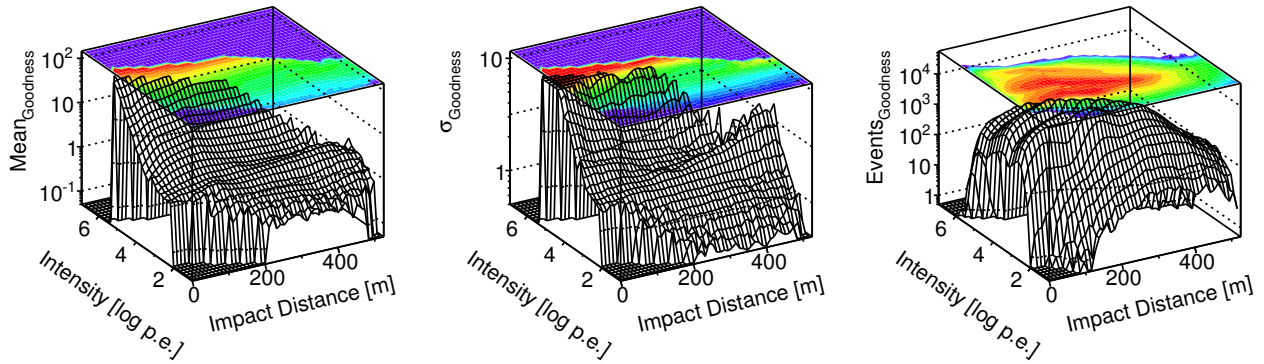
(b) *Left: Mean H.E.S.S. II, Middle: Sigma H.E.S.S. II, Right: Events H.E.S.S. II*

Figure 4.22.: *Mean* Goodness *for the two telescope types on the left versus the impact distance and the total image intensity in the corresponding camera for an exemplary zenith angle of* 18 °*. The corresponding width of the distribution is shown in the middle column. On the right is the number of events shown used to obtain the mean and the width. The total number of events is different because the lookup tables are filled for each telescope type. A clear dependence on the total image intensity is visible.*

To fill the lookup tables the *Goodness G* must satisfy the following relation using the log of the total image intensity in the camera I:

$$|G| < \exp\left[\frac{\ln(200) - \ln(1)}{4} \cdot \log(I) + \left(\ln(1) - \frac{\ln(200) - \ln(1)}{4}\right)\right] \tag{4.77}$$

In essence, the *Goodness* has to be below 1 at a camera intensity of 10 p.e. and below 200 at 100000 p.e. increasing linearly in the log of the intensity. Moreover, the angular distance between MonteCarlo true source position and reconstructed source position must be below 0.2 ° and the absolute of the energy offset (see Equation (4.82)) must be below 0.5 for an event to be filled in the lookup table. Using the mean μ and the width σ obtained from MonteCarlo gamma-ray simulations as a lookup as as seen in Figure 4.23 a *Reduced Scaled Goodness* can be defined for each telescope type using Equation (4.73):

$$RSG = \frac{G - \langle G \rangle}{\sigma_G} \tag{4.78}$$

As stated in [201] using the *Reduced Scaled Goodness* to define cut parameters is not the best option as

well. Therefore, applying the same idea as for the *Mean Reduced Scaled Length* and the *Mean Reduced Scaled Width*(see Section 3.8), a *Mean Reduced Scaled Goodness* is defined:

$$MRSG = \sum_t \frac{RSG_t}{\sqrt{N_{\text{Tel}}}} \tag{4.79}$$

The resulting reduced scaled and mean reduced scaled distributions of the distributions in Figure 4.21 can be seen in Figure 4.23.
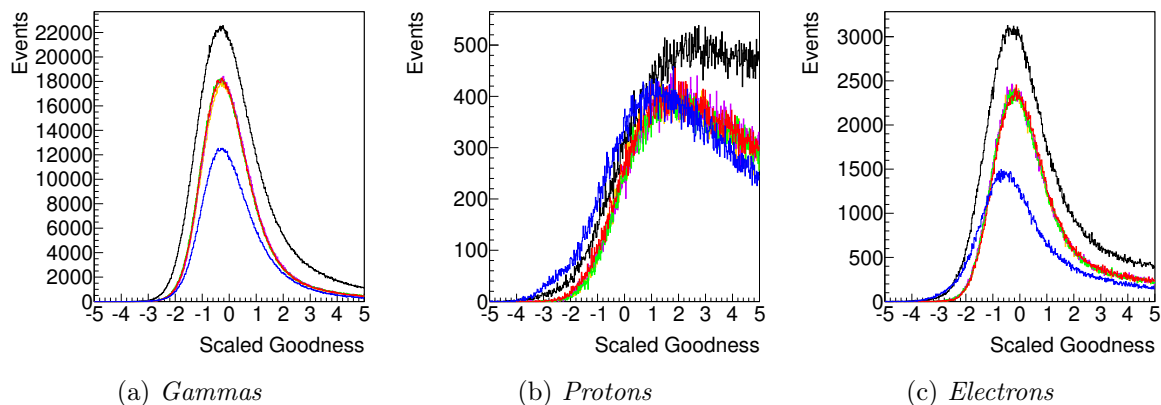

| (a) *Gammas* | (b) *Protons* | (c) *Electrons* |

Figure 4.23.: Reduced Scaled Goodness *distribution for each telescope (CT1 in orange, CT2 in violet, CT3 in green, CT4 in red and CT5 in blue) and* Mean Reduced Scaled Goodness *distribution in black for the distributions shown in Figure 4.21. The gamma-ray distributions are properly centered on zero with a width of unity expect a tail at higher goodness values. The shape of the proton distributions are clearly different.*

To enhance the performance of the reconstruction even further, an energy dependent cut on the error estimates of the log-likelihood fit is done. The absolute of the error estimate for each of the six *Fit Parameters* is filled into an reconstructed energy dependent *Linear Table*, see Appendix A, using 5 bins per decade in a range from $1\,\text{GeV}$ up to $1\,\text{EeV}$ for all the events of a given MonteCarlo gamma-ray shower production. To obtain the cut value on an error estimate for a given energy bin, the 95 percentile of the distribution in that bin is calculated and used as a maximum cut value. The resulting cut values for each energy bin are stored in a one dimensional *Linear Table* (which uses interpolation in between neighboring bins) and used during event separation to cut away badly reconstructed events. An example can be seen in Figure 4.24 for one of the error estimates of the *Fit Parameters*.

4.4.2. Separation Parameters

The *Mean Reduced Scaled Goodness* is primarily used for the gamma-hadron separation in this work. As stated before, the distributions for protons are expected to look different than the ones for gamma-rays. Therefore, a minimum and maximum cut value are defined using gamma-ray and proton MonteCarlo simulations. Note that electron MonteCarlo simulations are not used during the determination of the separation parameters because they also produce electromagnetic air showers like gamma-rays and including them in the determination of the separation parameters is not feasible.

To find the optimal cut values for the *MRSG*, the significance of the gamma-ray "signal" over the proton "background", the so-called *Quality Factor* is maximized:
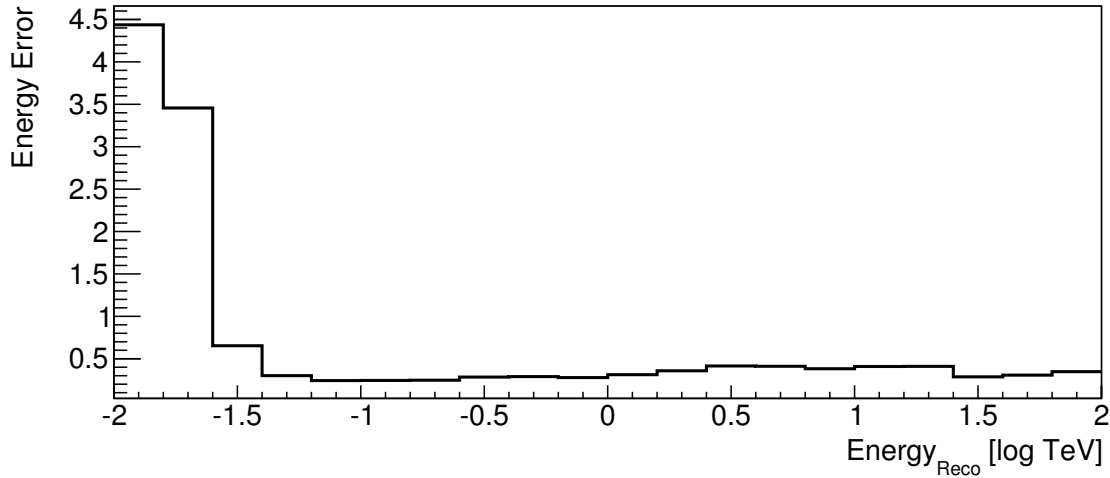
$$Q = \frac{E_\gamma}{\sqrt{E_P}} \tag{4.80}$$

Figure 4.24.: *Reconstructed energy dependent cut value on the error estimate of the primary energy in units of* $\ln \frac{E\,[\text{TeV}]}{E_{Crit}}$. *As expected, low energy events are not reconstructed properly. In the remaining energy range the cut value remains almost constant.*

Here E_γ is the gamma-ray efficiency of the cut while E_P is the proton efficiency. These efficiencies are defined using the number of events before applying the cut and the number of the events after applying the cut:

$$E = \frac{\text{Events}_{\text{After}}}{\text{Events}_{\text{Before}}} \tag{4.81}$$

To obtain the events before and after the cut *Linear Tables* (see Appendix A) are filled for the gamma-ray and proton shower MonteCarlo simulations. The x dimension ranges from -15 to 15 using 150 bins for the *MRSG*. The y dimension is just the number of events with the respective goodness of fit value. The distribution is normalized to the amount of events that were used to fill it; properly taking into account the number of events that were out of range of the x dimension definition. After all events have been filled into the *Linear Tables* the cumulative table is calculated, i.e. the content of bin i in the cumulative table is the sum of all bins from 0 to i of the non-cumulative table. Therefore, the fraction of events that survive a minimum and maximum cut is easily obtained using the cumulative table by subtracting the number of events at the minimum cut value from the number of events at the maximum cut value. Figure 4.25 shows an example of the described procedure.

To check for a dependence of the separation parameters on the reconstructed energy, the cumulative histograms are created in certain energy steps. 5 bins per decade in the log of the reconstructed energy are used in the range from $1\,\text{GeV}$ to $1\,\text{EeV}$. Due to the nature of cumulative distributions, they are always well defined, i.e. also for very few events the distributions look very similar to the ones with a lot of events. As a result separation parameters can be derived in a similar way for high and low statistic samples.

All fits are done using the GSL implementation of the Nelder-Mead Simplex algorithm [198, 202]. Figure 4.26 shows the gamma-ray and proton *Mean Reduced Scaled Goodness* distributions for the different energy bins together with the final cut values in each energy bin. The separation power of the *Mean Reduced Scaled Goodness* is clearly visible.

The resulting efficiencies and *Quality Factors* are shown in Figure 4.27. The cut values are stable over
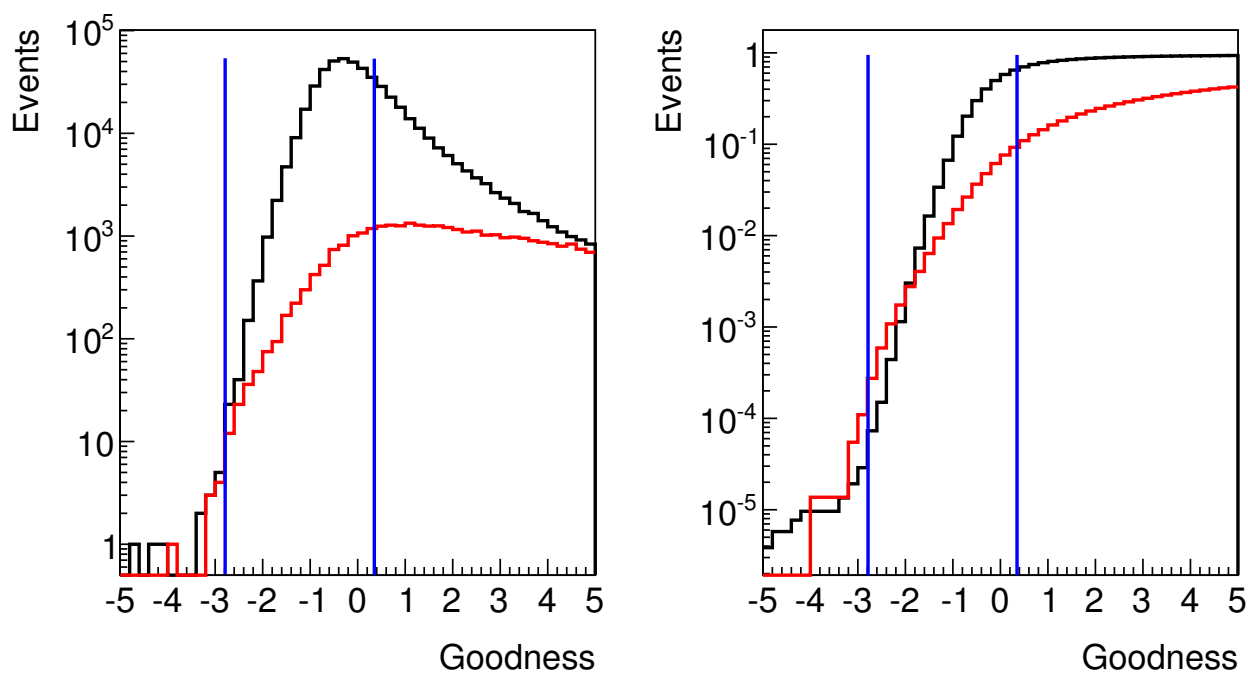
Figure 4.25.: *Exemplary gamma-ray (black) and proton distribution (red) of the* Mean Reduced Scaled Goodness *for the energy bin around* 2.1 TeV *and the corresponding cumulative distribution. The minimum and maximum cut value are indicated by the vertical blue lines. The fraction of events surviving the cut can be easily obtained using the cumulative distributions.*

the whole central energy range, i.e. the mean scaling of the goodness of fit parameters is working as expected. The energy dependence of the cut values is almost negligible (for H.E.S.S. Phase I energy independent cut values were used).
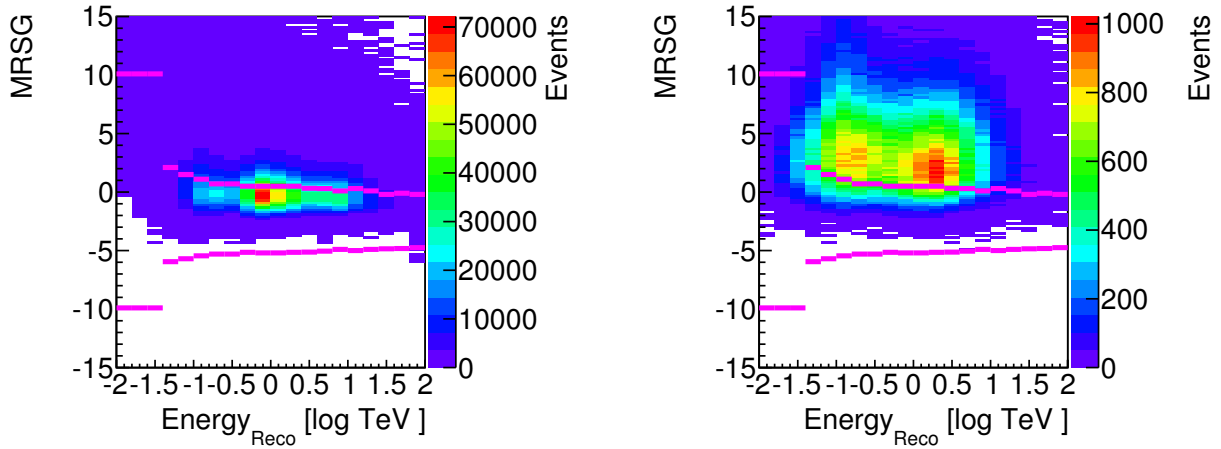
Figure 4.26.: Mean Reduced Scaled Goodness *distribution for gamma-rays on the left and protons on the right for an exemplary zenith angle of* 18 °. *The horizontal magenta lines indicate the minimum and maximum cut values obtained using a Simplex fit. At low energies the* MRSG *can't be used to distinguish between gamma-ray and proton induced air showers any more.*

(a) *Cut Efficiencies*

(b) *Cut Quality*
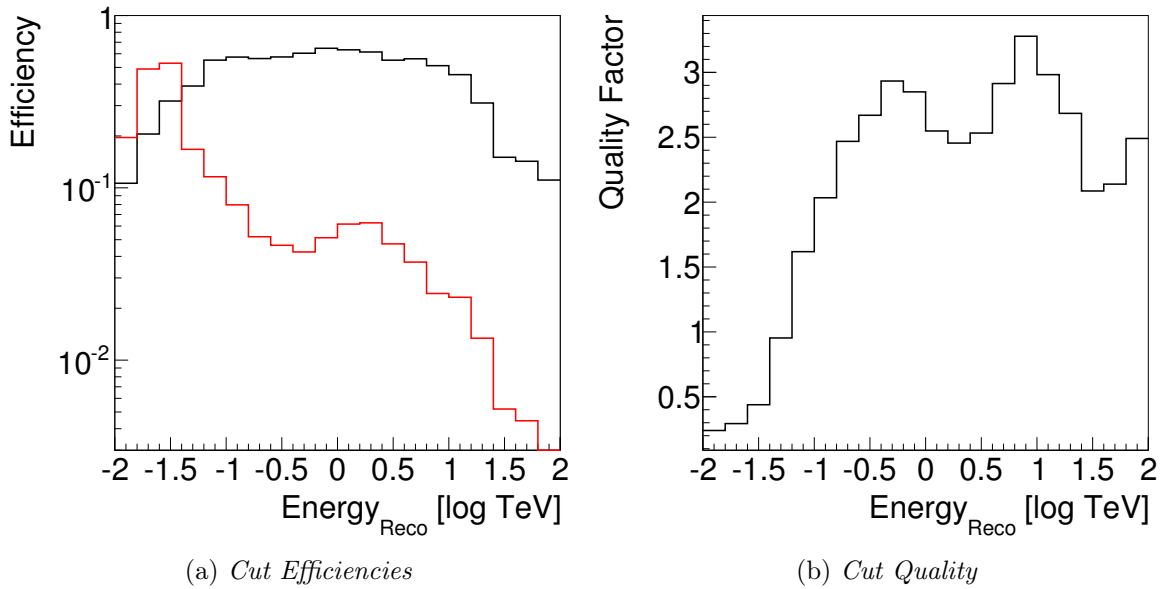
Figure 4.27.: *Cut efficiencies versus reconstructed energy are shown in the left plot(signal in black and background in red) and the* Quality Factor *in the right one. For low energies the separation of gamma-ray and proton induced air showers is nearly impossible. At high energies the separation is easy due to the bright showers and high multiplicity events. The two bumps in the distribution of the cut quality are most likely due to the different start energies of the input spectra as seen in Figure 4.28.*

4.5. Performance

To quantify the performance of a shower reconstruction technique the reconstructed *Shower Parameter* have to be compared with their MonteCarlo true values. Moreover, the detection capabilities of the analysis have to be estimated. For this several dedicated performance curves are calculated which also allow the comparison with other shower reconstruction techniques:

- Energy bias

- Energy resolution

- Angular bias

- Angular resolution

- Effective area

- Differential sensitivity

To obtain these distributions from MonteCarlo simulations an exemplary set of MonteCarlo parameters has to be chosen. The H.E.S.S. collaboration decided to use a zenith angle of 18° and an azimuth angle of 180° with an optical efficiency of the mirrors of the telescope of 80% as the main parameters for the MonteCarlo production. For this work, gamma-ray, electron an proton induced air showers using the *Kaskade* tool were generated using an integral source spectrum with an index of 2.0. To obtain enough showers at high energies several different minimum energies were used:

- 800000 showers with a minimum energy of 5 GeV

- 800000 showers with a minimum energy of 50 GeV

- 800000 showers with a minimum energy of 0.5 TeV

- 127440 showers with a minimum energy of 5 TeV

Figure 4.28 shows the resulting simulated event distributions versus primary energy, impact distance and primary depth. Note that using different minimum energies to increase statistics at higher energies creates systematics in the event reconstruction and gamma-hadron separation which are hard to control. It is advisable to use fixed energy MonteCarlo simulations if higher statistics are needed and not enough disk space and computing time is available to use spectrum MonteCarlo productions.

The maximum energy was set to 105 TeV. Showers were generated within a radius of 550 m around the array. For gamma-rays a point-source was used as the origin of the particles. For electrons and protons a homogeneous distribution with an angular radius of 7° was used. To reduce the necessary amount of simulated air showers a 30% higher quantum efficiency of the PMTs was assumed during the *Kaskade* simulations. During the detector simulation the amount of detected photons was corrected accordingly.

During the course of this work the detector simulation *SMASH* [203] had to be adjusted to properly reflect the new array configuration. This implied:

- Correction of the mirror positions of H.E.S.S. I.

- Implementation of the correct mirror design of H.E.S.S. II.

- Implementation of the correct Central Trigger behaviour, i.e. monoscopic H.E.S.S. II events and hybrid events with at least two telescopes of any kind.

- Implementation of the timing information available for every pixel in H.E.S.S. II, i.e. time of maximum and time over threshold for each gain channel.

- Obtaining all relevant camera electronics and camera calibration parameters.

- Several adjustments of the software to a hybrid array.

Using the H.E.S.S. Phase II detector configuration together with the simulated air showers, a set of MonteCarlo raw data events was generated. The event data format is identical to the one used during the analysis of real data except that the MonteCarlo true *Shower Parameters* are available. A source offset of $0.5\degree$ and $1.0\degree$ was used to simulate different wobble offset observations.

These MonteCarlo raw data events where exported from the H.E.S.S. data format to a custom made format using the BOOST *serialization* library together with the BOOST *iostream* library [190]. The resulting data files are a bzip2 [189] compressed binary format. The reason behind the event export is to allow for an "embarrassingly" parallel data processing of a given file, i.e. each event can be processed independently. Therefore, modern CPU architecture can be used more efficiently because the number of events is always bigger then the available number of hardware threads by several orders of magnitude and multi-threading can be used efficiently. Moreover, the resulting amount of memory which can be used for the *Full Model* scales linearly with the amount of cores because the model can be shared between all threads due to the read-only access during the shower reconstruction.

The performance curves are mainly dependent on the primary energy of the primary particle. Therefore, all plots are binned in the log of the true primary energy using 10 bins per decade in a range from 10 GeV up to 100 TeV. Each performance curve will now be discussed in detail. Note that the relative amount of low multiplicity events (two telescope events) is significantly higher compared to the amount of events seen by H.E.S.S. Phase I due to the heterogeneous array layout which might result in a slightly worse performance of the hybrid analysis.

(a) *Primary Energy Gamma* (b) *Impact Distance Gamma* (c) *Primary Depth Gamma*

(d) *Primary Energy Electron* (e) *Impact Distance Electron* (f) *Primary Depth Electron*

(g) *Primary Energy Proton* (h) *Impact Distance Proton* (i) *Primary Depth Proton*
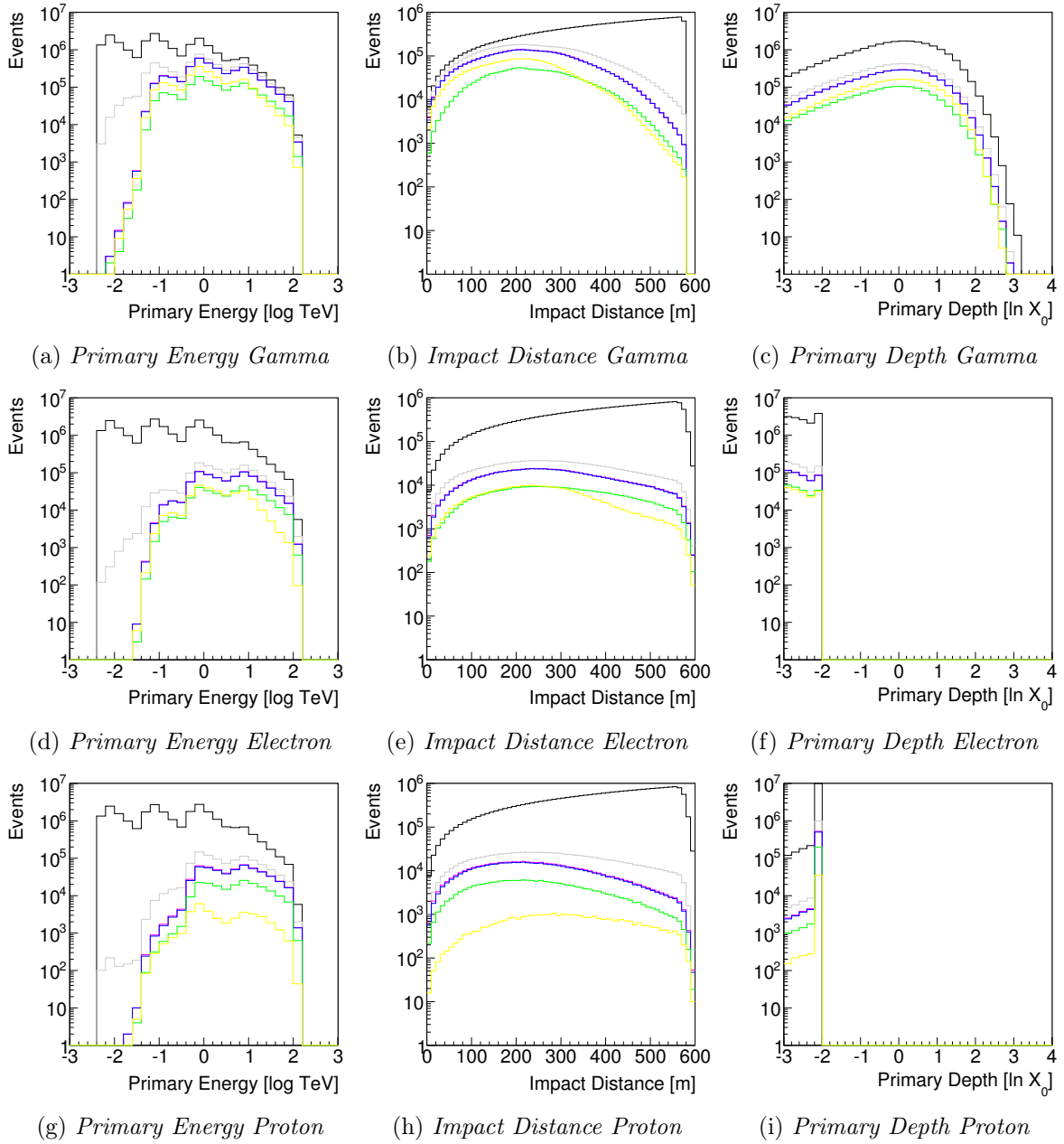
Figure 4.28.: *Distribution of MonteCarlo generated events versus primary energy, impact distance and primary depth for all three types of primary particles used during the simulations. Black lines indicate the amount of generated air showers, grey lines correspond to the showers that triggered the array, blue lines represent the showers that could be successfully reconstructed with a stereoscopic Hillas reconstruction, purple lines indicate air shower that had valid starting parameter for the log-likelihood fit. The green lines show those events for which the fit converged and the yellow lines show all events that survive the cut on the MRSG and the error estimates.*

4.5.1. Energy Bias & Resolution

To obtain the energy bias and the energy resolution, the following energy offset Δ_E is filled into a reconstructed energy dependent *Linear Table*, see Appendix A:

$$\Delta_E = \frac{E_{Reco} - E_{True}}{E_{True}} \tag{4.82}$$

The median of this distribution is called energy bias and the width energy resolution. To properly take into account the tails of the distribution and to be as independent as possible from low statistics, the 50 percentile $P_{\Delta_E}(50)$ is used for determining the median. The resolution is defined as the 68 % containment radius around the median. Therefore, the $P_{\Delta_E}(50 - 68/2) = P_{\Delta_E}(16)$ percentile as well as the $P_{\Delta_E}(84)$ percentile are calculated and the average distance to $P_{\Delta_E}(50)$ is used as the resolution. The procedure is shown in Figure 4.29 for an exemplary energy bin around 1 TeV.
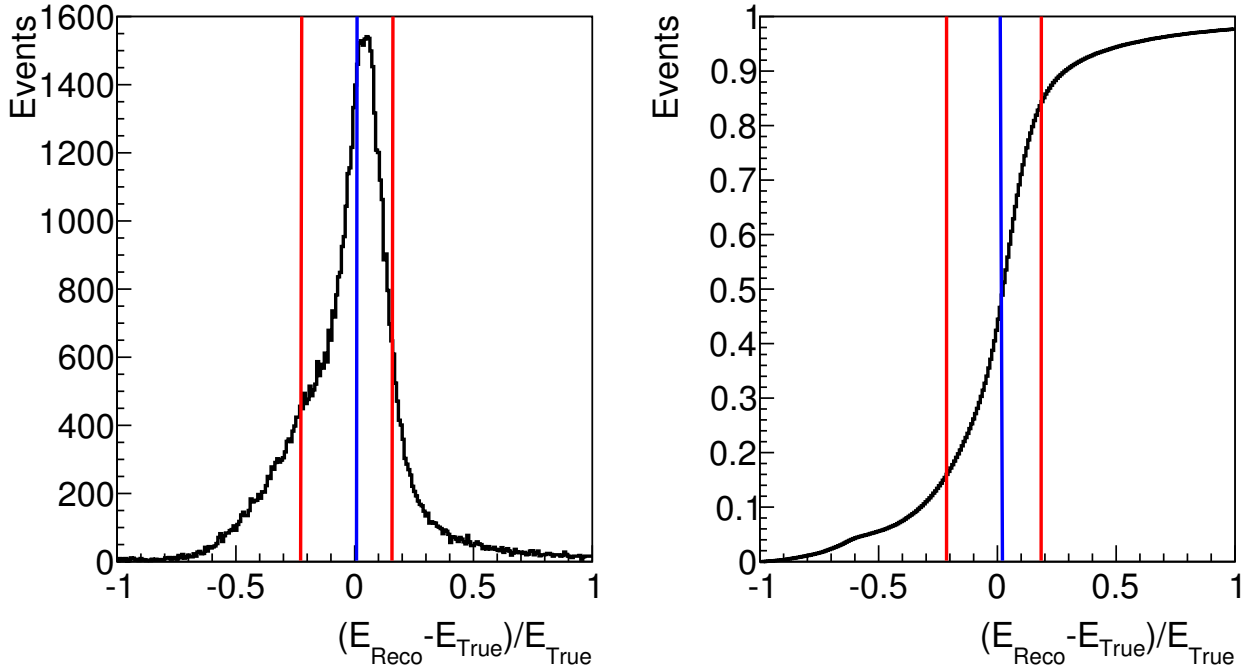
Figure 4.29.: *Distribution of the energy offset Δ_E for an exemplary energy bin on the left and the cumulative distribution on the right. The blue line indicates the median of the distribution which is called energy bias and the two red lines indicate the 68 % containment radius around the median. The average of the two radii is called energy resolution.*

Applying this method to the representative gamma-ray MonteCarlo production yields the curves shown in Figure 4.30a and Figure 4.30b. The energy range used for analyses is defined as the range in which the energy bias is below 10 %. For this work the resulting energy range would be from 100 GeV to 15.8 TeV. The comparison with the MAGIC II array [204] shows a compatible behaviour. The curves shown for the *Model Analysis* of H.E.S.S. Phase I [136] were created using a different definition of the energy resolution and are therefore offset. The bad performance at highest energies might be due to the smaller field of view of the camera of the H.E.S.S. II telescope resulting in more truncated images. The bad energy resolution at lowest energies is most likely dominated by a high number of two telescope events.
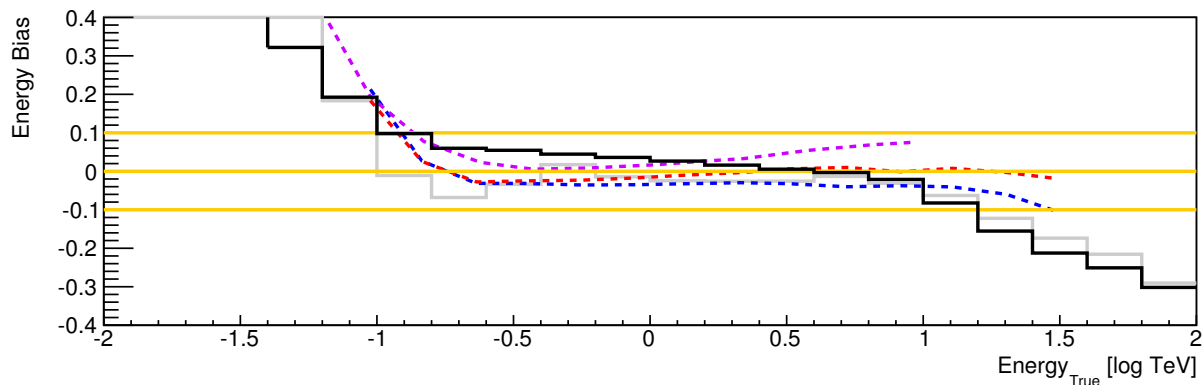
(a) *Energy Bias*
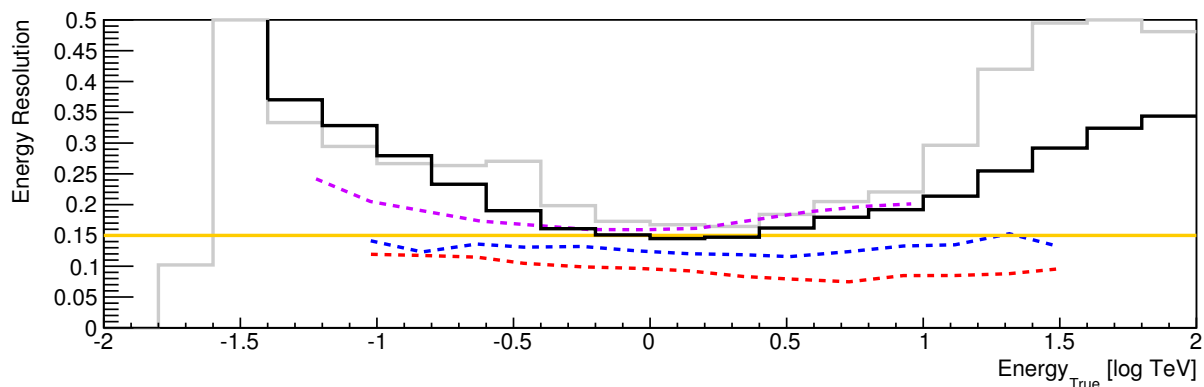
(b) *Energy Resolution*

Figure 4.30.: *Energy bias and energy resolution of the model reconstruction in black. The bias is below 10 %
(solid orange lines, one at −10 %, one at 0 % and one 10 %) in the central energy range and the energy resolution
is around 15 % (solid orange line). At low energies the resulting images are too faint to be properly reconstructed
and dominated by two telescope events. At high energies the images get truncated by the camera edge and the
energy and direction reconstruction is getting difficult. The solid grey line shows the best start parameter of
the fit and its clearly seen that the fit improves the energy bias and energy resolution (except near the edge of
energy range of the analysis). The dashed purple lines show the performance of the MAGIC II array [204]. The
dashed blue line shows a basic Hillas analysis for H.E.S.S. Phase I and the dashed red line corresponds to the
performance of the original Model analysis. The last two curves were taken from [136] and were created using a
different definition of the energy resolution and are therefore offset.*

4.5.2. Angular Bias & Resolution

To quantify the reconstruction capabilities of a point-source the angular bias and angular resolution are used. The angular bias is defined as the maximum of the theta distribution, i.e. the maximum of the distribution of the angular distance of the reconstructed source position to the true source position. It is assumed that the distribution is radial symmetric around the source position and the maximum of the distribution should therefore be in the first bin. The result is seen in Figure 4.31a. It is obvious that the source is reconstructed at the right position in central energy range.
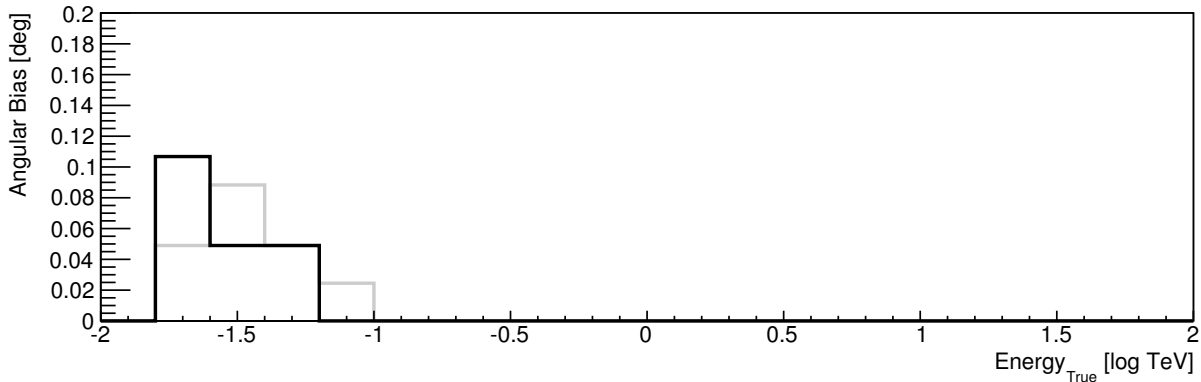
(a) *Angular Bias*
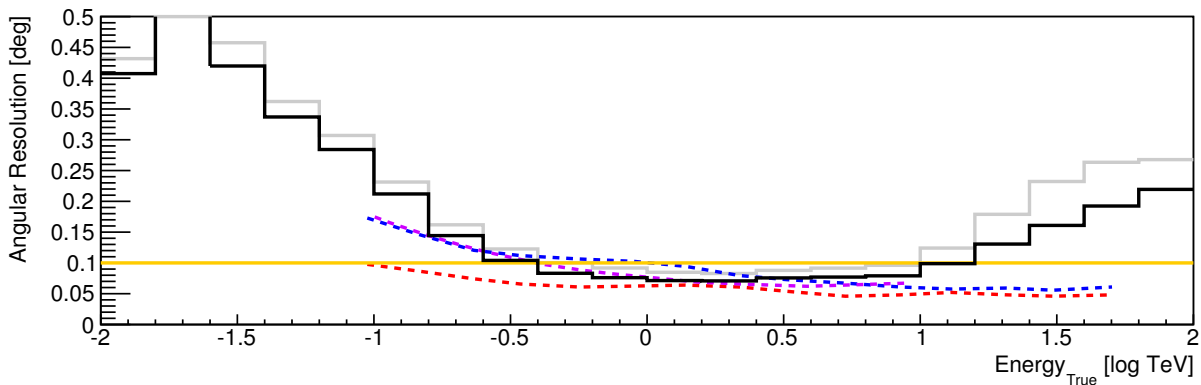
(b) *Angular Resolution*

Figure 4.31.: *Angular bias and angular resolution of the model reconstruction in black (the solid orange line indicates a source extension of 0.1 °). The source is always reconstructed at the center of the theta square distribution (a value of zero indicates that the maximum of the distribution is within the first bin, i.e. the offset is at most 0.0006 °). The angular resolution is getting better with increasing energy due to the shower images getting brighter and higher telescope multiplicities. At the highest energies image truncation at the camera edges start to worsen the angular resolution. The solid grey line shows the best start parameter of the fit and its clearly seen that the fit improves the angular resolution. The dashed purple lines show the performance of the MAGIC II array [204]. The dashed blue line shows a basic Hillas analysis for H.E.S.S. Phase I and the dashed red line corresponds to the performance of the original* Model *analysis. The last two curves are taken from [136].*

The angular resolution is defined as the square root of the 68 % containment radius using the 68 percentile of the θ^2 distribution. It is dependent of the energy and of the zenith angle and can be seen in Figure 4.31b. The performance is compatible to the original *Model Analysis* one as well as to the one of the MAGIC II array. At highest energies the small size of the field of view of the H.E.S.S. II camera starts to affect the performance again.

For the extraction of the signal of a point source, the size of the ON region has to be estimated using the so called θ^2 cut. Assuming the signal S and background B distributions to be defined as:

$$S(\theta^2) \propto \frac{1}{2\sigma^2} \exp\left(-\frac{\theta^2}{2\sigma^2}\right) \qquad\qquad B(\theta^2) \propto k_b \qquad (4.83)$$

the number of background and signal events using a cut value θ_0^2 can be written as:

$$N_S = \int_0^{\theta_0^2} \mathrm{d}\theta^2\, S(\theta^2) \propto 1 - \exp\left(-\frac{\theta_0^2}{2\sigma^2}\right) \qquad\qquad N_B = \int_0^{\theta_0^2} \mathrm{d}\theta^2\, B(\theta^2) \propto \theta_0^2 \qquad (4.84)$$
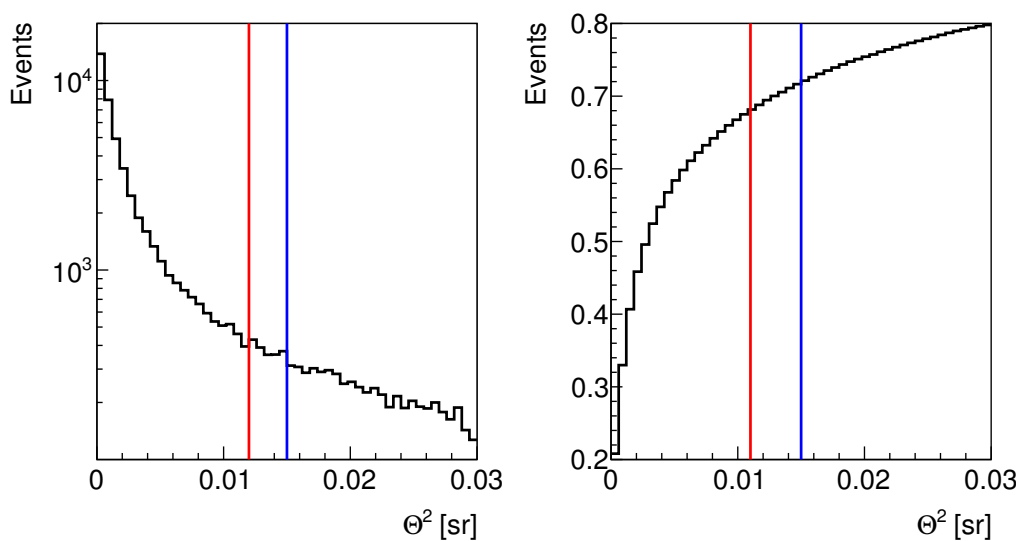
Figure 4.32.: *Theta square distribution for an exemplary energy bin on the left and the cumulative distribution on the right. The red and blue lines indicate the 68 % and 71.533 % containment radius around the source position.*

The significance is then given by:

$$\mathrm{Sign}(\theta_0^2) = \frac{N_S}{\sqrt{2N_B}} \qquad (4.85)$$

To find the maximum of this equation, the derivative has to be equal to zero and the resulting equation and its solution are:

$$1 + \frac{\theta_0^2}{\sigma^2} = \exp\left(-\frac{\theta_0^2}{2\sigma^2}\right) \qquad\qquad \theta_0^2 = -2\sigma^2 W_{-1}\left(\frac{1}{2\sqrt{e}}\right) - \sigma^2 \qquad (4.86)$$

Here $W_{k(x)}$ is the generalized Lambert function and the optimal θ_0^2 value is:

$$\frac{\theta_0^2}{\sigma^2} = 2.51286 \equiv \theta_0^2 \qquad (4.87)$$

Therefore, the 71.533 percentile is used as the energy dependent theta square cut value during the sensitivity calculations, see Section 4.5.4.

4.5.3. Effective Area

A measure for the detector efficiency is the so called effective area. It can easily be calculated by multiplying the ratio of the measured gamma-ray events N_{Det} and the simulated gamma-ray events N_{Sim} with the area around the array which was used as an impact zone during the MonteCarlo shower generation:

$$A_{\text{Eff}}(E_{\text{Rec}}) = \frac{N_{\text{Det}}(E_{\text{Rec}})}{N_{\text{Sim}}(E_{\text{Rec}})} \cdot \pi \cdot r_{\text{Sim}}^2 \tag{4.88}$$
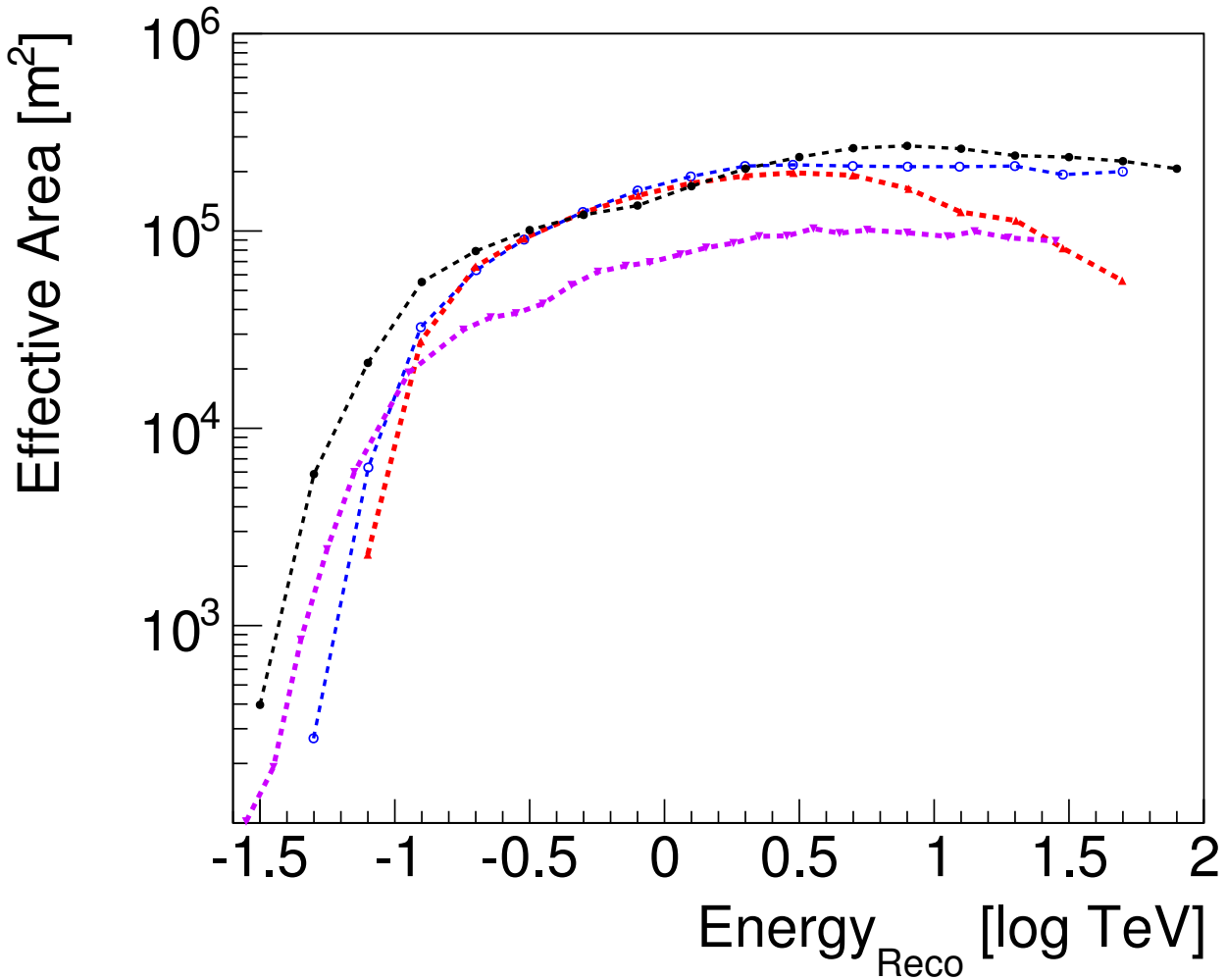
Figure 4.33.: *Effective areas for the different phases of the H.E.S.S. experiment. The read and blue lines correspond to the effective are for H.E.S.S. Phase I, the former for the original* Model Analysis *and the latter for a Hillas analysis (both curves taken from [136]). The black line indicates the effective area for the reconstruction described in this work. The purple line shows the corresponding curve of the MAGIC II array [204].*

It indicates in which energy range the detector is best suited to observe events. The effective area for the model analysis can be seen in Figure 4.33. It was generated using the official toolkit provided by the H.E.S.S. collaboration, see Holler [205]. The obtained curve is in full agreement with the expectations. The adapted *Model Analysis* performs better than the MAGIC II telescope array in the complete energy

range. Compared to H.E.S.S. Phase I similar results in the central energy range are obtained and better results in the low and high energy regime. The dip around 1 TeV is due to the selection cuts on the error estimates of the fit.

4.5.4. Sensitivity

The sensitivity of the detector is defined by its ability to detect a signal above a certain level of background. For an IACT experiment the signals are gamma-rays originating from a source with a specific spectrum. The background consists of protons (and heavier nuclei which are less abundant) and of cosmic electrons and positrons. To quantify the sensitivity of the detector a point-like gamma-ray source with a known spectrum is assumed. In gamma-ray astronomy the Crab Nebula is the standard candle for these kind of comparisons, see Chapter 2. To calculate the sensitivity using (Eq.) 17 of Li and Ma [185] the number of gamma-ray events N_S and the number of background events N_B have to be calculated from MonteCarlo simulations. The size of the point source is defined by an energy dependent θ^2 cut as described in Section 4.5.3. Assuming an observation time of 50 h the theoretical expected amount of photons for a given energy bin, i.e. an energy range, can be calculated using the spectrum published in [11].

Moreover, the theoretical expected amount of protons and electrons can also be obtained using their known spectra [206, 207]. The obtained distributions of number of particles versus energy need to be folded with the energy response function of the reconstruction being used. In addition, for each energy bin the amount of particles has to be multiplied with the detection efficiency of the given particle type in the respective energy bin using the effective area and the assumed detector volume (the area of the circle defined by the maximum impact distance used during the simulations), see Section 4.5.3. After applying all these steps the flux level at which a source is detected with $5\,\sigma$ can be calculated for each energy bin.

The resulting curve produced using the sensitivity script from Holler [205] is shown in Figure 4.34. For a detailed description of the calculation of sensitivity curves the reader is asked to consult Holler [18]. The resulting differential sensitivity is below expectations. It is only marginal better than the reference curve for the MAGIC II experiment [204] indicating a problem with the event reconstruction. In the low energy regime the H.E.S.S. Phase II array is dominated by low multiplicity events and the poor reconstruction of those events might explain the reduced sensitivity. Another explanation could be a problem in the calibration of the data because the *Model Analysis* is very sensitive to correct calibration values. The heterogeneous nature of the current detector, i.e. the CT5 telescope is part of almost any event that triggers the array to its very low dead time and huge mirror area, might also negatively effect the sensitivity. Further investigations are necessary but were beyond the scope of this work.

In the next Chapter the adapted *Model Analysis* will be applied to real data and the resulting performance will be compared to the MonteCarlo expectations.
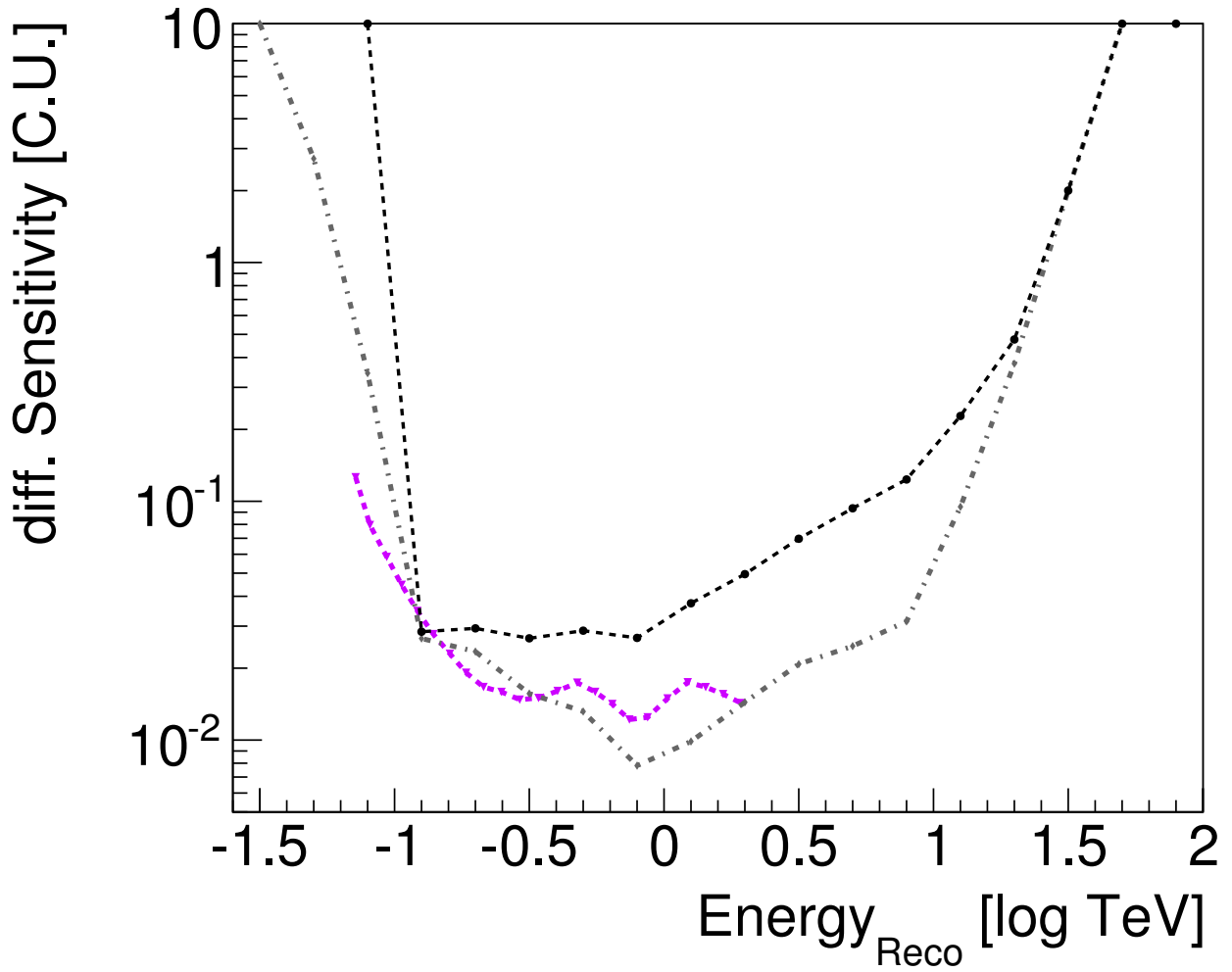
Figure 4.34.: *Differential sensitivity curves in units of the Crab Nebula. The black line indicates the sensitivity for the reconstruction described in this work using the sensitivity calculation from Li and Ma [185]. The grey line uses the same input data as the black line but calculates the sensitivity using the simple formula $N_S/\sqrt{N_B}$ instead. The purple line shows the corresponding curve of the MAGIC II array [204] using the simple formula. The performance of the adapted* Model Analysis *is not as good as expected from the effective area shown in Figure 4.33.*

5

Crab Nebula Observations with H.E.S.S.

In March 2013 the Fermi-LAT detected the second brightest flare of the Crab Nebula up until now [95]. Between 56355 and 56359 MJD the Fermi-LAT switched to a pointed target of opportunity observation mode and during this time period an increase of the flux above 100 MeV of almost a factor of 6 was detected. As during the other HE gamma-ray flares of the Crab Nebula, only the synchrotron component of the Nebula itself varied. The Crab Pulsar and the inverse Compton component of the nebula were found to be constant and on the same level as during the brightest flare in April 2011 [88]. The spectrum of the Crab Pulsar is best described by a power law with a sub-exponential cut-off whereas the inverse Compton spectrum follows a smoothly broken power law in the range of the Fermi-LAT measurements. The spectrum of the synchrotron component is assumed to follow a power law. Mayer et al. [95] showed that the flux of the synchrotron component of the Crab Nebula during the flare in March 2013 was $(4.05 \pm 0.08) \cdot 10^{-6} \, \mathrm{cm}^{-2}\mathrm{s}^{-1}$ with a photon spectral index $\Gamma = 3.09 \pm 0.03$ and extended up to energies of about 700 MeV.

Including the constant components of the Crab, the total flux in this energy band is found to be $(6.21 \pm 0.08) \cdot 10^{-6} \, \mathrm{cm}^{-2}\mathrm{s}^{-1}$. The best-fit position of the maximum emission region during the flare was found to be spatially coincident with the Crab Nebula. The pulsar itself did not show any unusual behaviour [95]. The temporal evolution of the Crab flare as seen by the Fermi-LAT is shown in Figure 5.1 for a fixed time binning of 6 h. The contemporaneous observations of other experiments in different wavelengths are shown as well. However, up until now only the VHE gamma-ray experiments VERITAS [100] and H.E.S.S. [208] have published their results after the Fermi-LAT publication.

The Fermi-LAT results published in Mayer et al. [95] show a flux doubling on a time scale of one Bayesian block bin as well as an overall increased flux level. To search for rapid flux changes, a Bayesian block analysis [209] of the same data set was done and the resulting light curve together with the evolution of the spectral index are shown in Figure 5.2. The shortest time scale for variability found using this approach is 5 h and compatible with previous findings. The peak flux of the Crab Nebula detected using the Bayesian block analysis is $(12.5 \pm 0.8) \cdot 10^{-6} \, \mathrm{cm}^{-2}\mathrm{s}^{-1}$ which is almost six times larger then the average quiescent flux. This corresponds to a factor of ≈ 20 for the synchrotron component alone (assuming constant flux levels for the pulsar and the IC component).

As seen in the bottom panel of Figure 5.2, the spectrum of the synchrotron component hardens with increased flux levels. Mayer et al. [95] showed that the spectral energy distributions (SEDs) shown in
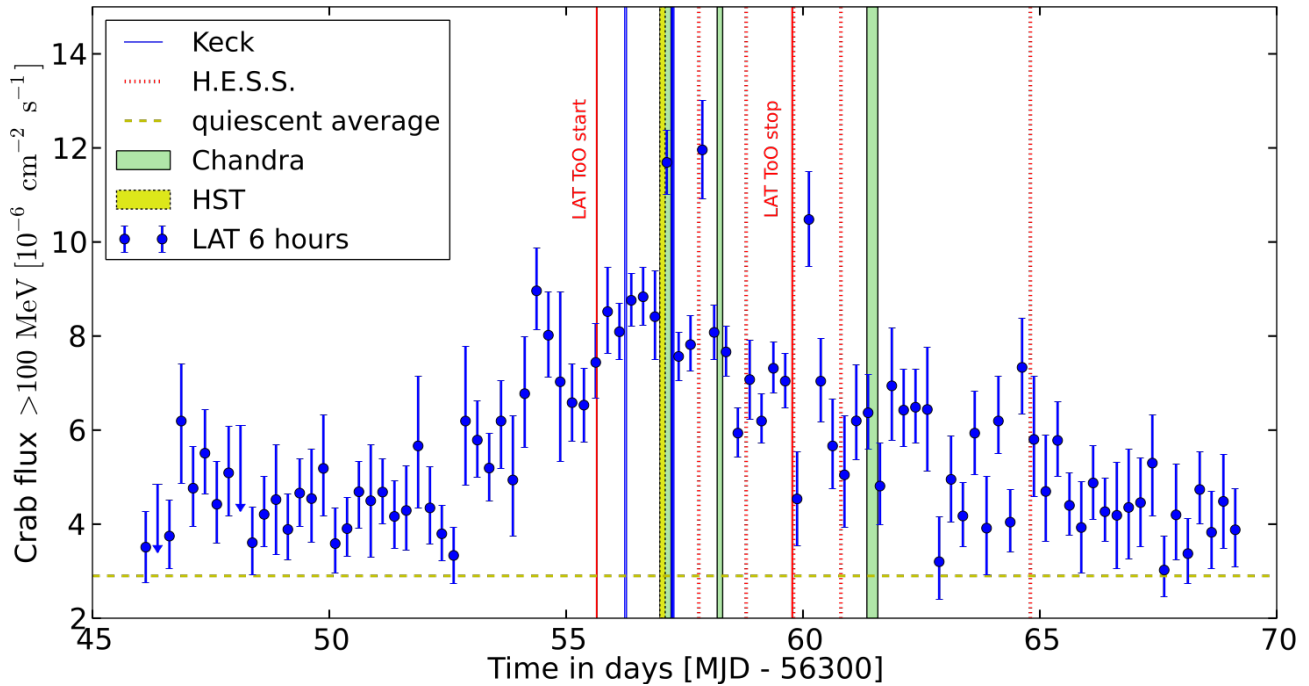
Figure 5.1.: *Total HE gamma-ray flux of the Crab Nebula and Pulsar binned in* 6 h *time intervals in blue. The synchrotron component was fitted while the average flux for the pulsar and the IC component were fixed. The contemporaneous observation windows of experiments in other wavelengths are overlaid in color. Figure taken from [95].*

Figure 5.3 for the 13 different Bayesian blocks are best described by a power law with an exponential cut-off. For the brightest block, the cut-off is found to be at 484^{+409}_{-166} MeV compatible with the cut-off reported in Buehler et al. [88] of 375 ± 26 MeV.

The contemporaneous observations of the Crab Nebula by the H.E.S.S. Phase I array were published in H.E.S.S. Collaboration et al. [208] and will now be presented in detail. Moreover, the event reconstruction algorithm for H.E.S.S. Phase II presented in Chapter 4 is applied to real data and first results will be shown.

5.1. H.E.S.S. Phase I Observations

At the beginning of March 2013 the H.E.S.S. II telescope was still in its commissioning phase and science data taking was not yet possible. Therefore, when the H.E.S.S. observations of the Crab Nebula were triggered by an *Astronomer's Telegram*[1] (ATel) from the Fermi-LAT collaboration [210], the H.E.S.S. II telescope was not yet fully operational and only included in the science data taking for one 28 min run on the 12th of March. Due to bad weather the H.E.S.S. Phase I array started data taking on the 6th March, only two days after the ATel. In total, ten observation runs were taken during and shortly after the pointed target of opportunity observation mode of the Fermi-LAT on the Crab Nebula was triggered. The list of the daily binned full data set can be seen in Table 5.1. The list of runs consists of four runs using the full H.E.S.S. Phase I array and six with one missing telescope each. For one run CT1 was excluded due to too many broken pixel in the camera, for one run CT3 was not used for observation due to tracking problems and for the other runs the CT2 camera was malfunctioning.

---

[1] http://www.astronomerstelegram.org
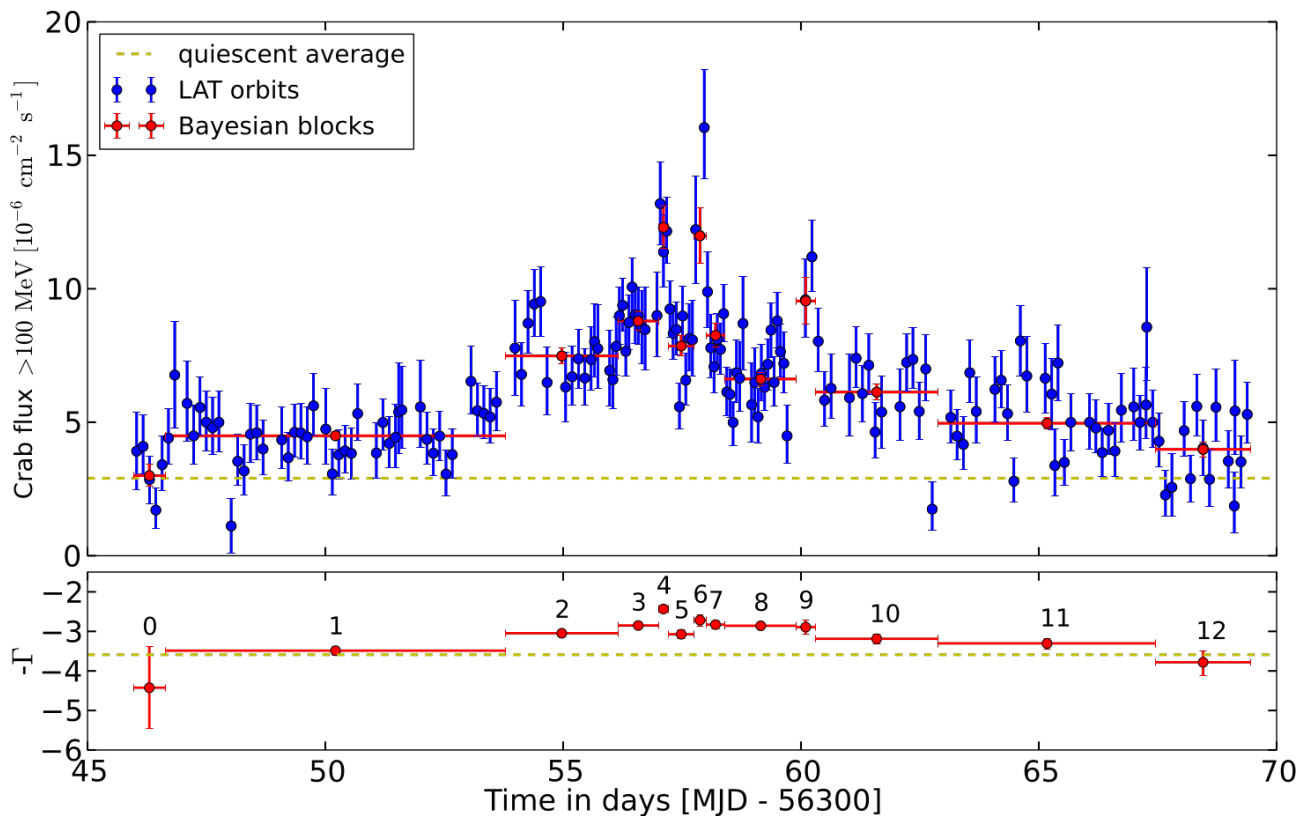
Figure 5.2.: *Red data points correspond to the total Crab flux levels derived using the Bayesian block method in the upper plot whereas blue points show the orbit-binned light curve. The bottom panel shows the time evolution of the spectral index of the synchrotron component of the corresponding Bayesian blocks in the upper figure with respect to the all-time average spectral index of the synchrotron component of the Crab Nebula. Figure taken from [95].*

Although the first night of observations was during the period of highest emission of the flare, the Fermi-LAT telescope never observed at the same time as the H.E.S.S. array. At the beginning of all nights at which the Crab Nebula was visible for the H.E.S.S. array at high zenith angles, the line of sight of the Fermi-LAT to the Crab was obstructed by the Earth. Therefore, the H.E.S.S. observations are not truly contemporaneous but close enough considering the smallest observed time scale of variability of 5 h.

For the reconstruction of the *Shower Parameters* and the data analysis the H.E.S.S. Analysis Package[2] (HAP) was used. The multivariate analysis of Ohm, van Eldik, and Egberts [170] was used for gamma-hadron separation applying ζ standard cuts for signal extraction. For background estimation, the *Reflected Background* and the *Ring Background* techniques were used. The former for the spectral analysis and the latter for the generation of sky maps. The significance was calculated using (Eq.) 17 in Li and Ma [185]. The results of this analysis are also shown in Table 5.1. The independent cross check was performed using the *Model Analysis* for the H.E.S.S. Phase I array as published in de Naurois and Rolland [136] and yielded compatible results. Contrary to other H.E.S.S. Phase I publications (see [11]), the systematic error on the flux normalization (i.e. the error on the energy estimation) was found to be 30 % when comparing the results of the two independent calibration chains used by H.E.S.S.

---

[2]Internal version number hap-12-03-pl02

Figure 5.3.: *Spectral energy distributions for the 12 different Bayesian blocks shown in Figure 5.2 for the synchrotron component of the Crab Nebula. The first block is not shown due to limited statistics. The solid lines indicate the best fit power laws whereas the dashed lines correspond to the best fit power laws with exponential cut-off. The dotted lines show the average synchrotron component. Figure taken from [95].*
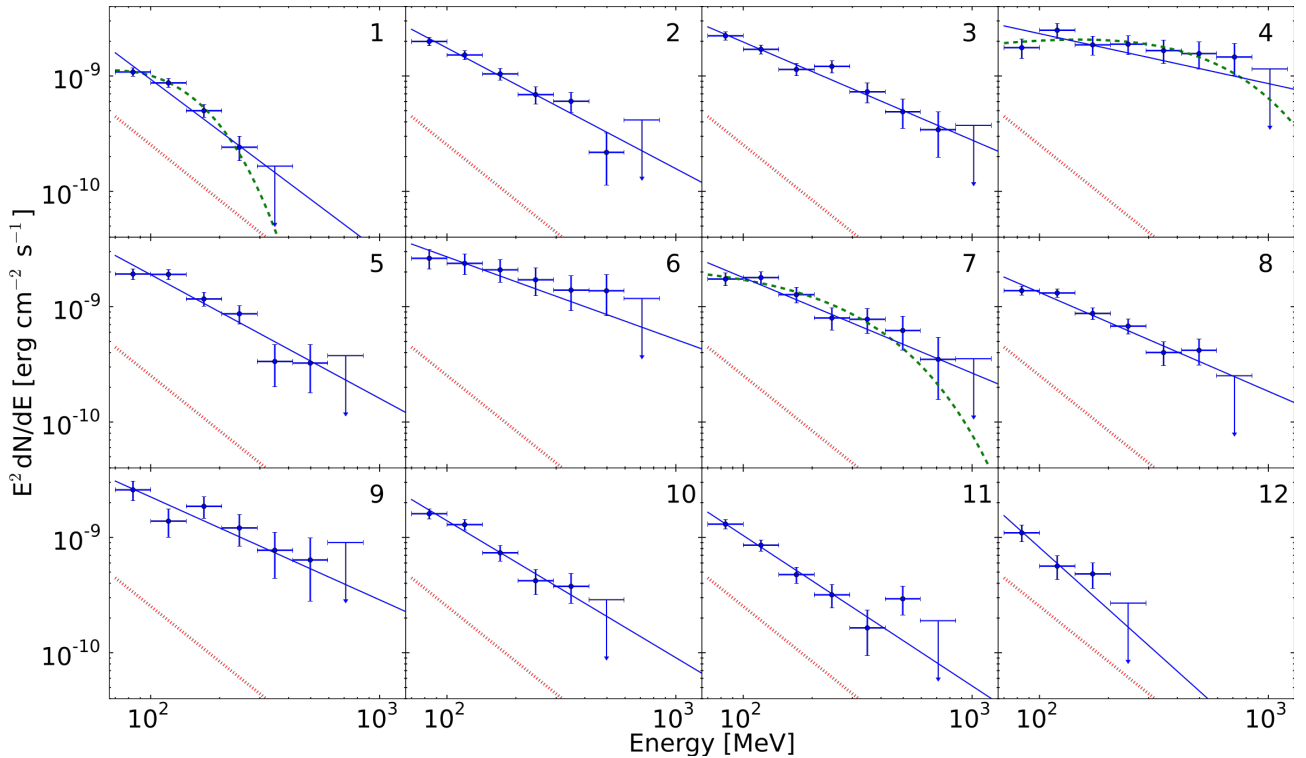
A dead time corrected live time of 4.4 h was obtained for the complete flare data set resulting in 754 excess events from the target region in total. For the spectral shape of the energy distribution of the Crab Nebula during the flare a simple power law and a power law with exponential cut-off were tested. Due to the limited statistics above 10 TeV of the data set in question, it was not possible to distinguish between the two models. Cross checks with a fake flare data set of Crab Nebula observation runs taken at other points in time with the same telescope multiplicities and zenith angles showed the same limiting statistics. Therefore, the model with the least amount of free parameters was chosen to describe the shape of the energy distribution of the Crab Nebula in an energy range from 0.681 TeV to 46.46 TeV. Consequently, all energy distributions were fitted with a simple power law. Table 5.2 lists the results of those fits. All obtained results are compatible with the previously published values in Aharonian et al. [11]. The spectrum of the full flare data set, a simple power law fit and the exponential cut-off power law from Aharonian et al. [11] as a reference, are shown in Figure 5.4.

To check for deviation of the spectrum obtained during the Crab Nebula flare and the one previously published, a χ^2-test was done. The spectrum from Aharonian et al. [11] can be seen as the null hypothesis to test for deviations above 1 TeV, 5 TeV and 10 TeV. A conservative approach is to assume canceling systematics, i.e. the systematics do not increase the difference between the two spectra and therefore do not create a "fake" deviation. Lobanov, Horns, and Muxlow [98] showed that for a flare in the MeV energy band a corresponding flux increase above several tens of TeV is expected. The resulting χ^2/ndf (number of degrees of freedom) values of 32.6/31, 15.7/14 and 5.0/7 indicate no significant deviation of the two spectra. To properly take the low statistics of four ON and one OFF event in the

Date 2013	MJD 56300	T_{live} (s)	Z_{mean} (deg.)	N_{ON}	N_{OFF}	Excess	Sign. σ
03-06	57.8	3181	54	202	498	175	20
03-07	58.8	3152	52	223	455	198	23
03-08	59.8	3155	53	184	460	159	19
03-09	60.8	4827	55	199	557	169	19
03-13	64.8	1596	54	62	173	53	11
full set	-	15911	54	870	2143	754	42

Table 5.1.: *Analysis results of the daily binned full data set of the H.E.S.S. Crab flare observations of March 2013. Given are the Modified Julian Date, the live-time T_{live}, the mean zenith angle Z_{mean}, the number of ON and OFF events, the excess and the significance. Table reproduced from [208].*

last bin of the flare spectrum into account, a likelihood profile was calculated as described in Rolke, López, and Conrad [211]. The deviation of the point with the highest energy in the spectrum of the flare data set with respect to the spectrum published in Aharonian et al. [11] was found to be $2.5\,\sigma$ which includes neither systematic nor statistical uncertainties on the spectrum from Aharonian et al. [11].

Date 2013	I_0 (1 TeV)	Index	Flux > 1 TeV	Flux > 5 TeV
03-06	3.5 ± 0.5	2.6 ± 0.1	1.89 ± 0.19	0.11 ± 0.03
03-07	4.2 ± 0.4	2.8 ± 0.1	2.37 ± 0.21	0.08 ± 0.03
03-08	3.5 ± 0.5	2.6 ± 0.1	2.24 ± 0.21	0.18 ± 0.04
03-09	3.3 ± 0.5	2.7 ± 0.1	1.76 ± 0.18	0.12 ± 0.03
03-13	5.2 ± 1.4	3.4 ± 0.3	2.06 ± 0.36	0.06 ± 0.05
full set	3.8 ± 0.2	2.7 ± 0.1	2.14 ± 0.10	0.12 ± 0.01

Table 5.2.: *Results of the spectral analysis for the observation dates shown in Table 5.1. The normalization at 1 TeV (I_0) is given in units of $10^{-11}\,\text{cm}^{-2}\text{s}^{-1}\text{TeV}^{-1}$ and integral fluxes above 1 TeV and above 5 TeV in units of $10^{-11}\,\text{cm}^{-2}\text{s}^{-1}$. The spectral shape assumed during the fit is a power law and the given errors are statistical only. The estimated systematic errors are 30 % for all fluxes and 0.1 for spectral indices. Table reproduced from [208].*

To further test for variations in the flux level during the Crab flare observations, night-wise integral fluxes were calculated above 1 TeV and 5 TeV as shown in Figure 5.5. Higher energy thresholds were found to be non-restrictive due to too low statistics. A fit of a constant to the night-wise integral fluxes resulted in an average flux of $(2.0 \pm 0.1) \cdot 10^{-11}\,\text{cm}^{-2}\text{s}^{-1}$ with a χ^2/ndf of 6.1/4 for the 1 TeV light curve. For the 5 TeV threshold the fit of the average flux is $(0.11 \pm 0.1) \cdot 10^{-11}\,\text{cm}^{-2}\text{s}^{-1}$ with a χ^2/ndf of 1.2/4. No significant deviation of the average flux level obtained from the one in Aharonian et al. [11] was found ($(2.26 \pm 0.08) \cdot 10^{-11}\,\text{cm}^{-2}\text{s}^{-1}$ and $(0.14 \pm 0.01) \cdot 10^{-11}\,\text{cm}^{-2}\text{s}^{-1}$ respectively).

The highest flux levels measured by the Fermi-LAT for the Crab flare in March 2013 were during the first night of the observations with the H.E.S.S. array. An event number based upper limit calculation using the method described in Rolke, López, and Conrad [211] cannot be used to obtain upper limits on the integral flux enhancement above 1 TeV and 5 TeV. The reason is that a plain cut in reconstructed energy does not take the energy response (migration and resolution) into account and the spectrum published in Aharonian et al. [11] was obtained using a different analysis and during different observation conditions. Instead, pairs of integral flux values from the 2006 and 2013 spectras are calculated (F_{2006} and F_{2013}) by integrating the response corrected spectral functions above the respective energy thresholds. Comparing
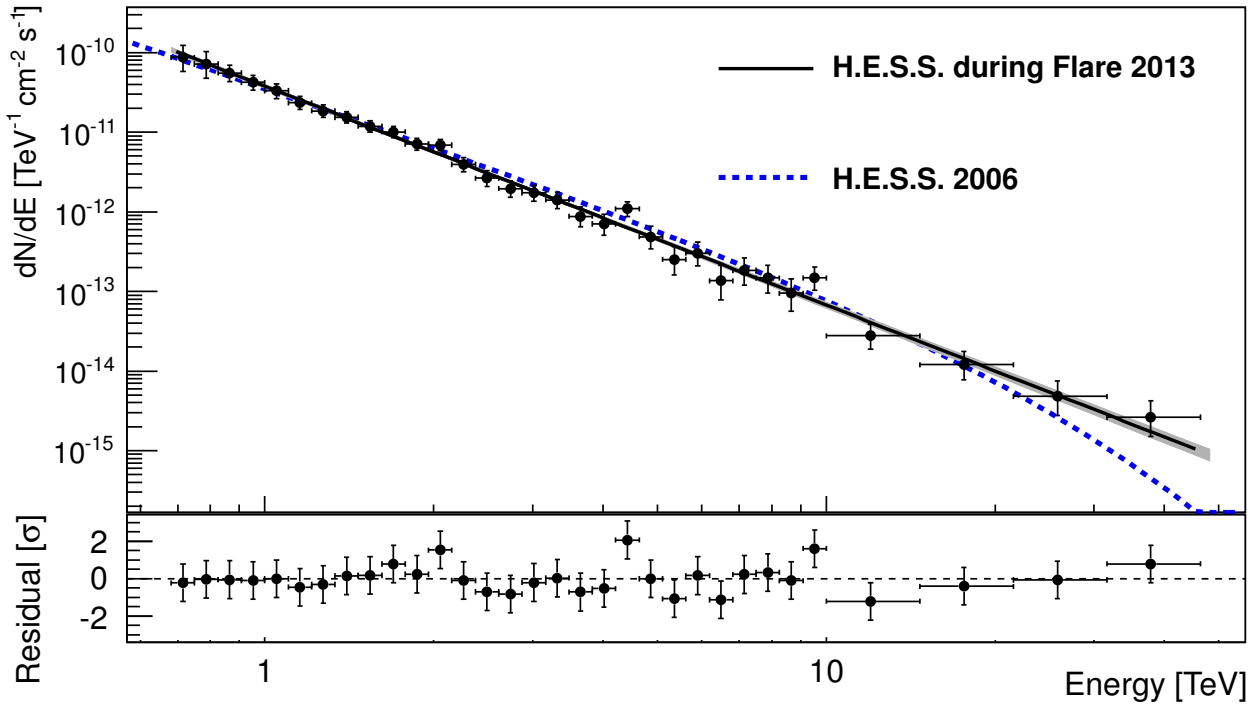
Figure 5.4.: *Spectrum of the Crab Nebula for the full flare data set represented by the black points. The solid black line shows the best fitting power law model and the grey shaded area corresponds to the $1\,\sigma$ error butterfly. The dashed blue line represents the exponential cut-off power law from Aharonian et al. [11]. Figure taken from [208].*

the two values of a pair automatically takes energy migration and efficiencies correctly into account. No significant deviation was found and conservative $95\,\%$ confidence level upper limits where calculated. They are defined as $F_{2006} + 2\sigma$ where σ is the quadratic sum of the statistical and systematical errors. For an energy threshold of $1\,\mathrm{TeV}$, the upper limit is found to be $3.66 \cdot 10^{-11}\,\mathrm{cm}^{-2}\mathrm{s}^{-1}$. The corresponding flux enhancement factor limit is < 1.63 with respect to the integral flux published in Aharonian et al. [11] and < 1.78 for an energy threshold of $5\,\mathrm{TeV}$.

The expectations for an enhanced signal during the flare of the Crab Nebula in March 2013 for VHE gamma-rays depends on the cause of the flaring component in the HE regime. As seen in previous flares, the synchrotron component in this regime hardens (see Figure 5.3). The reasons for this can either be a change in electric or magnetic field lines which would not change the expected flux of inverse-Compton (IC) photons at very high energies, or an enhanced production of electrons and positrons. In the latter case, an IC photon flare induced by the ambient scattered photons is expected in the VHE regime. Due to the fact that the observed synchrotron photon energies are greater than the maximum possible energy gained through shock-acceleration for electrons and positrons [103], a mild Doppler boosting of the observed photons is expected [212] or a completely different acceleration mechanism like magnetic reconnection [108]. Assuming an observation angle θ and a Lorentz factor Γ the resulting relativistic Doppler factor is given by:

$$\delta = [\Gamma(1 - \beta \cos\theta)]^{-1} \tag{5.1}$$

Using this Doppler factor, the maximum energy of the IC photons in the Klein-Nishima limit (the electrons producing the IC photons scattered on the ambient, predominantly optical, photons and the
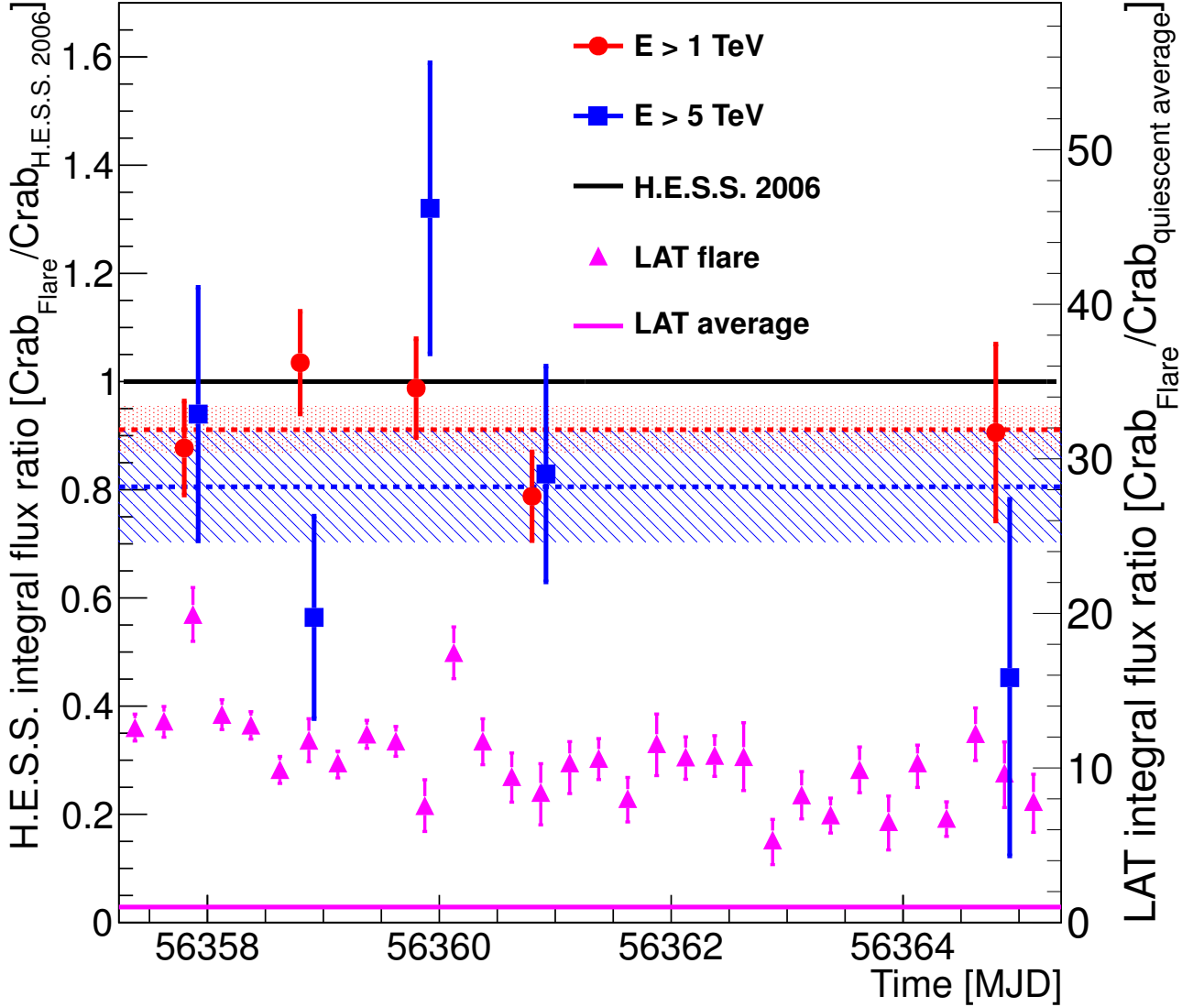
Figure 5.5.: *Night-wise integral flux values for energy thresholds of $E > 1\,\mathrm{TeV}$ (red circles) and $E > 5\,\mathrm{TeV}$ (blue squares) in units of the corresponding integral flux obtained from the spectrum published in Aharonian et al. [11]. The error bars depict the $1\,\sigma$ statistical errors. Colored dashed lines correspond to the fit of a constant to the respective light curve and the colored hatched and dotted areas mark the $1\,\sigma$ error contours. The magenta colored triangles show the integral flux ratio of the synchrotron component of the Crab Nebula detected by the Fermi-LAT. The solid magenta line indicates the corresponding all time average. Figure taken from [208].*

Klein-Nishina limit becomes important above electron energies around $\approx 30\,\mathrm{GeV}$ [213]) is:

$$E_{\mathrm{IC}} = 1.5\,\mathrm{PeV} \cdot \delta^{0.5} \cdot (E_{\mathrm{Syn}/100\,\mathrm{MeV}})^{0.5} \cdot (B/\mathrm{mG})^{-0.5} \qquad (5.2)$$

with B being the average magnetic field in the emission region and E_{Syn} the energy of the synchrotron component.

The highest expected signal in the VHE gamma-ray regime is at the level of tens of TeV, for details see Lobanov, Horns, and Muxlow [98]. At lower energies, the expected signal in the VHE regime is greatly depending on the expected flux at energies below $100\,\mathrm{MeV}$. The HE synchrotron component therefore has to be extrapolated to lower energies which is error prone [113, 212] and the expected contribution to the VHE signal is significantly smaller. Assuming that the flaring component follows a power law of the form $f_\nu \propto \nu^{-\alpha}$, the VHE IC component will scale with $f_\nu^{\mathrm{IC}}/f_\nu^{\mathrm{Syn}} \propto (\delta/B)^{1+\alpha}$ [214, 215]. The non-detection of variability in the Crab flare data set taken with the H.E.S.S. experiment in March 2013 and the contemporaneous flux measurements of the Fermi-LAT experiment limit the relativistic Doppler factor to $\delta \leq 100(B/122\,\mu\mathrm{G})$. The results are in agreement with the non-detection of a flaring VHE component as reported by Aliu et al. [100] and results from previous flare observations by other VHE experiments [216]. Previous claims by Bhat et al. [217] and Bartoli et al. [102] seem unlikely in the light of the results presented here. However, high angular resolution observations of the Crab Nebula do not reveal any evidence for particles moving with a a speed $v > 0.5c$ (which could explain a Doppler boosting of the particles towards our line of sight). Alternatively, the Doppler boosting could originate from a region close to the termination shock and the gamma-ray variability could originate from the optically resolved knot which is 0.6 ″ displaced from the pulsar [116].

5.2. H.E.S.S. Phase II Observations

The adapted *Model Analysis* for H.E.S.S. Phase II can be applied to real data obtained from Crab Nebula observations with the full five telescope array. Following the triggered ToO observations of the Crab Nebula during its flare in the HE regime in March 2013, one five telescope observation run was taken. However, the CT5 telescope was still in its commissioning phase and the weather conditions were poor, i.e. several clouds moved through the field of view during the $28\,\mathrm{min}$ of the run and therefore it was not used for the publication. Nonetheless, the analysis results obtained with the adapted *Model Analysis* for this run will be presented in the following.

To obtain a high statistic data set to properly verify the performance of the adapted *Model Analysis*, a set of 25 five telescope observation runs on the Crab Nebula is used. The average zenith angle of these observations is $\approx 48.2\,°$ compared to a zenith angle of $52.9\,°$ for the flare run. The calibration coefficients used for this analysis are still preliminary as are the pointing corrections (used to correct camera and telescope structure deformations). The autofocus mechanism of the H.E.S.S. II telescope was not used either and the camera was focused on a distance of $\approx 10\,\mathrm{km}$ (for details see [159]). This corresponds to the same focus as used by the smaller telescopes and the MonteCarlo simulations.

Unfortunately, the distributions of the fit errors for MonteCarlo simulations and real data differ (see Section 4.4 and Figure 4.24). Therefore, the results shown in this Chapter were produced without these cuts. However, it should be possible to calculate cuts using real data distributions as input obtaining the same performance improvements. Due to lack of time this was not done during the course of this work.

To test the proper calibration of the data and the gamma-hadron separation, the distribution of the *MRSG* for gamma-like and all events are compared to the ones obtained from MonteCarlo simulations as shown in Figure 5.6. The distributions for real data events are slightly shifted to the right, indicating a problem with the calibration of the data, i.e. the pedestal width, ADC to p.e. coefficient, etc. are not perfectly understood. A possible solution is to increase the δ value from Section 4.3.1 to adjust for the slightly different shower images. However, an in-depth understanding of the calibration of the instrument is necessary for a properly working *Model Analysis* and could not be obtained during the

(a) *Gamma MonteCarlo*

(b) *Gamma-like Data*

(c) *Proton MonteCarlo*

(d) *Background-like Data*
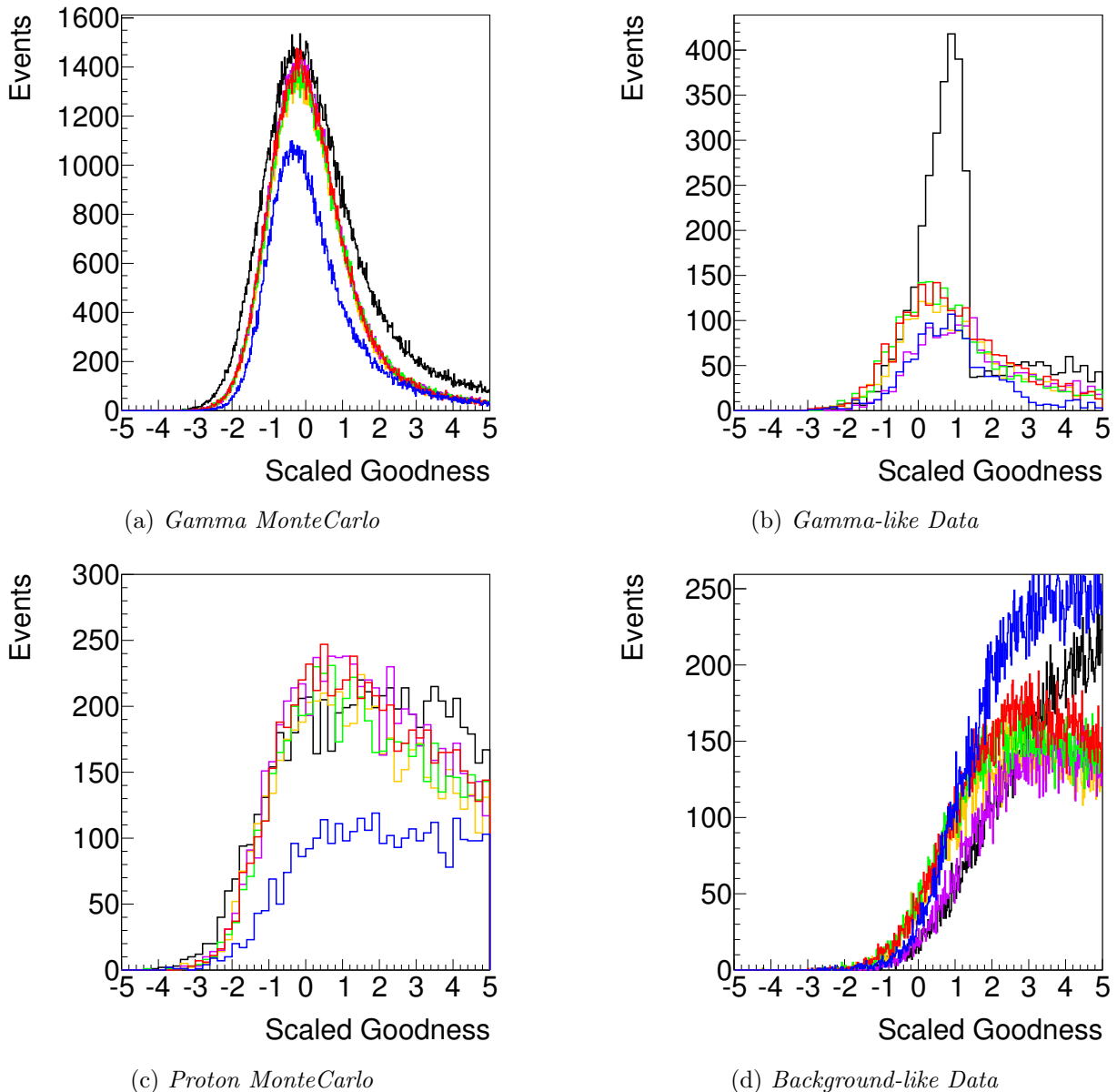
Figure 5.6.: Reduced Scaled Goodness *distributions for the five telescope Crab flare run (CT1 in orange, CT2 in violet, CT3 in green, CT4 in red and CT5 in blue. The solid black line is the* MRSG*). MonteCarlo distributions corresponding to the same observation conditions as during the data taking of the run are shown on the left. The real data distributions (right side) appear to be slightly shifted to the right and therefore less gamma-like events are expected. The step in the gamma-like distribution of* MRSG *is due to the energy dependent cut on the* MRSG.

course of this work because the final calibration procedures for the H.E.S.S. II telescope were not yet available at the time of the writing of this thesis.

To verify the validity of the reconstruction and to check for artificially created features due to hardware malfunctions in the cameras or software problems, the acceptance maps for gamma-like and background-like events are used. The distribution of the events in the *Nominal System* and *RaDec J2000 System* for

(a) *Gamma-like Acceptance Flare*

(b) *Gamma-like Acceptance All*

(c) *Background-like Acceptance Flare*

(d) *Background-like Acceptance All*
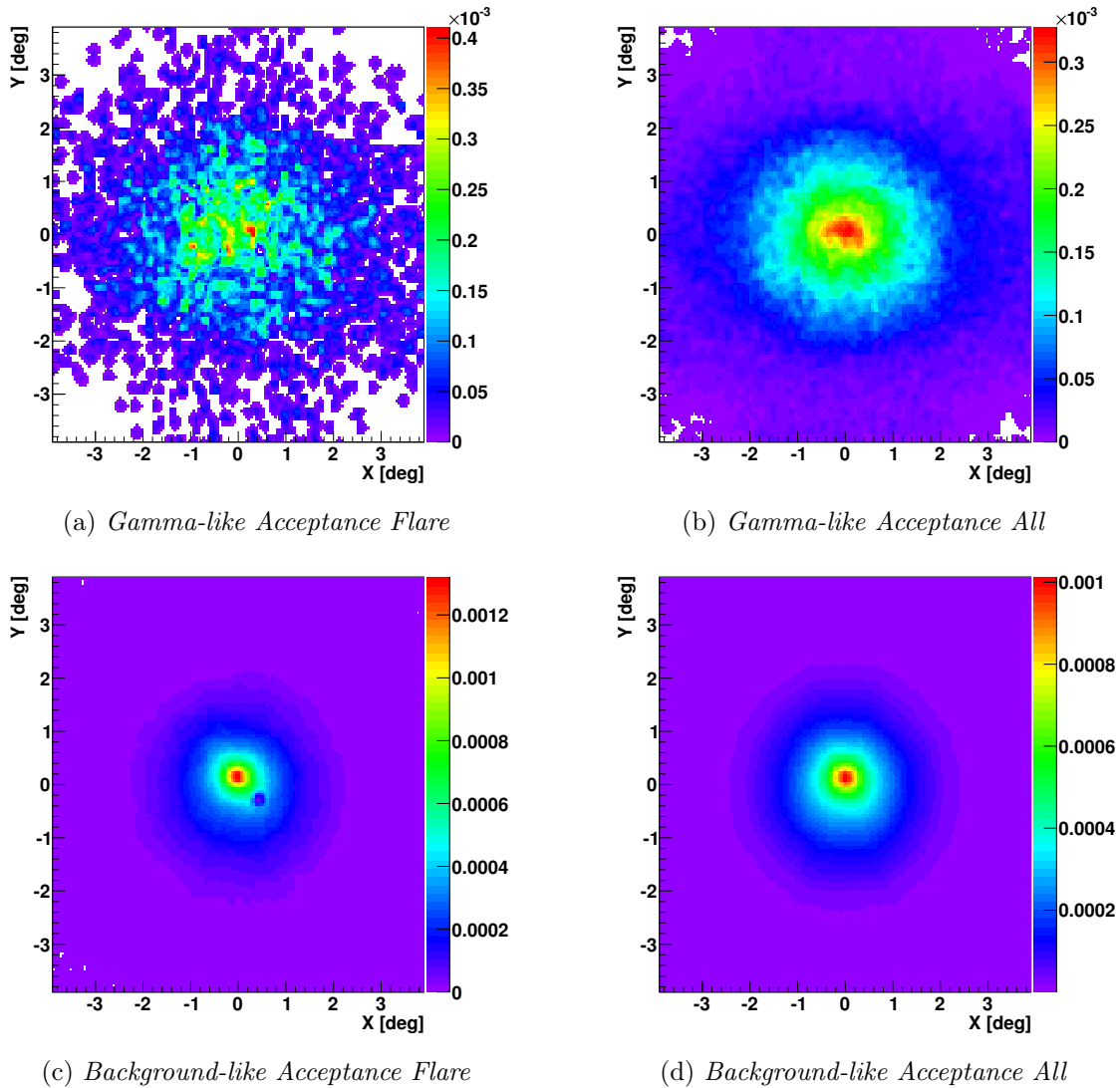
Figure 5.7.: *Gamma-like and background-like acceptance maps in the* Nominal System *for the two Crab Nebula data sets. The lack of statistics in the single run flare data set is obvious. The hole in the flare acceptance maps is due to the exclusion of the target region for acceptance calculation (normally the acceptance is averaged over multiple runs and, due to the different wobble offsets, no holes in the acceptance maps are present).*

the two data sets behave as expected and show a radial symmetrical behaviour. Figure 5.7 represents the acceptance for gamma-like and background-like events in the *Nominal System*. For the flare data set a live time of 28.8 min is obtained which reduces to 26.8 min after dead time correction. For the 25 Crab Nebula runs the live times sum up to 6.87 h and 5.22 h after dead time correction.

To check for a signal beyond the background rate in the source region, so called θ^2 histograms are used. The squared angular distance of the reconstructed source position with respect to the target position is calculated and filled into a histogram. The resulting distributions for the *Ring Background* technique are shown in Figure 5.8. As expected the Crab Nebula is only detected with $5.3\,\sigma$ in the flare data set. For the full data set the obtained significance is $35.7\,\sigma$ yielding a clear detection of the Crab Nebula. Using the uncorrected live time of the full data set, an estimate for the integral sensitivity I can be obtained. A 50 h live time observation is assumed and the minimum flux for a $5\,\sigma$ detection of a source

(a) θ^2 *Flare*

(b) θ^2 *All*

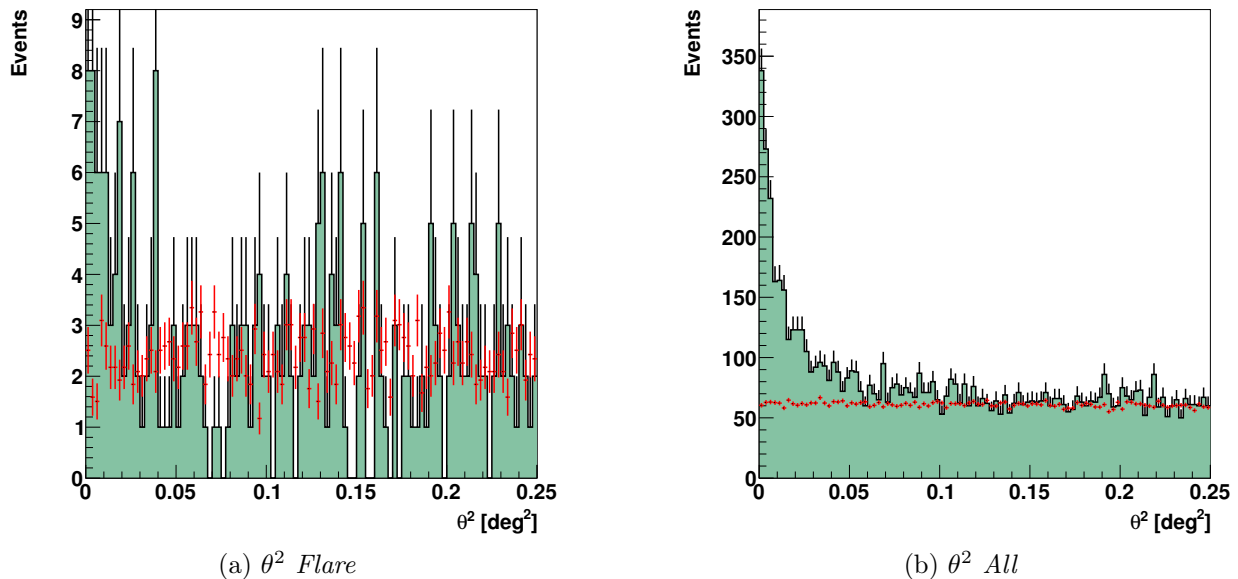Figure 5.8.: θ^2 *distributions obtained using the* Ring Background *technique for the Crab flare observation run and the full data set. Black lines together with the green filled area correspond to the events in the signal region whereas red points correspond to background events.*

in units of the integral flux of the Crab Nebula is calculated using the obtained significances:

$$I = \frac{5\,\sigma}{35.7\,\sigma\,\frac{\sqrt{50\,\text{h}}}{\sqrt{6.87\,\text{h}}}} \tag{5.3}$$

The resulting real data integral sensitivity for an average zenith angle of 48.2 ° is 5.2 % of the integral flux of the Crab Nebula. Using a dedicated MonteCarlo production at a zenith angle of 50 ° results in a MonteCarlo integral sensitivity prediction of 6 % which is in good agreement with the observed data.

Moreover, the extension of the Crab Nebula can be fitted and compared to the MonteCarlo expectation of the point spread function. The resulting value for the full data set is an $R68$ of 0.19 ° which is of the same order as the $R68$ obtained from MonteCarlo simulations (50 ° zenith angle) which is in between 0.15 ° and 0.2 ° in the central energy range.

Another test of the validity of the analysis is to plot the number of excess events versus the live time. The resulting curve is expected to increase linearly, any deviation indicates time variability or a problem in the calibration, reconstruction or analysis software. Additionally, the significance should increase with the square root of the live time. Both distributions are shown in Figure 5.9 and are in good agreement with the expected behaviour.

As a final step excess and significance maps using the acceptance maps shown in Figure 5.7 can be calculated. The obtained maps in the *RaDec J2000 System* are shown in Figure 5.11. A point source at the position of the Crab Nebula is clearly seen. The best-fit position of RA = 05$^\text{h}$34$^\text{m}$31$^\text{s}$ ± 2$^\text{s}$ and DEC = 21°58′48″ ± 26″ for the flare and RA = 05$^\text{h}$34$^\text{m}$31.2$^\text{s}$ ± 0.5$^\text{s}$ and DEC = 22°18′00″ ± 8″ for the full data set is in good agreement with the known position of the Crab Nebula at RA = 05$^\text{h}$34$^\text{m}$31.97$^\text{s}$ and DEC = 22°00′52.06″ considering the still preliminary pointing corrections. The flare data set clearly has poor statistical quality due to the bad weather conditions and the reduced data taking

(a) *Excess vs. time*

(b) *Significance vs. time*
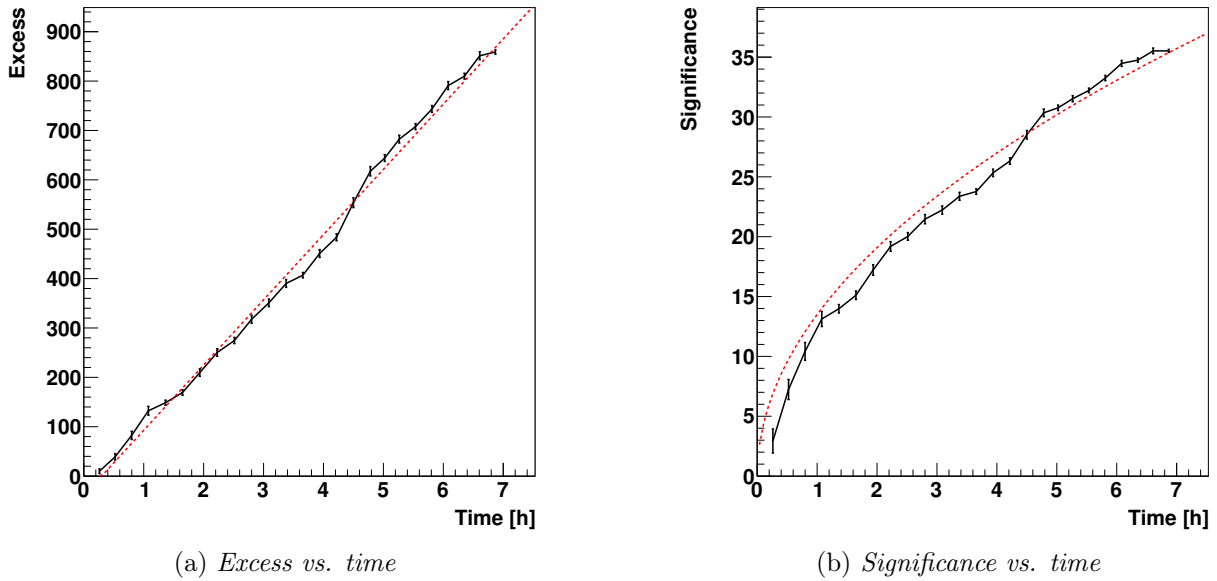
Figure 5.9.: *Evolution of the excess and the significance versus time in black for the full data set of five telescope Crab Nebula observation runs. The distributions follow the expected shape (shown as the dashed red lines).*

efficiency due to on going commissioning work (e.g. uncertain calibration values). However, no artifacts are seen in either of the maps that would indicate abnormal behaviour.

(a)

(b)
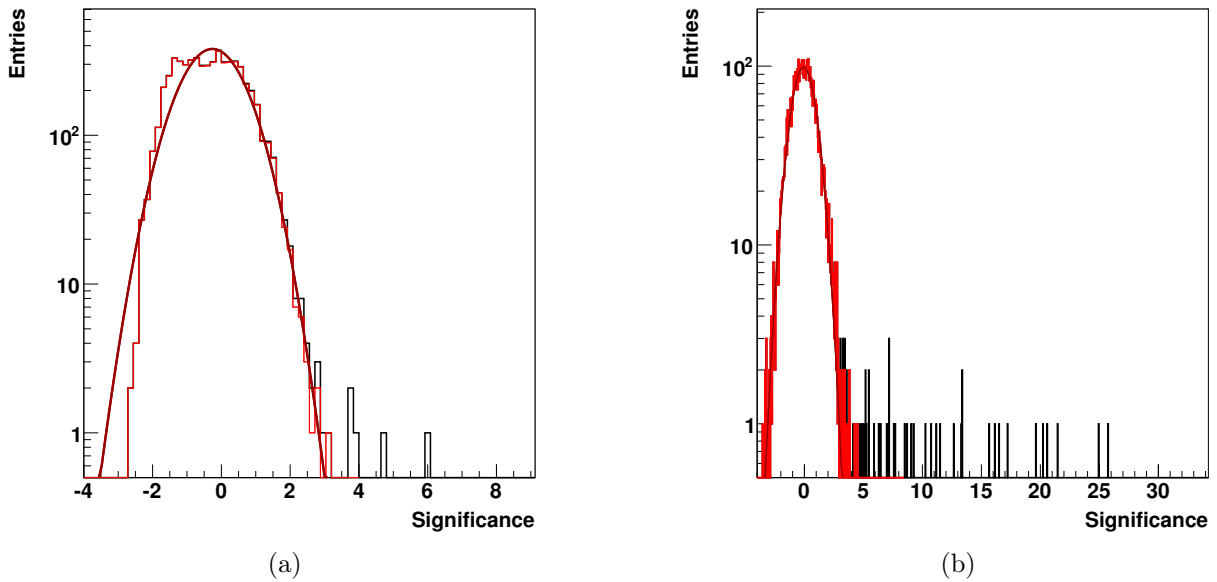
Figure 5.10.: *Distributions of the significance test statistics of the significance maps shown in Figure 5.11 together with a Gaussian fit. The Gaussian shape of the distributions are obvious. The flare run is again clearly lacking statistics and shows abnormal behaviour around −2. The full data set is in perfect agreement with the expectations and is described by a Gaussian centered at zero with a width of unity. The red lines corresponds to the data without the contribution of the source whereas the black lines includes the source.*

To quantify the validity of the significance maps the distribution of the contents can be fitted by a Gaussian. If the background is well understood, the mean of the Gaussian should be zero and the width should be unity. For the flare data set the fitted values are -0.260 ± 0.013 for the mean and 0.8964 ± 0.0072 for the width and for the full data set the mean is found to be -0.071 ± 0.013 and the sigma is 1.0004 ± 0.0099 as seen in Figure 5.10. The too small width of the distribution of the flare run is most likely due to lacking statistics and problems combined with the preliminary calibration and the acceptance calculation for a single observation run. However, the distribution of the full data set is in perfect agreement with the expectations.

To summarize, the Crab Nebula is reconstructed at the correct position in the sky for both data sets. The small offset in declination for the full data set is most likely attributed to the preliminary pointing corrections. The significance of the detection of the Crab Nebula is compatible with the expectations from MonteCarlo simulations. This is also true for the extension of the source which is compatible with a point-like source. No unusual behaviour of the Crab Nebula has been seen in the flare or the full data set. The background in the sky maps appears to be well understood for the 25 five telescope runs. To properly quantify the flux of the Crab Nebula, detailed studies of the systematics of the reconstruction are necessary, especially of the energy migration, and were not part of this work. Nonetheless, it was shown that the adapted *Model Analysis* works with real data obtained with the H.E.S.S. Phase II array and the results look promising.

(a) *Excess Flare*

(b) *Excess All*

(c) *Significance Flare*
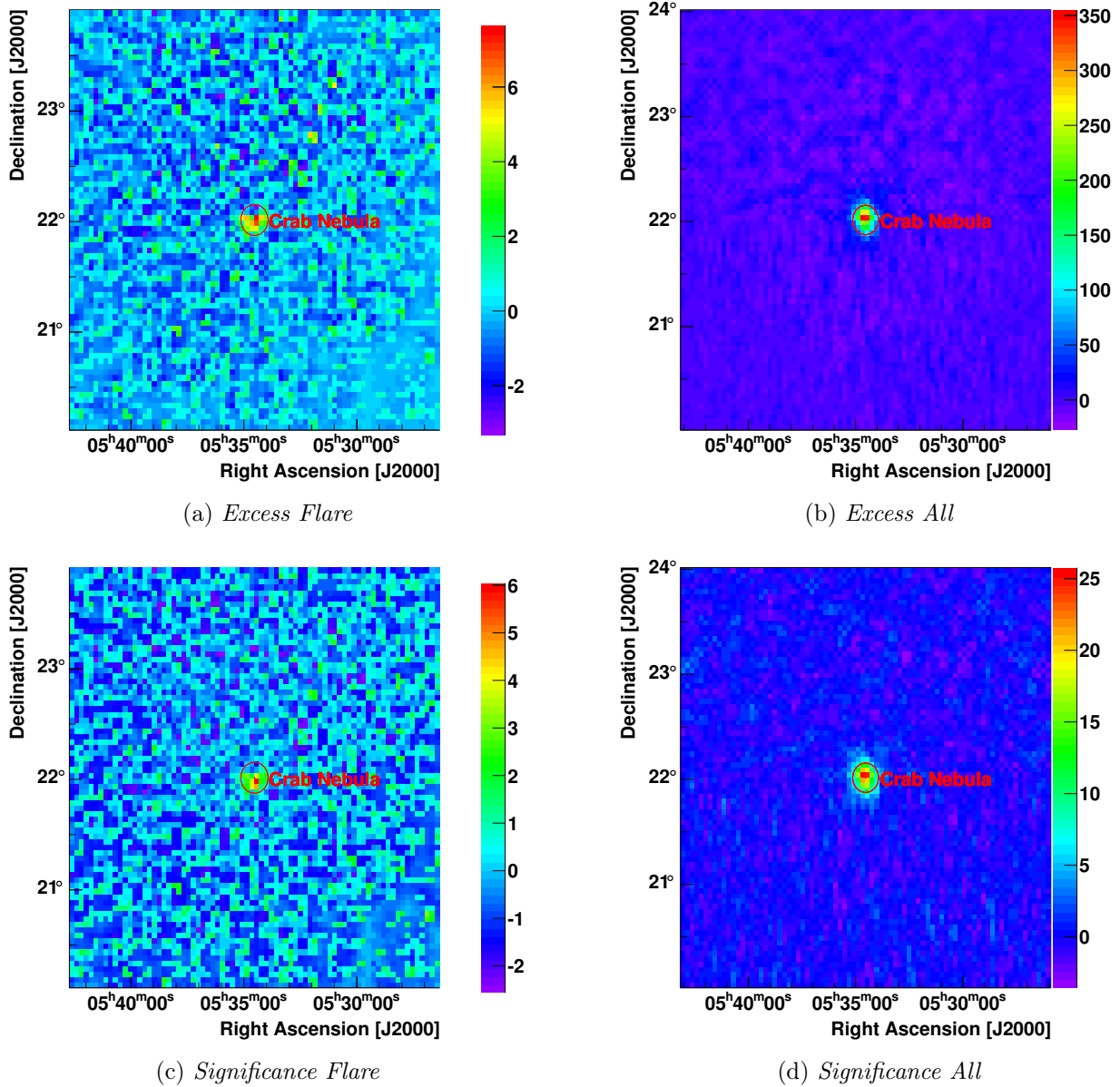
(d) *Significance All*

Figure 5.11.: *Excess maps for the flare run on the upper left and the full data set on the upper right. The corresponding significance maps are shown below. The flare run maps were generated using the* Template Background *technique which yields better results if only one run is analysed compared to the* Ring Background *technique used for the full data set. The Crab Nebula is clearly reconstructed as a point source at the expected position. No artifacts are visible in the maps of the full data set. The flare run excess maps lacks in statistic as indicated by the low number of events per bin.*

6

Conclusion

During the course of this work, the adaption of the most advanced shower reconstruction technique used by the H.E.S.S. collaboration, to the needs of the hybrid, five telescope array of H.E.S.S. Phase II, was described in detail. The performance of the reconstruction was verified using MonteCarlo simulations and its capabilities were demonstrated using real data obtained during observations of the Crab Nebula. The analysis of the data taken during the flare of the Crab Nebula in March 2013 was described and its implications discussed in detail.

The semi-analytical model used by the original *Model Analysis* for H.E.S.S. Phase I could be adapted to the different mirror and camera layout of the H.E.S.S. II telescope. The verification using MonteCarlo simulations of gamma-ray air showers showed that the differences between model generated showers and MonteCarlo generated showers are acceptable (i.e. below 10 % in the central energy range). A modified approach to the implementation of the fitting algorithm and the gamma-hadron separation was implemented and its performance was validated using MonteCarlo simulations. The resulting performance curves, for example the effective area and sensitivity curves, look promising and prove that the adapted shower reconstruction can achieve similar or better results compared to the one of H.E.S.S. Phase I and other hybrid shower reconstruction techniques. These performance predictions were validated using 25 observation runs taken on the Crab Nebula with the full five telescope H.E.S.S. Phase II array and showed good agreement.

The fraction of events that only trigger two telescopes increased from Phase I to Phase II. Combining this fact with the poor starting parameters for the *Model Analysis*, obtained for those events from a basic Hillas analysis, will reduce the performance. This is especially true at lower energies. Further investigations whether those events are to be rejected in general or if cuts on the error of the fit are able to elevate the problem are necessary. Moreover, improvements to the semi-analytical model are both possible and necessary. For example, the lookup tables used during the generation of the model templates are too sparse and need to be regenerated with higher statistics. The effect of the azimuth angle is not yet part of the model generation process either. The over all performance of the reconstruction method still needs improvement to ascertain the full potential of this advanced shower reconstruction technique and a full integration into the H.E.S.S. software framework is still missing and remains to be done.

Significant parts of the work presented here rely on a working MonteCarlo simulation chain, especially a proper detector simulation. Changing the existing software framework and collecting all necessary detector parameters are crucial to properly integrate H.E.S.S. II into the simulation chain. Applying major alterations to a software that has grown over the course of ten years is a challenge and has been achieved with minimal changes for most parts of the MonteCarlo simulation chain. Nonetheless, some parts of the code had to be rewritten as a basis for further developments with the next generation IACT experiment, CTA [15], in mind. Special care was taken to ensure multi-threading capabilities of the code in order to use the full potential of modern multi-core CPU architectures. Future software developments to include SIMD (single instruction multiple data) operations are necessary and should be included, for example, in the *Linear Tables* which would increase the performance of the software.

By now there are several multi-wavelength observations of Crab Nebula flares seen in HE gamma-rays. No counter part in any other energy range has been found so far. The contemporaneous observations of the flare in March 2013 with the H.E.S.S. array were presented in detail and the implications from the analysis of the data were discussed. The non-detection of a flare in the VHE gamma-ray regime and the resulting upper limits help to understand the possible origins of these flares. The presented results are in good agreement with results published by the VERITAS collaboration and contradict previous detection claims by the Argo-YBJ experiment.

Together with the limited energy resolution, the resulting limits on flux variations are not yet strong enough to exclude some of the suggested acceleration mechanisms. However, with the next generation IACT experiment on the horizon, a significant step towards understanding these HE gamma-ray flares can be made. The superior effective area at highest energies achieved by CTA by using a large number of small sized telescopes spread over a huge area, will increase the sensitivity by more than an order of magnitude compared to current third generation IACT arrays. With an energy resolution below 10 % [15], a detection of flux variations during one of the next flares might be possible. At least the resulting upper limits will be significantly better than those obtained now. If a flare would be detected by the CTA array, the better angular resolution might help to narrow down the region from where these flares originate. All in all the prospects of CTA are excellent and interesting times for VHE gamma-ray astronomy lie ahead of us.

A

Appendix

A. Linear Tables

The evaluation of an arbitrary n dimensional function $F(\vec{x})$ with $\vec{x} = (x_1, x_2, \ldots, x_n)$ is a common problem in many fields in physics. To save computing time the function $F(\vec{x})$ can be replaced by a model $M(\vec{\chi})$. It uses an n dimensional grid of points $\vec{P}$ as a lookup, each representing a precomputed value of the function $F(\vec{P})$ with a linear interpolation between grid points. These points form an n dimensional array which describes the behaviour of the function $F(\vec{x})$. For this work the so called *Linear Tables* developed by [136, 201] are used for this purpose. They were reimplemented and improved using for example the BOOST *multi-array* library [190] and the C++11 standard [218].

For one of the n dimensions i of the grid, a set of b_i bins, in a range from Min_{x_i} to Max_{x_i}, is used forming a n dimensional hypercube with the grid point $\vec{P}$ at its center. The bin's content is used by the model $M(\vec{\chi})$ to represent the function $F(\vec{x})$ in this region. In total an amount of $b_{tot} = \prod_i^n b_i$ bins are used for the model $M(\vec{\chi})$. A coordinate transformation function $T(\vec{x})$ is used to convert a coordinate $\vec{x}$ to a grid coordinate $\vec{\chi}$ of the underlying array of the model. The coordinate transformation for a given dimension is independent of the other dimensions and can, therefore, be calculated separately:

$$\vec{\chi} = T(\vec{x}) = T(x_1, x_2, \ldots, x_i) = \big(\chi_1(x_1), \chi_2(x_2), \ldots, \chi_i(x_i)\big) \tag{A.1}$$

A visualization of a two dimensional grid for equally spaced points can be seen in Figure A.1.

A.1. Linear Interpolation

To reduce the amount of points needed to sufficiently describe the function $F(\vec{x})$ in a certain range, therefore saving computing time, disk and memory space, the *Linear Tables* use a linear interpolation between grid points. Given a coordinate $\vec{x}$, with a corresponding grid coordinate $T(\vec{x}) = \vec{\chi}$ for which the interpolated value $I(\vec{x})$ has to be found the n dimensional linear interpolation can be broken down into a one dimensional linear interpolation for each dimension. Looking at the one dimensional case this resolves to finding the two grid points P^{Left} and P^{Right}, called *Bin Pair*, that enclose the grid coordinate $\chi = T(x)$. The linearly interpolated value using the weight function W is than given by:
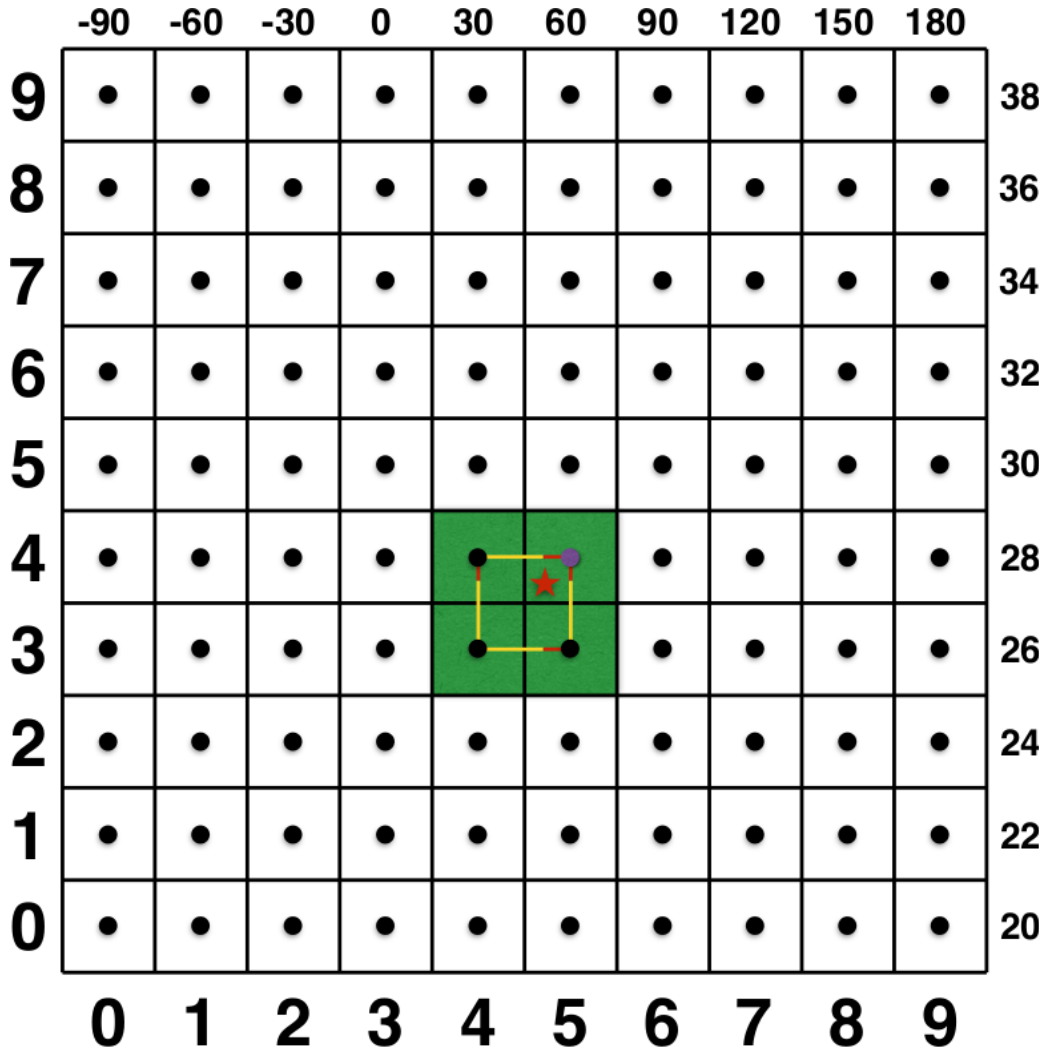
Figure A.1.: *Grid of a two dimensional* Linear Table. *The left and the lower axes are the grid coordinates, the x and y dimension contain 10 bins each. The right and the upper axes are the corresponding real coordinates. The black points indicate the grid points, i.e. the center of a bin. The red star indicates an example coordinate for which the interpolated value should be calculated. The purple point is the nearest grid point to the example coordinate. The green shaded area indicates the four hypercubes which grid points will be used for the interpolation. The red lines denote the distances in grid coordinates with the higher weight whereas the yellow lines are the distances in grid coordinates with the lower weight. The length of each line is indirectly proportional to the weight it represents.*

$$I(x) = W^{Left} \cdot M(P^{Left}) + W^{Right} \cdot M(P^{Right}) \tag{A.2}$$

$$W^{Left} = \frac{T(x) - P^{Left}}{P^{Right} - P^{Left}} = \frac{\chi - P^{Left}}{P^{Right} - P^{Left}} \tag{A.3}$$

$$W^{Right} = \frac{P^{Right} - T(x)}{P^{Right} - P^{Left}} = \frac{P^{Right} - \chi}{P^{Right} - P^{Left}} \tag{A.4}$$

For the n dimensional interpolation the amount of distinct grid points P that are used during the interpolation is equal to 2^n, the next neighbour pairs in every dimension, and the resulting formula is:

$$
\begin{aligned}
I_n =& W_n^{Left} \cdot I_{n-1}(\dots, P_n^{Left}) + W_n^{Right} \cdot I_{n-1}(\dots, P_n^{Right}) \\
=& W_n^{Left} \cdot \left[W_{n-1}^{Left} \cdot I_{n-2}(\dots, P_{n-1}^{Left}, P_n^{Left}) + W_{n-1}^{Right} \cdot I_{n-2}(\dots, P_{n-1}^{Right}, P_n^{Left}) \right] + \\
& W_n^{Right} \cdot \left[W_{n-1}^{Left} \cdot I_{n-2}(\dots, P_{n-1}^{Left}, P_n^{Right}) + W_{n-1}^{Right} \cdot I_{n-2}(\dots, P_{n-1}^{Right}, P_n^{Right}) \right] \\
=& W_n^{Left} \cdot W_{n-1}^{Left} \cdot \ \dots \ \cdot W_0^{Left} \cdot I(P_0^{Left}, \ \dots \ , P_{n-1}^{Left}, P_n^{Left}) + \\
& W_n^{Right} \cdot W_{n-1}^{Left} \cdot \ \dots \ \cdot W_0^{Left} \cdot I(P_0^{Left}, \ \dots \ , P_{n-1}^{Left}, P_n^{Right}) + \\
& W_n^{Left} \cdot W_{n-1}^{Right} \cdot \ \dots \ \cdot W_0^{Left} \cdot I(P_0^{Left}, \ \dots \ , P_{n-1}^{Right}, P_n^{Left}) + \\
& W_n^{Right} \cdot W_{n-1}^{Right} \cdot \ \dots \ \cdot W_0^{Left} \cdot I(P_0^{Left}, \ \dots \ , P_{n-1}^{Right}, P_n^{Right}) + \\
& \dots \\
& W_n^{Left} \cdot W_{n-1}^{Left} \cdot \ \dots \ \cdot W_0^{Right} \cdot I(P_0^{Right}, \ \dots \ , P_{n-1}^{Left}, P_n^{Left}) + \\
& W_n^{Right} \cdot W_{n-1}^{Left} \cdot \ \dots \ \cdot W_0^{Right} \cdot I(P_0^{Right}, \ \dots \ , P_{n-1}^{Left}, P_n^{Right}) + \\
& W_n^{Left} \cdot W_{n-1}^{Right} \cdot \ \dots \ \cdot W_0^{Right} \cdot I(P_0^{Right}, \ \dots \ , P_{n-1}^{Right}, P_n^{Left}) + \\
& W_n^{Right} \cdot W_{n-1}^{Right} \cdot \ \dots \ \cdot W_0^{Right} \cdot I(P_0^{Right}, \ \dots \ , P_{n-1}^{Right}, P_n^{Right})
\end{aligned} \tag{A.5}
$$

It is obvious that the dimensional ordering of the interpolation is not important and the interpolation formula can be implemented recursively in C++.

A.2. Gradient Information

In addition to the linear interpolation also the gradient information between neighbouring grid points can be calculated. Using the notation from Appendix A.1 the gradient for the one dimensional case is given by:

$$
\frac{\mathrm{d}I(x)}{\mathrm{d}x} = \frac{M(P^{Right}) - M(P^{Left})}{P^{Right} - P^{Left}} \tag{A.6}
$$

It is constant in between two grid points, therefore no weights are needed. For the n dimensional case the calculation of the gradient can also be done recursively. Given two dimensions i and k of the n available dimensions, the following equality is important for the gradient at a certain grid point:

$$
\begin{aligned}
\frac{\mathrm{d}I(\dots, x_i, x_k)}{\mathrm{d}k} =& \dots \cdot W_i^{Left} \dots \cdot \frac{I(\dots, P_i^{Left}, P_k^{Right}) - I(\dots, P_i^{Left}, P_k^{Left})}{P_k^{Right} - P_k^{Left}} + \\
& \dots \cdot W_i^{Right} \dots \cdot \frac{I(\dots, P_i^{Right}, P_k^{Right}) - I(\dots, P_i^{Right}, P_k^{Left})}{P_k^{Right} - P_k^{Left}} \\
=& \dots \cdot \left[\left(W_i^{Left} \cdot I(\dots, P_i^{Left}, P_k^{Right}) + W_i^{Right} \cdot I(\dots, P_i^{Right}, P_k^{Right}) \right) - \right. \\
& \left. \left(W_i^{Left} \cdot I(\dots, P_i^{Left}, P_k^{Left}) + W_i^{Right} \cdot I(\dots, P_i^{Right}, P_k^{Left}) \right) \right] \cdot \\
& \left(P_k^{Right} - P_k^{Left} \right)^{-1} \\
=& \frac{\mathrm{d}I(\dots, x_k, x_i)}{\mathrm{d}k}
\end{aligned} \tag{A.7}
$$

It does not matter whether the gradient is calculated before, after or in between the interpolation of the grid points, i.e. the n dimensional gradient formula using Equation (A.7) can be written as

$$
\begin{aligned}
\frac{\mathrm{d}I_n(\vec{x})}{\mathrm{d}i} =& W_n^{Left} \cdot W_{n-1}^{Left} \cdot \ \cdots \ \cdot W_0^{Left} \cdot \frac{\mathrm{d}I(P_0^{Left}, \ \cdots \ , P_{n-1}^{Left}, P_n^{Left})}{\mathrm{d}i} + \\
& W_n^{Right} \cdot W_{n-1}^{Left} \cdot \ \cdots \ \cdot W_0^{Left} \cdot \frac{\mathrm{d}I(P_0^{Left}, \ \cdots \ , P_{n-1}^{Left}, P_n^{Right})}{\mathrm{d}i} + \\
& W_n^{Left} \cdot W_{n-1}^{Right} \cdot \ \cdots \ \cdot W_0^{Left} \cdot \frac{\mathrm{d}I(P_0^{Left}, \ \cdots \ , P_{n-1}^{Right}, P_n^{Left})}{\mathrm{d}i} + \\
& W_n^{Right} \cdot W_{n-1}^{Right} \cdot \ \cdots \ \cdot W_0^{Left} \cdot \frac{\mathrm{d}I(P_0^{Left}, \ \cdots \ , P_{n-1}^{Right}, P_n^{Right})}{\mathrm{d}i} + \\
& \cdots \\
& W_n^{Left} \cdot W_{n-1}^{Left} \cdot \ \cdots \ \cdot W_0^{Right} \cdot \frac{\mathrm{d}I(P_0^{Right}, \ \cdots \ , P_{n-1}^{Left}, P_n^{Left})}{\mathrm{d}i} + \\
& W_n^{Right} \cdot W_{n-1}^{Left} \cdot \ \cdots \ \cdot W_0^{Right} \cdot \frac{\mathrm{d}I(P_0^{Right}, \ \cdots \ , P_{n-1}^{Left}, P_n^{Right})}{\mathrm{d}i} + \\
& W_n^{Left} \cdot W_{n-1}^{Right} \cdot \ \cdots \ \cdot W_0^{Right} \cdot \frac{\mathrm{d}I(P_0^{Right}, \ \cdots \ , P_{n-1}^{Right}, P_n^{Left})}{\mathrm{d}i} + \\
& W_n^{Right} \cdot W_{n-1}^{Right} \cdot \ \cdots \ \cdot W_0^{Right} \cdot \frac{\mathrm{d}I(P_0^{Right}, \ \cdots \ , P_{n-1}^{Right}, P_n^{Right})}{\mathrm{d}i}
\end{aligned}
\tag{A.8}
$$

Note that W_i is not part of the product of the weights because it is not part of the gradient formula for a single grid point, see Equation (A.7).

An exemplary five dimensional *Linear Table* can be seen in Figure A.2. It was filled using the following equation:

$$
M(x, y, z, k, l) = x^2 + y^3 + z^4 + k^2 l^2
\tag{A.9}
$$

To reduce the complexity of the example, only the k variable is changed. As expected the behaviour of the function is quadratic. The total gradients behave like the partial gradients $\frac{\partial M}{\partial k}$.

A.3. Dimensions

Each dimension i of a *Linear Table* is defined by the following attributes:

- Number of bins b_i

- Minimum value Min_{x_i}

- Maximum value Max_{x_i}

- Bin distance $d_i(\chi_i)$ for a given grid coordinate χ_i

- Behaviour of the *Linear Table* at the edges of the domain

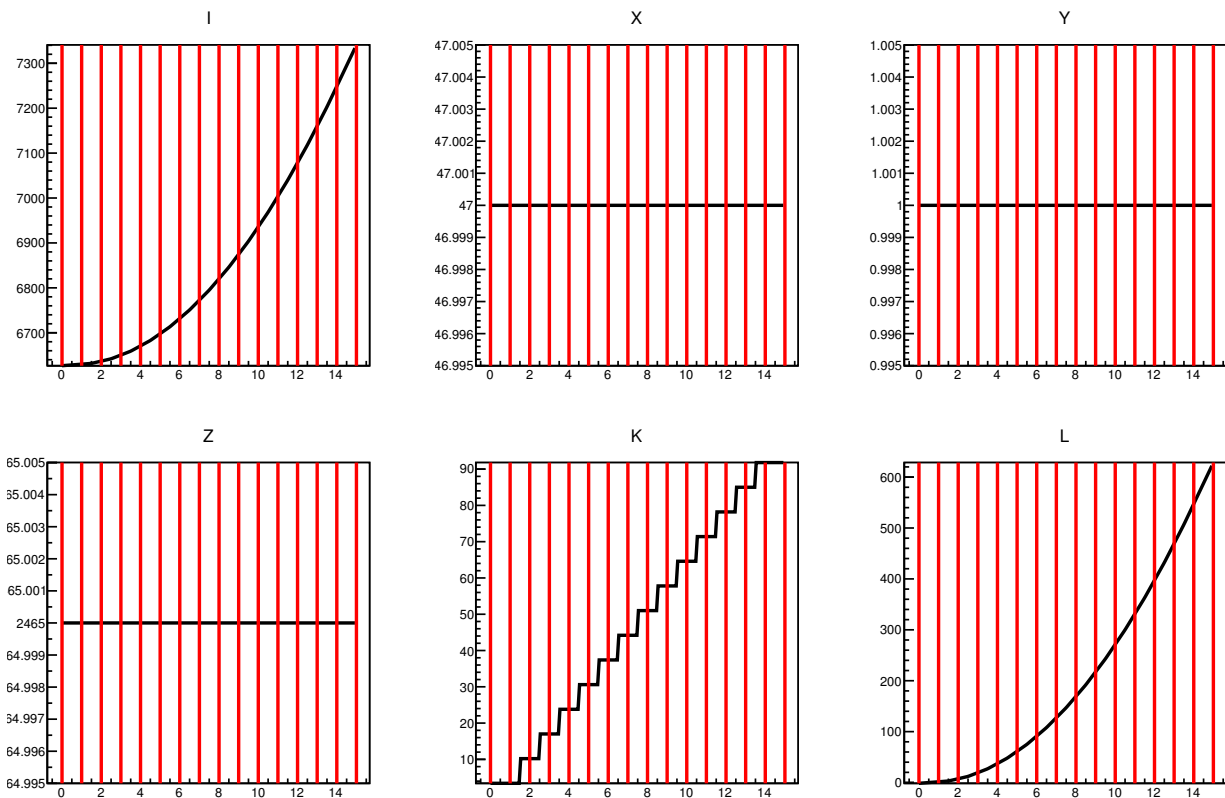- Symmetry of the dimension, i.e. axially symmetric around zero or not

Figure A.2.: *Example of interpolated values and corresponding gradients for a five dimensional* Linear Table *filled using Equation* (A.9)*. Only the value of the fourth dimension is changed while the others are fixed. The red lines are the positions of the grid points in the fourth dimension. The interpolated values and gradients behave as expected.*

While the first three attributes are self explanatory, the other require some further explanation. A dimension can either use equally spaced bins, a so called *Linear Dimension*, i.e. the bin distance d_i is the same for all the bins in the dimension i or the bin distance is arbitrary and needs to be stored separately, a so called *Non-Linear Dimension*. The latter is more computing intensive because next to the coordinate transformation also the bin distance has to be calculated every time an interpolated value is accessed. Therefore, using *Non-Linear Dimensions* should be avoided as much as possible.

For the behaviour of a dimension at the edge of its domain the following options are available:

Zero Interpolated value and gradient are zero outside of the domain of the *Linear Table*.

Constant The value of the last bin is returned as the interpolated value. For the interpolated gradient the gradient of the last *Bin Pair* is used.

Extrapolate The gradient together with the bin distance of the last *Bin Pair* is used to extrapolate the value at the requested position outside of the domain of the *Linear Table*. As the gradient, the one of the last *Bin Pair* is used.

The different behaviours can be seen in Figure A.3; a smaller *Linear Table* is added to a bigger *Linear Table* to show the different behaviours at the edges of the smaller *Linear Table*.
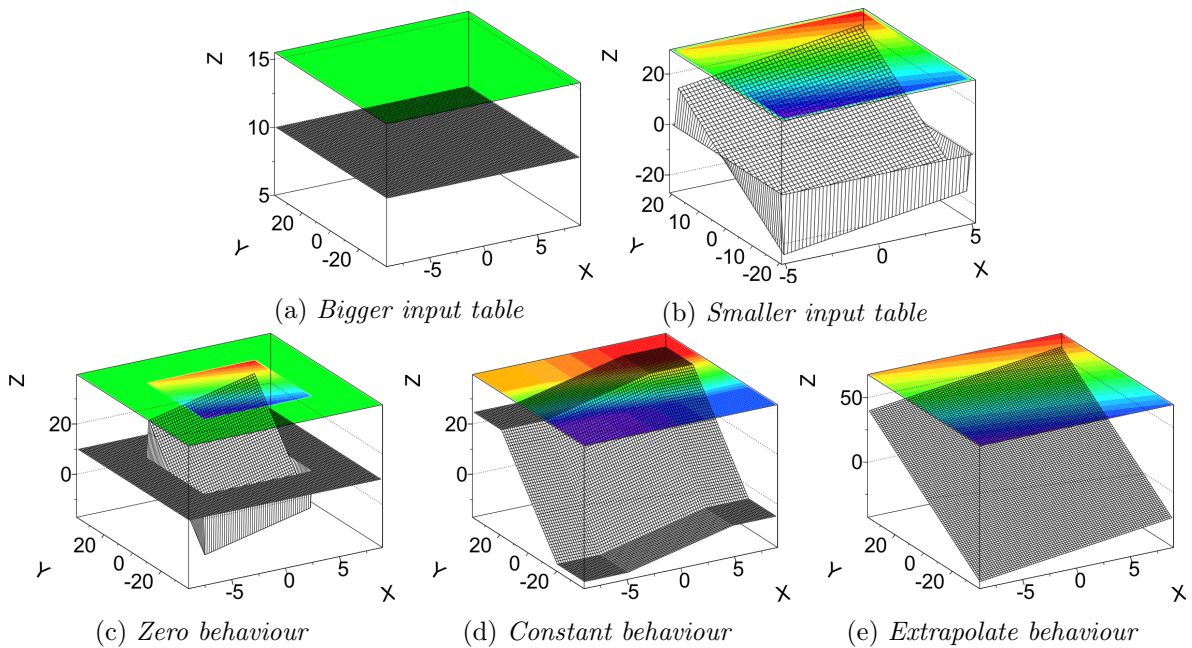
(a) *Bigger input table* (b) *Smaller input table*

(c) *Zero behaviour* (d) *Constant behaviour* (e) *Extrapolate behaviour*

Figure A.3.: *Example* Linear Tables *to show the different behaviours at the edges of a dimension. The two input tables are shown in the upper row with the left one being significantly bigger than the right one. In the lower row the three possibilities for different behaviour are plotted. The resulting images look as expected, i.e. zero, constant and extrapolating.*

A dimension can be axial symmetric around zero. As a result only the positive part of the *Linear Table* has to be stored, therefore disk and memory space are saved. The symmetry is taken care of during the coordinate transformation $T(\vec{x})$ where the sign of the gradient has to be inverted in the negative part of the *Linear Table*.

The behaviour, the symmetry and the choice of the bin distances used (linear or non-linear), can be freely combined in any possible way for any dimension. For example a two dimensional *Linear Table* with a *Linear Dimension* in the first and a *Non-Linear Dimension* in the second, is possible. In addition both dimensions can have a different behaviour at the edges of their respective domain and one can be axially symmetric while the other is not.

A.4. Features

A *Linear Table* can store arbitrary data types. During this work the primitive data type *double* was chosen for increased precision. Moreover, it is also possible to create *Linear Tables* of *Linear Tables*, i.e. the ability to save different sized *Linear Tables* at specific grid points of the outer *Linear Table*. For example, the *Linear Table* shown in Figure A.2 is effectively a three dimensional *Linear Table* of two dimensional *Linear Tables*. This flexibility is used to further save disk and memory space. Note that the base data type of all *Linear Tables* has to be the same though. The *Linear Tables* can be combined at arbitrary depth, i.e. *Linear Tables* of *Linear Tables* of *Linear Tables* and so on.

For ease of use, the four basic arithmetic operations, addition, subtraction, multiplication and division are supported by *Linear Tables* as long as either the base data type or a *Linear Table* of the same type and dimension is used.

In addition to the arithmetic capabilities of a *Linear Table*, it is also possible to create projections of a

Linear Table for a given dimension in a certain bin range. This can be used to create either slices or *Linear Tables* with an reduced amount of dimensions in an easy and generic way.

Another feature of the *Linear Table* is, that they can be smoothed in a given bin range r_i for each dimension i using one of the three implemented smoothing kernels. All kernels add the value of the bin they are applied on to all bins in a hypercube around the current one with an extension of $\pm r_i$ in each dimension and a custom weighting factor (this is not the weighting factor introduced in Appendix A.1). The different smoothing options are:

Constant A fixed weighting of 1 is used.

Linear A linearly decreasing weight from 1 at the center of the hypercube to 0 at its edges is applied to the current value of the bin.

Gaussian A Gaussian centered at the current bin with a $99.9\,\%$ containment radius equal to r_i is used to determine the weighting factor.

During the smoothing operation the total integral of the *Linear Table* is preserved and no content is lost at the edges of the *Linear Table*.

Moreover, a dedicated plotting framework for *Linear Tables* with one, two or three dimensions has been written using the ROOT plotting facilities of *TH1*, *TH2* and *TH3* histrograms. All plots like Figure A.2 or Figure A.3 of *Linear Tables* have been created using this framework in a generic way.

A.5. Implementation

The *Linear Tables* make full use of the object-orientated approach of the C++ language. They are implemented in a generic way using C++ templates [218] and BOOST *multi-arrays* [190] and can therefore store different data types, even other *Linear Tables*, see Appendix A.4. There is only one generic n dimensional implementation of a *Linear Table* class and one generic n dimensional implementation of a *Linear Table* of *Linear Tables*. They share a common base class to avoid code duplication where possible. The *GoogleTest* unit test framework [219] is used for almost $100\,\%$ code coverage with unit tests to ensure proper functionality of the *Linear Tables*.

Bibliography

[1]   Victor Francis Hess. *Beobachtungen der durchdringenden Strahlung bei sieben Freiballonfahrten.* Kaiserlich-Königlichen Hof-und Staatsdruckerei, in Kommission bei Alfred Hölder, 1912.

[2]   C. D. Anderson. „The Apparent Existence of Easily Deflectable Positives". In: *Science* 76 (Sept. 1932), pp. 238–239. DOI: 10.1126/science.76.1967.238.

[3]   C. D. Anderson and S. H. Neddermeyer. „Cloud Chamber Observations of Cosmic Rays at 4300 Meters Elevation and Near Sea-Level". In: *Physical Review* 50 (Aug. 1936), pp. 263–271. DOI: 10.1103/PhysRev.50.263.

[4]   C. M. G. Lattes, G. P. S. Occhialini, and C. F. Powell. „Observations on the Tracks of Slow Mesons in Photographic Emulsions". In: *Nature* 160 (Oct. 1947), pp. 453–456. DOI: 10.1038/160453a0.

[5]   G. D. Rochester and C. C. Butler. „Evidence for the Existence of New Unstable Elementary Particles". In: *Nature* 160 (Dec. 1947), pp. 855–857. DOI: 10.1038/160855a0.

[6]   Wikipedia. *Victor Francis Hess — Wikipedia, The Free Encyclopedia.* [Online; accessed 16-February-2014]. 2014. URL: http://en.wikipedia.org/w/index.php?title=Victor_Francis_Hess&oldid=595556296.

[7]   A. M. Hillas. „Cosmic Rays: Recent Progress and some Current Questions". In: *ArXiv Astrophysics e-prints* (July 2006). eprint: astro-ph/0607109.

[8]   Pierre Auger Collaboration et al. „Correlation of the Highest-Energy Cosmic Rays with Nearby Extragalactic Objects". In: *Science* 318 (Nov. 2007), pp. 938–. DOI: 10.1126/science.1151124. arXiv: 0711.2256.

[9]   W. Galbraith and J. V. Jelley. „Light Pulses from the Night Sky associated with Cosmic Rays". In: *Nature* 171 (Feb. 1953), pp. 349–350. DOI: 10.1038/171349a0.

[10] L. Thompson. *The discovery of air-Cherenkov radiation.* [Online; accessed 16-February-2014]. 2012. URL: http://cerncourier.com/cws/article/cern/50222.

[11] F. Aharonian et al. „Observations of the Crab nebula with HESS". In: *A&A* 457 (Oct. 2006), pp. 899–915. DOI: 10.1051/0004-6361:20065351. eprint: astro-ph/0607333.

[12] D. Ferenc and MAGIC Collaboration. „The MAGIC gamma-ray observatory". In: *Nuclear Instruments and Methods in Physics Research A* 553 (Nov. 2005), pp. 274–281. DOI: 10.1016/j.nima.2005.08.085.

[13] J. Aleksić et al. „Performance of the MAGIC stereo system obtained with Crab Nebula data". In: *Astroparticle Physics* 35 (Feb. 2012), pp. 435–448. DOI: 10.1016/j.astropartphys.2011.11.007. arXiv: 1108.1477 [astro-ph.IM].

[14] T. C. Weekes et al. „VERITAS: the Very Energetic Radiation Imaging Telescope Array System". In: *Astroparticle Physics* 17 (May 2002), pp. 221–243. DOI: 10.1016/S0927-6505(01)00152-9. eprint: astro-ph/0108478.

[15] M. Actis et al. „Design concepts for the Cherenkov Telescope Array CTA: an advanced facility for ground-based high-energy gamma-ray astronomy". In: *Experimental Astronomy* 32 (Dec. 2011), pp. 193–316. DOI: 10.1007/s10686-011-9247-0. arXiv: 1008.3703 [astro-ph.IM].

[16] S. P. Wakely and D. Horan. „TeVCat: An online catalog for Very High Energy Gamma-Ray Astronomy". In: *International Cosmic Ray Conference* 3 (2008), pp. 1341–1344.

[17] S. P. Wakely and D. Horan. *TeVCat: An online catalog for Very High Energy Gamma-Ray Astronomy*. [Online; accessed 16-February-2014]. 2014. URL: http://tevcat.uchicago.edu.

[18] Markus Holler. „Single-Telescope Reconstruction for the H.E.S.S. II Array using a Semi-Analytical Shower Model and its Application to the Crab Nebula and the Galactic Centre Region". Dissertation. 2014.

[19] R. Buehler and R. Blandford. „The Crab pulsar wind nebula: our laboratory of the non-thermal Universe". In: *ArXiv e-prints* (Sept. 2013). arXiv: 1309.7046 [astro-ph.HE].

[20] J. J. Hester. „The Crab Nebula: An Astrophysical Chimera". In: *ARA&A* 46 (Sept. 2008), pp. 127–155. DOI: 10.1146/annurev.astro.45.051806.110608.

[21] B. M. Gaensler and P. O. Slane. „The Evolution and Structure of Pulsar Wind Nebulae". In: *ARA&A* 44 (Sept. 2006), pp. 17–47. DOI: 10.1146/annurev.astro.44.051905.092528. eprint: astro-ph/0601081.

[22] M. Meyer, D. Horns, and H.-S. Zechlin. „The Crab Nebula as a standard candle in very high-energy astrophysics". In: *A&A* 523, A2 (Nov. 2010), A2. DOI: 10.1051/0004-6361/201014108. arXiv: 1008.4524 [astro-ph.HE].

[23] R. A. Chevalier. „Was SN 1054 A Type II Supernova?" In: *Supernovae*. Ed. by D. N. Schramm. Vol. 66. Astrophysics and Space Science Library. 1977, p. 53.

[24] D. H. Clark and F. R. Stephenson. *The historical supernovae*. 1977.

[25] V. Trimble. „The Distance to the Crab Nebula and NP 0532". In: *PASP* 85 (Oct. 1973), p. 579. DOI: 10.1086/129507.

[26] J. J. L. Duyvendak. „Further Data Bearing on the Identification of the Crab Nebula with the Supernova of 1054 A.D. Part I. The Ancient Oriental Chronicles". In: *PASP* 54 (Apr. 1942), pp. 91–94. DOI: 10.1086/125409.

[27] N. U. Mayall and J. H. Oort. „Further Data Bearing on the Identification of the Crab Nebula with the Supernova of 1054 A.D. Part II. The Astronomical Aspects". In: *PASP* 54 (Apr. 1942), pp. 95–104. DOI: 10.1086/125410.

[28] R. A. Fesen, J. M. Shull, and A. P. Hurford. „An Optical Study of the Circumstellar Environment Around the Crab Nebula". In: *AJ* 113 (Jan. 1997), pp. 354–363. DOI: 10.1086/118258.

[29] D. H. Clark et al. „Three-dimensional structure of the Crab Nebula". In: *MNRAS* 204 (July 1983), pp. 415–431.

[30] D. A. Frail, N. E. Kassim, T. J. Cornwell, and W. M. Goss. „Does the Crab Have a Shell?" In: *ApJ* 454 (Dec. 1995), p. L129. DOI: 10.1086/309794. eprint: astro-ph/9509135.

[31] D. H. Staelin and E. C. Reifenstein III. „Pulsating Radio Sources near the Crab Nebula". In: *Science* 162 (Dec. 1968), pp. 1481–1483. DOI: 10.1126/science.162.3861.1481.

[32] W. J. Cocke, M. J. Disney, and D. J. Taylor. „Discovery of Optical Signals from Pulsar NP 0532". In: *Nature* 221 (Feb. 1969), pp. 525–527. DOI: 10.1038/221525a0.

[33] R. N. Manchester, G. B. Hobbs, A. Teoh, and M. Hobbs. „The Australia Telescope National Facility Pulsar Catalogue". In: *AJ* 129 (Apr. 2005), pp. 1993–2006. DOI: 10.1086/428488. eprint: astro-ph/0412641.

[34] A. A. Abdo et al. „The Second Fermi Large Area Telescope Catalog of Gamma-Ray Pulsars". In: *ApJS* 208, 17 (Oct. 2013), p. 17. DOI: 10.1088/0067-0049/208/2/17. arXiv: 1305.4385 [astro-ph.HE].

[35] R. N. Manchester and J. H. Taylor. *Pulsars*. 1977, p. 36.

[36] A. G. Lyne, R. S. Pritchard, and F. G. Smith. „Crab pulsar timing 1982-87". In: *MNRAS* 233 (Aug. 1988), pp. 667–676.

[37] M. Bejger and P. Haensel. „Accelerated expansion of the Crab Nebula and evaluation of its neutron-star parameters". In: *A&A* 405 (July 2003), pp. 747–751. DOI: 10.1051/0004-6361:20030642. eprint: astro-ph/0301071.

[38] VERITAS Collaboration et al. „Detection of Pulsed Gamma Rays Above 100 GeV from the Crab Pulsar". In: *Science* 334 (Oct. 2011), pp. 69–. DOI: 10.1126/science.1208192. arXiv: 1108.3797 [astro-ph.HE].

[39] J. Aleksić et al. „Observations of the Crab Pulsar between 25 and 100 GeV with the MAGIC I Telescope". In: *ApJ* 742, 43 (Nov. 2011), p. 43. DOI: 10.1088/0004-637X/742/1/43. arXiv: 1108.5391 [astro-ph.HE].

[40] J. Aleksić et al. „Phase-resolved energy spectra of the Crab pulsar in the range of 50-400 GeV measured with the MAGIC telescopes". In: *A&A* 540, A69 (Apr. 2012), A69. DOI: 10.1051/0004-6361/201118166. arXiv: 1109.6124 [astro-ph.HE].

[41] S. C. Lundgren et al. „Giant Pulses from the Crab Pulsar: A Joint Radio and Gamma-Ray Study". In: *ApJ* 453 (Nov. 1995), p. 433. DOI: 10.1086/176404.

[42] J. M. Cordes et al. „The Brightest Pulses in the Universe: Multifrequency Observations of the Crab Pulsar's Giant Pulses". In: *ApJ* 612 (Sept. 2004), pp. 375–388. DOI: 10.1086/422495. eprint: astro-ph/0304495.

[43] M. V. Popov and B. Stappers. „Statistical properties of giant pulses from the Crab pulsar". In: *A&A* 470 (Aug. 2007), pp. 1003–1007. DOI: 10.1051/0004-6361:20066589. arXiv: 0704.1197.

[44] A. Shearer et al. „Enhanced Optical Emission During Crab Giant Radio Pulses". In: *Science* 301 (July 2003), pp. 493–495. DOI: 10.1126/science.1084919. eprint: astro-ph/0308271.

[45] M. J. Strader et al. „Excess Optical Enhancement Observed with ARCONS for Early Crab Giant Pulses". In: *ApJ* 779, L12 (Dec. 2013), p. L12. DOI: 10.1088/2041-8205/779/1/L12. arXiv: 1309.3270 [astro-ph.HE].

[46] A. V. Bilous et al. „Correlation of Fermi Photons with High-frequency Radio Giant Pulses from the Crab Pulsar". In: *ApJ* 728, 110 (Feb. 2011), p. 110. DOI: 10.1088/0004-637X/728/2/110. arXiv: 1101.1434 [astro-ph.GA].

[47] A. V. Bilous, M. A. McLaughlin, V. I. Kondratiev, and S. M. Ransom. „Correlation of Chandra Photons with the Radio Giant Pulses from the Crab Pulsar". In: *ApJ* 749, 24 (Apr. 2012), p. 24. DOI: 10.1088/0004-637X/749/1/24. arXiv: 1201.6484 [astro-ph.GA].

[48] E. Aliu et al. „Search for a Correlation between Very-high-energy Gamma Rays and Giant Radio Pulses in the Crab Pulsar". In: *ApJ* 760, 136 (Dec. 2012), p. 136. DOI: 10.1088/0004-637X/760/2/136. arXiv: 1210.4786 [astro-ph.HE].

[49] A. G. Lyne, R. S. Pritchard, and F. Graham-Smith. „Twenty-Three Years of Crab Pulsar Rotational History". In: *MNRAS* 265 (Dec. 1993), p. 1003.

[50] C. M. Espinoza, A. G. Lyne, B. W. Stappers, and M. Kramer. „A study of 315 glitches in the rotation of 102 pulsars". In: *MNRAS* 414 (June 2011), pp. 1679–1704. DOI: 10.1111/j.1365-2966.2011.18503.x. arXiv: 1102.1743 [astro-ph.HE].

[51] A. Słowikowska, G. Kanbach, M. Kramer, and A. Stefanescu. „Optical polarization of the Crab pulsar: precision measurements and comparison to the radio emission". In: *MNRAS* 397 (July 2009), pp. 103–123. DOI: 10.1111/j.1365-2966.2009.14935.x. arXiv: 0901.4559 [astro-ph.SR].

[52] P. Moran et al. „Optical polarimetry of the inner Crab nebula and pulsar". In: *MNRAS* 433 (Aug. 2013), pp. 2564–2575. DOI: 10.1093/mnras/stt931. arXiv: 1305.6824 [astro-ph.HE].

[53] S. S. Lawrence et al. „Three-Dimensional Fabry-Perot Imaging Spectroscopy of the Crab Nebula, Cassiopeia A, and Nova GK Persei". In: *AJ* 109 (June 1995), p. 2635. DOI: 10.1086/117477.

[54] A. M. Loll, J. J. Hester, W. P. Blair, and R. Sankrit. „A Northwest-Southeast Asymmetry in the Structure of the Crab Nebula". In: *American Astronomical Society Meeting Abstracts*. Vol. 39. Bulletin of the American Astronomical Society. Dec. 2007, p. 100.25.

[55] J. J. Hester et al. „Hubble Space Telescope and Chandra Monitoring of the Crab Synchrotron Nebula". In: *ApJ* 577 (Sept. 2002), pp. L49–L52. DOI: 10.1086/344132.

[56] A. Melatos et al. „Near-Infrared, Kilosecond Variability of the Wisps and Jet in the Crab Pulsar Wind Nebula". In: *ApJ* 633 (Nov. 2005), pp. 931–940. DOI: 10.1086/468176. eprint: astro-ph/0509914.

[57] M. P. Veron-Cetty and L. Woltjer. „Spectrophotometry of the continuum in the Crab Nebula". In: *A&A* 270 (Mar. 1993), pp. 370–378.

[58] T. Temim et al. „Spitzer Space Telescope Infrared Imaging and Spectroscopy of the Crab Nebula". In: *AJ* 132 (Oct. 2006), pp. 1610–1623. DOI: 10.1086/507076. eprint: astro-ph/0606321.

[59] K. Mori et al. „Spatial Variation of the X-Ray Spectrum of the Crab Nebula". In: *ApJ* 609 (July 2004), pp. 186–193. DOI: 10.1086/421011. eprint: astro-ph/0403287.

[60] A. Tziamtzis, P. Lundqvist, and A. A. Djupvik. „The Crab pulsar and its pulsar-wind nebula in the optical and infrared". In: *A&A* 508 (Dec. 2009), pp. 221–228. DOI: 10.1051/0004-6361/200912031. arXiv: 0911.0608 [astro-ph.HE].

[61] C.-Y. Ng and R. W. Romani. „Fitting Pulsar Wind Tori". In: *ApJ* 601 (Jan. 2004), pp. 479–484. DOI: 10.1086/380486. eprint: astro-ph/0310155.

[62] A. K. Harding, J. V. Stern, J. Dyks, and M. Frackowiak. „High-Altitude Emission from Pulsar Slot Gaps: The Crab Pulsar". In: *ApJ* 680 (June 2008), pp. 1378–1393. DOI: 10.1086/588037. arXiv: 0803.0699.

[63] Y. J. Du et al. „The annular gap model for γ-ray emission from young and millisecond pulsars". In: *MNRAS* 406 (Aug. 2010), pp. 2671–2677. DOI: 10.1111/j.1365-2966.2010.16870.x. arXiv: 1004.3213 [astro-ph.HE].

[64] A. J. Deutsch. „The electromagnetic field of an idealized star in rigid rotation in vacuo". In: *Annales d'Astrophysique* 18 (Jan. 1955), p. 1.

[65] P. Goldreich and W. H. Julian. „Pulsar Electrodynamics". In: *ApJ* 157 (Aug. 1969), p. 869. DOI: 10.1086/150119.

[66] R. D. Blandford. „To the Lighthouse". In: *Lighthouses of the Universe: The Most Luminous Celestial Objects and Their Use for Cosmology*. Ed. by M. Gilfanov, R. Sunyeav, and E. Churazov. 2002, p. 381. DOI: 10.1007/10856495_59. eprint: astro-ph/0202265.

[67] J. Li, A. Spitkovsky, and A. Tchekhovskoy. „Resistive Solutions for Pulsar Magnetospheres". In: *ApJ* 746, 60 (Feb. 2012), p. 60. DOI: 10.1088/0004-637X/746/1/60. arXiv: 1107.0979 [astro-ph.HE].

[68] P. A. Sturrock. „A Model of Pulsars". In: *ApJ* 164 (Mar. 1971), p. 529. DOI: 10.1086/150865.

[69] M. A. Ruderman and P. G. Sutherland. „Theory of pulsars - Polar caps, sparks, and coherent microwave radiation". In: *ApJ* 196 (Feb. 1975), pp. 51–72. DOI: 10.1086/153393.

[70] J. K. Daugherty and A. K. Harding. „Electromagnetic cascades in pulsars". In: *ApJ* 252 (Jan. 1982), pp. 337–347. DOI: 10.1086/159561.

[71] M. G. Baring. „High-energy emission from pulsars: the polar cap scenario". In: *Advances in Space Research* 33 (2004), pp. 552–560. DOI: 10.1016/j.asr.2003.08.020. eprint: astro-ph/0308296.

[72] A. Cheng, M. Ruderman, and P. Sutherland. „Current flow in pulsar magnetospheres". In: *ApJ* 203 (Jan. 1976), pp. 209–212. DOI: 10.1086/154068.

[73] K. S. Cheng, C. Ho, and M. Ruderman. „Energetic radiation from rapidly spinning pulsars. I - Outer magnetosphere gaps. II - VELA and Crab". In: *ApJ* 300 (Jan. 1986), pp. 500–539. DOI: 10.1086/163829.

[74] R. W. Romani and I.-A. Yadigaroglu. „Gamma-ray pulsars: Emission zones and viewing geometries". In: *ApJ* 438 (Jan. 1995), pp. 314–321. DOI: 10.1086/175076. eprint: astro-ph/9401045.

[75] K. S. Cheng. „High-energy radiation from pulsars: a three-dimensional model approach". In: *Advances in Space Research* 33 (2004), pp. 561–570. DOI: 10.1016/j.asr.2003.04.020. eprint: astro-ph/0308223.

[76] R. L. Ingraham. „Algorithm for Solving the Nonlinear Pulsar Equation". In: *ApJ* 186 (Dec. 1973), pp. 625–630. DOI: 10.1086/152530.

[77] F. C. Michel. „Rotating Magnetosphere: Acceleration of Plasma from the Surface". In: *ApJ* 192 (Sept. 1974), pp. 713–718. DOI: 10.1086/153109.

[78] Y. E. Lyubarsky. „The termination shock in a striped pulsar wind". In: *MNRAS* 345 (Oct. 2003), pp. 153–160. DOI: 10.1046/j.1365-8711.2003.06927.x. eprint: astro-ph/0306435.

[79] L. Sironi and A. Spitkovsky. „Particle Acceleration in Relativistic Magnetized Collisionless Electron-Ion Shocks". In: *ApJ* 726, 75 (Jan. 2011), p. 75. DOI: 10.1088/0004-637X/726/2/75. arXiv: 1009.0024 [astro-ph.HE].

[80] Y. Mizuno, Y. Lyubarsky, K.-I. Nishikawa, and P. E. Hardee. „Three-dimensional Relativistic Magnetohydrodynamic Simulations of Current-driven Instability. II. Relaxation of Pulsar Wind Nebula". In: *ApJ* 728, 90 (Feb. 2011), p. 90. DOI: 10.1088/0004-637X/728/2/90. arXiv: 1012.2770 [astro-ph.HE].

[81] O. Porth, S. S. Komissarov, and R. Keppens. „Solution to the sigma problem of pulsar wind nebulae". In: *MNRAS* 431 (Apr. 2013), pp. L48–L52. DOI: 10.1093/mnrasl/slt006. arXiv: 1212.1382 [astro-ph.HE].

[82] N. F. Camus, S. S. Komissarov, N. Bucciantini, and P. A. Hughes. „Observations of 'wisps' in magnetohydrodynamic simulations of the Crab Nebula". In: *MNRAS* 400 (Dec. 2009), pp. 1241–1246. DOI: 10.1111/j.1365-2966.2009.15550.x. arXiv: 0907.3647 [astro-ph.HE].

[83] M. Lyutikov. „A high-sigma model of pulsar wind nebulae". In: *MNRAS* 405 (July 2010), pp. 1809–1815. DOI: 10.1111/j.1365-2966.2010.16553.x. arXiv: 0911.0324 [astro-ph.HE].

[84] A. M. Atoyan and F. A. Aharonian. „On the mechanisms of gamma radiation in the Crab Nebula". In: *MNRAS* 278 (Jan. 1996), pp. 525–541.

[85] D. Volpi, L. Del Zanna, E. Amato, and N. Bucciantini. „Non-thermal emission from relativistic MHD simulations of pulsar wind nebulae: from synchrotron to inverse Compton". In: *A&A* 485 (July 2008), pp. 337–349. DOI: 10.1051/0004-6361:200809424. arXiv: 0804.1323.

[86] L. Sironi and A. Spitkovsky. „Acceleration of Particles at the Termination Shock of a Relativistic Striped Wind". In: *ApJ* 741, 39 (Nov. 2011), p. 39. DOI: 10.1088/0004-637X/741/1/39. arXiv: 1107.0977 [astro-ph.HE].

[87] N. Bucciantini, J. Arons, and E. Amato. „Modelling spectral evolution of pulsar wind nebulae inside supernova remnants". In: *MNRAS* 410 (Jan. 2011), pp. 381–398. DOI: 10.1111/j.1365-2966.2010.17449.x.

[88] R. Buehler et al. „Gamma-Ray Activity in the Crab Nebula: The Exceptional Flare of 2011 April". In: *ApJ* 749, 26 (Apr. 2012), p. 26. DOI: 10.1088/0004-637X/749/1/26. arXiv: 1112.1979 [astro-ph.HE].

[89] A. A. Abdo et al. „Gamma-Ray Flares from the Crab Nebula". In: *Science* 331 (Feb. 2011), pp. 739–. DOI: 10.1126/science.1199705. arXiv: 1011.3855 [astro-ph.HE].

[90] M. Tavani et al. „Discovery of Powerful Gamma-Ray Flares from the Crab Nebula". In: *Science* 331 (Feb. 2011), pp. 736–. DOI: 10.1126/science.1200083. arXiv: 1101.2311 [astro-ph.HE].

[91] M. Balbo, R. Walter, C. Ferrigno, and P. Bordas. „Twelve-hour spikes from the Crab Pevatron". In: *A&A* 527, L4 (Mar. 2011), p. L4. DOI: 10.1051/0004-6361/201015980. arXiv: 1012.3397 [astro-ph.HE].

[92]   M. Ackermann et al. „The Fermi All-sky Variability Analysis: A List of Flaring Gamma-Ray Sources and the Search for Transients in Our Galaxy“. In: *ApJ* 771, 57 (July 2013), p. 57. DOI: 10.1088/0004-637X/771/1/57. arXiv: 1304.6082 [astro-ph.HE].

[93]   R. Ojha, R. Buehler, E. Hays, and M. Dutka. „Fermi LAT detection of enhanced gamma-ray emission from the Crab Nebula region“. In: *The Astronomer's Telegram* 4239 (July 2012), p. 1.

[94]   E. Striani et al. „Variable Gamma-Ray Emission from the Crab Nebula: Short Flares and Long "Waves"“. In: *ApJ* 765, 52 (Mar. 2013), p. 52. DOI: 10.1088/0004-637X/765/1/52. arXiv: 1302.4342 [astro-ph.HE].

[95]   M. Mayer et al. „Rapid Gamma-Ray Flux Variability during the 2013 March Crab Nebula Flare“. In: *ApJ* 775, L37 (Oct. 2013), p. L37. DOI: 10.1088/2041-8205/775/2/L37. arXiv: 1308.6698 [astro-ph.HE].

[96]   V. Vittorini et al. „Spectral Evolution of the 2010 September Gamma-ray Flare from the Crab Nebula“. In: *ApJ* 732, L22 (May 2011), p. L22. DOI: 10.1088/2041-8205/732/2/L22. arXiv: 1104.0115 [astro-ph.HE].

[97]   M. Morii et al. „MAXI GSC Monitoring of the Crab Nebula and Pulsar during the GeV Gamma-Ray Flare in 2010 September“. In: *PASJ* 63 (Nov. 2011), p. 821.

[98]   A. P. Lobanov, D. Horns, and T. W. B. Muxlow. „VLBI imaging of a flare in the Crab nebula: more than just a spot“. In: *A&A* 533, A10 (Sept. 2011), A10. DOI: 10.1051/0004-6361/201117082. arXiv: 1107.0182 [astro-ph.HE].

[99]   M. C. Weisskopf et al. „Chandra, Keck, and VLA Observations of the Crab Nebula during the 2011-April Gamma-Ray Flare“. In: *ApJ* 765, 56 (Mar. 2013), p. 56. DOI: 10.1088/0004-637X/765/1/56. arXiv: 1211.3997 [astro-ph.HE].

[100]   E. Aliu et al. „A Search for Enhanced Very High Energy Gamma-Ray Emission from the 2013 March Crab Nebula Flare“. In: *ApJ* 781, L11 (Jan. 2014), p. L11. DOI: 10.1088/2041-8205/781/1/L11. arXiv: 1309.5949 [astro-ph.HE].

[101]   H. E. S. S. Collaboration et al. „H.E.S.S. Observations of the Crab during its March 2013 GeV Gamma-Ray Flare“. In: *ArXiv e-prints* (Nov. 2013). arXiv: 1311.3187 [astro-ph.HE].

[102]   B. Bartoli et al. „Enhanced TeV gamma ray flux from the Crab Nebula observed by the ARGO-YBJ experiment“. In: *The Astronomer's Telegram* 4258 (July 2012), p. 1.

[103]   P. W. Guilbert, A. C. Fabian, and M. J. Rees. „Spectral and variability constraints on compact sources“. In: *MNRAS* 205 (Nov. 1983), pp. 593–603.

[104]   D. A. Uzdensky, B. Cerutti, and M. C. Begelman. „Reconnection-powered Linear Accelerator and Gamma-Ray Flares in the Crab Nebula“. In: *ApJ* 737, L40 (Aug. 2011), p. L40. DOI: 10.1088/2041-8205/737/2/L40. arXiv: 1105.0942 [astro-ph.HE].

[105]   D. C. Ellison and G. P. Double. „Diffusive shock acceleration in unmodified relativistic, oblique shocks“. In: *Astroparticle Physics* 22 (Nov. 2004), pp. 323–338. DOI: 10.1016/j.astropartphys.2004.08.005. eprint: astro-ph/0408527.

[106]   L. Sironi, A. Spitkovsky, and J. Arons. „The Maximum Energy of Accelerated Particles in Relativistic Collisionless Shocks“. In: *ApJ* 771, 54 (July 2013), p. 54. DOI: 10.1088/0004-637X/771/1/54. arXiv: 1301.5333 [astro-ph.HE].

[107]   E. Amato and J. Arons. „Heating and Nonthermal Particle Acceleration in Relativistic, Transverse Magnetosonic Shock Waves in Proton-Electron-Positron Plasmas“. In: *ApJ* 653 (Dec. 2006), pp. 325–338. DOI: 10.1086/508050. eprint: astro-ph/0609034.

[108]   B. Cerutti, G. R. Werner, D. A. Uzdensky, and M. C. Begelman. „Simulations of Particle Acceleration beyond the Classical Synchrotron Burnoff Limit in Magnetic Reconnection: An Explanation of the Crab Flares“. In: *ApJ* 770, 147 (June 2013), p. 147. DOI: 10.1088/0004-637X/770/2/147. arXiv: 1302.6247 [astro-ph.HE].

[109] H. Baty, J. Petri, and S. Zenitani. „Explosive reconnection of double tearing modes in relativistic plasmas: application to the Crab flares". In: *MNRAS* 436 (Nov. 2013), pp. L20–L24. DOI: `10.1093/mnrasl/slt104`. arXiv: `1308.0906 [astro-ph.HE]`.

[110] E. G. Zweibel and M. Yamada. „Magnetic Reconnection in Astrophysical and Laboratory Plasmas". In: *ARA&A* 47 (Sept. 2009), pp. 291–332. DOI: `10.1146/annurev-astro-082708-101726`.

[111] B. Cerutti, D. A. Uzdensky, and M. C. Begelman. „Extreme Particle Acceleration in Magnetic Reconnection Layers: Application to the Gamma-Ray Flares in the Crab Nebula". In: *ApJ* 746, 148 (Feb. 2012), p. 148. DOI: `10.1088/0004-637X/746/2/148`. arXiv: `1110.0557 [astro-ph.HE]`.

[112] P. Sturrock and M. J. Aschwanden. „Flares in the Crab Nebula Driven by Untwisting Magnetic Fields". In: *ApJ* 751, L32 (June 2012), p. L32. DOI: `10.1088/2041-8205/751/2/L32`. arXiv: `1205.0039 [astro-ph.HE]`.

[113] W. Bednarek and W. Idec. „On the variability of the GeV and multi-TeV gamma-ray emission from the Crab nebula". In: *MNRAS* 414 (July 2011), pp. 2229–2234. DOI: `10.1111/j.1365-2966.2011.18539.x`. arXiv: `1011.4176 [astro-ph.HE]`.

[114] M. Lyutikov, N. Otte, and A. McCann. „The Very High Energy Emission from Pulsars: A Case for Inverse Compton Scattering". In: *ApJ* 754, 33 (July 2012), p. 33. DOI: `10.1088/0004-637X/754/1/33`. arXiv: `1108.3824 [astro-ph.HE]`.

[115] A. M. Bykov, G. G. Pavlov, A. V. Artemyev, and Y. A. Uvarov. „Twinkling pulsar wind nebulae in the synchrotron cut-off regime and the γ-ray flares in the Crab Nebula". In: *MNRAS* 421 (Mar. 2012), pp. L67–L71. DOI: `10.1111/j.1745-3933.2011.01208.x`. arXiv: `1112.3114 [astro-ph.HE]`.

[116] S. S. Komissarov and M. Lyutikov. „On the origin of variable gamma-ray emission from the Crab nebula". In: *MNRAS* 414 (July 2011), pp. 2017–2028. DOI: `10.1111/j.1365-2966.2011.18516.x`. arXiv: `1011.1800 [astro-ph.HE]`.

[117] Y. E. Lyubarsky. „Highly magnetized region in pulsar wind nebulae and origin of the Crab gamma-ray flares". In: *MNRAS* 427 (Dec. 2012), pp. 1497–1502. DOI: `10.1111/j.1365-2966.2012.22097.x`. arXiv: `1209.1589 [astro-ph.HE]`.

[118] F. Aharonian et al. „The H.E.S.S. Survey of the Inner Galaxy in Very High Energy Gamma Rays". In: *ApJ* 636 (Jan. 2006), pp. 777–797. DOI: `10.1086/498013`. eprint: `astro-ph/0510397`.

[119] F. Aharonian et al. „A low level of extragalactic background light as revealed by γ-rays from blazars". In: *Nature* 440 (Apr. 2006), pp. 1018–1021. DOI: `10.1038/nature04680`. eprint: `astro-ph/0508073`.

[120] F. Aharonian et al. „Energy Spectrum of Cosmic-Ray Electrons at TeV Energies". In: *Physical Review Letters* 101.26, 261104 (Dec. 2008), p. 261104. DOI: `10.1103/PhysRevLett.101.261104`. arXiv: `0811.3894`.

[121] F. Aharonian et al. „Probing the ATIC peak in the cosmic-ray electron spectrum with H.E.S.S." In: *A&A* 508 (Dec. 2009), pp. 561–564. DOI: `10.1051/0004-6361/200913323`. arXiv: `0905.0105 [astro-ph.HE]`.

[122] F. Aharonian et al. „An Exceptional Very High Energy Gamma-Ray Flare of PKS 2155-304". In: *ApJ* 664 (Aug. 2007), pp. L71–L74. DOI: `10.1086/520635`. arXiv: `0706.0797`.

[123] F. Aharonian et al. „Very high energy gamma rays from the direction of Sagittarius A*". In: *A&A* 425 (Oct. 2004), pp. L13–L17. DOI: `10.1051/0004-6361:200400055`. eprint: `astro-ph/0406658`.

[124] F. Aharonian et al. „Discovery of very-high-energy γ-rays from the Galactic Centre ridge". In: *Nature* 439 (Feb. 2006), pp. 695–698. DOI: `10.1038/nature04467`. eprint: `astro-ph/0603021`.

[125] F. A. Aharonian et al. „High-energy particle acceleration in the shell of a supernova remnant". In: *Nature* 432 (Nov. 2004), pp. 75–77. DOI: `10.1038/nature02960`. eprint: `astro-ph/0411533`.

[126] J. Abraham et al. „The fluorescence detector of the Pierre Auger Observatory". In: *Nuclear Instruments and Methods in Physics Research A* 620 (Aug. 2010), pp. 227–251. DOI: `10.1016/j.nima.2010.04.023`.

[127] H. Bridge, H. Courant, and B. Rossi. „Nuclear Interactions of the Decay Products of a Neutral V-Particle". In: *Physical Review* 85 (Jan. 1952), pp. 159–159. DOI: `10.1103/PhysRev.85.159`.

[128] V. Sahakian, F. Aharonian, and A. Akhperjanian. „Cherenkov light in electron-induced air showers". In: *Astroparticle Physics* 25 (May 2006), pp. 233–241. DOI: `10.1016/j.astropartphys.2006.02.003`.

[129] R. Engel, D. Heck, and T. Pierog. „Extensive Air Showers and Hadronic Interactions at High Energy". In: *Annual Review of Nuclear and Particle Science* 61 (Nov. 2011), pp. 467–489. DOI: `10.1146/annurev.nucl.012809.104544`.

[130] J. Matthews. „A Heitler model of extensive air showers". In: *Astroparticle Physics* 22 (Jan. 2005), pp. 387–397. DOI: `10.1016/j.astropartphys.2004.09.003`.

[131] M. de Naurois. „Very High Energy astronomy from H.E.S.S. to CTA. Opening of a new astronomical window on the non-thermal Universe". Habilitation. Laboratoire Leprince-Ringuet, 2012. URL: `http://tel.archives-ouvertes.fr/tel-00687872`.

[132] W. Heitler. *Quantum theory of radiation.* 1954.

[133] J. F. Carlson and J. R. Oppenheimer. „On Multiplicative Showers". In: *Physical Review* 51 (Feb. 1937), pp. 220–231. DOI: `10.1103/PhysRev.51.220`.

[134] B. Rossi and K. Greisen. „Cosmic-Ray Theory". In: *Reviews of Modern Physics* 13 (Oct. 1941), pp. 240–309. DOI: `10.1103/RevModPhys.13.240`.

[135] S. Le Bohec et al. „A new analysis method for very high definition imaging atmospheric Cherenkov telescopes as applied to the CAT telescope." In: *Nuclear Instruments and Methods in Physics Research A* 416 (Oct. 1998), pp. 425–437. DOI: `10.1016/S0168-9002(98)00750-5`. eprint: `astro-ph/9804133`.

[136] M. de Naurois and L. Rolland. „A high performance likelihood reconstruction of γ-rays for imaging atmospheric Cherenkov telescopes". In: *Astroparticle Physics* 32 (Dec. 2009), pp. 231–252. DOI: `10.1016/j.astropartphys.2009.09.001`. arXiv: `0907.2610 [astro-ph.IM]`.

[137] D. Heck et al. *CORSIKA: a Monte Carlo code to simulate extensive air showers.* Feb. 1998.

[138] M. P. Kertzman and G. H. Sembroski. „Computer simulation methods for investigating the detection characteristics of TeV air Cherenkov telescopes". In: *Nuclear Instruments and Methods in Physics Research A* 343 (Apr. 1994), pp. 629–643. DOI: `10.1016/0168-9002(94)90247-X`.

[139] G. Molière. „Theorie der Streuung schneller geladener Teilchen II. Mehrfach- und Vielfachstreuung". In: *Zeitschrift Naturforschung Teil A* 3 (1948), p. 78.

[140] P. A. Čerenkov. „Visible Radiation Produced by Electrons Moving in a Medium with Velocities Exceeding that of Light". In: *Physical Review* 52 (Aug. 1937), pp. 378–379. DOI: `10.1103/PhysRev.52.378`.

[141] IE Tamm and IM Frank. „Coherent radiation of fast electrons in a medium". In: *Dokl. Akad. Nauk SSSR.* Vol. 14. 3. 1937, pp. 107–112.

[142] Göring, D. „Analysis of the Poisson Structure of H.E.S.S. Sky Maps with Minkowski Functionals". Diploma Thesis. Friedrich-Alexander-Universität Erlangen-Nürnberg, 2008. URL: `http://www.ecap.nat.uni-erlangen.de/publications/pub/2008_Goering_Diplom.pdf`.

[143] A. M. Hillas. „The sensitivity of Cerenkov radiation pulses to the longitudinal development of cosmic-ray showers". In: *Journal of Physics G Nuclear Physics* 8 (Oct. 1982), pp. 1475–1492. DOI: `10.1088/0305-4616/8/10/017`.

[144] Konrad Bernlöhr. *CORSIKA and SIM TELARRAY – A package for the simulation of the imaging atmospheric Cherenkov technique and an investigation of important environmental parameters*

for such simulations. H.E.S.S. 1998. URL: http://www.mpi-hd.mpg.de/hfm/~bernlohr/mpik/report/report.ps.gz.

[145] Konrad Bernlöhr. *A simulation package for the H.E.S.S. Cherenkov telescope array.* H.E.S.S. 2014. URL: http://www.mpi-hd.mpg.de/hfm/~bernlohr/HESS/Software/sim_hessarray/.

[146] T. C. Weekes et al. „Observation of TeV gamma rays from the Crab nebula using the atmospheric Cerenkov imaging technique". In: *ApJ* 342 (July 1989), pp. 379–395. DOI: 10.1086/167599.

[147] A. M. Hillas. „Cerenkov light images of EAS produced by primary gamma". In: *International Cosmic Ray Conference* 3 (Aug. 1985), pp. 445–448.

[148] A. Daum et al. „First results on the performance of the HEGRA IACT array". In: *Astroparticle Physics* 8 (Dec. 1997), pp. 1–11. DOI: 10.1016/S0927-6505(97)00031-5.

[149] G. Pühlhofer et al. „The techn. performance of the HEGRA system of imaging air Cherenkov telescopes". In: *Astroparticle Physics* 20 (Dec. 2003), pp. 267–291. DOI: 10.1016/j.astropartphys.2003.06.001. eprint: astro-ph/0306123.

[150] A. Kohnle et al. „Stereoscopic imaging of air showers with the first two HEGRA Cherenkov telescopes". In: *Astroparticle Physics* 5 (Aug. 1996), pp. 119–131. DOI: 10.1016/0927-6505(96)00011-4.

[151] Balzer, A. „Systematic studies of the H.E.S.S. camera calibration". Diploma Thesis. Friedrich-Alexander-Universität Erlangen-Nürnberg, 2010. URL: http://www.ecap.nat.uni-erlangen.de/publications/pub/2010_Balzer_Diplom.pdf.

[152] W. F. Wargau. „Comparing Seeing Measurements at S. A. A. O./Sutherland, Gamsberg/Namibia and ESO/ La Silla". In: *Monthly Notes of the Astronomical Society of South Africa* 53 (1994), p. 88.

[153] M. Sarazin. *Gamsberg Astroclimatological Summary Report.* 1995. URL: http://www.eso.org/gen-fac/pubs/astclim/espas/gamsberg/gamsbergsum.ps.

[154] J. M. Davies and E. S. Cotton. „Design of the quartermaster solar furnace". In: *Solar Energy* 1 (Apr. 1957), pp. 16–22. DOI: 10.1016/0038-092X(57)90116-0.

[155] F. Acero et al. „Localizing the VHE γ-ray source at the Galactic Centre". In: *MNRAS* 402 (Mar. 2010), pp. 1877–1882. DOI: 10.1111/j.1365-2966.2009.16014.x. arXiv: 0911.1912 [astro-ph.GA].

[156] Stefan Gillessen. „Sub-Bogenminuten-genaue Positionen von TeV-Quellen mit H.E.S.S." Dissertation. 2004. URL: http://www.bsz-bw.de/cgi-bin/xvms.cgi?SWB11244050.

[157] F. Aharonian et al. „Calibration of cameras of the H.E.S.S. detector". In: *Astroparticle Physics* 22 (Nov. 2004), pp. 109–125. DOI: 10.1016/j.astropartphys.2004.06.006. eprint: astro-ph/0408145.

[158] P. Hofverberg et al. „Commissioning and initial performance of the H.E.S.S. II drive system". In: *ArXiv e-prints* (July 2013). arXiv: 1307.4550 [astro-ph.IM].

[159] J. Bolmont et al. „The camera of the fifth H.E.S.S. telescope. Part I: System description". In: *ArXiv e-prints* (Oct. 2013). arXiv: 1310.5877 [astro-ph.IM].

[160] A. Balzer et al. „The H.E.S.S. central data acquisition system". In: *Astroparticle Physics* 54 (2014), pp. 67–80. ISSN: 0927-6505. DOI: http://dx.doi.org/10.1016/j.astropartphys.2013.11.007. URL: http://www.sciencedirect.com/science/article/pii/S0927650513001655.

[161] W. T. Welford and R. Winston. *High collection nonimaging optics.* 1989.

[162] Wikipedia. *Round-robin scheduling — Wikipedia, The Free Encyclopedia.* [Online; accessed 4-June-2013]. 2013. URL: http://en.wikipedia.org/w/index.php?title=Round-robin_scheduling&oldid=557149038.

[163]   Sai-lai Lo and Steve Pope. „The Implementation of a High Performance ORB over Multiple Network Transports". In: *In Middleware 98: IFIP International Conference on Distributed Systems Platforms and Open Distributed Processing*. 1998, pp. 157–172.

[164]   OMG. *The Common Object Request Broker: Architecture and Specification*. Tech. rep. 2.0. Object Management Group, 1995.

[165]   Russel Sandberg et al. *Design and Implementation or the Sun Network Filesystem*. 1985.

[166]   GlusterFS. *Clustered File Storage that can scale to petabytes*. [Online; accessed 26-June-2013]. 2013. URL: http://www.gluster.org/.

[167]   Wikipedia. *Python (programming language) — Wikipedia, The Free Encyclopedia*. [Online; accessed 10-February-2014]. 2014. URL: http://en.wikipedia.org/w/index.php?title=Python_(programming_language)&oldid=594704716.

[168]   Wikipedia. *MySQL — Wikipedia, The Free Encyclopedia*. [Online; accessed 10-February-2014]. 2014. URL: http://en.wikipedia.org/w/index.php?title=MySQL&oldid=594623290.

[169]   Rene Brun and Fons Rademakers. „ROOT - An Object Oriented Data Analysis Framework". In: *AIHENP'96 Workshop, Lausane*. Vol. 389. 1996, pp. 81–86.

[170]   S. Ohm, C. van Eldik, and K. Egberts. „γ/hadron separation in very-high-energy γ-ray astronomy using a multivariate analysis method". In: *Astroparticle Physics* 31 (June 2009), pp. 383–391. DOI: 10.1016/j.astropartphys.2009.04.001. arXiv: 0904.1136 [astro-ph.IM].

[171]   Sebastian, Funk. „Online Analysis of Gamma-ray Sources with H.E.S.S." Diploma Thesis. Humboldt University Berlin, 2005. URL: http://www-eep.physik.hu-berlin.de/HESS/theses/pdfs/diplom_sebastian_funk.pdf.

[172]   François Brun. *Search for weak or transient sources in the inner Galactic plane regions with H.E.S.S. Application to the study of the W49B supernova remnant region*. Dissertation. 2011. URL: http://tel.archives-ouvertes.fr/tel-00645861.

[173]   N. Gehrels and P. Mészáros. „Gamma-Ray Bursts". In: *Science* 337 (Aug. 2012), pp. 932–. DOI: 10.1126/science.1216793. arXiv: 1208.6522 [astro-ph.HE].

[174]   N. Gehrels, E. Ramirez-Ruiz, and D. B. Fox. „Gamma-Ray Bursts in the Swift Era". In: *ARA&A* 47 (Sept. 2009), pp. 567–617. DOI: 10.1146/annurev.astro.46.060407.145147. arXiv: 0909.1531 [astro-ph.HE].

[175]   P. L. Nolan et al. „Fermi Large Area Telescope Second Source Catalog". In: *ApJS* 199, 31 (Apr. 2012), p. 31. DOI: 10.1088/0067-0049/199/2/31. arXiv: 1108.1435 [astro-ph.HE].

[176]   W. B. Atwood et al. „The Large Area Telescope on the Fermi Gamma-Ray Space Telescope Mission". In: *ApJ* 697 (June 2009), pp. 1071–1102. DOI: 10.1088/0004-637X/697/2/1071. arXiv: 0902.1089 [astro-ph.IM].

[177]   W. S. Paciesas et al. „The Fermi GBM Gamma-Ray Burst Catalog: The First Two Years". In: *ApJS* 199, 18 (Mar. 2012), p. 18. DOI: 10.1088/0067-0049/199/1/18. arXiv: 1201.3099 [astro-ph.HE].

[178]   C. Meegan et al. „THE fermi gamma-ray burst monitor". In: *ApJ* 702, 791 (Sept. 2009), pp. 791–804. DOI: 10.1088/0004-637X/702/1/791. arXiv: 0908.0450 [astro-ph.IM].

[179]   D. Lennarz et al. „Searching for TeV emission from GRBs: the status of the H.E.S.S. GRB programme". In: *ArXiv e-prints* (July 2013). arXiv: 1307.6897 [astro-ph.HE].

[180]   A. Balzer et al. „The H.E.S.S. Phase II Data Acquisition System". In: *Proc. CHEP 2013, Amsterdam*. 2013. URL: https://indico.cern.ch/event/214784/contribution/12.

[181]   J. Brucker. „Investigation of H.E.S.S. skymaps by means of Minkowski Functionals". Diploma Thesis. Friedrich-Alexander-Universität Erlangen-Nürnberg, 2007. URL: http://www.ecap.nat.uni-erlangen.de/publications/pub/2007_brucker_Diplom.pdf.

[182] D. Berge. „The gamma-ray supernova remnant RX J1713.7-3946 with H.E.S.S.“ Dissertation. Ruperto-Carola University of Heidelberg, 2006. URL: http://www.mpi-hd.mpg.de/hfm/HESS/public/phdtheses/Thesis_Berge.pdf.

[183] Y. Becherini, M. Punch, and H.E.S.S. Collaboration. „Performance of HESS-II in multi-telescope mode with a multi-variate analysis“. In: *American Institute of Physics Conference Series*. Ed. by F. A. Aharonian, W. Hofmann, and F. M. Rieger. Vol. 1505. American Institute of Physics Conference Series. Dec. 2012, pp. 741–744. DOI: 10.1063/1.4772366.

[184] R. D. Parsons and J. A. Hinton. „A Monte Carlo Template based analysis for Air-Cherenkov Arrays“. In: *ArXiv e-prints* (Mar. 2014). arXiv: 1403.2993 [astro-ph.IM].

[185] T.-P. Li and Y.-Q. Ma. „Analysis methods for results in gamma-ray astronomy“. In: *ApJ* 272 (Sept. 1983), pp. 317–324. DOI: 10.1086/161295.

[186] D. Berge, S. Funk, and J. Hinton. „Background modelling in very-high-energy γ-ray astronomy“. In: *A&A* 466 (May 2007), pp. 1219–1229. DOI: 10.1051/0004-6361:20066674. eprint: astro-ph/0610959.

[187] G. P. Rowell. „A new template background estimate for source searching in TeV gamma -ray astronomy“. In: *A&A* 410 (Oct. 2003), pp. 389–396. DOI: 10.1051/0004-6361:20031194. eprint: astro-ph/0310025.

[188] M. Lemoine-Goumard and H.E.S.S. Collaboration. „Selection and 3D-reconstruction of gamma-ray-induced air showers with H.E.S.S.“ In: *High Energy Gamma-Ray Astronomy*. Ed. by F. A. Aharonian, H. J. Völk, and D. Horns. Vol. 745. American Institute of Physics Conference Series. Feb. 2005, pp. 697–702. DOI: 10.1063/1.1878486.

[189] Julian Seward. *bzip2 and libbzip2, version 1.0.5: A program and library for data compression*. 2013. URL: http://www.bzip.org.

[190] Rene Rivera, B Dawes, and D Abrahams. *Boost c++ libraries*. 2013. URL: http://www.boost.org.

[191] R. A. Fisher. „On an absolute criterion for fitting fre quency curves“. In: *Messenger of Mathematics* 41 (1912). Ed. by R. A. Fisher, pp. 155–160.

[192] R. A. Fisher. „On the mathematical foundations of theoretical statistics“. In: *Philosophical Transactions of the Royal Society of London, A* 222 (1922). Ed. by R. A. Fisher, pp. 309–368.

[193] Donald W. Marquardt. „An algorithm for least-squares estimation of nonlinear parameters“. In: *SIAM Journal on Applied Mathematics* 11.2 (1963), pp. 431–441. DOI: 10.1137/0111030. URL: http://dx.doi.org/10.1137/0111030.

[194] Abraham Charnes, EL Frome, and Po-Lung Yu. „The equivalence of generalized least squares and maximum likelihood estimates in the exponential family“. In: *Journal of the American Statistical Association* 71.353 (1976), pp. 169–171.

[195] Ananth Ranganathan. „The levenberg-marquardt algorithm“. In: *Tutoral on LM Algorithm* (2004).

[196] Wikipedia. *Gauss–Newton algorithm — Wikipedia, The Free Encyclopedia*. [Online; accessed 3-December-2013]. 2013. URL: http://en.wikipedia.org/w/index.php?title=Gauss%C3%A2%C2%80%C2%93Newton_algorithm&oldid=577027204.

[197] Wikipedia. *Gradient descent — Wikipedia, The Free Encyclopedia*. [Online; accessed 3-December-2013]. 2013. URL: http://en.wikipedia.org/w/index.php?title=Gradient_descent&oldid=555039176.

[198] Mark Galassi and Brian Gough. *GNU scientific library: reference manual*. 2013.

[199] Danny C Sorensen. „Newton's method with a model trust region modification“. In: *SIAM Journal on Numerical Analysis* 19.2 (1982), pp. 409–426.

[200] Luc Demortier and Louis Lyons. „Everything you always wanted to know about pulls". In: *CDF note* 43 (2002).

[201] Mathieu de Naurios. *Model Analysis Internal Doumentation*. internal manual. H.E.S.S. Dec. 2013. URL: `http://llr.in2p3.fr/sites/hess/hess-documentation/parisanalysis/group_ _ParisAnalysis__ModelAnalysis.html`.

[202] John A Nelder and Roger Mead. „A simplex method for function minimization". In: *The computer journal* 7.4 (1965), pp. 308–313.

[203] J. Guy and M. de Naurois. *SMASH - Simulations with SASH*. internal manual. H.E.S.S. Mar. 2014. URL: `http://llr.in2p3.fr/sites/hess/hess-documentation/smash/`.

[204] J. Sitarek et al. „Physics performance of the upgraded MAGIC telescopes obtained with Crab Nebula data". In: *ArXiv e-prints* (Aug. 2013). arXiv: `1308.0141 [astro-ph.IM]`.

[205] Markus Holler. *Calculating Differential and Integral Sensitivities from Monte Carlo Simulations*. internal manual. H.E.S.S. June 2013. URL: `https://hess-confluence.desy.de/confluence/ download/attachments/720961/sensitivity.pdf`.

[206] A. V. Karelin et al. „The Proton and Helium cosmic ray spectra from 50 GeV to 15 TeV". In: *Astrophysics and Space Sciences Transactions* 7 (June 2011), pp. 235–238. DOI: `10.5194/astra-7-235-2011`.

[207] O. Adriani et al. „Cosmic-Ray Electron Flux Measured by the PAMELA Experiment between 1 and 625 GeV". In: *Physical Review Letters* 106.20, 201101 (May 2011), p. 201101. DOI: `10.1103/PhysRevLett.106.201101`. arXiv: `1103.2880 [astro-ph.HE]`.

[208] H.E.S.S. Collaboration et al. „H.E.S.S. observations of the Crab during its March 2013 GeV gamma-ray flare". In: *A&A* 562, L4 (Feb. 2014), p. L4. DOI: `10.1051/0004-6361/201323013`. arXiv: `1311.3187 [astro-ph.HE]`.

[209] J. D. Scargle. „Studies in Astronomical Time Series Analysis. V. Bayesian Blocks, a New Method to Analyze Structure in Photon Counting Data". In: *ApJ* 504 (Sept. 1998), p. 405. DOI: `10.1086/306064`. eprint: `astro-ph/9711233`.

[210] R. Ojha, E. Hays, R. Buehler, and M. Dutka. „Fermi LAT detection of a new gamma-ray flare from the Crab Nebula region". In: *The Astronomer's Telegram* 4855 (Mar. 2013), p. 1.

[211] W. A. Rolke, A. M. López, and J. Conrad. „Limits and confidence intervals in the presence of nuisance parameters". In: *Nuclear Instruments and Methods in Physics Research A* 551 (Oct. 2005), pp. 493–503. DOI: `10.1016/j.nima.2005.05.068`. eprint: `physics/0403059`.

[212] K. Kohri, Y. Ohira, and K. Ioka. „Gamma-ray flare and absorption in the Crab nebula: lovely TeV-PeV astrophysics". In: *MNRAS* 424 (Aug. 2012), pp. 2249–2254. DOI: `10.1111/j.1365-2966.2012.21388.x`. arXiv: `1202.6439 [astro-ph.HE]`.

[213] J. A. Hinton and W. Hofmann. „Teraelectronvolt Astronomy". In: *ARA&A* 47 (Sept. 2009), pp. 523–565. DOI: `10.1146/annurev-astro-082708-101816`. arXiv: `1006.5210 [astro-ph.HE]`.

[214] C. D. Dermer, S. J. Sturner, and R. Schlickeiser. „Nonthermal Compton and Synchrotron Processes in the Jets of Active Galactic Nuclei". In: *ApJS* 109 (Mar. 1997), p. 103. DOI: `10.1086/312972`.

[215] M. Georganopoulos, F. A. Aharonian, and J. G. Kirk. „External Compton emission from relativistic jets in Galactic black hole candidates and ultraluminous X-ray sources". In: *A&A* 388 (June 2002), pp. L25–L28. DOI: `10.1051/0004-6361:20020567`. eprint: `astro-ph/0110379`.

[216] R. Zanin. „MAGIC measurement of the Crab Nebula spectrum over three decades in energy". In: *International Cosmic Ray Conference* 7 (2011), p. 71. arXiv: `1110.2987 [astro-ph.HE]`.

[217] P. N. Bhat et al. „Sporadic emission of ultra high energy gamma rays from Crab pulsar". In: *Advances in Space Research* 3 (1984), pp. 135–138. DOI: `10.1016/0273-1177(84)90078-4`.

[218]   ISO. *ISO/IEC 14882:2011 Information technology — Programming languages — C++*. Geneva, Switzerland: International Organization for Standardization, Feb. 28, 2012, 1338 (est.) URL: `http://www.iso.org/iso/iso_catalogue/catalogue_tc/catalogue_detail.htm?csnumber=50372`.

[219]   Google. *Google C++ Testing Framework*. 2013. URL: `https://code.google.com/p/googletest`.

Danksagungen

Als allererstes möchte ich mich bei allen Personen bedanken, die mich während meiner Promotion unterstützt haben. Letzters gilt im Besonderen für Anneli, Markus, Matthias und Michael die mich in meinen dunkleren Zeiten immer motiviert und wieder aufgerichtet haben. Während meiner fast vierjährigen Zeit als Doktorand und meinen nun bald fünf Jahren in H.E.S.S. habe ich mit vielen verschiedenen Menschen aus den verschiedensten Ländern zusammengearbeitet; oft sind daraus Freundschaften entstanden, die mir bis heute sehr wichtig sind. Mein besonderer Dank gilt:

- Meinem Betreuer und Doktorvater Christian Stegmann, der seit meiner Zeit als Diplomand stets Vertrauen in meine Fähigkeiten hatte und mir unzählige Möglichkeiten zur freien Entfaltung geboten hat. Die mir während meiner Promotion gewährten Freiheiten haben sehr dazu beigetragen, dass ich nicht nur den Kurs meiner Arbeit sondern auch den Verlauf des H.E.S.S. Experiments mit beeinflussen konnte.

- Der gesamten H.E.S.S. Kollaboration für das entgegengebrachte Vertrauen und für die Auszeichnung mit dem H.E.S.S.-Preis.

- Anton für die gemeinsame Zeit in Erlangen, unsere Namibiaaufenthalte sowie unserem gemeinsamem Leidensweg und den daraus resultierenden endlosen Diskussionen über die Modelrekonstruktion.

- Anneli für ihr offenes Ohr, die vielen gemeinsamen Erlebnisse und die tolle Zusammenarbeit.

- Matthias für all die inspirierende Gespräche, ob im Büro oder privat, die Zeit in Namibia und das Antreiben in der Endphase meiner Promotion.

- Michael für die tolle Zeit während unseren Namibiareisen, die Übernahme des DAQ-Handys und für unsere unzähligen Kinobesuche.

- Markus für die gemeinsame Zeit als Diplomanden in Erlangen, unsere WG in Berlin und vielem mehr.

- Mathieu für die Möglichkeit seine Analyse weiterentwickeln zu dürfen, den Forschungsaufenthalt an der École Polytechnique und die verbrachte Zeit auf Site in Namibia.

- François B., Kora, François T., Jean-Paul, Albert, Toni, Frikki, Patrick, Petter, Andreas, Attila, Rico, Dominic, Christian und allen anderen mit denen ich viel Zeit auf Site in (und manchmal im Rest von) Namibia verbracht habe.

- Der Zeuthener H.E.S.S.-Gruppe mit Anhang: Kora, Michi & Bine, Bev, Emmett, Gianluca, Stefan, Christian, Markus, Anneli, Matthias und dem gesamten DESY Zeuthen für die inspirierende Atmosphäre.

Erklärung

Hiermit erkläre ich an Eides Statt, dass ich die vorliegende Arbeit selbst angefertigt habe; die aus fremden Quellen direkt oder indirekt übernommenen Gedanken sind als solche kenntlich gemacht.

Die Arbeit wurde bisher keiner Prüfungsbehörde vorgelegt und auch noch nicht veröffentlicht.

Potsdam, den 15. Dezember 2014